

CARDIFF UNIVERSITY

**Polythiophene Nanowires for use in Organic
Electronic Applications**

by

Mark D. Hampton

September, 2012

Thesis submitted for the degree of
Doctor of Philosophy

Cardiff University
School of Physics and Astronomy

Declarations

This work has not been submitted in substance for any other degree or award at this or any other university or place of learning, nor is being submitted concurrently in candidature for any degree or other award.

Signed

Date

STATEMENT 1 This thesis is being submitted in partial fulfillment of the requirements for the degree of PhD.

Signed

Date

STATEMENT 2 This thesis is the result of my own independent work/ investigation, except where otherwise stated. Other sources are acknowledged by explicit references. The views expressed are my own.

Signed

Date

STATEMENT 3 I hereby give consent for my thesis, if accepted, to be available for photocopying and for inter-library loan, and for the title and summary to be made available to outside organisations.

Signed

Date

Contents

1	Introduction	1
1.1	History	2
1.2	Poly(3-hexylthiophene-2,5'-diyl)	3
1.3	Poly(3,3'''-didodecyl-quarter-thiophene)	4
1.4	Organic Photovoltaics	5
1.4.1	Inorganic Photovoltaics	6
1.4.2	Development of Organic Photovoltaics	7
1.5	Field Effect Transistors	9
1.5.1	Inorganic Field Effect Transistors	10
1.5.2	Organic Field Effect Transistors	10
1.5.3	Water-gated Organic Field Effect Transistors	11
1.6	Organic Sensors	12
1.6.1	Water-gated Organic Field Effect Transistors Sensors	12
1.7	P3HT in Applications	13
1.7.1	P3HT Organic Photovoltaics	13
1.7.2	P3HT Organic Field Effect Transistors	14
1.7.3	P3HT Sensors	14
1.8	PQT-12 in Applications	15
1.8.1	PQT-12 Organic Photovoltaics	15

1.8.2	PQT-12 Organic Field Effect Transistors	17
1.9	Nanowires	18
1.9.1	Development	18
1.9.2	Uses	20
1.9.3	Nanowire Organic Photovoltaics	22
1.10	The Thesis	22
2	Theory of Device Operation	33
2.1	Organic Photovoltaics	33
2.1.1	Operating Principles of Organic Photovoltaics	33
2.2	Organic Field-Effect Transistors	40
2.2.1	Operating Characteristics	43
2.3	Charge Transport Models	45
2.3.1	Band Transport	46
2.3.2	Hopping Transport	48
2.3.3	Variable Range Hopping	49
2.3.4	Multiple Trap and Release	49
2.3.5	Grain Boundary Models	50
3	Experimental Techniques	53
3.1	Introduction	53
3.2	Atomic Force Microscopy	53
3.2.1	Tapping Mode Atomic Force Microscopy	56
3.2.2	Feature De-convolution	61
3.3	Ultra Violet-Visible Spectroscopy	63
3.3.1	Introduction and Basic Operation	63
3.3.2	Bonds Involved in Absorption	63
3.3.3	Beer's Law	64

3.3.4	Absorption Onset	64
3.3.5	Equipment	65
3.4	Photoluminescence	66
3.4.1	Introduction and Basic Operation	66
3.4.2	Equipment	68
3.5	Cyclic Voltammetry	69
3.5.1	Introduction and Basic Operation	69
3.5.2	Electric Double Layer	69
3.5.3	Nernst Equation	70
3.5.4	Mass Transport	70
3.5.5	Calculation Against $\text{Fe}(\text{C}_5\text{H}_5)_2$ Standard	72
3.5.6	Set Up	72
3.6	X-ray Diffraction	73
3.6.1	Introduction and Basic Operation	73
3.6.2	Scattering	74
3.6.3	Refraction	82
3.6.4	Domain Sizing and Paracrystallinity	82
3.6.5	Setup	85
4	Growth	93
4.1	Introduction	93
4.1.1	Review	94
4.2	Experimental	97
4.3	Results	98
4.3.1	Feature De-convolution	98
4.3.2	P3HT-Anisole NW Formation	98
4.3.3	P3HT-Cyclohexanone NW Formation	105

4.3.4	PQT-12-Toluene NW Formation	108
4.3.5	PQT-12-Chlorobenzene NW Formation	111
4.3.6	PQT-12-Trimethylbenzene NW Formation	113
4.3.7	Further Polymer-Solvent Combinations	115
4.3.8	UV-Vis	117
4.3.9	XRD	120
4.3.10	Orienting NWs	133
4.4	Discussion	137
4.4.1	P3HT	138
4.4.2	PQT-12	140
4.4.3	Absorption Spectra	140
4.5	Conclusions	141
5	Doping of Nanowires and their use in Organic Photovoltaics	149
5.1	Introduction	149
5.1.1	Why Dyes?	150
5.2	Experimental Details	154
5.2.1	Dyes	154
5.2.2	OPV Devices	155
5.3	P3HT-NW and PQT-12-NW OPV Device Performance	159
5.3.1	Results	159
5.3.2	Discussion	167
5.4	Dye-intercalation	168
5.4.1	Chemical Dye Structures	168
5.4.2	Experimental	170
5.4.3	Results	171
5.4.4	Discussion	172

5.5	Dye Intercalated OPVs	175
5.5.1	Results	175
5.5.2	Discussion	192
5.6	Conclusions	193
6	Organic Field-Effect Transistors and Sensing	199
6.1	Introduction	199
6.1.1	Publications	199
6.1.2	Background to Sheffield Group Research	200
6.1.3	Exposure Effects of Air on Polythiophenes	204
6.1.4	Water-Gated OFETs	206
6.2	Experimental	208
6.2.1	Device Preparation	208
6.2.2	Environment Control System	208
6.2.3	Device Characterisation	210
6.3	Results	212
6.3.1	Dry-gated OFETs, and Chemiresistor Sensors	212
6.3.2	Water-Gating	221
6.4	Discussion	225
6.4.1	Dry-gated OFETs, and Chemiresistor Sensors	225
6.4.2	WGOFETs	227
6.5	Design of New Electrodes	228
6.6	Conclusions	231
7	Conclusions	237
7.1	Nanowire Growth and Structure	238
7.2	Nanowire Doping and OPVs	240
7.3	Organic Field-effect Transistors and Sensors	241

7.4 Future Potential	243
A Chemistry Data	245
B OFET and Sensor Data	253

List of Figures

1.1	Molecular structure of polyacetylene	3
1.2	Structures of RR-P3HT and PQT-12	3
2.1	Schematic of the energy harvesting process of a bulk hetero- junction OPV	34
2.2	OPV energy level diagram describing principle operation of a device	35
2.3	Schematics of OFET structures	41
2.4	Schematic of OFET operation	42
2.5	Energy band diagram describing threshold voltage, V_T	43
2.6	Schematic of OFET operating regimes	44
2.7	Energy level sketch of 1-dimensional density-of-states	47
3.1	Schematic of AFM operating in tapping mode	54
3.2	Sketch of tip de-convolution	62
3.3	Diagram of Thomson scattering of an X-ray by an electron. . .	75
3.4	Sketch of X-ray diffraction	78
3.5	Grazing-incidence beam line geometry	87
4.1	Growth of P3HT NWs in anisole - AFM scans	100
4.2	Growth of P3HT NWs in anisole - AFM scans	101

4.3	Frequency distributions of P3HT anisole NW heights.	104
4.4	Growth of P3HT NWs in cyclohexanone - AFM scans	106
4.5	Growth of P3HT NWs in cyclohexanone - AFM scans	107
4.6	Growth of PQT-12 NWs in toluene - AFM scans	109
4.7	Growth of PQT-12 NWs in toluene - AFM scans	110
4.8	Growth of PQT-12 NWs in chlorobenzene - AFM scans	112
4.9	Growth of PQT-12 NWs in trimethylbenzene - AFM scans	114
4.10	AFM scans of further polymer-solvent combinations, where the solutions had been left to mature for 48 hours after cooling to room temperature.	116
4.11	Colour transistion of PQT-12 decalin solutions.	117
4.12	Absorption spectra describing PQT-12 toluene NW formation as a function of time from solution reaching room temp.	118
4.13	Absorption spectra for PQT-12 NW solution: as grown, rinsed, and supernatant.	119
4.14	Absorption spectra for non-NW and NW P3HT in anisole.	120
4.15	P3HT nanowire X-ray diffraction patterns as cast and annealed	122
4.16	Proposed monoclinic NW crystalline structure	123
4.17	P3HT NW OOP a-lattice parameter evolution through time and temperature during thermal annealing	127
4.18	P3HT nanowire domain sizes versus time through annealing	128
4.19	P3HT nanowire disorder versus time	128
4.20	OOP Line Profiles for P3HT NWs	129
4.21	OOP line profiles for P3HT Anisole NWs with fitted Gaussians.	130
4.22	PQT-12 nanowire X-ray diffraction patterns, as cast and an- nealed	132
4.23	PQT-12 trimethylbenzene NW diffraction pattern at 123°C.	133

4.24	Deposition methods for NW orientation - AFM scans	136
5.1	Solar spectra vs. P3HT nanowire OPV absorption	151
5.2	DSSC (Gratzel) OPV structure schematic	153
5.3	OPV device structure schematic	156
5.4	PCEs and VOC for varying non-NW to crystalline ratio in P3HT nanowire and PQT-12 nanowire OPV devices	162
5.5	J_{SC} and FF for varying non-NW to crystalline ratio in P3HT nanowire and PQT-12 nanowire OPV devices	163
5.6	J-V curves for devices deposited at 60°C.	164
5.7	P3HT-NW:PCBM OPV external quantum efficiency	166
5.8	Dye structures	169
5.9	OPV material energy band diagram	171
5.10	Dye intercalated NW emission spectra; dyes 1a and 1d	173
5.11	Dye intercalated NW emission spectra; dyes 2a and 2d	174
5.12	P3HT-NW:Dye:PCBM OPV performance metrics	177
5.13	Batch 4 J-V curves	182
5.14	Batch 5 J-V curves	183
5.15	Batch 6 J-V curves	184
5.16	Batch 7 J-V curves	185
5.17	Batch 4 annealed J-V curves	186
5.18	Batch 5 annealed J-V curves	187
5.19	Batch 6 annealed J-V curves	188
5.20	Batch 7 annealed J-V curves	189
6.1	Schematic of OFET test circuit	201
6.2	Example OFET test circuit outputs.	202
6.3	Example data extraction from OFET output graphs.	203

6.4	Schematic of water-gated OFET	208
6.5	Diagram of the gaseous analyte environment control system set-up	209
6.6	Device resistance and threshold voltage response during heat- ing of a P3HT nanowire OFET device	213
6.7	Device resistance response of P3HT nanowire OFET device during preliminary tests of exposure to octylamine	214
6.8	Device resistance response of P3HT nanowire OFET device to multiple exposures to octylamine	216
6.9	Transconductance of P3HT nanowire and P3HT film OFET devices in response to varying humidity	218
6.10	AFM images of humidity tested devices	219
6.11	NW-Film conductance response vs. RH comparison	220
6.12	Time evolution of output curves from water-gated P3HT NW OFETs	223
6.13	Time evolution of output curves from water-gated P3HT film OFETs	224
6.14	Photolithography and metal foil shadow mask electrode designs	229
6.15	Silicon nitride shadow mask electrode designs	230
A.1	Cyclic voltammograms of dyes 1a-1d.	246
A.2	Cyclic voltammograms of dyes 2a-2d.	247
A.3	Cyclic voltammograms of dyes 3 and 4.	248
A.4	Cyclic voltammograms of P3HT and PCBM	249
A.5	UV-Vis spectra of dyes 1a-2a	250
A.6	Dye intercalated NW emission spectra; dyes 1b and 1c	251

B.1	Time evolution of output curves from water-gated P3HT NW OFETs	254
B.2	Electrode shadow mask design	255

List of Tables

4.1	Average dimensions of final wires and first appearance of nanowires for all polymer-solvent combinations	118
4.2	P3HT nanowire domain sizes	125
4.3	P3HT nanowire paracrystallinity g-factor	125
4.4	P3HT nanowire lattice constants	126
5.1	P3HT-NW:PCBM and PQT-12-NW:PCBM OPV device metrics	161
5.2	Energy levels of dyes used in intercalated OPV devices	170
5.3	As cast dye OPV performance metrics	176
5.4	Annealed dye OPV performance metrics	191
6.1	Water-gated FET contact angles	222
A.1	Combustion analysis results	245

List of Abbreviations and Symbols

ϵ	Molar absorptivity
μ	Charge carrier mobility
μ_B	Charge carrier mobility in bulk
μ_{GB}	Charge carrier mobility at grain boundaries
v_d	Drift velocity
ψ_B	Bulk potential
ψ_S	Surface potential
a_{ox}	Oxidant chemical activity
a_{red}	Reductant chemical activity
AFM	Atomic force microscope/microscopy
AM	Air mass coefficient
BHJ	Bulk heterojunction
C60	Buckminsterfullerene
C_i	Insulator capacitance per unit area
cAFM	Conductive atomic force microscopy
CdSe	Cadmium selenide
CNT	Carbon nanotube
CV	Cyclic voltammetry
DB	Direct beam
e	Charge on an electron
E_A	Activation energy
E_C	Conduction band lower edge energy level

E_F	Fermi energy level
E_i	Intrinsic Fermi level
E_V	Valence band upper edge energy level
EDL	Electric double layer
EGOFET	Electrolyte-gated organic field-effect transistor
FET	Field-effect transistor
FF	Fill factor
G_Q	Conductance quantum
GaAs	Gallium arsenide
GIXRD	Grazing-incidence x-ray diffraction
h	Planck's constant
h_f	Sample feature height
HOMO	Highest occupied molecular orbital
I	Measured light intensity
I_0	Incident light intensity
$I_{D,LIN}$	Linear regime drain current
$I_{D,SAT}$	Saturation regime drain current
I_{OECT}	Electrochemical current
I_{OFET}	Field-effect current
InP	Indium phosphide
IP	In-plane
ISFET	Ion-sensitive field-effect transistor
ITO	Indium tin oxide
J_m	Maximum current density
J_{SC}	Short circuit current density
KPFM	Kelvin probe force microscopy
L	Channel length
LFM	Lateral force microscopy
LUMO	Lowest occupied molecular orbital
m	Mass

MEH-PPV	Poly[2-methoxy-5-(2-ethylhexyloxy)-1,4-phenylenevinylene])
MTR	Multiple trap and release
MWCNT	Multi-walled carbon nanotube
n	Number of charge carriers
NW	Nanowire
ODCB	1,2-dichlorobenzene
ODCB	Orthodichlorobenzene
OFET	Organic field-effect transistor
OLED	Organic light emitting diode
OOP	Out-of-plane
OPV	Organic photovoltaic
P3AT	Poly(3-alkyl thiophene)
P3AT	Poly(alkylthiophene-2,5'-diyl)
P3HT	Poly(3-hexylthiophene-2,5'-diyl)
P3PT	Poly(3-pentylthiophene-2,5'-diyl)
PAC	Polyacetylene
PC ₇₀ BM	Phenyl-C70-butyric acid ester
PCBM	Phenyl-C61-butyric acid methyl ester
PCE	Power conversion efficiency
PL	Photoluminescence
PMMA	Poly(methyl methacrylate)
PQT-12	Poly(3'''-didodecyl quarter thiophene)
q	Charge on electron
R _s	Sample sphere radius
R _T	AFM tip apex radius
RH	Relative Humidity
RR-P3HT	Regio-regular poly(3-hexylthiophene-2,5-diyl)
RRand-P3HT	Regio-random poly(3-hexylthiophene-2,5-diyl)
S	AFM image artifact length

SAM	Self-assembled monolayer
SPM	Scanning probe microscope/microscopy
STM	Scanning tunneling microscopy
SWCNT	Single-walled carbon nanotube
T	Temperature
t	Time
TFT	Thin film transistor
tm-AFM	Tapping mode atomic force microscopy
UV-Vis	Ultra-violet visible spectroscopy
V_G	Gate bias
V_m	Maximum voltage
V_{OC}	Open circuit voltage
V_{SD}	Source-drain bias
V_{SO}	Switch-on voltage
V_T	Threshold voltage
VOC	Volatile organic compounds
VRH	Variable range hopping
W	Channel width
WGOFET	Water-gated organic field-effect transistor
XRD	X-ray diffraction

Acknowledgments

There is a long list of people who I owe a lot of thanks and gratitude to for their help and encouragement throughout the production of this thesis. It has been an interesting, life questioning experience, and I have learnt a lot about myself and the processes involved in learning, exploring how people work, and understanding the motivations that drive people. Of course, I also learnt something about the material described within this thesis!

My first thanks go to my friends and family; my parents, Roy and Diane Hampton, who have provided me with loving support and of course plenty of financial support through my many years of academic study. I would like to show my thanks to my brother, Matthew, who has most likely not received quite the same level of monetary support from our parents due to myself having been the financial vacuum sucking it up. A huge acknowledgement must go to Laura Browne as she's put up with me and my already limited amount of free time, and coped with me when I wasn't on the best of form due to the challenges of the PhD!

I would like to thank my supervisors Emyr Macdonald and Martin Elliott, they guided my research, corrected my mistakes, and put faith in me at the beginning of the project.

My colleagues and co-PhDs from my lab and office: Samuele Lilliu for his tireless drive, good times shared at the synchrotrons and his invaluable

XRD-GUI software; Ellis Pires, again for his sharing of the synchrotron 'fun', and his endless discussions of work, life and the worries and woes of the World; Gareth for his valuable instant understanding of all things computer related, and his company in riding out the duration of our PhDs; Eduardo, Henje and Neil for their help around the lab, inspiration and good times in Cardiff; Steffan Cook for his discussions regarding NWs toward the end of my project.

Thanks also go to the numerous people that I have worked with in collaboration in various aspects of my PhD: Tiziano Agostinelli from Jenny Nelson's group at Imperial College, London for his assistance in the XRD experiments; the staff of the Diamond Light Source, especially those on beamlines I16 and I07, and the staff of ESRF, especially those on beamline BM28; Andrew Pearson, Darren Watters and Paul Staniec from David Lidzey's group at the University of Sheffield, and also James Kingsley of Ossila, for their assistance in the production of NW OPVs; Andrew Hallett and Jenn Jones from Simon Pope's Chemistry group at Cardiff University for their assistance in the synthesis of chromophores and optical and chemical characterisation techniques; Antonis Dragoneas, Abdullah Al Naim, and Delia Puzzovio of the Martin Grell group for their assistance in the fabrication and characterisation of NW OFETs and sensors; Karen Barnett and Chris Dunscombe for their help and teaching in the clean room, and Ian Robinson for making sure all my laboratory needs were taken care of at Cardiff.

Finally, a thank you to yourself for taking the time to read my thesis, part or all of it, and criticising, scanning over or enjoying my work.

Abstract

The growth and formation of polythiophene nanowires (NWs) was studied using atomic force microscopy (AFM), UV-Vis spectroscopy, and X-ray diffraction (XRD). This was followed by the successful development of a novel technique for doping the nanowires, which led to the doped NWs being investigated in the active blend of organic photovoltaics (OPVs). Finally exploratory work was carried out on the feasibility of NWs as humidity and octylamine sensors, and as the semiconducting medium in water-gated organic field-effect transistors (WGOFETs).

AFM revealed that the NWs were formed typically with heights of 1~10 nm, widths of 20~80 nm, and lengths exceeding 10 μm . The dimensions and the rate of growth of the NWs were affected by the polymer-solvent combination. XRD of the poly(3-hexylthiophene-2,5'-diyl) (P3HT) NWs suggested a structure that is in agreement with that of P3HT films found in the literature. There is vertical stacking of the alkyl-chains in the NWs, π -stacking of the thiophene chains along the long axis of the wires and the polymer back bones lie perpendicular to the length of the wire. It was seen that the NWs possessed a more compact alkyl chain stacking than the P3HT films. In situ thermal annealing of the NWs led to expansion of the alkyl chain stacking, an increase in domain sizes and a decrease in paracrystallinity. Poly(3,3'''-didodecyl-quarter-thiophene) (PQT-12) NWs displayed a meta-stable structure as cast, turning amorphous above 100°C, and recrystallising during cooling.

Photoluminescence (PL) and combustion analysis provided indirect evidence to suggest successful intercalation of anthraquinone based dye molecules

into P3HT and PQT-12 NWs during the growth phase, which is a novel and facile doping technique. Dye-intercalated P3HT-NW:PCBM OPVs showed an increase in power conversion efficiency (PCE) and open circuit voltage (V_{OC}), and a decrease in short-circuit density (J_{SC}) for one dye (2d) where the HOMO was deeper than that of both P3HT and PCBM.

Octylamine and humidity chemiresistor sensors were successfully fabricated from P3HT NWs. The chemiresistors showed an increase in resistance upon exposure to as little as 3.6 ppm of octyl-amine, and a ~13-fold increase in resistance at 36 ppm. P3HT NW humidity sensors had a greater response than a P3HT film, with a 75-fold increase in conductance at 90% relative humidity (RH) compared to less than 25% increase for the film. Both film and P3HT NW devices had a threshold of 50% RH below which no significant change in conductance was measured.

P3HT was successfully water-gated; NWs had a lower resistance than P3HT film water-gated organic field effect transistor (WGOFET) devices, while greater off-current was seen in the NW devices. P3HT-NW devices were found to be more sensitive than film devices indicated by a lower threshold voltage, and the electrochemical current to field-effect current, I_{OECT}/I_{OFET} , was lower for NWs compared to the film.

Chapter 1

Introduction

Organic electronics is a topic of research leading away from the traditional silicon based technology of the transistor, light-emitting diode, and photovoltaic cell, and instead employing polymers, macromolecules and small molecules in high-throughput, low cost electronics. The aims in using organic materials for these applications is to make production inexpensive and facile, and to explore additional possibilities over the contemporary inorganic applications. While organic materials may never fully replace inorganic semiconductors, as they are still very far off in their absolute performance, the low cost and ease of production means that they will be the preferred choice for certain applications. For example, an organic light emitting diode (OLED) television screen can be produced with as high a resolution as an inorganic one but the materials can be prepared much more easily. An organic photovoltaic (OPV) will not contribute to large scale energy production as the efficiency is much too low, so that the area required to produce a useful quantity of power would be much too vast. Organic materials though, can fill niche markets, with the possibility of flexible solar cells, allowing these to be attached to your bag or coat, and to trickle charge

your smartphone or laptop battery. The flexibility can be utilised in displays, and your smartphone or tablet could soon have a roll-out screen.

The reasons for the performance differences between organic and inorganic materials lies in their low mobility, partly related to their poor crystallinity. The charge transfer physics of these materials will be addressed in more detail in § 2.3. The high degree of long distance ordering in an inorganic crystal together with their high dielectric constant means that the free charges are highly delocalised and can travel a large number of lattice spaces without scattering. The high mobility of the materials mean that they respond strongly to external electric fields, and hence have high performances. Organics on the other hand, tend to possess much poorer crystalline packing with ordering only over a shorter range, and a much lower dielectric constant. The charges in these materials tend to be highly localised and need to tunnel or hop from lattice site to lattice site. They possess much lower mobility and as a result have much poorer performance for high speed electronics and low efficiencies.

We briefly summarise the history of organic electronics, followed by an in-depth analysis of polythiophene nanowire devices, in particular OPVs and OFETs (organic field-effect transistors) as these are the primary concerns of this thesis.

1.1 History

The first highly conducting polymer was reported in 1977 by Heeger, MacDiarmid and Shirakawa[1], in the form of iodine-doped polyacetylene (PAC) (figure 1.1), earning the trio the Nobel prize in chemistry in 2000. This began the era of conducting polymers, and was followed by the electro-

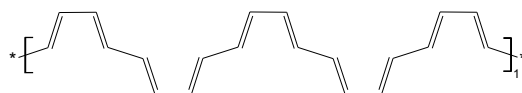


Figure 1.1: Molecular structure of polyacetylene

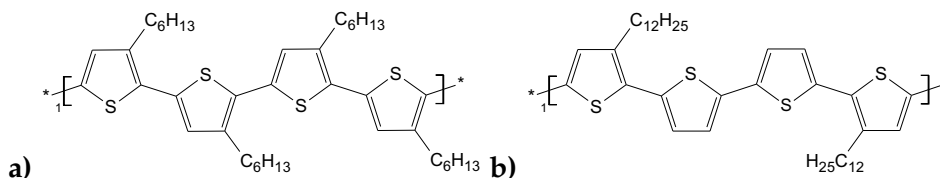


Figure 1.2: Structures of a) Regioregular-poly(3-hexylthiophene-2,5'-diyl) (RR-P3HT or commonly P3HT) and b) poly(3,3''- didodecyl-quarterthiophene) (PQT-12).

polymerisation of several other aromatic compounds, including thiophene, furan and benzene. The characteristic feature of PAc is its extended conjugated π -system, which allows for some delocalisation of charge carriers along the chain and leads to its relatively high conductivity.

1.2 Poly(3-hexylthiophene-2,5'-diyl) (P3HT)

The molecular structure of the polymer poly(3-hexylthiophene-2,5'-diyl) (P3HT) is depicted in figure 1.2 a). Originally the polymers were grown via electropolymerisation [2], and led to a polymer, by today's standards, with poor electrical properties, due to the poor quality of the resultant material with many impurities and structural deformations.

Polymerised thiophene has a similar structure to PAc but with the addition of the sulphur atom, which brings some structural rigidity to the chain. This improves charge transport by increasing long range ordering in the polymer and also aids crystallisation. The addition of alkyl side-chains to polythiophene to produce poly(3-alkylthiophene) (P3AT) improved the solubility of the polymer allowing for solution based processing. There are

three schemes for the site location of the alkyl chains for adjacent thiophene rings, these are: 2-5' (head to tail), 2-2' (head to head), and 5-5' (tail to tail). Polymers that possess a mixture of these schemes are known as regiorandom, and, as a result of the crossing of the alkyl chains, the thiophene rings twist out of the plane and this decreases the conjugation length. Polymers possessing nearly exclusively head to tail scheme are known as regioregular. This scheme allows the thiophene rings to sit in plane leading to an increased conjugation length and improved charge transport.

Thiophene polymerisation improvements were made by McCullough[3] in 1992, and led to a much higher regioregularity. Further techniques for the polymerisation of P3ATs were developed by Rieke[4] in 1992 and by McCollough[5, 6] in 1999.

1.3 Poly(3,3'''-didodecyl-quarter-thiophene) (PQT-12)

The molecular structure of the polymer poly(3,3'''-didodecyl-quarter-thiophene) (PQT-12) is shown in figure 1.2 b). PQT-12 was developed by Ong[7] in an attempt to create a polymer that would produce excellent thin film transistor (TFT) performance under ambient conditions. Its design was such that the alkyl chains, as with P3HT, allow for solution processability, the structural regularity induces molecular self-assembly, and the π -conjugation balances the transistor functionality and oxidative doping stability. This last property is achieved through its deeper HOMO in comparison to P3HT (-5.24 eV[8] compared to 5.00 eV for P3HT), making it less prone to oxidation, hence improving its stability in air.

1.4 Organic Photovoltaics (OPV)

The development of photovoltaic cells goes back to the 1800s, with Alexandre Becquerel observing the photovoltaic effect in 1839 with an electrode in a conductive solution exposed to light. The photovoltaic effect was observed further, with working devices being created throughout the 1800s, and several US patents received under the title of "Solar Cell" in the late 1880s and 1890s. A number of inorganic semiconducting materials were utilised in the early 1900s in solar cells and related research. This included copper and copper oxide used by Wilhelm Hallwachs, and cadmium selenide (CdSe), still used as a photovoltaic material today, by Audobert and Stora. In 1954 Bell Laboratories produced the first modern silicon solar cell with an efficiency of approximately 6%.

Efficiency of solar cells more than doubled by the start of 1960, with a 14% efficient solar cell being produced by Hoffman Electronics. Solar cells became utilised in space applications with the 1962 Telstar communications satellite receiving its power from solar cells.

From the 1960s onward, with the commercialisation of solar cells and their use in extraterrestrial applications, prices of solar energy began to drop. Hoffman Electronics 1955 2% efficient commercial solar cell had a power cost of \$1785/Watt. Today in the UK full photovoltaic systems can be installed on a domestic building for approximately £3000 per kWp, 500 times cheaper than the cost of the Hoffman cell by itself, without adjustment for inflation[9].

While the costs have decreased tremendously, the cost of energy from inorganic photovoltaics has still not reached grid parity, in that it is still more expensive to produce electricity from traditional inorganic solar cells

than it is from fossil fuels and nuclear. Recent reports have put the cost of building new solar farms in the UK at 20.2-38 p per kW h[10], in comparison to new nuclear sites at 9.9 p per kW h [11], and coal *with CO₂ capture* at 14.8 p per kW h[11]. These are the costs of generating electricity at the point of connection to the grid and so include initial capital, costs of operation, fuel, etc.

The large costs of the inorganic photovoltaic come from their production; silicon in the single crystal silicon cells is very intensive in energy and time to produce. A benefit of using organic materials is the high absorption coefficients in comparison to inorganic semiconductors which allow for thinner devices, on the order of 100 nm for the active material, compared to 100 μ m for crystalline silicon. On the other hand, organics tend to possess much narrower absorption bands and typically only absorb over the visible spectrum whilst inorganic semiconductors absorb up to 1000 nm (1.1 eV).

1.4.1 Inorganic Photovoltaics

Currently the vast majority of photovoltaics are fabricated from inorganic materials, with the most popular types being silicon - crystalline, amorphous - and III-V materials such as GaAs. Power conversion efficiency (PCE) is the main indicator of a solar cell's performance and is typically given as the power output of the device as a percentage of the power of the light incident on the device. The best performing cells to date are thin film GaAs with a PCE of 28.3 ± 0.8 %, crystalline InP (22.1 ± 0.7 %), crystalline silicon (25.0 ± 0.5 %), and multicrystalline silicon (20.4 ± 0.5 %)[12].

The PCE of these devices are nearing the theoretical limit for single layer devices for the AM1.5 solar radiation. AM1.5, corresponds to the solar spectrum at a solar zenith angle of 48.2°, or the equivalent of the path length of

1.5 times the distance through the atmosphere. It is used to represent the average radiation as experienced by many of the World's major population centres which lie some distance from the equator.

1.4.2 Development of Organic Photovoltaics

Photovoltaic properties were reported using organic materials back in 1958, with an interesting system of magnesium phthalocyanine disks coated with a thin film of air-oxidised tetramethyl *p*-phenylenediamine[13].

In 1986 Tang[14] produced an improvement in the power conversion efficiency of the organic solar cells when he introduced the first donor/acceptor planar heterojunction organic solar cell. This design took advantage of the differing electron affinities to separate the charges of an exciton at the interface between the two materials. The efficiency of the device was 1% under AM2 illumination.

Sariciftci et al[15] introduced the first polymer:C60 solar cell in 1993. It was identified for its potential for photovoltaic energy conversion with the suggestion of increasing the effective area of the heterojunction interface.

An increase in performance of OPVs was achieved by Yu[16] in 1995 with the introduction of the bulk heterojunction, where the donor and acceptor materials are blended together producing an interpenetrating network that increases the interface area within the OPV, allowing for much greater charge separation and yield. The materials used in this blend were poly[2-methoxy-5-(2-ethylhexyloxy)-1,4-phenylenevinylene] (MEH-PPV) and C₆₀, and the device yielded an efficiency of 2.9% under monochromatic illumination.

P3HT:PCBM OPV devices were demonstrated by Chirvase et al[17]. This material combination has proved to be highly popular. It has been used extensively as a standard for researching the effects of any changes to the

preparation and structure of OPV devices, where the large volume of research carried out on it allowed for easy comparison between adjustments in fabrication parameters. It was soon found to not yield the highest efficiencies and other materials for use in the bulk heterojunction have taken over in popularity.

The performance of an organic solar cell is dependent on a complex interplay of many factors, including photon absorption, charge separation, and charge transport and extraction. There is an extensive number of parameters in fabrication and processing of organic devices that affect these factors. The main aim is to absorb as much light as possible and harvest every excited electron as a result of the light absorption. The harvesting requires separation of electron-hole pairs, transport of the charge carriers to their relevant electrodes and then extraction of the charge carriers, all while avoiding charge recombination.

The main stage in organic solar cell performance improvement lies in improving the morphology of the active blend in order to induce long range order and crystallinity, while at the same time producing domain sizes for the different phases of the blend that are of the order of the exciton diffusion length and that make continuous pathways to the relevant electrodes. Many processing techniques have been investigated to achieve this.

Thermal annealing was shown to increase the PCE of the devices. This was revealed to be as a result of an improved morphology of the heterojunction blend, allowing for more efficient exciton dissociation and charge collection[18]. Along with thermal annealing, solvent annealing, where exposure of the active blend to solvent vapour was shown to have a similar effect as thermal annealing in that an improved morphology could be achieved[19].

Heliatek announced this year that their organic tandem device had achieved an efficiency of 10.7% [20], which trumped Mitsubishi Chemical's 2011 efficiency record of 9.2% [21]. Heliatek produced a cell utilising oligomers in a tandem structure, where two devices which absorb over different ranges of the solar spectrum are sandwiched together. A non-tandem, single unit structured device using the oligomers produced a PCE of 7%.

Finally, large-scale fabrication, and device stability and lifetimes are required to be developed in order to produce a workable commercial product.

1.5 Field Effect Transistors (FETs)

A design for a transistor was first described by the Austro-Hungarian physicist J.E.Lilienfield in patents applied for in Canada in 1925 and USA in 1926[22]. A description for the possibility of controlling the resistance of a semiconducting medium using an electric field was described in a British patent by the German, Oskar Heil in 1935[23].

The basic idea of an OFET is that the density of charge carriers within a semiconducting channel connecting two contacts (*source* and *drain*) is modulated (or 'gated') via a bias applied to a third (*gate*) contact which is insulated from the channel. The semiconducting channel, insulator and gate contact act as a capacitor and can be used to accumulate charge within the channel. This charge can then flow between the source and drain when an appropriate bias is applied between them. A more detailed description of the operation of an OFET can be found in § 2.2.

1.5.1 Inorganic Field Effect Transistors

The most common semiconductor material used in inorganic FETs is silicon, which is usually highly doped and can have an electron mobility of $1,450 \text{ cm}^2/\text{Vs}$ and a hole mobility of $500 \text{ cm}^2/\text{Vs}$, both at 300 K. Other materials that are used include the III-V semiconductor gallium arsenide (GaAs). This has an electron mobility in excess of that of silicon, at $8,000 \text{ cm}^2/\text{Vs}$, allowing it to operate with a frequency of 250 GHz which makes it useful for high-frequency applications. GaAs also has the advantages over silicon of relative insensitivity to heat due to the wider band gap, and less noise due to the higher carrier mobility and lower device parasitic resistance.

Other III-V materials used in FETs include indium antimonide with an electron mobility of $80,000 \text{ cm}^2/\text{Vs}$, and is used in high frequency transistors due to the high mobility[24].

The II-VI material cadmium sulphide was one of the first semiconducting materials used to make thin film transistors (TFTs), and possess an electron mobility of $350 \text{ cm}^2/\text{Vs}$ [25].

1.5.2 Organic Field Effect Transistors (OFETs)

A number of materials that have been explored for use in FETs include inorganic-organic blends. Graphene and carbon nanotubes (CNTs) have been used in OFETs and have been shown to possess very high charge carrier mobilities. Graphene was shown to have an electron mobility of $200,000 \text{ cm}^2/\text{Vs}$ [26].

CNT FETs were demonstrated back in 1998[27], where a single CNT position between two Pt electrodes was switched between conducting and insulating states via application of a voltage to Si gate. CNT FETs have been

developed greatly since 1998, and now demonstrate field-effect mobilities of greater than $79,000 \text{ cm}^2/\text{Vs}$ [28].

Other organic materials are being investigated in OFETs. Their mobilities aren't as impressively high as those possessed by CNTs and graphene but they are showing promising signs of performance. Single crystal OFETs have been developed such as those of Podzorov et al which utilise single crystal Rubrene with a hole mobility of $8 \text{ cm}^2/\text{Vs}$ [29]. The high degree of order in this crystal allows for efficient charge transport.

Oligomers have been used in OFETs. The oligomer 5,7,12,14-tetrachloro-6,13-diazapentacene (TCDAP) was used by Islam et al and had a electron mobility of $3.39 \text{ cm}^2/\text{VS}$ [30].

1.5.3 Water-gated Organic Field Effect Transistors (WGOFETs)

Water-gated OFETs (WGOFET) were developed by Kergoat et al in 2010[31], being based on the electrolyte-gated OFET (EGOFET)[32]. An EGOFET consists of a planar layout of source and drain contacts connected by a semiconducting material, with an electrolytic solution located on top which is typically gated by a metallic probe. Upon application of a bias to the gate probe an electric double layer (EDL) is established at the electrolyte-semiconductor interface. The EDL behaves like a capacitor with the semiconductor upon which charge accumulates. Bias applied to the drain causes this charge to flow. This behaviour is similar to that of a solid-state transistor but allows for low operating voltages. This is due to the high capacitance at the electrolyte-semiconductor interface because of the very thin EDL which is of the order of 0.1 \AA .

Kergoat produced WGOFETs initially using either a rubrene single crystal or a P3HT film between gold source and drain electrodes; de-ionised

water was used in place of the electrolyte used in EGOFETs and gold was used as the gate electrode. The devices operated similarly to a solid-state device but showed lower mobility. The lower mobility was attributed to charge transport that is highly sensitive to surface defects and roughness of the semiconductor surface, where there is contact with the water and a higher density of charge carriers. These devices operated over a low voltage range of less than 1V for both the drain and the gate biases, which is an attractive property for low-energy electronics.

Kergoat improved upon the original P3HT device and showed that improved electrical performance could be achieved using P3HT blended with PMMA[33]. Mobilities were higher, up to $0.15\text{cm}^2/\text{Vs}$, an increase of over two orders of magnitude.

1.6 Organic Sensors

Organic sensors have been developed for various uses including sensing volatile compounds produced in explosives[34, 35, 36] and given off by plant matter under attack from insect infestations[37]. Organic sensors have also been used in sensing strain[38], and in pressure sensors[39]. Various methods to realise the sensor, including changes in the conductivity of the sensor and changes in the luminescence, have been utilised.

1.6.1 WGOFET sensors

The ability to detect water-borne analytes is a highly attractive prospect: the detection of contaminated drinking water and sensing biomolecules for medical purposes are two important applications. WGOFETs have the advantage over EGOFETs in that they are compatible with biomolecules. The

cations in the electrolyte of an EGOFET can interact with the biomolecules via electrostatic means, and therefore become screened. Charged molecules become surrounded by ions of the opposite charge due to electrostatic interactions. The electrostatic potential occurring due to the charged molecules decays exponentially with distance as a result of the surrounding oppositely charged ions. The distance over which mobile charges screen out electric fields is known as the Debye length. Using a solution with a high ion concentration in the EGOFET, such as phosphate buffered saline, the Debye length is less than 1 nm. Using 18 M Ω de-ionised water it is approximately 200 nm. This screening results in the biomolecules not being 'sensed' by the semiconductor of the OFET. This effect was shown by Kergoat[40] when demonstrating that DNA could be detected by WGOFETs.

1.7 P3HT in Applications

1.7.1 P3HT OPVs

P3HT has become the polymer of choice for testing OPVs, as it has now been so extensively experimented on that new developments and ideas are first tested on P3HT. P3HT has also been used in OFETs, OLEDs and sensors. Typically P3HT has been used as an electron donor along with PCBM as the acceptor. The maximum reported efficiency of a device using these materials is 6.5% as reported by Lee et al[41]. This is 2.7% points below Mitsubishi Chemical's 2011 efficiency record of 9.2%[21] for an organic device, and 4.2% points below Heliatek's record of 10.7% for an organic device which utilised a tandem structure.

1.7.2 P3HT OFETs

P3HT has been studied as the semiconducting channel material of field-effect transistors[42, 43, 44], with the first P3HT OFET being produced by Assadi in 1988[45]. It has largely been studied as a p-type semiconductor, where the predominate charge carriers are holes. Mobilities of $10^{-5} - >0.1 \text{ cm}^2/\text{Vs}$ have been recorded[43], which are lower than that of single organic crystals such as rubrene, where charge carrier mobilities as high as $15 \text{ cm}^2/\text{Vs}$ have been recorded[46]. Of course, these are not able to compete with high mobilities of inorganic semiconductors, where the electron and hole mobilities at 300K are 1,450 and $500 \text{ cm}^2/\text{Vs}$ for silicon, 8,000 and $400 \text{ cm}^2/\text{Vs}$ for gallium arsenide (GaAs), and 80,000 and $1,250 \text{ cm}^2/\text{Vs}$ for indium antimonide (InSb)[24]. Record ultrahigh electron mobilities of $200,000 \text{ cm}^2/\text{Vs}$ have been recorded in graphene[47].

1.7.3 P3HT Sensors

P3HT has been used in various types of sensors: chemiresistive sensors[48, 37]; strain sensing photocurrent sensors[49]; and ion-sensitive FETs[50].

Khot[48] used a dip-coating method to produce films of P3HT for chemoresistive sensors that were utilised for sensing alcoholic volatile organic compounds (VOCs). The VOCs that were detected were 3-methyl-1-butanol and 1-hexanol, which are found to be present in spoiled and Salmonella typhimurium contaminated beef packages. The devices were reproducible, with lower detection limits of 10 and 15 ppm for the two VOCs respectively.

VOC sensing P3HT chemiresistors were also produced by Weerakoon[37], where they were used to detect γ -terpinene, a chemical emitted by pine trees during bark beetle infestations. The presence of γ -terpinene increased the

resistance of optimised P3HT films by two orders of magnitude at room temperature; the detection limit was found to be 36 ppm. The authors believed that the analytes physically blocked the charge conduction in the films therefore increasing the resistance of the films.

Zan[51] used P3HT as a capping layer on amorphous gallium zinc oxide TFTs. With these TFTs 100ppb of ammonia and acetone were sensed separately and the response was reversible. Vapour molecules, which were oxidising or reducing, acted as electron acceptors or donors and changed the potential of the P3HT layer and therefore the current of the underlying gallium zinc oxide TFT.

Scarpa[50] produced ion-sensitive field effect transistors (ISFETs) using P3HT as the semiconducting sensing medium. It was found that the transistor did not deteriorate when measurements were performed in electrolytes. Where degradation was seen, when operating in liquid, an alternating current operating mode could be used to compensate. Scarpa found that ions and analytes sensed by the P3TH ISFETs were diffusing through the polymer reaching the dielectric interface where electrical conduction took place.

Strain sensors were fabricated by Ryu[49] using a nanocomposite of P3HT and multi-walled carbon nanotubes (MWCNTs), where the level of photocurrent generated by the nanocomposite scaled with the applied level of strain.

1.8 PQT-12 in Applications

1.8.1 PQT-12 OPVs

As PQT-12 has a deeper HOMO than that of P3HT (-5.24 eV[8] compared to 5.00 eV for P3HT). It is believed that it would be more stable in air and less

prone to degradation which would make it suitable for organic electronic devices such as OPVs. A few studies have been carried out to investigate its performance as a electron donor in BHJ OPVs.

Wantz et al[52] produced OPVs using PQT-12 where they blended the polymer with PCBM and achieved an efficiency of only 0.3-0.4%. By varying the ratios of PQT-12 to PCBM they found that the highest efficiency devices required an excess of PCBM. In contrast to P3HT devices, where the ratios are typically 1:1 or slightly in favour of the polymer[53], 3 times as much PCBM as PQT-12 was required. This ratio of polymer to fullerene was thought to balance the charge carrier mobilities in each of the materials of the blend, lowering space charges and therefore decreasing recombination. They found that thermal annealing improved the device performance, as has been found in P3HT film devices. This trend in polymer:PCBM ratio was also noted by Thompson[54]. Here an optimal annealing temperature of 100°C yielded the highest efficiencies. DSC thermograms of PQT-12 showed that the polymer goes through a crystal-to liquid crystal transition at 95°C and a liquid crystal-to-isotropic transition at 110°C. While the bulk mobilities of P3HT and PQT-12 in relation to OPV devices are similar, the reason for the poor performance of the PQT-12 OPVs compared to P3HT devices has yet to be found but is thought to lie in the blend morphologies and phase segregation of the polymers and the fullerene.

Vemulamada's examination of PQT-12 OPVs utilised PC₇₀BM as the electron acceptor in the active blend[55] and produced devices with a PCE of 1.4%. The optimum blend ratio of PQT-12:PC₇₀BM was found to be 1:2 in this case and increased PC₇₀BM degraded performance of the devices. The efficiency of the devices was believed to be limited primarily by the morphology with an absence of sufficient percolation pathways to the respective

electrodes.

1.8.2 PQT-12 OFETs

PQT-12 was initially created for the purpose of producing a material with improved environmental stability via a deep HOMO yet would exhibit excellent OFET performance with high mobility through high crystallinity[7]. Primary studies on PQT-12 OFETs with bottom-gate top-contact structure yielded excellent TFT properties, with an as cast mobility of $0.02\text{-}0.05\text{ cm}^2/\text{Vs}$, which rose to $0.14\text{ cm}^2/\text{Vs}$ after annealing at $120\text{-}140^\circ\text{C}$. On/off ratios were 10^6 as cast rising to 10^7 after annealing.

Salleo's work[56] showed that the performance of PQT-12 devices could be controlled through manipulation of the morphology of the semiconducting channel film by processing the material at different temperatures. Further work by Ong[8] showed that the morphology of the film plays an important role in the performance of the devices when they examined nanoparticles of PQT-12 that formed in solution of dichlorobenzene. Surface treatment of the silicon substrate with a silane self-assembled monolayer (SAM) increased the mobility of the device for films not containing nanoparticles, while the nanoparticle device had further increased mobility. A combination of surface treatment and nanoparticles yielded mobilities of $0.06\text{ cm}^2/\text{Vs}$. Annealing of the surface treated nanoparticle devices produced mobilities as high as $0.2\text{ cm}^2/\text{Vs}$.

Hsieh[57] developed nanocomposite TFTs based on non-percolating networks of single-walled carbon nanotubes (SWCNTs) and PQT-12 thin films created through ink-jet printing. They found an effective hole mobility of $0.23\text{ cm}^2\text{V}^{-1}\text{s}^{-1}$, which is an enhancement of 7 over ink-jet printed pristine PQT-12 TFTs.

1.9 Nanowires (NWs)

There are many 1-D nanostructures that are currently of great interest (nanowires, -fibers, -whiskers and -ribbons) ranging over a great deal of materials from inorganics to organics. This section will focus mainly upon the research that has been undertaken in polythiophene nanowires grown via the whisker method, and those materials and methods that are closely related to those topics of research.

1.9.1 Development

Organic nanowires were first grown via the whisker method by Ihn et al[58] in 1993; the organic polymer was dissolved in a heated marginal solvent and then allowed to crystallise as the solvent cooled to room temperature. They found that under these conditions P3ATs will form crystals with heights and widths of a few nanometres up to tens of nanometres and lengths of a few micrometres. They also found that the solvents that allowed for this process to happen was dependent on the alkyl-side chain length, where a longer side chain needed a poorer solvent to form nanowires compared to the polymer with a longer side chain. This can be expected as the longer the side chain the more soluble the polymer is. The process of crystallisation occurs through the decrease in solvent action as the solvent becomes poorer as it cools, after the polymer was dissolved by the solvent being good at higher temperatures.

A similar method for P3HT nanowire production has been demonstrated by Kiriy et al[59], where the polymer is dissolved in a good solvent at room temperature and is then crystallised out of the solution by the addition of a poor solvent. This reduces the effectiveness of the solution forcing the

polymer to crystallise out of the solution. Kiriya demonstrated this by adding hexane to a P3AT chloroform solution. They suggested that the resulting nanowires had a helical conformation, although this structure is discordant with more popular models of P3AT crystallisation.

Malik et al[60] investigated the gelation of P3ATs in solution of xylene. They proposed that a two stage process occurs in the gelation process and this may be extended to more dilute solutions. First a coil-to-rod transformation occurs where the disordered dissolved polymer chains straighten. The second step is fibrillar crystallisation of the rods. The initial coil-to-rod transformation was accompanied by a red shift in the absorption spectrum of the solutions which was due to an increase in the conjugation length because of the straightening of the polymer backbone. This appears to be the prevailing theory of formation of P3AT fibers in solution.

Samitsu et al[61] looked at the growth of P3ATs and several other polymers using Ihn's whisker method of cooling a solution containing a marginal solvent. They found that regio-random (RRand) P3HT failed to produce NWs. RRand-P3HT has the alkyl side chains located randomly off the thiophene rings compared to regio-regular (RR) P3HT where the side chain takes up regular positioning off the thiophene rings. This indicated that the NW formation relied partly on the alignment of the polymer main chain, and that the randomly oriented side chains could disrupt NW formation by obstructing the main chain alignment. Samitsu also found that PQT-12 would also assemble into NWs via the same whisker method when using toluene as the solvent.

Oosterbaan et al[62], when using the whisker method, found a correlation between the growth of P3AT nanowires, the refractive index of the solvent and the side-chain length of the polymer. The refractive index is

a function of the dielectric constant, itself linked to the polarity of the solvent, and hence its ability to dissolve the polymer and its suitability to form nanowires. This also ties in with the solubility of the nanowires based on their side-chain length as mentioned previously.

It has been suggested that anisole is an excellent solvent for growing P3HT nanowires, as determined by Oosterbaan in the above paper, and as used by Samitsu[63] when they studied the structural, optical, and electronic properties of P3ATs.

While the whisker method is a popular and effective method for growing polythiophene nanowires alternative approaches exist, for example the method as exhibited by Tran in 2008[64] in which a small amount of an additive is introduced into the polymerisation reaction. In the case of polythiophene nanofibers, thiophene and terthiophene in solution of o-dichlorobenzene are rapidly mixed with a solution of FeCl_3 in acetonitrile, which is vigorously mixed and then left to rest for a day. Following this, the product is then centrifuged out and washed with large amounts of solvent.

Using an extension of the above method D'Arcy[65] used a novel method in 2010 to form a monolayer of the nanowires on any substrate. In a mixture of oil, water and nanowires, after some preparation the nanowires accumulate on two water-oil interfaces and can be deposited on to a substrate forming a perfect monolayer.

1.9.2 Uses

Berson et al[66] demonstrated in 2007, that P3HT nanofibers could be used in photovoltaic applications when they blended P3HT NWs with [6,6]-Phenyl C6 butyric acid methyl ester (PCBM). They found that the nanofibers, whilst not having a dramatic increase in power conversion efficiency compared to

a similar film, did have an improvement in efficiency in the as-cast devices compared to a film. The efficiencies then became much the same as an annealed film after device annealing. Interestingly the group also found that there was an optimum ratio of non-crystalline to crystalline material that gave the best PCE in their devices; this requirement was also seen by Bertho et al[67] in their experiments. It is believed that the non-crystalline material acts to connect the NWs and improve the pathways to the hole collecting electrode, without which the orientation and separation of the NWs means that there are many dead ends, and a large amount of recombination of charges occur.

Most recently Kim et al[68] looked at the efficiency of OPVs as a function of ageing time of the P3HT nanowire dichlorobenzene solution and found that 60 hours gave the optimal OPV performance; solution ageing times over 60 hours gave rise to larger aggregates of P3HT leading to poor charge separation.

Sun et al[69] looked at the performance of solar cells using nanowires grown using the whisker method utilising a marginal solvent but with the addition of a small amount of a good solvent. The authors added 10% and 20% volume of chlorobenzene to the anisole solution at the start of the NW preparation and found an increased amount of crystallinity and the formation of narrow NWs compared to a pure anisole solvent solution.

Several groups have investigated the electrical properties of nanowires by building organic field effect transistor (OFET) devices, and looking at nanowire networks and single wires. Merlo and Frisbie carried out work in 2003[70] and 2004[71] using P3HT nanowires grown via the whisker method and looked at the electrical properties of multiple and single nanowires under an inert atmosphere of N_2 .

Yonemura[72] placed P3HT NWs into strong magnetic fields and found that the NWs oriented with their long axis perpendicular to the direction of the magnetic field. The anisotropy of the magnetic susceptibilities of the $\pi - \pi$ stacking of the thiophene rings in the NWs led to this orientation.

1.9.3 Nanowire OPVs

As discussed previously in § 1.9.2, Berson et al[66] created the first P3HT NW solar cells in an attempt to utilise the dimensions of the NWs to achieve the ideal interpenetrating morphology that is required for efficient exciton dissociation and charge separation.

1.10 The Thesis

The thesis describes an investigation of nanowires of the conjugated polymers P3HT and PQT-12 to understand their formation, morphology and structure. It also includes work investigating their performance in organic electronics as photovoltaic devices, transistors and sensors. We also develop a new class of hybrid material that was conceived as a result of the above work, where dye molecules are intercalated into the nanowires without major disruption of their structure. Exploratory studies were carried out on the dye-intercalated NWs where the dyes were used to improve the performance of the devices. The performance enhancement of the dyes was expected through improving the absorption of light of the devices whilst attempting to optimise the energy level alignment within them. The optimisation of the energy level alignment was essential to retain the charge carrier separation and transfer which is an essential operating principle of the devices. Finally an exploration of the materials as vapour and liquid sensors

was conducted, with a shortened response time over films expected due to their increased surface area.

Chapter 2 gives an introduction to some of the theoretical aspects of organic photovoltaics, organic field-effect transistors, and charge transport mechanisms. Chapter 3 introduces the main experimental techniques used, including scanning probe microscopy, UV-vis spectroscopy, photoluminescence spectroscopy, and X-ray diffraction. There are a few further experimental techniques used in the thesis and these are addressed at the relevant sections. Chapter 4 examines the growth of the nanowires in different solvents using the four diagnostic techniques listed in chapter 3, aiming to shed light on the formation and structure of the nanowires. Chapter 5 is concerned with the performance of the nanowires as the electron donor in the active blend in OPV devices. A comparison is drawn between devices constructed with PQT-12 and P3HT nanowires, and an enhancement of the performance of P3HT NW devices is sort via intercalation of chromophores. Chapter 6 presents data obtain when producing OFET devices, and testing the nanowires as sensors of humidity and octyl-amine. Chapter 7 presents a discussion of the results and looks at future experiments to extend the work presented in this thesis.

Bibliography

- [1] Nobelprize.org. The nobel prize in chemistry 2000. http://www.nobelprize.org/nobel_prizes/chemistry/laureates/2000/, 2012. [Online; accessed 20-February-2012].
- [2] Tourillon G and Garnier F. New electrochemically generated organic conducting polymers. *Journal of Electroanalytical Chemistry and Interfacial Electrochemistry*, 135(1):173 – 178, 1982.
- [3] McCullough R D and Lowe R D. Enhanced electrical conductivity in regioselectively synthesized poly(3-alkylthiophenes). *Journal of the Chemical Society, Chemical Communications*, pages 70–72, 1992.
- [4] Chen T A and Rieke R D. The first regioregular head-to-tail poly(3-hexylthiophene-2,5-diyl) and a regiorandom isopolymer: nickel versus palladium catalysis of 2(5)-bromo-5(2)-(bromozincio)-3-hexylthiophene polymerization. *Journal of the American Chemical Society*, 114(25):10087–10088, 1992.
- [5] Loewe R S, Khersonsky S M, and McCullough R D. A simple method to prepare head-to-tail coupled, regioregular poly(3-alkylthiophenes) using grignard metathesis. *Advanced Materials*, 11(3):250–253, 1999.
- [6] Loewe R S, Ewbank P C, Liu J, Zhai L, and McCullough R D. Regioregular, head-to-tail coupled poly(3-alkylthiophenes) made easy by the GRIM method: Investigation of the reaction and the origin of regioselectivity. *Macromolecules*, 34(13):4324–4333, 2001.
- [7] Ong B S, Wu Y, Liu P, and Gardner S. High-performance semiconducting polythiophenes for organic thin-film transistors. *Journal of the American Chemical Society*, 126(11):3378–3379, 2004.
- [8] Ong B S, Wu Y, Liu P, and Gardner S. Structurally ordered polythiophene nanoparticles for high-performance organic thin-film transistors. *Advanced Materials*, 17(9):1141–1144, 2005.

- [9] Energy Saving Trust UK. Generate your own electricity. <http://www.energysavingtrust.org.uk/Generate-your-own-energy/Solar-panels-PV>, 2012. [Online; accessed 28-June-2012].
- [10] ARUP. Review of the generation costs and deployment potential of renewable electricity technologies in the UK. Technical report, ARUP, 2011.
- [11] Mott MacDonald. UK electricity generation costs update. Technical report, Mott MacDonald, 2010.
- [12] Green M A, Emery K, Hishikawa Y, Warta W, and Dunlop E D. Solar cell efficiency tables (version 39). *Progress in Photovoltaics: Research and Applications*, 20(1):12–20, 2012.
- [13] David K and Melvin C. Photovoltaic effect and photoconductivity in laminated organic systems. *The Journal of Chemical Physics*, 29(4):950–951, 1958.
- [14] Tang C W. Two-layer organic photovoltaic cell. *Applied Physics Letters*, 48(2):183–185, 1986.
- [15] Sariciftci N S, Braun D, Zhang C, Srdanov V I, Heeger A J, Stucky G, and Wudl F. Semiconducting polymer-buckminsterfullerene heterojunctions: Diodes, photodiodes, and photovoltaic cells. *Applied Physics Letters*, 62(6):585–587, 1993.
- [16] Yu G, Gao J, Hummelen J C, Wudl F, and Heeger A J. Polymer photovoltaic cells: Enhanced efficiencies via a network of internal donor-acceptor heterojunctions. *Science*, 270(5243):1789–1791, 1995.
- [17] Chirvase D, Chiguvare Z, Knipper M, Parisi J, Dyakonov V, and Hummelen J C. Temperature dependent characteristics of poly(3 hexylthiophene)-fullerene based heterojunction organic solar cells. *Journal of Applied Physics*, 93(6):3376–3383, 2003.
- [18] Ma W, Yang C, Gong X, Lee K, and Heeger A J. Thermally stable, efficient polymer solar cells with nanoscale control of the interpenetrating network morphology. *Advanced Functional Materials*, 15(10):1617–1622, 2005.
- [19] Li G, Yao Y, Yang H, Shrotriya V, Yang G, and Yang Y. Solvent annealing effect in polymer solar cells based on poly(3-hexylthiophene) and methanofullerenes. *Advanced Functional Materials*, 17(10):1636–1644, 2007.

- [20] www.heliatek.com. Heliatek sets new world record efficiency of 10.7% for its organic tandem cell. <http://www.heliatek.com/?p=1923&lang=en#>, 2012. [Online; accessed 27-June-2012].
- [21] Mitsubishi Chemical. Achieving World's highest conversion efficiency with OPV. <http://www.m-kagaku.co.jp/english/aboutmcc/RC/special/feature1.html>, 2012. [Online; accessed 27-June-2012].
- [22] Lilienfeld J E. Method and Apparatus for Controlling Electric Currents. Technical report, United States Patent Office, 1930.
- [23] Heil O. Improvements in or relating to electrical amplifiers and other control arrangements and devices. Technical report, European Patent Office, 1935.
- [24] Sze S M and Ng K K. *Physics of semiconductor devices*. Wiley-Interscience publication. Wiley-Interscience, 2007.
- [25] Weimer P K. The TFT a new thin-film transistor. *Proceedings of the IRE*, 50(6):1462–1469, June 1962.
- [26] Morozov S V, Novoselov K S, Katsnelson M I, Schedin F, Elias D C, Jaszczak J A, and Geim A K. Giant intrinsic carrier mobilities in graphene and its bilayer. *Physical Review Letters*, 100:016602, Jan 2008.
- [27] Tans S J, Verschueren A R M, and Dekker C. Room-temperature transistor based on a single carbon nanotube. *Nature*, 393:49–52, 1998.
- [28] Dürkop T, Getty S A, Cobas E, and Fuhrer M S. Extraordinary mobility in semiconducting carbon nanotubes. *Nano Letters*, 4(1):35–39, 2004.
- [29] Podzorov V, Sysoev S E, Loginova E, Pudalov V M, and Gershenson M E. Single-crystal organic field effect transistors with the hole mobility $8 \text{ cm}^2/\text{V s}$. *Applied Physics Letters*, 83(17):3504–3506, 2003.
- [30] Islam M, Pola S, and Tao Y-T. High mobility n-channel single-crystal field-effect transistors based on 5,7,12,14-tetrachloro-6,13-diazapentacene. *Chem. Commun.*, 47:6356–6358, 2011.
- [31] Kergoat L, Herlogsson L, Braga D, Piro B, Pham M-C, Crispin X, Berggren M, and Horowitz G. A water-gate organic field-effect transistor. *Advanced Materials*, 22(23):2565–2569, 2010.
- [32] Kergoat L, Piro B, Berggren M, Horowitz G, and Pham M-C. Advances in organic transistor-based biosensors: from organic electrochemical transistors to electrolyte-gated organic field-effect transistors. *Analytical and Bioanalytical Chemistry*, 402:1813–1826, 2012.

- [33] Kergoat L, Battaglini N, Miozzo L, Piro B, Pham M-C, Yassar A, and Horowitz G. Use of poly(3-hexylthiophene)/poly(methyl methacrylate) (P3HT/PMMA) blends to improve the performance of water-gated organic field-effect transistors. *Organic Electronics*, 12(7):1253 – 1257, 2011.
- [34] Dudhe R S, Seena V, Mukherji S, Kumar A, and Rao V R. Organic Sensors for Explosive Detection. In *2009 4th international conference on computers and devices for communication (CODEC 2009)*, pages 510–515, 2009. 4th International Conference on Computers and Devices for Communication, Kolkata, INDIA, DEC 14-16, 2009.
- [35] Dudhe R S, Sinha J, Kumar A, and Rao V R. Polymer composite-based ofet sensor with improved sensitivity towards nitro based explosive vapors. *Sensors and Actuators B: Chemical*, 148(1):158 – 165, 2010.
- [36] Dudhe R S., Sinha J, Sutar D S, Kumar A, and Rao V R. Poly(3-hexylthiophene) and hexafluoro-2-propanol-substituted polysiloxane based OFETs as a sensor for explosive vapor detection. *Sensors and actuators A-physical*, 171(1, SI):12–18, NOV 2011. 3rd International Symposium on Shape Memory Materials for Smart Systems/E-MRS Spring Meeting, Strasbourg, France, Jun 07-11, 2010.
- [37] Weerakoon K A, Shu J H, and Chin B A. A chemiresistor sensor with a poly3-hexylthiophene active layer for the detection of insect infestation at early stages. *Sensors Journal, IEEE*, 11(7):1617 –1622, july 2011.
- [38] Granero A J, Wagner P, Wagner K, Razal J M, Wallace G G, and Panhuis M I H. Highly Stretchable Conducting SIBS-P3HT Fibers. *Advanced functional materials*, 21(5):955–962, MAR 8 2011.
- [39] Hwang J, Jang J, Hong K, Kim K N, Han J H, Shin K, and Park C E. Poly(3-hexylthiophene) wrapped carbon nanotube/poly(dimethylsiloxane) composites for use in finger-sensing piezoresistive pressure sensors. *Carbon*, 49(1):106–110, Jan 2011.
- [40] Kergoat L, Piro B, Berggren M, Pham M-C, Yassar A, and Horowitz G. Dna detection with a water-gated organic field-effect transistor. *Organic Electronics*, 13(1):1 – 6, 2012.
- [41] Lee S-H, Kim D-H, Kim J-H, Lee G-S, and Park J-G. Effect of metal-reflection and surface-roughness properties on power-conversion efficiency for polymer photovoltaic cells. *The Journal of Physical Chemistry C*, 113(52):21915–21920, 2009.
- [42] Bao Z, Dodabalapur A, and Lovinger A J. Soluble and processable regioregular poly(3-hexylthiophene) for thin film field-effect transistor

- applications with high mobility. *Applied Physics Letters*, 69(26):4108–4110, 1996.
- [43] Sirringhaus H, Tessler N, and Friend R H. Integrated optoelectronic devices based on conjugated polymers. *Science*, 280(5370):1741–1744, 1998.
 - [44] Veres J, Ogier S, Lloyd G, and de Leeuw D. Gate insulators in organic field-effect transistors. *Chemistry of Materials*, 16(23):4543–4555, 2004.
 - [45] Assadi A, Svensson C, Willander M, and Inganäs O. Field-effect mobility of poly(3-hexylthiophene). *Applied Physics Letters*, 53(3):195–197, 1988.
 - [46] Sundar V C, Zaumseil J, Podzorov V, Menard E, Willett R L, Someya T, Gershenson M E, and Rogers J A. Elastomeric transistor stamps: Reversible probing of charge transport in organic crystals. *Science*, 303(5664):1644–1646, 2004.
 - [47] Bolotin K I, Sikes K J, Jiang Z, Klima M, Fudenberg G, Hone J, Kim P, and Stormer H L. Ultrahigh electron mobility in suspended graphene. *Solid State Communications*, 146(9 - 10):351 – 355, 2008.
 - [48] Khot L, Panigrahi S, and Sengupta P. Development and evaluation of chemoresistive polymer sensors for low concentration detection of volatile organic compounds related to food safety applications. *Sensing and Instrumentation for Food Quality and Safety*, 4:20–34, 2010. 10.1007/s11694-010-9093-1.
 - [49] Ryu D and Loh K J. Strain sensing using photocurrent generated by photoactive p3ht-based nanocomposites. *Smart Materials and Structures*, 21(6):065016, 2012.
 - [50] Scarpa G, Idzko A-L, Yadav A, and Thalhammer S. Organic isfet based on poly (3-hexylthiophene). *Sensors*, 10(3):2262–2273, 2010.
 - [51] Zan H-W, Li C-H, Yeh C-C, Dai M-Z, Meng H-F, and Tsai C-C. Room-temperature-operated sensitive hybrid gas sensor based on amorphous indium gallium zinc oxide thin-film transistors. *Applied Physics Letters*, 98(25):253503, 2011.
 - [52] Wantz G, Lefevre F, Dang M T, Laliberte D, Brunner P L, and Dautel O J. Photovoltaic solar cells using poly(3,3-didodecylquaterthiophene). *Solar energy materials and solar cells*, 92(5):558–563, MAY 2008.
 - [53] Kingsley J W, Green A, and Lidzey D G. Fabrication and optimization of p3ht:pcbm organic photovoltaic devices. In Zakya H. Kafafi and

Paul A. Lane, editors, *Proceedings of SPIE*, volume 7416, page 74160T. SPIE, 2009.

- [54] Thompson B C, Kim B J, Kavulak D F, Sivula K, Mauldin C, and Fréchet J M J. Influence of alkyl substitution pattern in thiophene copolymers on composite fullerene solar cell performance. *Macromolecules*, 40(21):7425–7428, 2007.
- [55] Vemulamada P, Hao G, Kietzke T, and Sellinger A. Efficient bulk heterojunction solar cells from regio-regular- poly(3,3''didodecyl quaterthiophene)/PC70BM blends. *Organic Electronics*, 9(5):661 – 666, 2008.
- [56] Salleo A, Chen T W, Volkel A R, Wu Y, Liu P, Ong B S, and Street R A. Intrinsic hole mobility and trapping in a regioregular poly(thiophene). *Physical Review B*, 70(11), SEP 2004.
- [57] Hsieh G-W, Li F M, Beecher P, Nathan A, Wu Y, Ong B S, and Milne W I. High performance nanocomposite thin film transistors with bilayer carbon nanotube-polythiophene active channel by ink-jet printing. *Journal of Applied Physics*, 106(12):123706, 2009.
- [58] Ihn K J, Moulton J, and Smith P. Whiskers of poly(3-alkylthiophene)s. *Journal of Polymer Science Part B: Polymer Physics*, 31(6):735–742, 1993.
- [59] Kiriya N, Jähne E, Adler H-J, Schneider M, Kiriya A, Gorodyska G, Minko S, Jehnichen D, Simon P, Fokin A A, and Stamm M. One-dimensional aggregation of regioregular polyalkylthiophenes. *Nano Letters*, 3(6):707–712, 2003.
- [60] Sudip Malik and Arun K. Nandi. Influence of alkyl chain length on the gelation mechanism of thermoreversible gels of regioregular poly(3-alkyl thiophenes) in xylene. *Journal of Applied Polymer Science*, 103(4):2528–2537, 2007.
- [61] Samitsu S, Shimomura T, and Ito K. Nanofiber preparation by whisker method using solvent-soluble conducting polymers. *Thin Solid Films*, 516(9):2478 – 2486, 2008. The 7th International Conference on Nano-Molecular Electronics (ICNME 2006).
- [62] Oosterbaan W D, Vrindts V, Berson S, Guillerez S, Douheret O, Ruttens B, D’Haen J, Adriaensens P, Manca J, Lutsen L, and Vanderzande D. Efficient formation, isolation and characterization of poly(3-alkylthiophene) nanofibres: probing order as a function of side-chain length. *Journal of Materials Chemistry*, 19:5424–5435, 2009.
- [63] Samitsu S, Shimomura T, Heike S, Hashizume T, and Ito K. Effective production of poly(3-alkylthiophene) nanofibers by means of whisker

method using anisole solvent: Structural, optical, and electrical properties. *Macromolecules*, 41(21):8000–8010, 2008.

- [64] Tran H D, Wang Y, D’Arcy J M, and Kaner R B. Toward an understanding of the formation of conducting polymer nanofibers. *ACS Nano*, 2(9):1841–1848, 2008.
- [65] D’Arcy J M, Tran H D, Tung V C, Tucker-Schwartz A K, Wong R P, Yang Y, and Kaner R B. Versatile solution for growing thin films of conducting polymers. *Proceedings of the national academy of sciences of the United States of America*, 107(46):19673–19678, Nov 16 2010.
- [66] Berson S, De Bettignies R, Bailly S, and Guillerez S. Poly(3-hexylthiophene) fibers for photovoltaic applications. *Advanced Functional Materials*, 17(8):1377–1384, 2007.
- [67] Bertho S, Oosterbaan W D, Vrindts V, D’Haen J, Cleij T J, Lutsen L, Manca J, and Vanderzande D. Controlling the morphology of nanofiber-P3HT:PCBM blends for organic bulk heterojunction solar cells. *Organic Electronics*, 10(7):1248 – 1251, 2009.
- [68] Kim J S, Lee J H, Park J H, Shim C, Sim M, and Cho K. High-efficiency organic solar cells based on preformed poly(3-hexylthiophene) nanowires. *Advanced Functional Materials*, 21(3):480–486, 2011.
- [69] Sun S, Salim T, Wong L H, Foo Y L, Boey F, and Lam Y M. A new insight into controlling poly(3-hexylthiophene) nanofiber growth through a mixed-solvent approach for organic photovoltaics applications. *Journal of Materials Chemistry*, 21:377–386, 2011.
- [70] Merlo J A and Frisbie C D. Field effect conductance of conducting polymer nanofibers. *Journal of Polymer Science Part B: Polymer Physics*, 41(21):2674–2680, 2003.
- [71] Merlo J A and Frisbie C D. Field effect transport and trapping in regioregular polythiophene nanofibers. *The Journal of Physical Chemistry B*, 108(50):19169–19179, 2004.
- [72] Yonemura H, Yuno K, Yamamoto Y, Yamada S, Fujiwara Y, and Tanimoto Y. Orientation of nanowires consisting of poly(3-hexylthiophene) using strong magnetic field. *Synthetic Metals*, 159(9 - 10):955 – 960, 2009. International Symposium on Control of Super-Hierarchical Structures and Innovative Functions of Next-Generation Conjugated Polymers, Oct 21-23 2008, Hyogo, Japan.

Chapter 2

Theory of Device Operation

The main theoretical aspects of organic photovoltaics (OPVs), organic field-effect transistors (OFETs), and organic sensors are introduced in this following chapter along with some of the primary mechanisms for charge transport, including that of 1-D structures, and doping in organic materials. Whilst the purpose of this chapter is to serve as an introduction to these topics as required for the later work in this thesis, there are several texts available that give a more thorough treatment of the theoretical aspects of these topics, in particular the authoritative text by Sze and Ng[1] for much of the OFET theory, and the text by Nelson[2] for OPVs.

2.1 Organic Photovoltaics (OPVs)

2.1.1 Operating Principles of Organic Photovoltaics

Photon Absorption Organic photovoltaics harvest photons via a light-absorbing, charge-transporting active blend of electron accepting and donating materials sandwiched between charge carrier collecting electrodes. The processes can be seen in figures 2.1 and 2.2 for the case of a bulk heterojunction

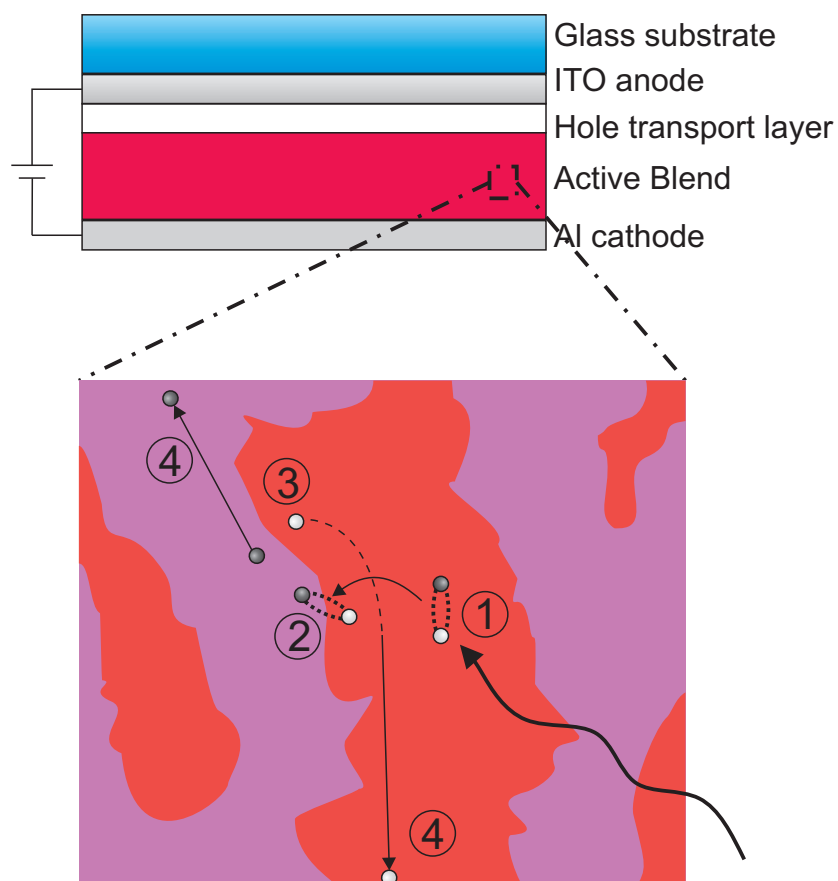


Figure 2.1: Schematic of the energy harvesting process of a bulk heterojunction OPV. The top figure shows the structure of a typical OPV. The bottom figure shows the process of photon absorption producing an exciton at 1, followed by drift of the exciton to the interface of the donor and acceptor materials at 2, followed by dissociation of the charges at 3, and finally transport of the charges toward the electrodes at 4.

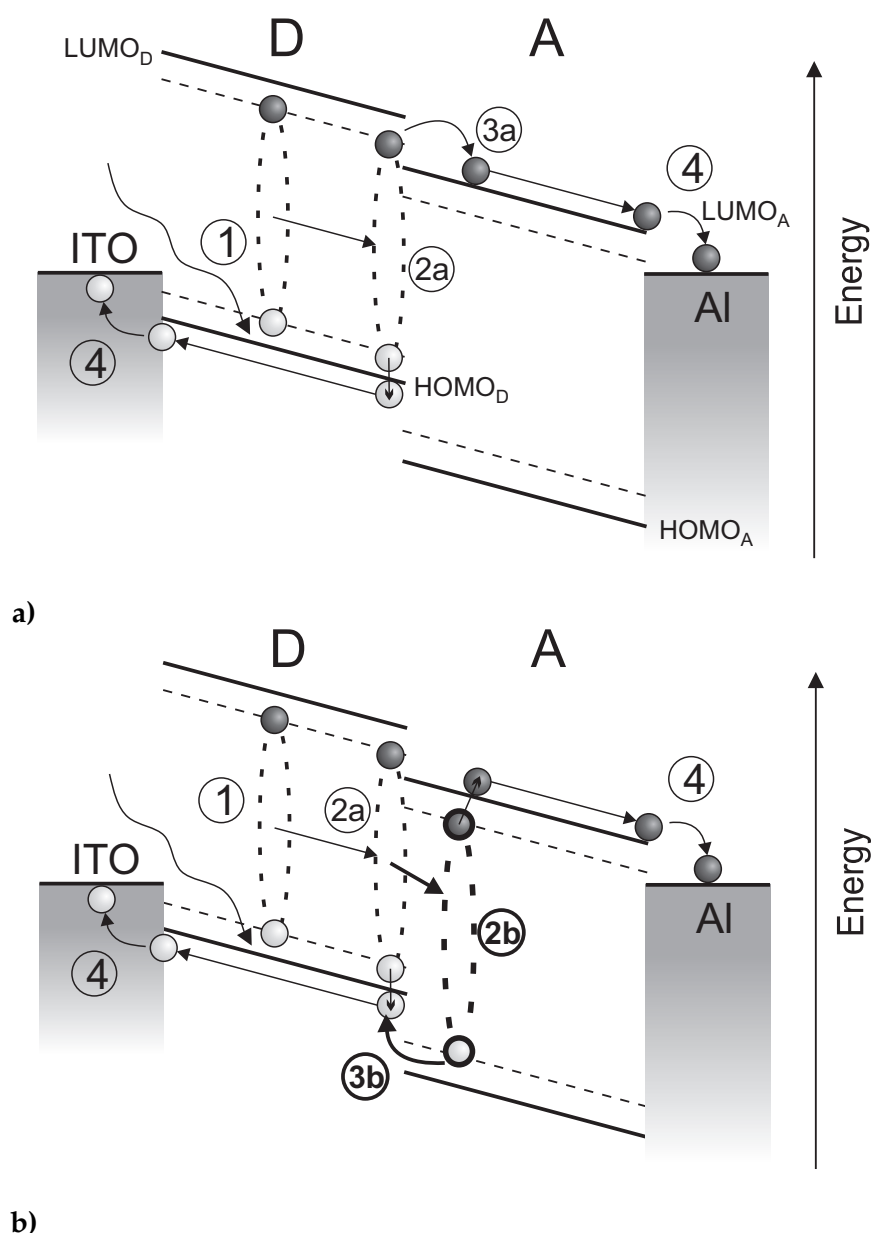


Figure 2.2: OPV energy level diagram describing principle operation of a device. D is the electron donor material, A is the electron acceptor. The full lines represent the top of the HOMOs and bottom of the LUMOs of the materials, whilst the dashed lines represent the energy levels of the Coulombically bound excitons. Photon absorption occurs at 1 creating an exciton, which drifts to the interface at 2a. a) The case describing exciton dissociation at the D-A interface via electron transfer from D to A at 3a caused by the in built E-field. (b) The case describing energy transfer in the form of the exciton moving from D to A at 2b followed by the dissociation of the exciton with the hole moving from A to D at 3b. In both cases the charges are then driven to the electrodes at 4 via the built in e-field.

cell as described later. Upon absorption of a photon by the active blend, an electron is promoted to an excited state leaving behind a hole (figures 2.1 and 2.2 - (1)). A fraction of these excitations, on the order of 10^{-2} , are created directly as free carriers[3, 4] which decay on a subpicosecond to nanosecond time scales, the rest are Coulombically bound electron-hole pairs known as an excitons. The initial, directly created charge carriers are thought to be born through rapid (~ 100 fs) hot exciton dissociation. Free charge carriers occupy energy states at the HOMO and LUMO levels. The excitons possess a binding energy in the range of 0.1-1.4 eV[5], which is the difference between the optical transition of the material and the energies of free charge carriers, the excitons therefore reside just within the LUMO-HOMO levels of their material.

Exciton Dissociation In order to make use of the energy within the Coulombically bound excitons the charges need to be dissociated and separated from one another. Where an active blend in a typical OPV is comprised of one material with a higher electron affinity (acceptor material) than the other (donor material), an exciton that diffuses to the interface between the two materials can be dissociated (figures 2.1 - (2) and 2.2 - (2a)). The process of exciton migration to an acceptor-donor interface must happen over a short period of time and distance as an exciton in a conjugated polymer typically has a lifetime on the order of 100ps[6], and a diffusion length of 4-20nm[7, 8, 9, 10, 11], when the exciton will normally undergo radiative recombination.

Once the electron has moved on to the acceptor material at the boundary the charges can be separated by the built in potential that exists within the two materials (figures 2.1 - (3) and 2.2 - (3a)). The charges will only dis-

sociate where the energy difference between the LUMOs of the donor and acceptor materials is greater than the binding energy of the exciton, in order to make this an energetically favourable process. The separated charges can then be collected at their respective electrodes (figures 2.1 and 2.2 - (4)), and be used as useful electrical energy. Whilst this is the generally expected process, it has also been suggested by some groups that energy transfer occurs with the exciton moving to the acceptor (figure 2.2 - (2b)) followed by dissociation with the hole moving back to the donor (figures 2.2 - (3b)) [12].

Competing Processes

Although the above description sounds somewhat simple there are many competing processes that prevent the successful harvesting of light and subsequent conversion to electrical power, and it is these processes that have to be balanced in order to produce a highly efficient organic solar cell.

Device Geometry One of the first major problems in OPVs was overcome to a great extent by the development of the bulk heterojunction (BHJ) by Yu in 1995 [13]. By producing an interpenetrating network of acceptor and donor materials the average distance that an exciton would have to travel in order to reach an interface was greatly reduced, allowing for much thicker films to be used and hence a greater photon harvest could occur. The previous single material and layered active regions meant that only thin sections of these regions would be contributing to the operation of the solar cell as all excitons created more than a few tens of nanometres away from an interface would recombine and be lost before having the opportunity to dissociate.

Morphology As discussed above, the morphology of the two components of the BHJ is crucial to minimising the distance the exciton must travel to an interface for charge separation. The diffusion length of an exciton in an organic material is of the order of 10 nm, and in P3HT it has been shown to be 4 nm[14]. For longer exciton diffusion paths there is a high probability of recombination of the electron and hole. Therefore individual domains of the blend should ideally be no more than twice the diffusion length across so that there is a high chance that the exciton can diffuse to an interface and experience charge separation before there is the chance of recombination. While the domains should ideally have a small cross-section it is also important that there are continuous pathways of these domains right through the blend that reach the electrodes in order that the charges can then be extracted from the device.

Whilst the exciton diffusion length for P3HT is 4 nm, there could be a longer range for the charge transfer itself in polymer:fullerene blends, where in one study of MEH-PPV:C60 blends it was found that this length could be as much as 8nm; this was interpreted as delocalisation of the excitations[15].

Getting this morphology just right depends on the materials used in the blend, the deposition method and parameters of the deposition method - such as solvent used - and post deposition treatment - such as thermal or solvent annealing. Unfortunately it does not appear to be possible to achieve a 'perfect' morphology due to the trade-offs between competing processes, and the properties of the components of the active blend.

The Energy Gap The energy gap of the light absorbing materials determines the spectrum of light that can be absorbed by the blend, in that a smaller energy gap allows for lower frequency photons to be absorbed there-

fore extending the spectrum of light that can be harvested into the infra-red region. Of course there is an advantage to absorbing more light, but on the other hand the smaller the band gap the less energy is stored in the bound exciton and can eventually be recovered by the OPV. It is thought that the main determinate of the open circuit voltage of an OPV, a performance indicating parameter of a device, is the difference between the LUMO of the acceptor and the HOMO of the donor, and by reducing the band gap of the absorbing material you will almost certainly be reducing the $\text{LUMO}_{\text{acc}}/\text{HOMO}_{\text{don}}$ difference.

Balanced Charge Transport This factor is in part a consequence of molecular design and in part due to processing of the OPV device. For an efficiently operating device the transport of holes in the donor and the transport of electrons in the acceptor should be balanced in order that a build up of one charge type doesn't further limit transport through the blend and provide sites for recombination of previously separated charges.

The second factor affecting the mobility of the materials in the blend is the processing parameters used, in that different deposition parameters and post-deposition treatment can affect the crystallinity of the blend and therefore how easily the charges can move from molecule to molecule.

Performance Parameters

There are several parameters that describe the performance of an OPV. The first parameter is the open circuit voltage V_{OC} , which is the maximum voltage produced by the device under illumination, measured under open circuit conditions with zero current flowing. This parameter approximates to the difference between the LUMO of the acceptor and the HOMO of the

donor.

The next performance parameter is the short circuit current density J_{SC} . It is the current flowing through the terminals of the device under illumination when the device is shorted with no bias between the terminals.

The fill factor F is the third parameter; it describes the 'squareness' of the J-V curve of the device and is the ratio of the maximum power of the device and the product of the theoretical maximum power (V_{OC}/J_{SC}).

$$FF = \frac{J_m V_m}{J_{sc} V_{oc}} \quad (2.1)$$

The final performance parameter is the efficiency ν , of the device. This is the ratio of the incident power and the maximum power output of the device.

$$\nu = \frac{P_m}{E \times A_c} \quad (2.2)$$

where P_m is the maximum power point, E is the input light irradiance in W/m^2 and A_c is the surface area of the solar cell.

2.2 Organic Field-Effect Transistors (OFETs)

Organic field effect transistors are generally of the form of a MISFET - a metal-insulator-semiconductor field-effect transistor - where the metal is the gate electrode, isolated from the semiconductor, which is the organic material, by an insulating layer. The metal-insulator is often made from silicon:silicon oxide, or a metal and its oxide such as Al:Al₂O₃.

Along with the gate, insulator and semiconducting medium, the other components are the substrate that supports the whole structure - although

this is sometimes simply the gate material - and then the source and drain electrodes. There are four configurations for OFETs as illustrated in figure 2.3, and these are the bottom-gate coplanar, bottom-gate staggered, top-gate coplanar, and top-gate staggered.

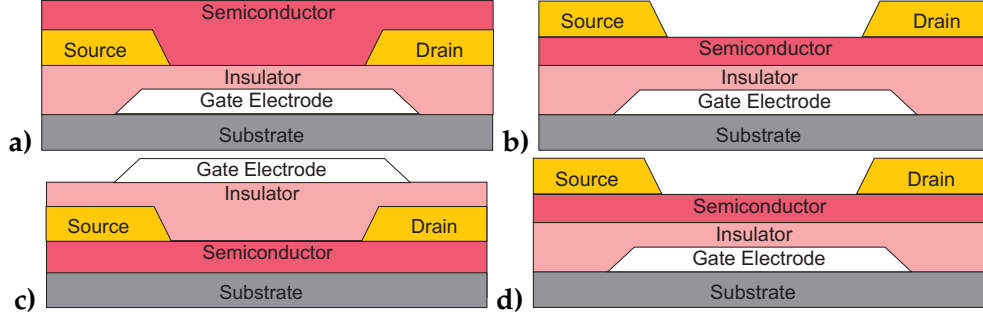


Figure 2.3: Schematic cross-sections of OFET structures. a) bottom-gate coplanar, b) bottom-gate staggered, c) top-gate coplanar, d) top-gate staggered

In its basic form a FET acts like a parallel plate capacitor, where a voltage applied to the gate causes orientation of the dipoles in the insulator and an accumulation of charge in the semiconductor (figure 2.4 a)). These charges in the semiconductor at the insulator-semiconductor interface are then relatively free to move. When a bias is then applied between the source and drain contacts a current is measured as the charges flow between these two contacts (figure 2.4 b)). An increase in the bias applied to the gate causes an increase in the number of accumulated charges and hence an increase in the current that flows between the source and drain.

The current that flows through the channel to the drain operates in two main regimes. Firstly the linear regime, where the current scales approximately linearly with source-drain bias, V_{SD} ,

$$I_{D,lin} = \frac{W\mu C_i}{L} \left[(V_G - V_T)V_{SD} + \frac{V_{SD}^2}{2} \right] \quad (2.3)$$

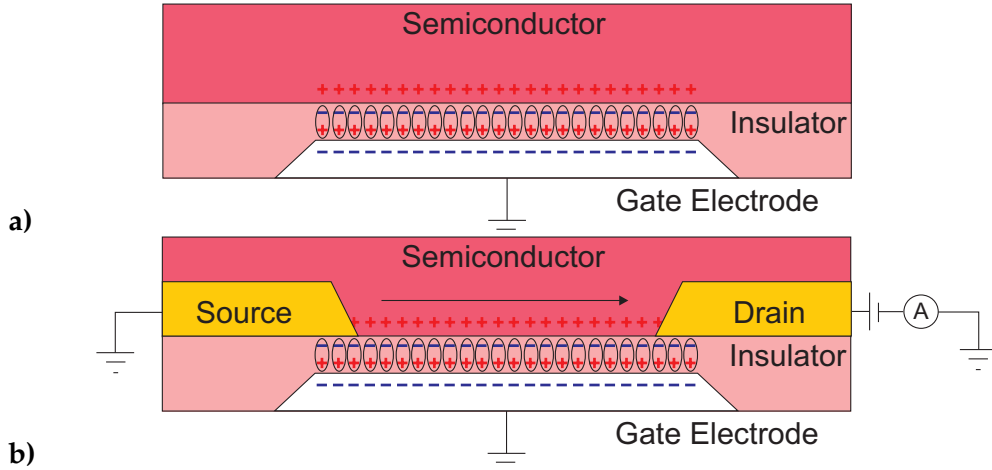


Figure 2.4: Schematic of OFET operation. a) Charge accumulation in parallel plate capacitor, b) Source-Drain bias. Bias applied to the gate electrode causes orientation of dipoles in the insulator and accumulation of charge in the semiconductor. The bias applied at the drain (b) creates an E-field which drives charges from the source, where they are injected, to the drain where they are collected.

where, W and L are the width and length of the channel respectively, μ is the mobility, C_i is the capacitance per unit area of the insulator, V_G is the gate bias, V_T is the threshold bias, and V_{SD} is the source-drain bias. For small source-drain biases 2.3 is approximately linear as the second term containing V_{SD} can be ignored.

The second regime is the saturation regime, where the current remains largely constant for any further larger values of V_{SD} ,

$$I_{D,sat} = \frac{W\mu C_i}{2L}(V_G - V_T)^2 \quad (2.4)$$

For intermediate values of V_{SD} , 2.3 describes the transition from linear increases in I to the saturation value. The I-V behaviour of a FET can be seen in figure 2.6.

The threshold bias has slightly different definitions for inorganic and

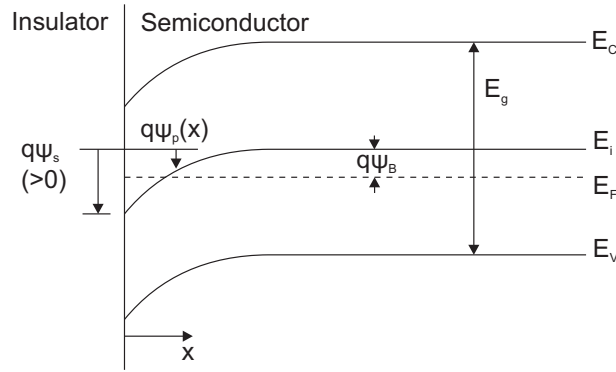


Figure 2.5: Energy band diagram describing threshold voltage, V_T . V_T occurs when strong inversion is achieved, shown here. The surface potential $q\psi_s$ is double that of the Fermi level, E_F and the level of charge carriers in the bulk, $q\psi_B$.

organic FETs, but has a similar effect on the operating characteristics of a device. In inorganic FETs V_T is defined as the gate bias required to induce strong inversion, which itself is defined as the bias at which the surface potential of the semiconductor at the insulator interface is twice that of the potential between the Fermi level and the level of charge carriers in the bulk (as in figure 2.5). For an organic FET the threshold voltage marks the gate bias at which there is appreciable drain current, it also marks a transition in the operation of the device. The threshold bias is explained in slightly more detail later in the text along with the switch-on voltage V_{SO} , which marks another transition in OFET operation and is marked by the gate voltage at which the drain current is at its minimum.

2.2.1 Operating Characteristics

The operating characteristics will now be discussed in more detail. As described previously the basic design of an OFET is that of a MISFET in a thin film transistor (TFT) configuration. A semiconductor film of several to tens

of nanometres thick is supported by a substrate, with an insulating medium sandwiched between the semiconductor and a gate electrode. Finally there are two electrodes attached at either end of a portion of the semiconductor, called the channel, to inject and extract charges. The semiconductor-insulator-gate acts as a parallel plate capacitor, where an application of a bias on the gate causes an accumulation of charges in the semiconductor at the interface with the insulator. These charges are then relatively free to move between source and drain upon application of a bias between the contacts. The bias on the gate controls the quantity of accumulated charge and in effect acts, just as its name suggests, as a gate to the charge that then flows between the source and drain contacts.

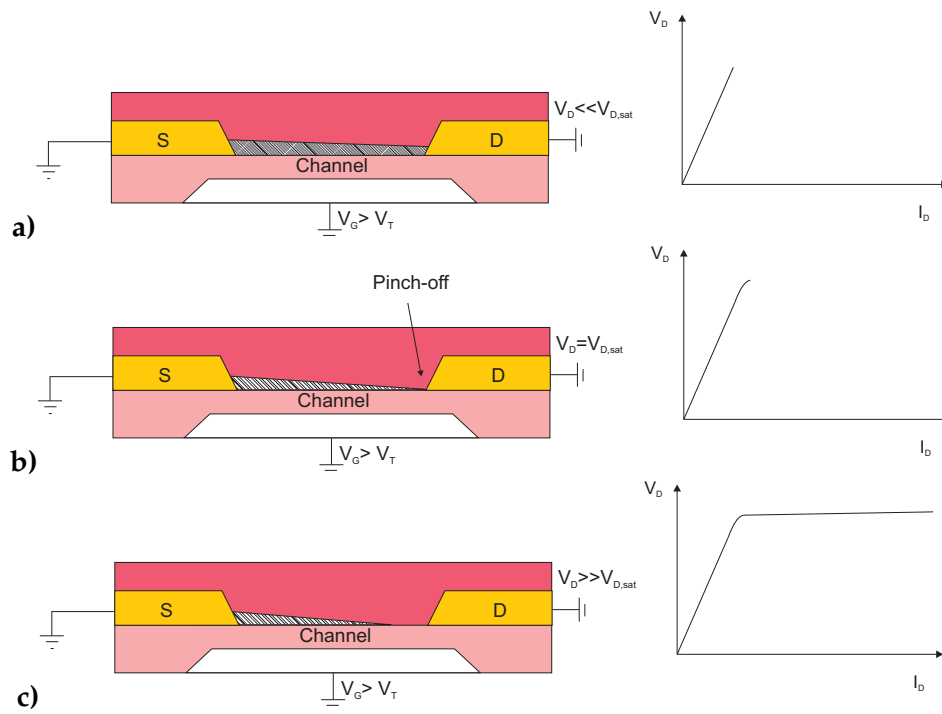


Figure 2.6: Schematic of OFET operating regimes. a) OFET operating in linear linear regime, b) at pinch-off, c) in saturation. The grey region depicts the accumulated charge carriers.

When the source-drain bias is less than the difference between gate bias

and threshold bias ($V_{SD} < (V_G - V_T)$), the drain current increases linearly with increasing source-drain bias, demonstrating ohmic behaviour (figure 2.6(a)). As the source-drain bias increases and matches the gate bias pinch-off occurs and the drain current stops increasing. Pinch-off occurs as the free charge carriers are essentially depleted at the end of the channel and there are no further charge carriers to contribute to the current. This occurs where the source-drain bias and the gate/threshold bias match, making the field zero at this point (figure 2.6(b)). Finally as the source-drain bias increases past the value at which of pinch-off occurs the current then remains constant, as there are no further free charge carriers to contribute to the current. The pinch-off point in the channel moves further towards the source contact and the depletion region increases. The charge carriers that contribute to the current are swept rapidly through this depletion region by the large electric field acting between source and drain (figure 2.6(c)).

2.3 Charge Transport Models

There are several models of charge transport in organic semiconductors, which include band transport, hopping transport, variable range hopping (VRH), multiple trap and release (MTR), and grain boundary models. The key predictor of each model is the variation of mobility with temperature[16].

The mobility μ , describes the motion of charge carriers under the influence of an E-field.

$$\mu = \frac{v_d}{E} \quad (2.5)$$

where v_d is the drift velocity of the charge carrier under the influence of an external electric field, E. This is the typical relationship between the

E-field and mobility although μ experiences an E-field dependence under high E-fields.

2.3.1 Band Transport

The band transport model provides an excellent description of the charge transport of inorganic crystals, and also goes to explain the high mobility of these materials.

The Pauli exclusion principle forbids more than two electrons of opposite spins from occupying the same energy state. As two atoms are brought close together the molecular orbits overlap leading to splitting of the energy levels. As further atoms are brought together, as in a crystal, the energy levels split again until the very large number of states form a continuum of energy levels.

The periodic potential created by the Coulombic interaction of the electrons with the atomic nuclei of the crystal gives rise to forbidden gaps within the continuum of states, and leads to energy bands. These bands are separated into conduction bands, where the electrons are free to move, and valence bands, where the electrons are more tightly bound to the atomic nuclei. The upper edge of the valence band marks the highest occupied molecular orbital (HOMO), while the lower edge of the conduction band marks the lowest unoccupied molecular orbital (LUMO). The magnitude of the energy gap between the bands, known as the band gap, and the distribution of the electrons and holes in these bands determines the electrical properties of the material and leads to the distinction between metals, semiconductors and insulators.

The charge carriers in the band model exhibit decreased mobility with high T as they are scattered by the thermal motion of the lattice, ie. phonon

scattering.

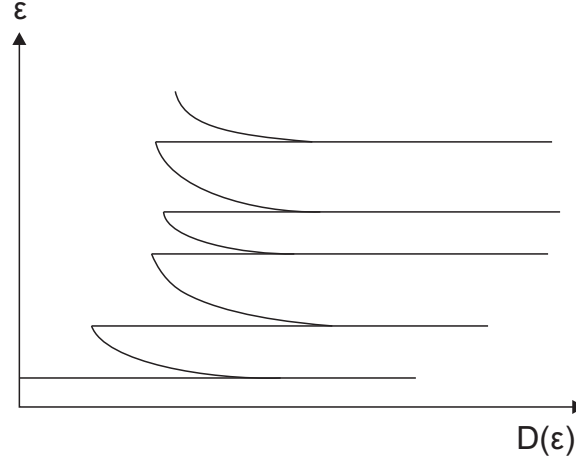


Figure 2.7: Energy level sketch of 1-dimensional density-of-states, showing the subbands.

1-D Charge Transport

1-D structures, in which two of the dimensions are on the order of 10^{-9}m or less while extending beyond this in the third dimension, exhibit interesting properties not seen in bulk and 3-D structures[17]. The electrons in these systems are confined laterally and therefore occupy energy levels that are different to those of the traditional continuum of energy levels and bands found in bulk materials.

This confinement leads to peaks, or subbands, in the density of states called Van Hove singularities (figure 2.7).

The conductance in a 1-D conductor is quantised, giving a stepped increase in current with increasing bias. A perfectly conducting 1-D structure has a conductance that is a multiple of the conductance quantum G_Q ,

$$G_Q = 2e^2/h = 7.748 \times 10^{-5} \Omega^{-1} \quad (2.6)$$

If the structure is not perfectly conducting then the overall conductance is G_Q multiplied by the probability of electron transmission $P(\epsilon_F)$ of the structure,

$$G(\epsilon_F) = (2e^2/h)P(\epsilon_F) \quad (2.7)$$

2.3.2 Hopping Transport

In band transport the charge carriers are scattered and hence slowed down by phonons, whereas hopping transport involves phonon-assistance of a charge carrier over a potential barrier that separates two adjacent molecular or ionic sites[18].

In this model the charge carriers are highly localised and hop from site to site. The mean free path of the charge carriers is less than one lattice constant, with scattering taking place at nearly every relocation. The mobility is temperature related by the following:

$$\mu \propto \exp(-E_A/kT) \quad (2.8)$$

where E_A is an activation energy. In this case the mobility increases with temperature, due to the increase in phonons providing the activation energy for the charge carriers to hop from site to site.

The localisation of the charges in organic materials can be brought about via disorder in the system, whereas an inorganic crystal shows long range ordering. Self-localisation of charges occur where the presence of a charge deforms the molecule that it resides in, where this charge and associated deformation is termed a polaron.

2.3.3 Variable Range Hopping (VRH)

In variable range hopping the charge carriers hop to non-adjacent sites[19]. The charge carriers can now hop to distant sites that require a low activation energy or to near sites requiring a high activation energy.

In this model the mobility has the following relationship with temperature,

$$\mu \propto \exp \left[-(T_0/T)^{1/(d+1)} \right] \quad (2.9)$$

where d is the number of dimensions of the system. The conductivity is then given by

$$\sigma = \sigma_0 \exp \left[-(T_0/T)^{1/(d+1)} \right] \quad (2.10)$$

where σ_0 is the known conductivity at a measured temperature T_0 .

The VRH model assumes that localised states are distributed over the entire energy gap. In a VRH model proposed by Vissenberg[20], there is an exponential distribution of localised states. This then gives rise to a charge carrier dependent mobility and activation energy. The mobility dependence on temperature is then the same as (2.8).

2.3.4 Multiple Trap and Release (MTR)

In the MTR model, the charge carriers move along in bands but are regularly trapped and released from trap states that are located in the transport bands; these traps are uniformly distributed throughout the material. The traps are created by defects in the material, which can be structural (vacancies, dislocations, and grain boundaries), chemical (substitutional and inter-

stitial chemical impurities), and surface (dangling bonds). Trapped carriers possess zero mobility until they are thermally activated to mobile states.

The two forms of the MTR model are, that there are trap states at one energy level, or there are a (exponential) distribution of states; the distribution of states being a more realistic scenario.

2.3.5 Grain Boundary Models

One final model is that of the grain boundaries which assumes that all of the trap states are located at the grain boundaries in the material. Here the mobility can be separated into contributions from the bulk and the grain boundary[21].

$$\frac{1}{\mu} = \frac{1}{\mu_{GB}} + \frac{1}{\mu_B} \quad (2.11)$$

where μ_{GB} is the grain boundary mobility and μ_B is the mobility in the bulk. If $\mu_B \gg \mu_{GB}$ then the overall mobility will be dominated by the grain boundaries.

Bibliography

- [1] Sze S M and Ng K K. *Physics of semiconductor devices*. Wiley-Interscience publication. Wiley-Interscience, 2007.
- [2] Nelson J. *The physics of solar cells*. Series on Properties of Semiconductor Materials. Imperial College Press, 2003.
- [3] Hendry E, Schins J M, Candeias L P, Siebbeles L D A, and Bonn M. Efficiency of exciton and charge carrier photogeneration in a semiconducting polymer. *Physical Review Letters*, 92(19):196601, May 2004.
- [4] Hendry E, Koeberg M, Schins J M, Siebbeles L D A, and Bonn M. Free carrier photogeneration in polythiophene versus poly(phenylene vinylene) studied with thz spectroscopy. *Chemical Physics Letters*, 432(4 - 6):441 – 445, 2006.
- [5] Hill I G, Kahn A, Soos Z G, and Pascal Jr R A. Charge-separation energy in films of π -conjugated organic molecules. *Chemical Physics Letters*, 327(3 - 4):181 – 188, 2000.
- [6] Piris J, Dykstra T E, Bakulin A A, van Loosdrecht P H M, Knulst W, Trinh M T, Schins J M, and Siebbeles L D A. Photogeneration and ultrafast dynamics of excitons and charges in P3HT/PCBM blends. *The Journal of Physical Chemistry C*, 113(32):14500–14506, 2009.
- [7] Halls J J M, Pichler K, Friend R H, Moratti S C, and Holmes A B. Exciton diffusion and dissociation in a poly(p-phenylenevinylene)/C₆₀ heterojunction photovoltaic cell. *Applied Physics Letters*, 68(22):3120–3122, 1996.
- [8] Pettersson L A A, Roman L S, and Inganäs O. Modeling photocurrent action spectra of photovoltaic devices based on organic thin films. *Journal of Applied Physics*, 86(1):487–496, 1999.
- [9] Theander M, Yartsev A, Zigmantas D, Sundström V, Mammo W, Andersson M R, and Inganäs O. Photoluminescence quenching at a polythiophene:C₆₀ heterojunction. *Physical Review B*, 61(19):12957–12963, May 2000.

- [10] Savenije T J, Warman J M, and Goossens A. Visible light sensitisation of titanium dioxide using a phenylene vinylene polymer. *Chemical Physics Letters*, 287(1 - 2):148 – 153, 1998.
- [11] Haugeneder A, Neges M, Kallinger C, Spirkel W, Lemmer U, Feldmann J, Scherf U, Harth E, Gügel A, and Müllen K. Exciton diffusion and dissociation in conjugated polymer/fullerene blends and heterostructures. *Physical Review B*, 59(23):15346–15351, Jun 1999.
- [12] Matthew T L, Lim Y-F, and Malliaras G G. Two-step exciton dissociation in poly(3-hexylthiophene)/fullerene heterojunctions. *Applied Physics Letters*, 92(14):143308, 2008.
- [13] Yu G, Gao J, Hummelen J C, Wudl F, and Heeger A J. Polymer photovoltaic cells: Enhanced efficiencies via a network of internal donor-acceptor heterojunctions. *Science*, 270(5243):1789–1791, 1995.
- [14] Lürer L, Egelhaaf H-J, Oelkrug D, Cerullo G, Lanzani G, Huisman B-H, and de Leeuw D. Oxygen-induced quenching of photoexcited states in polythiophene films. *Organic Electronics*, 5(1 - 3):83 – 89, 2004. Current Trends in Crystalline Organic Semiconductors: Growth Modelling and Fundamental Properties.
- [15] Vacar D, Maniloff E S, McBranch D W, and Heeger A J. Charge-transfer range for photoexcitations in conjugated polymer/fullerene bilayers and blends. *Physical Review B*, 56(8):4573–4577, Aug 1997.
- [16] Gutmann F, Lyons L E, and Keyzer H. *Organic semiconductors*. Number pt. 2 in Organic Semiconductors. R.E. Krieger Pub. Co., 1983.
- [17] Kittel C. *Introduction to solid state physics*. Wiley, 2005.
- [18] Pope M and Swenberg C E. *Electronic processes in organic crystals and polymers*. Monographs on the physics and chemistry of materials. Oxford University Press, 1999.
- [19] Mott N F. Conduction in non-crystalline materials. *Philosophical Magazine*, 19(160):835–852, 1969.
- [20] Vissenberg M C J M and Matters M. Theory of the field-effect mobility in amorphous organic transistors. *Physical Review B*, 57(20):12964–12967, May 1998.
- [21] Horowitz G and Hajlaoui M E. Grain size dependent mobility in polycrystalline organic field-effect transistors. *Synthetic Metals*, 122(1):185 – 189, 2001. Proceedings of the E-MRS 2000 Spring Meeting, Symposium I.

Chapter 3

Experimental Techniques

3.1 Introduction

This section introduces some of the main experimental techniques used throughout this thesis, giving details of theory and purpose of the techniques. The techniques used in this thesis include atomic force microscopy (AFM), ultra violet-visible spectroscopy (UV-Vis), photoluminescence (PL), cyclic voltammetry (CV), and x-ray diffraction (XRD). Any other less significant experimental tasks will be briefly discussed in the relevant chapters, and the main device characterisation techniques were discussed in the relevant previous chapters.

3.2 Atomic Force Microscopy (AFM)

Atomic force microscopy (AFM) is a surface imaging technique from the family of scanning probe microscopy (SPM). SPM is a powerful technique used for the study of surfaces at or near the atomic scale, using a small physical probe that raster scans over a sample; a feedback loop then re-

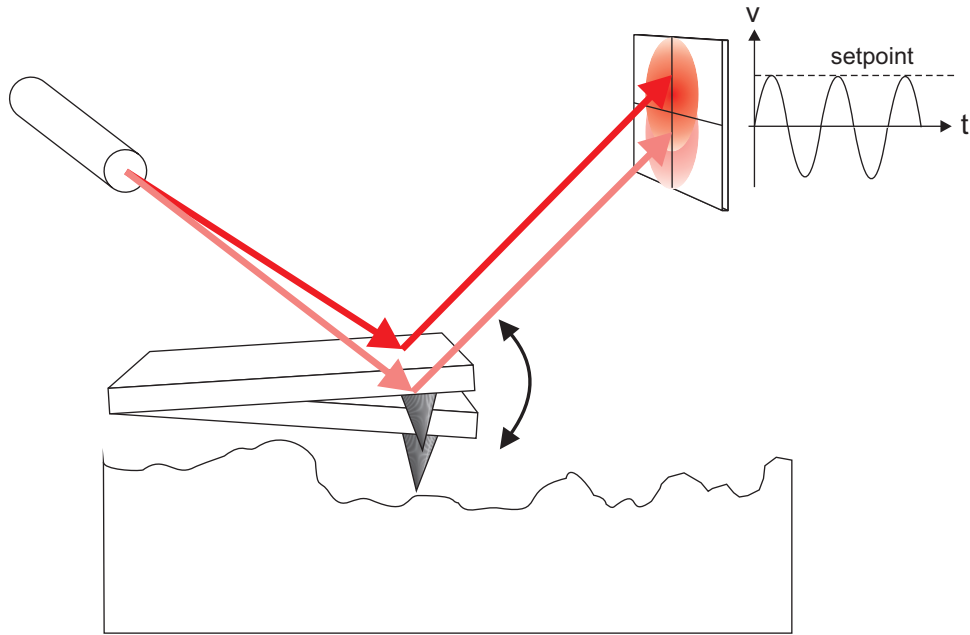


Figure 3.1: Schematic of AFM operating in tapping mode

sponds to interactions between the probe tip and the sample and adjusts a parameter, for instance distance between probe tip and sample or current, to build up an image of the surface of the sample. Lateral resolution of the order of nanometers can be achieved depending on the technique in use. For a good treatment of the physics of the AFM the text by Sarid[1] is suggested.

AFM was first developed in 1986 by G.Binnig, C.F.Quate and C.Gerber[2] and, along with the other SPM techniques, was developed to overcome the limitation in resolution of optical microscopes. The basic operating principle of AFM (figure 3.1) is that a tip of radius of a few nanometres located on the end of a macroscopic cantilever interacts with the contours of a sample surface via van der Waals forces, dipole-dipole interactions, and electrostatic forces as it is raster scanned. This interaction causes the cantilever to deform which is then detected by a feedback system, most commonly a laser reflected off the back of a cantilever and detected with a diode array.

There are several different AFM modes and SPM techniques, these include but are not limited to:

Contact mode AFM - the tip remains in constant contact with the surface of the sample during imaging.

Tapping mode AFM (tm-AFM) - the cantilever oscillates at its resonant frequency, so that the tip does not remain in permanent contact with the surface, and is therefore less destructive of the surface and the tip itself.

Kelvin probe force microscopy (KPFM) - also known as surface probe microscopy, allows the work function of materials to be observed at the tens of nanometers scale. The cantilever is not driven at its resonance frequency, rather an AC voltage is applied to the cantilever at the resonance frequency, and then a DC voltage is then applied to the tip in order null any vibrations induced by the potential difference of the tip and sample caused by the work function of the sample.

Electrostatic force phase microscopy (EFM-phase) - this technique is similar to KPFM but it probes the electrostatic force between the tip and sample, using an oscillating cantilever and a DC bias applied between the tip and sample. The phase change in the oscillating tip is detected in order to probe the force gradient.

Lateral force microscopy (LFM) - In this mode the cantilever is in contact with the sample and is scanned perpendicularly to its length. The torsional forces experienced by the cantilever due to the friction between the sample and the tip are measured. This allows for imaging of high and low relative frictional sites on the sample surface.

Scanning tunnelling microscopy (STM) - a tunnelling current I , is passed through a conducting tip or wire to the sample whilst tunnelling through the gap between tip and sample. A topographical image is produced by maintaining the current magnitude by maintaining the tip sample separation S . Further information can be garnered from the sample by means of adjusting the feedback parameters, or by producing I-V and I-S curves.

Conductive AFM (cAFM) - this technique combines the topographical output of AFM with the conductivity surface profiling of STM by using a conductive cantilever utilising the usual AFM feedback to image the height of the surface whilst allowing a current to pass between tip and surface.

3.2.1 Tapping Mode AFM

Tapping mode AFM was the main SPM technique utilised in this thesis, and so will be theory which is treated most rigorously. In order to have a full understanding of the theory of AFM, it is important to look at the mechanics of a microscopic cantilever, a harmonic oscillator and the intermolecular forces that the cantilever experiences when probing a sample.

Before the treatment of these topics, it is important to cover the feedback mechanism of the system. The system used in this thesis was a Veeco Multimode III SPM, and so much of the feedback theory will be based on this system.

The Feedback Loop

The feedback system in an AFM monitors the tip-sample interaction, maintains particular setpoints and allows the system software to build up an image of the selected monitored parameters, be they height, phase, or force data to name a few[3].

The Probe An AFM tapping mode probe, typically consists of a cantilever of approximately 100-200 μm in length, 40 μm in width and a thickness of 4~8 μm , with a tip located within a few microns of the end. The tip itself is typically conical or pyramidal, although a few specialist tip shapes exist including carbon nanotube ended tips. A common tapping mode tip will have a radius of curvature of 10 nm or less with an aspect ratio (tip length to radius ratio) of 3:1, while supersharp tips can have radii down to 2nm and increased aspect ratios of better than 3.5:1 [4]. The cantilever material will typically be silicon or silicon nitride. The cantilever is attached to the end of a chip with length and width on the order of millimetres and a thickness of several hundred micrometers.

Feedback The tapping mode probe is oscillated at its resonance frequency by a piezoelectric crystal while being raster scanned over the surface of the sample. The scanning of the probe and the tip-sample separation movement is performed by a piezoelectric scanner. A photodiode, which is split vertically into two sections, detects the oscillations of the cantilever via a laser which is reflected off its top surface. The voltage difference between the outputs of the two portions of the photodiode produces a sinusoidal output, which is monitored by the feedback loop. The feedback loop works to maintain a user specified RMS amplitude to this output. So as the tip is

brought closer to the surface the increased repulsive forces felt by the tip due to interaction with the surface cause a reduction in the amplitude in the tip oscillations and hence the photodiode output. As the tip-sample distance increases, the repulsive forces between the tip and sample decrease and so the oscillation amplitude increases and the photodiode output increases in amplitude also. The output of the photodiode therefore reacts in this manner as the tip meets features during its scan of the sample, whether they are raised or relief features. The feedback mechanism maintains this setpoint output voltage by applying a voltage to the z-axis of the piezo scanner, therefore constant force is felt between the sample and tip and hence the tip-sample separation is maintained. It is the signal that is sent back to the z-axis piezo that is also monitored by the software and used to construct height data in the scan image.

Gains The output voltage from the photodiode is not applied directly to the z-axis of the piezo but goes through some processing beforehand. The processing that is applied to the signal includes the gain, which is separated into three individual components: the proportional, the integral and the 'LookAhead' gain. The proportional gain is in effect a multiplier of the signal, ie. it applies a proportional amount of the signal. The integral gain acts to reduce the cumulative error between the tip-sample distance and the setpoint value that will build up through use of a proportional gain alone. The LookAhead gain uses the previous scan lines to predict up coming regular features of the sample and will ready the system before meeting one of these features. The LookAhead gain is only useful when using on a sample with regular repeating features, and should otherwise be minimised or turned off.

When LookAhead gain is >0 it is the first gain to be calculated, and this then operates on the integral gain. With the integral gain set to >0 this calculates a running average of the error as follows,

$$z_{acc}^{new} = \text{error} \cdot G_{int}^{LA} + z_{acc}^{old} \quad (3.1)$$

where z_{acc}^{new} is the new average error calculated by adding the old average error z_{acc}^{old} to the product of the integral gain and the current value of error.

The proportional gain G_{prop} is calculated last, and calculates the voltage required to be sent to the z-axis of the piezo in proportion to the error from the setpoint.

$$z \text{ voltage} = z_{acc}^{new} + \text{error} \cdot G_{prop} \quad (3.2)$$

Microscopic Cantilever Mechanics

The microscope probe, as previously described, consists of a cantilever fixed at one end, from where it is mechanically driven to vibrate, and a tip located at the other end which has a near atomically sharp probe which interacts with the sample surface.

Harmonic Oscillator

A harmonic oscillator, where a mass m is attached to one end of a massless spring with spring constant k , where the other end of the spring is fixed, can be represented by the following equation,

$$F = -kx = m \frac{d^2x}{dt^2} \quad (3.3)$$

where x is the magnitude of the displacement from the equilibrium po-

sition, and t is time.

The solution to this equation is given by $x = A_0 \exp^{i\omega_0 t}$, where A_0 is the amplitude of oscillation and $\omega_0 = \sqrt{k/m}$.

If we introduce a term to describe damping of an oscillator this more realistically represents a system where energy is continuously being lost, the equation for a damped harmonic oscillator is then

$$m \frac{d^2 x}{dt^2} = -kx - b \frac{dx}{dt} \quad (3.4)$$

where the second term on the RHS is the damping force, b is the damping coefficient.

To take this system further we can include a driving force keeping the oscillator in motion, the equation for a driven damped oscillator is then

$$m \frac{d^2 x}{dt^2} = F(t) - kx - b \frac{dx}{dt} \quad (3.5)$$

where $F(t)$ is the driving force being applied externally to the oscillator. This can be arranged into the form

$$\frac{d^2 x}{dt^2} + b \frac{dx}{dt} + \omega_0^2 x = F(t) \quad (3.6)$$

This equation then describes the motion of the cantilever in a tapping mode AFM, where the driving force is that of a piezo-electrical crystal and the damping is provided by the interaction of the tip with the surface features of the sample that is being scanned.

3.2.2 Feature De-convolution

Due to the finite shape of the tip, tip-cone and sample features, the image produced by the AFM will always lead to an image that is a convolution between the surface topography and the tip geometry. The raised features of the sample can interact with the sides of the tip cone as opposed to the tip apex causing the tip to be raised up to overcome the feature before the tip apex meets the feature and therefore producing an image that increases the horizontal dimensions of the feature. This also applies to relief features, or where the tip needs to be lowered over the falling side of a raised feature.

A process to de-convolute the image was developed during the research in this thesis. First of all an approximate tip shape and scale were required. The tips used in the experiments were Nanosensors Point Probe Plus (PPP-NCH-W) silicon cantilevers, with a pyramidal tip and a tip apex radius quoted as being less than 7 nm. A sample of well spaced spheres with known radii of <5 nm is initially scanned using the AFM. Assuming minimal vertical deformation of the spheres and a spherical tip apex the tip radius can be calculated using the following equation[5],

$$W^2 = 16R_T R_S = 8R_T h \quad (3.7)$$

where W is the measured sphere width, R_T is the tip apex radius, R_S is the sphere radius, and h is the measured height of the feature which should be the same as twice the sphere radius for a non-compressible sphere (figure 3.2 a)).

The spherical features used in this thesis were cadmium selenide (CdSe) quantum dots coated in a capping agent, with a radius of 2~3 nm.

Once the tip apex radius has been calculated the artifact, ie. the addi-

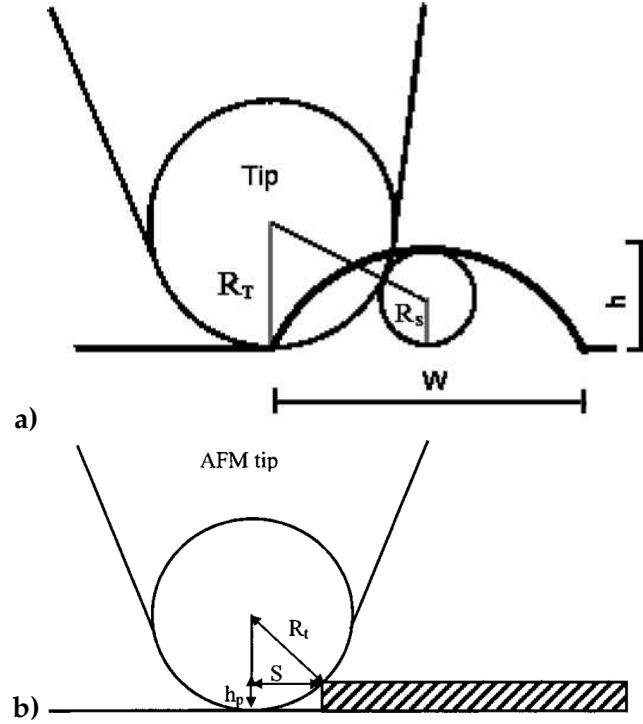


Figure 3.2: Sketch of tip de-convolution

tional width, of a measured feature can be calculated. The nanowires in the experiments in this thesis have been assumed to possess rectangular cross sections, and in most cases they also possess heights that are of the order of the tip-apex radius or smaller. For a rectangular sample the following equation can be used to calculate the actual feature width from the measured feature width[6],

$$A = 2S = 2\sqrt{2R_T h_f - h_f^2} \quad (3.8)$$

where A is the artifact size, S is the artifact on one side of the feature, and h_f is the feature height (figure 3.2 b)).

3.3 Ultra Violet-Visible Spectroscopy (UV-Vis)

3.3.1 Introduction and Basic Operation

Ultra-Violet Visible spectroscopy (UV-Vis) is used to determine the absorption coefficients of materials at visible and ultra-violet wavelengths, and also allows for the identification of certain species within a sample.

Absorption of UV/Vis light UV-Vis spectroscopy works via the absorption of photons by the electrons of a host material. The electrons are promoted to higher energy levels upon absorption of the incident photon, as long as the energy of the photon is at least as large as the energy gap between the ground state and the next lowest energy state of the electron[7].

Information Garnered The technique of UV-Vis allows for the quantification of the energy gap between the ground state of an electron and the next lowest state. This is identified as the wavelength at which absorption starts, known as absorption onset. The absorption coefficient, which is a measure of the amount of light that is absorbed by a material at a particular frequency, can also be quantified (see §3.3.3).

3.3.2 Bonds Involved in Absorption

The energy required to promote an electron to the next available energy state depends on what type of bonding the electron is involved in inside the molecule. UV-Vis uses a light in the wavelength range of approximately 200-1000 nm, or 1.2-6.2 eV. This energy will excite electrons involved in π bonding into anti-bonding orbitals, and will also excite n -electrons, which are electrons in non-bonding molecular orbitals, into σ^* and π^* anti-bonding

orbitals, but is not large enough to excite electrons from σ orbitals.

Some UV-Vis spectrometers, which operate under vacuum, are able excite σ orbitals as they can utilise light in the far ultra-violet (10-200 nm, or 6.2-124 eV). Light in the far ultra-violet is absorbed by the constituents of the air and so requires operation under vacuum.

3.3.3 Beer's Law

Beer's Law relates the absorbance A , of a sample to the path length b , and the concentration c , of the absorbing species,

$$-\log \frac{I}{I_0} = A = \epsilon bc \quad (3.9)$$

I is the measured intensity of light after passing through the sample, and I_0 is the incident intensity, and ϵ is the molar absorptivity.

3.3.4 Absorption Onset

The absorption spectra of a sample can unveil details of the material species that it contains, the energy gap between the materials HOMO and LUMO, and the quantity of material species in the sample. UV-Vis spectroscopy utilises the electromagnetic spectrum between 200nm and 1000nm. More specialised UV-Vis spectrometers that operate in vacuum or with a chamber filled with a gas such as helium can work below 200nm but due to the absorption by nitrogen, water and oxygen, most standard UV-Vis spectrometers that operate in ambient environments work between this range.

3.3.5 Equipment

The equipment used in the experiments involved in this thesis was a Jasco V-570 spectrophotometer, which is a typical example of a commercially available spectrometer.

The main components of a spectrometer are the light source with monochromator, a chamber in which the sample and reference cells are located, and a detector. The system used here utilised a double-beam system, such that the source radiation is split into two beams of equal intensity which traverse two light paths of identical length; one through the reference cell and one through the sample cell. Comparison of the intensity of the light which has passed through the reference and sample allows for corrections to be made to compensate for absorption by the cells and solvent, and the fluctuations in the power of the radiation source.

A light source which has uniform intensity over the whole range of wavelengths to be used is the ideal. The V-570 uses a halogen lamp with a useable wavelength range of 330-2500 nm, and a deuterium gas discharge lamp with a useful wavelength range of 190-350 nm. To maintain a uniform intensity over the range of wavelengths the current supplied to the bulb filament is controlled. In order to sweep through the range of wavelengths a Czerny-Turner monochromator is used. A Czerny-Turner monochromator uses broad band light which is diffracted by a slit placed at the effective focus of a curved mirror. The light reflected from this mirror is effectively collimated. The collimated light is then diffracted by a grating and reflected off another curved mirror. This second curved mirror refocusses the now dispersed light through an exit slit and onto a target. Rotation of the diffraction grating causes the dispersed light to move relative to the exit slit, allowing for selected wavelengths to illuminate the sample and reference. The system

used here has a stray light level of 0.1%, a spectral bandwidth as small as 0.4 nm, and a resolution of 0.5 nm.

The detector in the V-570 system consists of a photomultiplier and a peltier-cooled PbS photocell. The photomultiplier consists of an evacuated tube containing a cathode which an incoming photon strikes leading to the release of an electron. This electron will strike a dynode which is held at a positive bias relative to the cathode. The dynode releases more electrons, which then strike a succession of dynodes releasing a cascade of electrons which finally fall on to an anode giving a large measurable signal for each incoming photon. The gain in a typical photomultiplier containing nine or more dynodes can be as high as 10^9 electrons per photon.

Sample and reference cells are quartz cuvettes in order that no absorption occurs at the wavelengths of interest, and are chemically inert to organic solvents. Due to the use of a double-beam, matched cells are used where the absorption of the two cells is equal or nearly equal so as to minimise any error.

3.4 Photoluminescence

3.4.1 Introduction and Basic Operation

Photoluminescence (PL) uses light in the near infra-red to the ultra-violet range to excite the molecules of a sample and record the resulting luminescence[7, 8].

In luminescence, emission of photons by excited state electrons returning to ground state energy levels are recorded. Photoluminescence can be separated into two types, fluorescence and phosphorescence.

Fluorescence occurs where an electron in the singlet state returns to the

ground state; this transmission is generally rapid and the excited state electron has a lifetime typically on the order of 10s of ns or less.

Phosphorescence occurs where the photon emission is from an electron in the triplet state, where the ground state electron has the same spin orientation as the excited state electron and therefore transmission of the excited state electron to the ground state is forbidden. Lifetimes in this case are much longer, typically milliseconds to seconds.

To probe the energy levels using PL, light is typically used to excite the electrons from the ground state to excited states, this is because the energy difference between the excited states is generally too large to populate the excited states via thermal means.

Upon absorption of a photon an electron is excited, and will be promoted to one of the vibrational levels in a higher electronic excited state. Normally the electron rapidly decays to the lowest vibrational level in the first electronic excited state in an internal conversion process, which occurs within 10^{-12} s, far quicker than decay to the electronic ground state occurs. Decay to one of the vibrational levels of the electronic ground state then occurs, leading to emission of a photon, the electron may then decay further to a lower vibrational level. It is the transmission from the lowest vibrational first electronic excited state to one of the vibrational states of the electronic ground state that is measured and leads to vibrational structure in an emission spectra.

Electrons in an excited singlet state can undergo transition to the triplet state via intersystem crossing, that is the spin of the excited electron reverses and is no longer paired with the ground state electron. Intersystem crossing from a triplet state to the singlet state are forbidden, as is decay from the excited triplet state to the ground state, and hence lifetimes are much longer;

this is known as Phosphorescence.

The vibrational levels seen in the luminescence spectra are similar to those seen in the UV-Vis spectra as the vibrational levels are much the same for the ground and excited electronic states.

Two modes of operation for photoluminescence are excitation and emission spectroscopy.

Excitation spectroscopy In excitation spectroscopy the wavelength of the incident light is swept while one wavelength is monitored.

Emission spectroscopy In emission spectroscopy the sample is illuminated at a fixed wavelength while the measured light wavelength is swept.

3.4.2 Equipment

The equipment used in these experiments was a JobinYvon-Horiba Fluorolog-3 spectrometer. A similar set up is used in fluorescence as in UV-Vis measurements, but here the emitted light intensity versus the emitted or incident light wavelength is measured. Also the emitted light needs to pass through a monochromator in order to determine the intensity of particular emitted wavelengths. The Fluorolog-3 system used two Czerny-turner with a grating monochromator. The light source was a 450 W xenon short-arc lamp, with an off-axis mirror for light collection and focusing. Detection was provided by a photomultiplier.

3.5 Cyclic Voltammetry (CV)

3.5.1 Introduction and Basic Operation

Cyclic voltammetry (CV) is an electrochemical technique that allows for the rapid location of the redox potentials of an electroactive species. For a complete treatment of the CV technique the text by Wang[9] is recommended.

In a typical set up an analyte is mixed into an electrolyte solution. Three electrodes are used; a reference electrode maintaining a constant potential, a working electrode which provides the sweeping potential and an auxiliary or counter electrode through which a current can flow. The working electrode makes a potential sweep, and upon reaching the the oxidation potential of the analyte a current will begin to flow as electrons move from the analyte to the working electrode. With the potential sweeping in the opposite direction, upon reaching the reduction potential of the analyte a current will again flow as electrons are moved from the working electrode to the analyte.

This above description is a rather simplistic view of CV and there are several factors to take into account that complicate the experimental technique, including diffusion rates of the analyte, sweep rates, and calibration.

3.5.2 Electric Double Layer

When a bias is applied to an electrode immersed in an electrolyte a thin layer of ions opposing the charge on the electrode builds up at the electrode-electrolyte interface, this is known as the *compact layer*. The oppositely charged ions screen the remainder of the electrolyte solution from the potential field which drops off linearly and rapidly through this layer. Due to Brownian motion some of the charges diffuse to and fro this layer, and

as a result the remainder of the potential drops off more slowly through a broader *diffusion layer*.

3.5.3 Nernst Equation

The Nernst equation describes relationship between the chemical gradient in an electrochemical cell and the electric gradient which balances it. This is important in cyclic voltammetry where the spatial distribution of ions creates a chemical gradient and the potential applied to the electrodes causes an electric gradient.

$$E = E^0 - \left[\frac{RT}{zF} \right] \ln \frac{a_{red}}{a_{ox}} \quad (3.10)$$

where E is the reduction potential of the analyte at temperature T , E^0 is the standard reduction potential, R is the universal gas constant, z is the number of moles of electrons transferred in the reaction, F is Faraday's constant which is the number of Coulombs per mole of electrons ($F = 9.649 \times 10^4 \text{Cmol}^{-1}$), and a_{red} and a_{ox} are the chemical activity for the reductant and oxidant of the analyte respectively.

3.5.4 Mass Transport

Where the kinetics of the electron transfer between the redox analyte and the electrode are rapid, the mass transfer via diffusion of the redox analyte to the electrode surface dominates the current. In this case the Nernst equation 3.10 describes the concentrations of the redox analyte at the electrode surface.

As a more negative potential is applied to the electrode the concentration of the oxidised analyte at the electrode surface decreases. If the electron transfer rate is very rapid then the current i , will be directly related to the

diffusion rate of the oxidised analyte to the electrode surface,

$$i = nFAJ \quad (3.11)$$

here n is the number of electrons, A is the surface area of the electrode and J is the flux of the oxidised analyte to the electrode surface. Where the flux is given by Fick's law,

$$J = -D \left(\frac{dC}{dx} \right)_{x=0} \quad (3.12)$$

where D is the diffusion coefficient of the analyte and the concentration gradient of the oxidised species at the electrode surface is given by $(dC/dx)_{x=0}$.

When there is no potential applied to the electrode there is then no concentration gradient. As the potential of the electrode is decreased the concentration of the oxidised analyte at the electrode surface is decreased leading to an increased concentration gradient. The increased concentration gradient leads to increased diffusion through Fick's law 3.12, and hence an increase in the current. As the potential of the electrode continues to decrease the bulk of the solution will eventually become depleted of the oxidised analyte, the concentration gradient will then decrease and so will the current.

When the potential is then swept back from the largest negative point back through to zero there is a drop in current as the surface concentration begins to increase as the analyte is oxidised. The current flow becomes large as the concentration gradient becomes large, until the bulk concentration increases.

3.5.5 Calculation Against $\text{Fe}(\text{C}_5\text{H}_5)_2$ Standard

In order to calculate the energy of the redox potentials and therefore calculate the HOMO and LUMO energy levels of the electroactive material, the results must be compared to that of a known standard. Once the initial CV sweeps have been performed using the species under examination, the standard is added to the electrolyte/analyte solution and the further sweeps are carried out. As long as the standard and the analyte do not react, then the location of the redox potentials of the standard will allow for calculation of the analyte energy levels. The standard used in the experiments in this thesis was $\text{Fe}(\text{C}_5\text{H}_5)_2$.

The reduction potential for Ferrocene in this set up was known to be at 0.46V[10].

3.5.6 Set Up

The set up for the experiments carried out in this thesis are as follows.

A Parstat 2273 potentiostat was used in conjunction with a three-electrode cell. The working electrode was a platinum disc of diameter 1.0 mm, and the auxiliary electrode was a platinum wire. The reference electrode was a silver wire separated from the test solution by a fine-porosity frit. The solutions were comprised of 10ml of CH_3CN with 0.1 mol dm^{-3} of $[\text{NBu}_4][\text{PF}_6]$ as the supporting electrolyte and $0.1 \times 10^{-3} \text{ mol dm}^{-3}$ of analyte. The solutions were purged with a stream of N_2 gas prior to the experiments and then maintained under a positive pressure of N_2 during the experiments. Potentials were measured against a Ferrocene standard.

3.6 X-ray Diffraction (XRD)

A brief introduction to the technique of x-ray diffraction (XRD) is given here, with the focus on grazing incidence x-ray diffraction (GIXRD); for a more comprehensive explanation several texts are recommended [11, 12, 13]. Covered here also is a description of the beamlines, experimental set up and analysis software used for the XRD experiments.

3.6.1 Introduction and Basic Operation

The technique of X-ray diffraction is a very powerful technique that allows for the interpretation of the atomic structure of crystalline materials. A beam of electromagnetic radiation of wavelength 0.1-100Å is directed at a sample, which diffracts the beam at an angle determined by the separation of the sample's atomic spacings and the wavelength of the incoming radiation. The angle and intensity of the diffracted beam can be detected using either a point or area detector and the structure of the sample can then be inferred from the recorded data.

History and Development

X-rays were first discovered in 1895 by Willhelm Röntgen. In 1912, Paul Peter Ewald and Max von Laue discussed the possibility that crystals could be used as a diffraction grating for X-rays. This was tested by von Laue and two technicians later that year and it was found that a beam of X-rays shone through a copper sulphate crystal produced a large number of well-defined spots arranged in a pattern on a photographic plate. Von Laue later won the Nobel Prize in Physics for his work in which he developed a law connecting the scattering angles and the size and orientation of the unit-cell spacings in

a crystal.

X-ray sources [14, 15] Modern day synchrotrons provides high intensity beams of X-rays for diffraction purposes, with brilliances on the order of 10^{20} photons/s/mrad²/mm²/0.1 % bandwidth.

These synchrotrons generally consist of a linear accelerator (or linac), a booster synchrotron and then a large storage ring. The electrons are produced in the linac, and accelerated in the booster synchrotron, finally they are brought up to and maintain at speed in the storage ring, where the beamlines are fed off.

3.6.2 Scattering

To understand x-ray diffraction it is best to begin with the simplest system which is that of an incident electromagnetic wave being scattered by a single electron, and is described by Thomson scattering. Following this the more complicated system of two electrons will be considered before moving onto a bulk material.

Thomson Scattering

To begin with, the scattering of an x-ray by a single atom shall be considered. Classically, an incident electric field exerts a force on the electron causing it to oscillate and emit a scattered spherical wave, as depicted in figure 3.3. The wavelength of the scattered wave possesses the same wavelength but is 180° out of phase with the incident wave, this describes Thomson scattering, an elastic scattering process. Inelastic scattering also occurs but elastic scattering is the main process that is utilised in the study of material structures. The incident radiation is described by a plane wave of amplitude E_x0 with

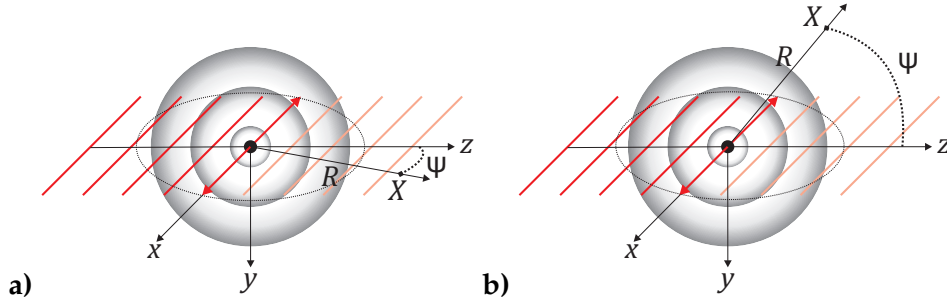


Figure 3.3: Diagram of Thomson scattering of an X-ray by an electron. The electric field of an incident plane wave (red lines), which propagates along the z-axis with the electric field polarised in the x-direction, sets the electron into motion which then emits a spherical wave (grey circles). The wave peaks of the incident and the scattered spherical waves are 180° out of phase due to Thomson scattering. R is the distance to point X , and ψ is the angle between point X and the direction of propagation when it lies in the plane of polarization in a) and it is the angle between the between point X and the plane of polarisation of the incident wave, in b).

the E-field given by $E_{in} = E_{x0}e^{i\omega t}$.

If an observation point X , is taken in the plane of polarisation of the incident beam E-field, then using Maxwell's equations the ratio of the E-fields of the radiated to incident beams can be derived[11], and is found to be:

$$\frac{E_{rad}}{E_{in}} = - \left(\frac{e^2}{4\pi\epsilon_0 mc^2} \right) \frac{e^{ikR}}{R} \cos \psi \quad (3.13)$$

where e is the charge on the electron, m is the electron's mass, ϵ_0 is the permittivity of free space, and c is the speed of light in a vacuum. ψ is the angle between the observation point and the direction of propagation of the incident beam as shown in figure 3.3 a). The term $\cos\psi$ accounts for the fact that the acceleration of the oscillating electron observed at X decreases as ψ increases, and is zero at $\psi = \pi/2$. The prefactor is the *Thomson scattering length* r_0 , also known as the classical electron radius,

$$r_0 = \left(\frac{e^2}{4\pi\epsilon_0 mc^2} \right) = 2.82 \times 10^{-5} \text{Å} \quad (3.14)$$

An X-ray detector will typically record individual photons. It will measure the scattered intensity I_{sc} , which is the number of photons detected per second.

The ratios of the intensities of the scattered beam to the incident beam can be written as,

$$\frac{I_{sc}}{I_0} = \frac{|E_{rad}|^2 R^2 \Delta\Omega}{|E_{in}|^2 A_0} \quad (3.15)$$

I_0 is the incident beam intensity, $R^2 \Delta\Omega$ is the cross-sectional area of the scattered beam, $\Delta\Omega$ is the solid angle subtended by the detector, and A_0 is the cross-sectional area of the incident beam. The energy per unit area of the beams is proportional to the modulus squared of the electric fields.

The scattered intensity is typically normalised by the incident flux (I_0 / A_0) and the solid angle of the detector. This leads to the definition of the differential cross-section,

$$\left(\frac{d\sigma}{d\Omega} \right) = \frac{(\text{Number of X-rays scattered per second into } \Delta\Omega)}{(\text{Incident flux})(\Delta\Omega)} \quad (3.16)$$

Using equations 3.13 and 3.15 the differential cross-section for Thomson scattering is

$$\left(\frac{d\sigma}{d\Omega} \right) = \frac{I_{sc}}{(I_0 / A_0) \Delta\Omega} = \frac{|\mathbf{E}_{rad}|^2 R^2}{|\mathbf{E}_{in}|^2} = r_0^2 \cos^2 \psi \quad (3.17)$$

Due to the fact that the observation point X, may not lie in the plane of the polarisation of the E-field of the incident beam then a polarisation

factor P , can introduced so that the differential scattering cross-section then becomes

$$\left(\frac{d\sigma}{d\Omega}\right) = r_0^2 P \quad (3.18)$$

where

$$P = \begin{cases} 1 & \text{in plane perpendicular to polarisation} \\ \cos^2 \psi & \text{in plane of polarisation} \\ 1/2(1 + \cos^2 \psi) & \text{unpolarised radiation} \end{cases} \quad (3.19)$$

A synchrotron source is typically polarised in the horizontal plane.

Two Electron Scattering

The next system to consider, which is only slightly more complicated than the single electron system is that of two electrons separated by distance r , as depicted in figure 3.4. The incident beam has wavevector \mathbf{k} , whilst the scattered beam has wavevector \mathbf{k}' . Due to the separation of the electrons the incident beam impinging on the electron at \mathbf{r} has to travel further than the beam impinging on the electron at the origin, denoted by O. This results in a phase difference of $\mathbf{k} \cdot \mathbf{r}$. A further phase difference occurs in the scattered beams of $\mathbf{k}' \cdot \mathbf{r}$, and so the total phase difference of the beams as witnessed by an observer is $(\mathbf{k}' \cdot \mathbf{r} - \mathbf{k} \cdot \mathbf{r})$ or $(\mathbf{k}' - \mathbf{k}) \cdot \mathbf{r}$, which then allows for the introduction of the scattering vector \mathbf{Q} defined as the difference between the incident and scattered wavevectors,

$$\mathbf{Q} = \mathbf{k}' - \mathbf{k} \quad (3.20)$$

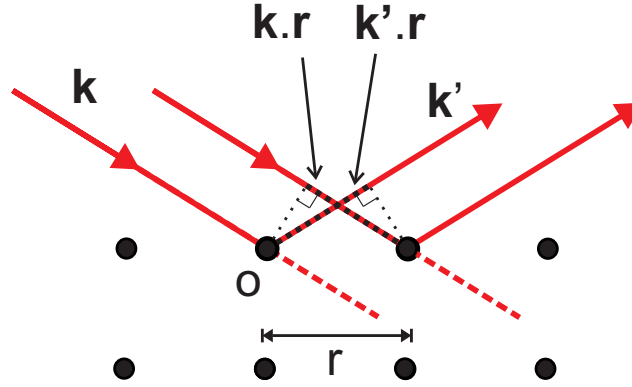


Figure 3.4: Sketch of X-ray diffraction

Therefore the phase difference $\Delta\phi(\mathbf{r})$ is given by

$$\Delta\phi(\mathbf{r}) = (\mathbf{k} - \mathbf{k}') \cdot \mathbf{r} = \mathbf{Q} \cdot \mathbf{r} \quad (3.21)$$

As we are dealing with elastic scattering where $|\mathbf{k}| = |\mathbf{k}'|$, the magnitude of the \mathbf{Q} vector is given by $|\mathbf{Q}| = 2|\mathbf{k}| \sin \theta = (4\pi/\lambda) \sin \theta$.

One Atom

The next step in the description of scattered x-rays, is to introduce the scattering from an electron density surrounding an atom with Z electrons, and specified by a number density $\rho(\mathbf{r})$. The scattering from a distribution of electrons is similar to the two electron scattering, where the phase difference of a wave scattered from the origin and one scattered from a volume element is as equation 3.21.

So a volume element $d\mathbf{r}$ at \mathbf{r} will contribute an amount $-r_0\rho(\mathbf{r})d\mathbf{r}$ to the scattered field with a phase factor of $e^{i\mathbf{Q}\cdot\mathbf{r}}$.

The total scattering length of the atom is given by

$$r_0 f^0(\mathbf{Q}) = r_0 \int \rho(\mathbf{r}) e^{i\mathbf{Q}\cdot\mathbf{r}} d\mathbf{r} \quad (3.22)$$

where $f^0(\mathbf{Q})$ is known as the atomic form factor, and is a measure of the scattering amplitude of a electromagnetic wave by an isolated atom.

While $f^0(\mathbf{Q})$ is known as the atomic form factor, there are in fact another two terms known as the dispersion corrections. $f'(\hbar\omega)$ describes the reduced scattering length from the tightly bound K shell electrons when the x-ray energy is much less than the binding energy of the K shell. $f''(\hbar\omega)$ represents the dissipation in the system, and describes the phase lag of the electron with respect to the driving field. These terms do not have any appreciable dependence on \mathbf{Q} .

A Crystal

To achieve a measurable signal, a very large number of scattering sites are required, such as those found in a crystal. Here the sites are the molecules which are periodically arranged in space. The crystal can be broken down in to two components: the lattice sites, which are the regular points in space where the identical repeating units reside, and the unit cell, which is the repeating unit, and comprises of a fixed pattern of atoms.

\mathbf{R}_n represents the lattice vectors that define the lattice, such that

$$\mathbf{R}_n = n_1\mathbf{a}_1 + n_2\mathbf{a}_2 + n_3\mathbf{a}_3 \quad (3.23)$$

and \mathbf{r}_j are the positions of the individual atoms within the unit cell. Therefore, the position of any particular atom in the crystal can be given by $\mathbf{R}_n + \mathbf{r}_j$

The scattering amplitude for the crystal can now be given by the product of the two terms,

$$F^{crystal}(\mathbf{Q}) = \underbrace{\sum_{\mathbf{r}_j} f_j(\mathbf{Q}) e^{i\mathbf{Q} \cdot \mathbf{r}_j}}_{\text{Unit cell structure factor}} \overbrace{\sum_{\mathbf{R}_n} e^{i\mathbf{Q} \cdot \mathbf{R}_n}}^{\text{Lattice sum}} \quad (3.24)$$

The first term gives the scattering amplitude for the atoms in the unit cell, and is termed the unit cell structure factor, where $f_j(\mathbf{Q})$ is the atomic form factor of the j 'th atom in the molecule. The second term is the sum over all of the lattice sites. A factor of $-r_0$ is again required if the intensity is required in absolute units.

The lattice sum is different compared to the unit cell form factor in that it contains a vast number of terms. For a micron sized square crystallite has sides on the order of 10^4 the length of the unit cell, so that the number of terms of 10^{12} . The lattice sum contains a sum of phase factors which adds to order unity, except where all phases are a multiple of 2π ; in this case the sum is equal to a huge number of terms. So it is now important to solve for

$$\mathbf{Q} \cdot \mathbf{R}_n = 2\pi \times \text{integer} \quad (3.25)$$

The Reciprocal Lattice

In order to find solutions to equation 3.25 we can construct the reciprocal lattice. This lattice has dimensions of reciprocal space, and basis vectors $(\mathbf{a}_1^*, \mathbf{a}_2^*, \mathbf{a}_3^*)$, where

$$\mathbf{a}_i \cdot \mathbf{a}_j^* = 2\pi \delta_{ij} \quad (3.26)$$

Points on the reciprocal lattice are therefore specified by

$$\boxed{\mathbf{G} = h\mathbf{a}_1^* + k\mathbf{a}_2^* + l\mathbf{a}_3^*} \quad (3.27)$$

where h, k , and l are integers. It will now be apparent that if \mathbf{Q} coincides with a reciprocal lattice point, the scattering amplitude will be non-vanishing, as

$$\mathbf{G} \cdot \mathbf{R}_n = 2\pi(hn_1 + kn_2 + ln_3) \quad (3.28)$$

where h, k, l, n_i are integers, and so their sum is an integer.

For the observation of x-ray diffraction the Laue condition is fulfilled:

$$\boxed{\mathbf{Q} = \mathbf{G}} \quad (3.29)$$

The following equations allow for the construction of the reciprocal lattice in three dimensions,

$$\mathbf{a}_1^* = 2\pi \frac{\mathbf{a}_2 \times \mathbf{a}_3}{V}, \quad \mathbf{a}_2^* = 2\pi \frac{\mathbf{a}_3 \times \mathbf{a}_1}{V}, \quad \mathbf{a}_3^* = 2\pi \frac{\mathbf{a}_1 \times \mathbf{a}_2}{V} \quad (3.30)$$

where $V = \mathbf{a}_1 \cdot (\mathbf{a}_2 \times \mathbf{a}_3)$ and is the volume of the unit lattice.

Bragg's Law The Bragg condition describes the criteria for a diffraction pattern that arises from the constructive interference caused by the scattering of x-rays from an ordered crystal. It is equivalent to the Laue condition and is characterised by the Bragg equation,

$$m\lambda = 2d \sin \theta \quad (3.31)$$

where d is the lattice spacing, θ is the angle of incidence of the radiation with respect to the crystal planes, of wavelength λ and m is the order of diffraction.

3.6.3 Refraction

The refractive index of x-rays can be given by:

$$n = 1 - \delta + i\beta \quad (3.32)$$

n is typically less than unity for x-rays but by approximately 10^{-5} , with δ of the order of 10^{-5} in solid materials and 10^{-8} in air.

The critical angle,

$$\alpha_c = \sqrt{2\delta} \quad (3.33)$$

below which total external reflection occurs, is of the order of milli-radian.

Below α_c there is an evanescent wave which propagates within the refracting medium and parallel to the interface, with the amplitude dying out rapidly into the material. This gives penetration of only a few nanometres, rather than the many micrometres at angles above α_c , which allows for selective study between the surface and the bulk of a material.

3.6.4 Domain Sizing and Paracrystallinity

Domain Sizing

From the x-ray line profiles that are produced from the data it is possible to extract the 'particle' or 'domain' sizes of the materials under examination. A typical crystal can be made up of many smaller grains, and particularly in the case of a nanowire sample in which each wire is on the order of tens of nanometres in height and width and a few microns in length, some of these dimensions can be extracted from the data. For a nanowire it might not

be expected that the entire length forms one perfect crystal and rather that there are discontinuities along the long axis. For grain sizes from around $0.1 \mu\text{m}$ and below the diffraction patterns are very sensitive to the grain sizes and line broadening begins to occur, where the extent of the broadening is given by

$$B = \frac{K\lambda}{D \cos \theta} \quad (3.34)$$

where B is the full width half maximum (FWHM) broadening of the diffraction line in radians, and D is the diameter of the crystal particle. K is the Scherrer constant and is often cited in the literature to be 0.9, and was in fact derived in Scherrer's original paper to be $K = 2[2 \ln(2)/\pi]^{1/2} \approx 0.93$, see [13].

In reciprocal space we know that

$$\Delta q = \frac{4\pi}{\lambda} \cos(\theta) \frac{B}{2} \quad (3.35)$$

We identify the breadth $B = \Delta(2\theta)$ with the width of the Bragg spot with regards to the scattering angle and obtain[16]

$$D = \frac{2\pi K}{\Delta q} \quad (3.36)$$

Paracrystallinity

A perfect infinite crystal would be composed of atoms lying on a predictable lattice and would lead to a delta comb line profile. In reality, line broadening occurs due to the finite size of the coherent scattering domains of small crystals. Also atoms of real crystals deviate from the perfect positioning on the lattice leading to further line broadening. The deviation from the

perfect positioning on the lattice can be classified into two categories, non-cumulative disorder and cumulative disorder.

Non-cumulative disorder is a short range effect characterised by random statistical fluctuations about the perfect lattice positioning, and the average lattice is preserved. The main cause of this non-cumulative disorder is thermal lattice vibrations.

Cumulative disorder leads to long range disorder, and describes statistically homogeneous disturbances to the perfect lattice positioning. This causes broadening of the diffraction peaks with FWHM increasing with the diffraction order. The paracrystalline model, as developed by Hosemann et al[17], is used to describe cumulative disorder. This model has been used previously to describe polycrystalline polymers where the disorder was caused by impurities, dislocations, non-ideal chain packing, and polymer backbone twisting[18, 16, 19]. Cumulative paracrystalline disorder is described by the disorder parameter 'g-factor' or the degree of disorder. Estimates of the domain size and the g-factor can be extracted from the plot of the square of the FWHM of the diffraction peaks Δq , versus the diffraction order h raised to the fourth power,

$$\Delta q^2 = \left(\frac{2\pi}{D}\right)^2 + \left(\frac{2\pi}{d}\right)^2 (\pi g h)^4 \quad (3.37)$$

where gd is the standard deviation of the distribution function of the inter-plane spacings d . This equation applies for $g^2 h^2 \ll 1$. The slope and intercept give g and the domain size D respectively.

In this project the Williamson-Hall model[20, 21], as used by Wu et al[22], was employed by the software in order to extract the degree of disorder and the domain sizing from the data.

3.6.5 Setup

Beamlines

XRD experiments were carried out on beamlines I07 and I16 at the Diamond Light Source, UK, and on BM28 at European Synchrotron Radiation Facility (ESRF), France[14, 15]. BM28 is a bending magnet type beamline, with an 11-axis Huber diffractometer and a MAR CCD area detector. I07 is an insertion device type beam line that utilises a cry-cooled undulator, with a 2+3 circle diffractometer and hexapod, and uses a Pilatus 2M detector. I16 is also an insertion device beamline and utilises an undulator, with a 6-circle kappa diffractometer and a Pilatus 2M detector.

Chamber

In order to produce diffraction patterns with a high signal-to-noise ratio a custom experimental chamber was fabricated and attached to the diffractometer at the beamlines. The chamber was a sealed aluminium unit that was filled with Helium in order to minimise back scatter of the X-rays. The chamber had kapton windows for the incident and diffracted beam to pass through and a series of slits to further reduce the back scatter.

Inside the chamber the sample was fixed to a copper heater block using a thermally conductive paint. The copper block was mounted in the chamber via a ceramic spindle to reduce heat transfer to other parts of the chamber and to minimise thermal expansion, which could move the sample out of the incident X-ray beam during heating.

Thermocouples were mounted on the edge of the sample and on the copper heater block in order to monitor the sample temperature.

Geometry

The geometry of the sample and detector geometry is described in figure 3.5. A side view is presented in part a) with the sample represented by the grey square. The incident radiation, with wavenumber \mathbf{k}_i , enters from the left and impinges on the sample at an angle α_i from the horizontal. A portion of the beam is reflected at the same angle α_i . Part of the beam is transmitted and is refracted at an angle of α'_i from the horizontal as determined by Snell's law. The refracted beam is diffracted at an angle α_f from the horizontal, and has wavenumber \mathbf{k}_f . 2θ is the angle measured between the incident beam and the diffracted beam, $2\theta_B$ is the angle between the refracted incident beam and the diffracted beam, and $\Delta 2\theta$ is the difference between 2θ and $2\theta_B$. The reference frame of X,Y,Z is that relative to the plane of the sample, while the co-ordinates of X',Y' and Z' is relative to alignment to the incident beam, with Y = Y'. The angle $2\theta_v$ is the angle between the incident beam (or the X' axis) and the normal to the detector in the X'-Z' plane. The $2\theta_h$ is the angle between the incident beam (or the X-axis) and the normal to the detector in the X-Y plane.

Diffracted beams in the X-Z plane are described as out-of-plane (OOP) and diffracted beams in the X-Y plane are described as in-plane (IP). The scattering vector \mathbf{Q} can be decomposed into the following vector components, q_\perp in the OOP direction and q_\parallel in the IP direction.

The effects of refraction are considered negligible for the IP scattered beam. The data analysis software used in this thesis takes into consideration the refractive correction for the OOP line profiles. Further information regarding the refractive correction along with derivations of the error committed when considering the OOP exit angle α_f due to the incident wave rather than the refracted wave, can be found in Lilliu's thesis[23] and work by Toney et al[24].

Software

Data analysis was completed using Matlab code ('GI-XRD-GUI') written by a colleague, Samuelle Lilliu, of Cardiff University, School of Physics and Astronomy. The software allowed for the calibration of the experimental set up (sample-detector distance, etc.), line profiles, removal of background signal, curve fitting, and data extraction such as domain sizes and disorder measurements. For a more detailed description of the software see Dr.Lilliu's PhD thesis[25].

Calibration Initially the direct beam (DB) was located on the acquired XRD image; a local region of interest (ROI) was used to extract the DB position. A thin lead beam stop allowed for transmittance of the DB at an intensity that could be seen on the images whilst not saturating and damaging the detectors. In some cases, where a thick, non-transmitting beam stop was used, a circle fit technique was used, where an approximate DB position and an intense diffraction ring were indicated by the user, and the software would fit a circle to the ring and identify the centre. This process has a lower accuracy but could be improved with several iterations and using a batch of images.

The software could calculate the sample detector distance by tracking the DB on batches of images captured during vertical and horizontal scans of the detector.

Given the DB position and the sample-detector distance the software allowed for conversion of the pixels to Q-values.

Line Profile Analysis Line profiles were taken as 'cake segments' about the DB, where the length of the profile, the arc length and the number of

sample points between the arc could be specified. using this 'cake slice' approach improved the signal to noise ratio. The intensity was smoothed using a Savitzky-Golay filter, which is a generalised moving average.

Tangential profiles could also be taken for a fixed pixel radius with a arc about the DB, and a user specified pixel width. Intensity values were extracted at each point of each of the circles and then radially summed.

Once line profiles were produced, the background could be subtracted and fits made to the peaks. In order to do this 'fit blocks' could be defined, that is portions of the line profile could be selected. The background would then be subtracted by selecting fit blocks to the portions between the peaks, and an arbitrary number of Gaussian were then fitted. A number of other background techniques were available including nearest neighbour, linear, and cubic spline.

For each fitting Gaussian, the parameters could be controlled by inputting boundaries for a,b and c.

$$f(x) = a \exp \left(\left(\frac{x-b}{c} \right)^2 \right) \quad (3.38)$$

After background subtraction fit blocks could be used to define the portion of the line profile to which the peak was required to be fit. Multiple Gaussians could be used to fit to single peaks; this allowed for the peak broadening to be taken into account. It was then possible to fit a Pearson VII distribution to the multiple Gaussians. The Pearson VII fit is given by [20]

$$f(x) = \left[1 + \left(\sqrt[m]{2} - 1 \right) (x - x_0)^2 / w^2 \right]^{-m} \quad (3.39)$$

x_0 corresponds to the centre of the peak, w is the width and m is found by the software's algorithm. The Pearson distribution can be seen as a function

between a Gaussian ($m \rightarrow \infty$) and a Cauchy-Lorentz ditribution ($m \rightarrow 1$).

The software could identify peaks in the line profiles, and allowed for the parameters to be based on the peak positions and intensities. This allowed for tracking of the peaks when batch processing a series of images where the peaks may involve, eg. during annealing scans.

Bibliography

- [1] Sarid D. *Scanning Force Microscopy: With Applications to Electric, Magnetic, and Atomic Forces*. Oxford series on optical sciences. Oxford University Press, 1994.
- [2] Binnig G, Quate C F, and Gerber C. Atomic force microscope. *Physical Review Letters*, 56(9):930–933, Mar 3 1986.
- [3] *di Multimode SPM Instruction Manual*, revision b edition, 2004.
- [4] www.nanoscience.com. Nanoscience instruments, April 2012. [Online; accessed 19th April 2012].
- [5] Wang Y and Chen X. Carbon nanotubes: A promising standard for quantitative evaluation of AFM tip apex geometry. *Ultramicroscopy*, 107(4 - 5):293 – 298, 2007.
- [6] Plaschke M, Schäfer T, Bundschuh T, Ngo Manh T, Knopp R, Geckeis H, and Kim J I. Size characterization of bentonite colloids by different methods. *Analytical Chemistry*, 73(17):4338–4347, 2001.
- [7] Robinson J W, Frame E M S, and Frame G M. *Undergraduate instrumental analysis*. M. Dekker, 2005.
- [8] Lakowicz J R. *Principles of Fluorescence Spectroscopy*. Number v.1 in Principles of Fluorescence Spectroscopy. Springer, 2006.
- [9] Wang J. *Analytical Electrochemistry*. John Wiley & Sons, 2004.
- [10] Connelly N G and Geiger W E. Chemical redox agents for organometallic chemistry. *Chemical Reviews*, 96(2):877–910, 1996.
- [11] Als-Neilsen J and McMorrow D. *Elements of Modern X-ray Physics*. Wiley, 2001.
- [12] Cullity B D. *Elements of X-ray Diffraction*. Addison-Wesley, Second edition, 1978.
- [13] Warren B E. *X-ray Diffraction*. Addison-Wesley, 1969.

- [14] Diamond.ac.uk. Diamond light source, March 2012. [Online; accessed 20th March 2012].
- [15] www.ESRF.eu. European synchrotron radiation facility, April 2012. [Online; accessed 17th April 2012].
- [16] Smilgies D-M. Scherrer grain-size analysis adapted to grazing-incidence scattering with area detectors. *Journal of Applied Crystallography*, 42:1030–1034, Dec 2009.
- [17] Hosemann R. Der ideale parakristall und die von ihm gestreute kohärente röntgenstrahlung. *Zeitschrift für Physik*, 128:465–492, 1950.
- [18] Hindeleh A M and Hosemann R. Microparacrystals: The intermediate stage between crystalline and amorphous. *Journal of Materials Science*, 26:5127–5133, 1991.
- [19] Hindeleh A M and Hosemann R. Paracrystals representing the physical state of matter. *Journal of Physics C: Solid State Physics*, 21(23):4155, 1988.
- [20] Birkholz M. *Thin Film Analysis by X-Ray Scattering*. John Wiley & Sons, 2006.
- [21] Rivnay J, Noriega R, Kline R J, Salleo A, and Toney M F. Quantitative analysis of lattice disorder and crystallite size in organic semiconductor thin films. *Phys. Rev. B*, 84:045203, Jul 2011.
- [22] T-M Wu, Blackwell J, and C S N. Determination of the axial correlation lengths and paracrystalline distortion for aromatic copolyimides of random monomer sequence. *Macromolecules*, 28(22):7349–7354, 1995.
- [23] Lilliu S. *Organic Photodetectors Optimization and Nanoscale Investigation*. PhD thesis, School of Physics and Astronomy, Cardiff University, 2011.
- [24] Toney M F and Brennan S. Observation of the effect of refraction on x rays diffracted in a grazing-incidence asymmetric bragg geometry. *Phys. Rev. B*, 39:7963–7966, Apr 1989.
- [25] Samuele L. *Organic Photodetectors Optimization and Nanoscale Investigation*. PhD thesis, Cardiff School of Physics and Astronomy, Cardiff University, 2011.

Chapter 4

Growth

4.1 Introduction

Pre-formed crystals of polythiophenes have found a lot of interest as they achieve what a lot of post production treatment techniques try to do in devices such as OPVs and OFETs, which is achieve a high degree of crystallinity in an attempt to improve charge carrier transport. What is important in these crystals, or nanowires (NWs), is how they crystallise, i.e. the growth mechanisms and the final structural characteristics. If these could be understood fully then the potential to control the physical characteristics of the NWs may exist, leading to improvements in device performance when used in OPVs and OFETs.

In this chapter the dimensions of P3HT and PQT-12 NWs grown in several different organic solvents are investigated using AFM, along with the rate of growth of the NWs during cooling of the solutions and subsequent maturation of the solutions once room temperature has been reached. UV-Vis was also used to investigate the absorption properties of the NW form of the NWs compared to the dissolved polymer. Finally XRD was used to

investigate the structure of the NWs after they have precipitated out of solution and also during and after annealing. All results are presented together followed by discussion of these results.

4.1.1 Review

NW growth Polythiophene nanowires were first reported by Ihn et al[1] in 1993, who found that poly(3-alkylthiophenes) would crystallise out of solution when dissolved in marginal solvents at elevated temperatures and subsequently cooled down. They found the ability to grow NWs in a particular solvent was dependent on the length of the alkyl chain attached to the thiophene ring of the polymer; this could be explained by the increased solubility associated with a longer alkyl chain, and the mechanism of growth where a marginal solvent would be a good solvent at elevated temperatures and become poorer as the temperature decreased.

Samitsu[2] studied various polymers for their potential to form NWs in several solvents using variations on the whisker method of production as described by Ihn. They studied regio-random (RRand) P3HT, where the position of the alkyl side chain is located randomly off the thiophene rings, as opposed to regio-regular where the alkyl side chain takes up regular positioning. They found that the success of NW formation relied on the regularity of the alkyl chain positioning, and the RRand P3HT failed to produce NWs. This indicated that the NW formation relied partly on the alignment of the polymer main chain, and the randomly oriented side chains could disrupt NW formation by obstructing the main chain alignment.

Samitsu found that PQT-12 would also assemble into NWs via the same whisker method, when using toluene as the solvent.

Samitsu[3] investigated further the formation of P3HT NWs using anisole

solvent. Anisole was found by Oosterbaan[4] as a favourable solvent for P3HT NW production due to the high yield of NWs and the low quantity of accompanying precipitates.

Oosterbaan performed a fairly comprehensive study of several different P3ATs with a range of solvents and linked the success of wire formation, where they looked at yield and additional precipitates, and linked this to the dielectric constant of the solvent. The dielectric constant is general indicator of a solvent's polarity and therefore would suggest whether it is a good, poor or marginal solvent.

Wu[5] grew poly(3-pentylthiophene) (P3PT, with alkyl side chain of 5 carbon atoms) NWs using 1,2-dichlorobenzene (ODCB) and found that there was some effect on the NW width when the concentration of the polymer in the solution was changed. Widths decreased from 17.2 nm at a low concentration, through 17.0 nm at medium concentration to 16.4 nm at a high concentration, although all values were within the error range. Also, the length, and hence aspect ratio, decreased with increasing concentration.

P3BT NWs were grown by Xin[6, 7] using an ODCB solution, and found the NWs to have widths of 11-15 nm when grown in the presence of PCBM, and had aspect ratios of 500-900.

Alternative routes to growth of NWs have been achieved where a P3HT is dissolved in a good solvent at room temperature and crystallisation is induced via addition of a poor solvent[8]. NWs have also been known to grow when P3HT has been left in solution with a marginal-good solvent for an extended period of time.

Kim[9] produced P3HT NWs using solvent vapour approach where films were spun from chloroform solution under vapour pressures of 6.2 kPa and above. The NWs produced were therefore grown on the substrate rather

than in solution. The higher the vapour pressures used, the greater the aspect ratio of the NWs; widths of the wires were determined to be 21 ± 7 nm and heights of 4-5 nm.

Growth Mechanism Malik et al[10] investigated the gelation of P3ATs in solution of xylene. They proposed that a two stage process occurs in the gelation process and this may be extended to more dilute solutions. First a coil-to-rod transformation occurs where the disordered dissolved polymer chains straighten. The second step is fibrillar crystallisation of the rods. The initial coil-to-rod transformation was accompanied by a red shift in the absorption spectrum of the solutions which was due to an increase in the conjugation length because of the straightening of the polymer backbone. This appears to be the prevailing theory of formation of P3AT fibers in solution.

XRD and Structure Prosa's[11, 12] XRD diffraction work led to the first model of crystallised films of P3ATs. Further work was carried out by Arosio[13] and Tashiro[14]. Aasmundtveit[15] carried out XRD on P3OT films and found structural anisotropy. Wu carried out XRD on poly(3-pentylthiophene-2,5'-diyl) (P3PT) NWs and found them to be highly ordered with a lattice spacing of 15 \AA in the direction of alkyl-chain stacking, which was smaller than that of P3HT as was expected due to the shorter alkyl side chains[5].

Kayunkid[16] provided a comprehensive study of packing of highly ordered epitaxial P3HT films using electron diffraction and molecular modelling. They determined that the films possessed a monoclinic unit cell with space group $P2_1/c$ and two chains per cell, lattice spacings of $a = 1.60$ nm, $b = 0.78$ nm and $c = 0.78$ nm, and angle $\gamma = 86.5^\circ$.

XRD analysis of solvent vapour-induced NWs by Kim et al[9] showed

high order and strong orientation with the thiophene chains perpendicular to the SiO_x substrate and the long-axis, $\pi - \pi$ stacking running parallel to the substrate. Their analysis suggested that the alkyl-chain stacking (a-lattice parameter) had a distance of 16.8 Å which is comparable to P3HT films.

4.2 Experimental

Nanowires were grown using the whisker method as reported in the literature[1]. P3HT (ADS Dyes, M_W (GPC) = 28000, PDI = 1.7) was dissolved in solvent at a concentration of 0.5 mg/ml at 90°C and then allowed to cool at a rate of approximately 25°C/hr on top of the heater until it reached room temperature. PQT-12 (ADS Dyes, M_W (GPC) = 35 000, PDI = 2.6) was dissolved in solvent at 90°C and then cooled at a rate of 25°C per hour, until it had reached room temperature.

Samples made for AFM investigation were spun cast by taking samples from the cooling solutions at regular temperature and time intervals. The samples were spun cast from 40 µm of solution at 4000 rpm for 40s, on to SiO_2 substrates. The samples were investigated using a Veeco Multimode III SPM operating in tapping mode AFM.

UV-Vis was performed on NWs suspended in solution. UV-Vis was performed on a Jasco V-570 spectrophotometer.

The XRD setup and data analysis software was described in detail previously (section 3.6). Samples for XRD were prepared from solutions that had been centrifuged and the supernatant removed a minimum of 3 times and then left at a higher concentration in order to produce a thick mat of NWs so that a sufficiently strong signal diffraction signal could be measured. A 40 µm drop of the high concentration solutions were then dropcast onto 10

mm square, 1 mm thick SiO₂ substrates and left to dry for 2 hours under vacuum.

4.3 Results

4.3.1 Feature De-convolution

De-convolution of AFM features to correct for tip geometry effects was described in §3.2.2. Where de-convolution was performed related strongly to the FWHM measurements for all NWs. Where de-convolution was not performed the FWHM was used.

Kim[9] used a similar approach to measure the widths of their NWs produced using a solvent vapour approach, and found that their deconvolved AFM width measurements (average 21 ± 7 nm) agreed well with their TEM measurements (20~22 nm).

4.3.2 P3HT-Anisole NW Formation

AFM scans of the evolution of P3HT NWs grown in anisole are shown in figures 4.1 and 4.2. A 0.5 mg/ml solution of P3HT in anisole was cooled at a rate of 25°C/hour to form nanowires. Small sample droplets were taken at specific temperature and time intervals during this process and spin-coated spin-coated on to silicon substrates, which were then imaged using tapping-mode AFM. Initially small NW 'seeds' were seen at 70°C, along with a large amount of non-NW material. These seeds had lengths of 100~300 nm, heights of 3.9 ± 1.5 nm, and widths of 31.7 ± 8.2 nm.

Significant growth was witnessed at the beginning between 50 and 45°C (figure 4.1 c) and d)). The average height of the NWs didn't change much (4.7 ± 2.8 nm and 4.5 ± 1.5 nm at 50°C and 30 mins at room temperature re-

spectively) and nor did the widths (26.2 ± 3.6 nm 32.2 ± 4.6 nm at 50°C and 30 mins respectively) as the temperature of the solution decreased and time increased. The length of the NWs increased rapidly between 50 and 45°C going from an average of 124 ± 73.9 nm to 397 ± 253 nm, and then also between 40 and 35°C going from an average of 1170 ± 170 nm to extending to over $3\mu\text{m}$. Lengths weren't measurable after 35°C . A visual inspection suggested that increased substrate coverage occurred from 35 to 30°C but the AFM images remained largely unchanged after this point.

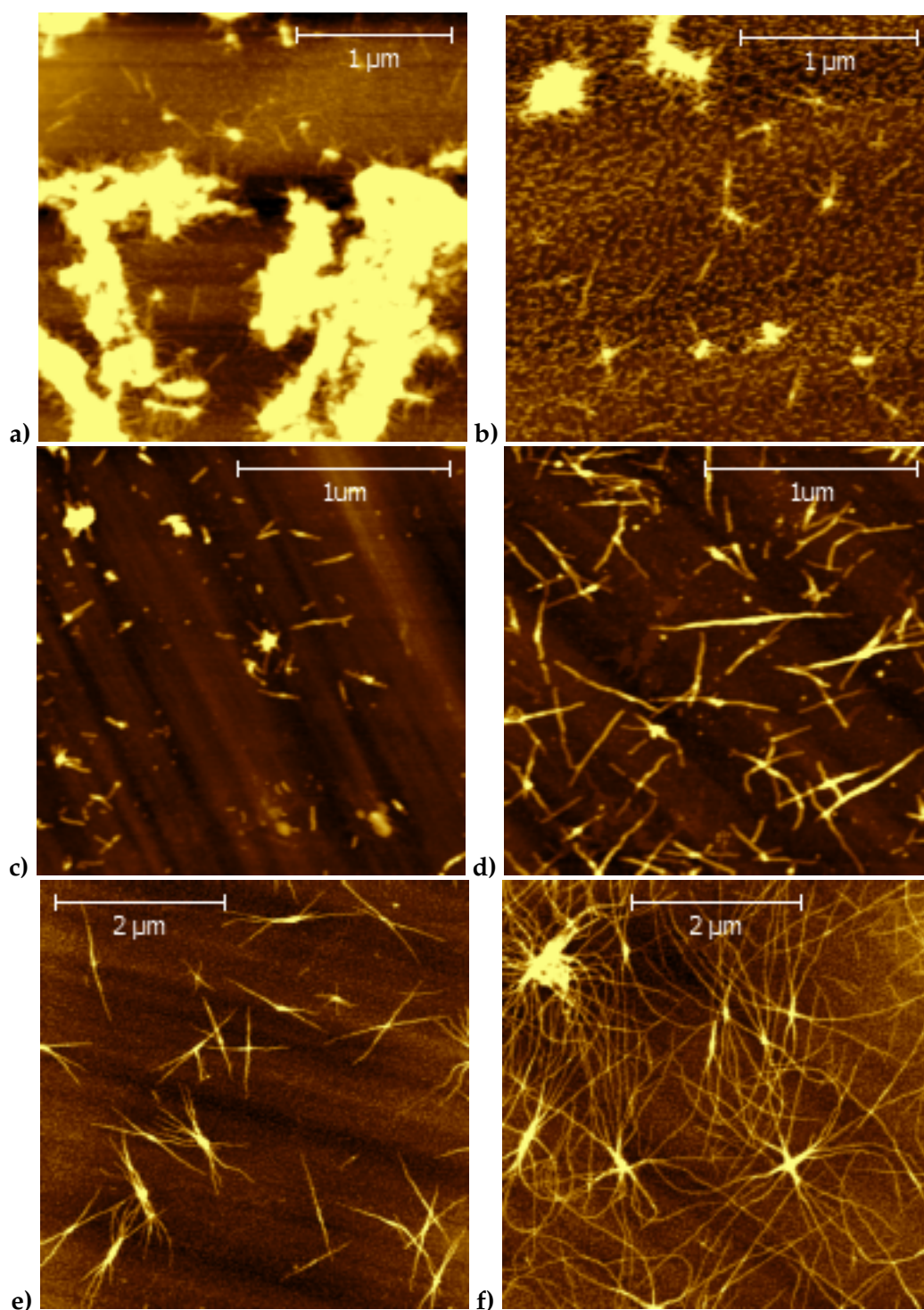


Figure 4.1: Growth of P3HT NWs in anisole. AFM scans taken of NWs deposited at a) 70°C, b) 60°C, c) 50°C, d) 45°C, e) 40°C, and f) 35°C, , where the deposited solution droplets were taken from a main solution where the main solution was cooling at a constant rate of approximately 25°C/hr. NW 'seeds' seen early on with a large amount of non-NW material, followed by increasing length, and webbing, before large networks begin forming.

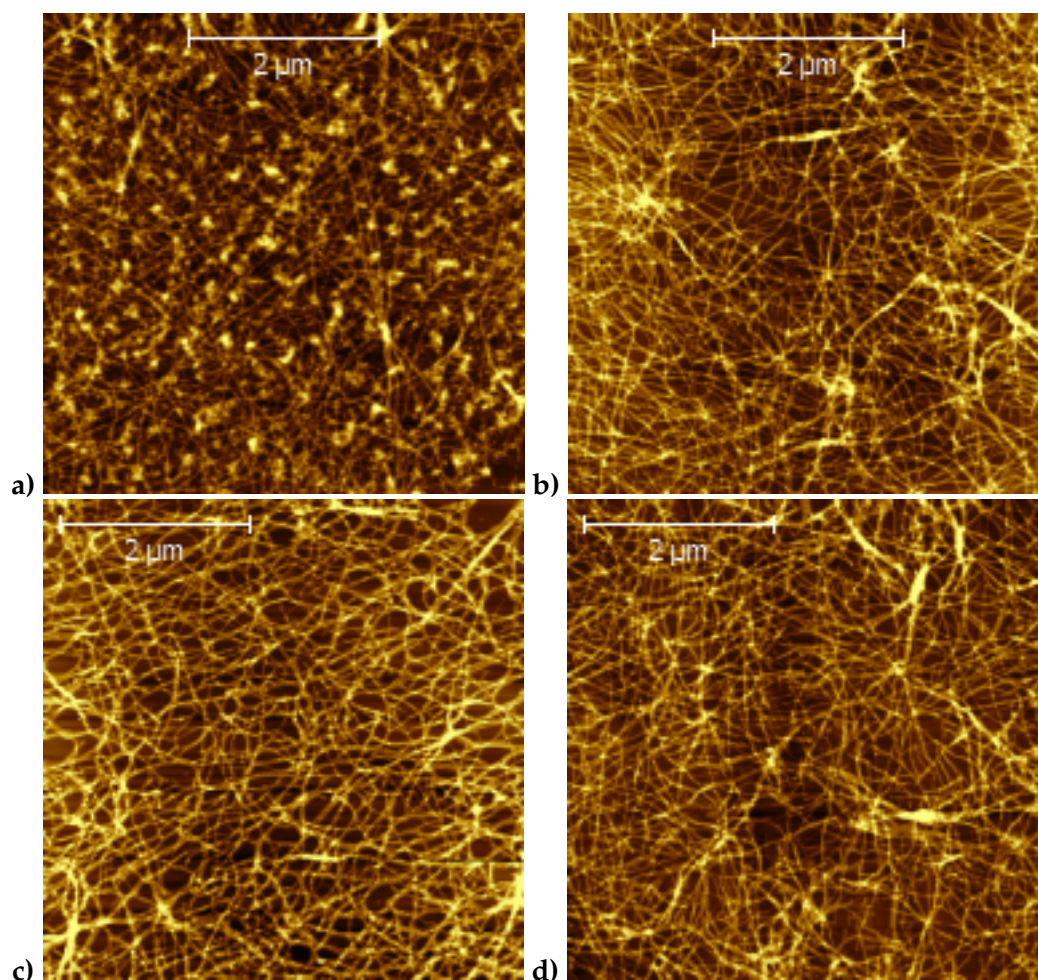


Figure 4.2: Growth of P3HT NWs in anisole. AFM scans taken of NWs deposited at a) 30°C, b) 25°C, c) 30 mins at RT, and d) 1 hour at RT. Little evolution seen via the AFM scans from 30°C onward. Patches of non-NW material were spread throughout the network in the 30°C scan.

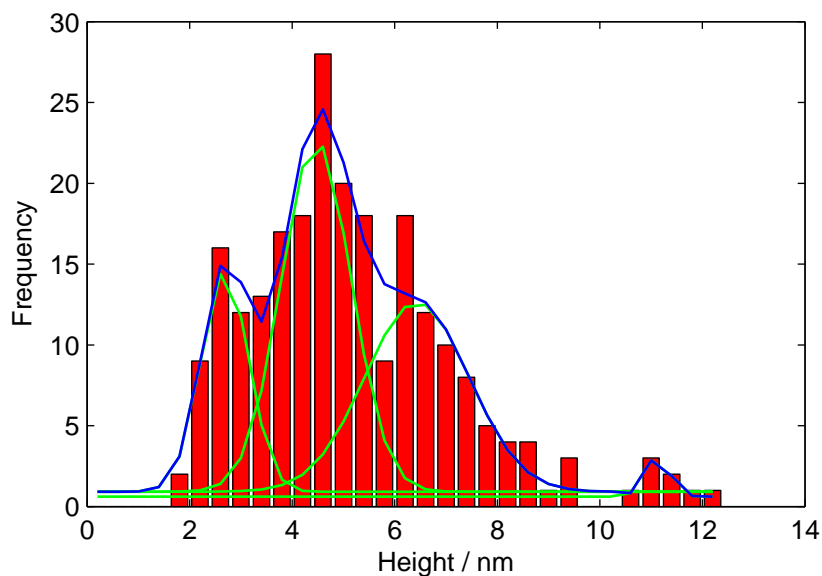
Dimensions

Figure 4.3 a) is a histogram of the heights of a sample of NWs measured at each stage of evolution, beginning at 70°C, decreasing through room temperature, and then held at room temperature for 30 mins and 1 hour. Three main peaks are seen in the graph, with a small fourth peak circa 11 nm. The first peak is seen at 2.7 nm, the next two peaks are at 4.5 nm and 6.4 nm, with the last peak at 11.1 nm. The lattice spacing for alkyl-chain stacking in P3HT NWs grown in anisole is seen to be circa 1.6 nm (see §4.3.9). Addition of multiples of 1.7 to 2.7 yields 4.3, 5.9, and 10.7, suggesting that the observed NW heights are an integral number of the alkyl-chain stacking lattice spacings.

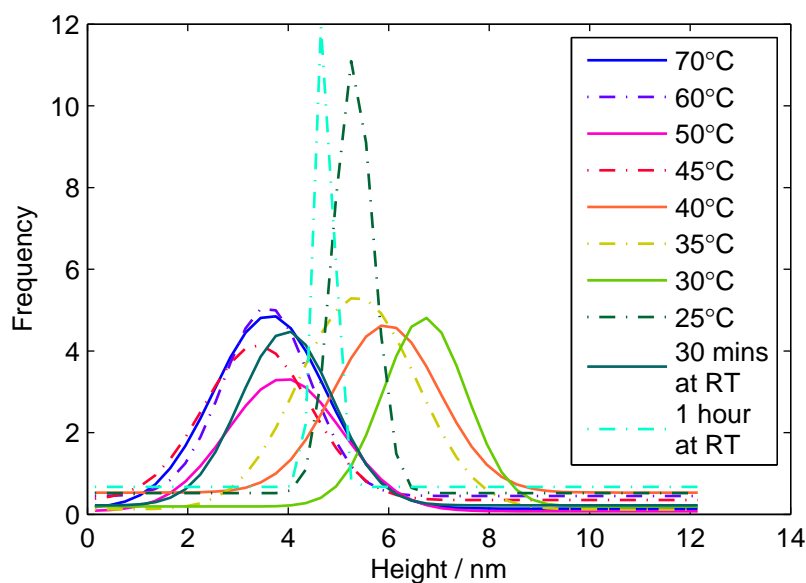
Figure 4.3 b) shows Gaussian curves which were fitted to frequency distribution data of NW heights as measured from AFM scans of P3HT anisole NWs deposited at different temperatures as the solution cooled, and also at several times intervals after reaching RT. So, for each NW sample that was used in the AFM study, the heights of the NWs were plotted as a histogram and a Gaussian curve as fitted to the data.

The data in the figure shows that peaks for deposition temperatures 70, 60, 50, 45°C and 30 mins after reaching RT are all centered around 3.4 nm. The other peaks are at increased heights, ranging from the peak for 1 hour at RT centred around 4.65 ± 0.25 nm, up to the peak for 30°C at 6.75 ± 0.25 nm. The data is inconclusive and is limited in the sample sizes (approximately 40 NWs per sample), but could be interpreted as follows. The initial NWs that form are on average 2 polythiophene chains stacked near vertically in height, and as the solution matures through decreasing temperature and time spent at RT the average NW is constructed of more stacking P3HT chains. One deviation from this in the data is that of the 30 mins at RT sample which

has the fitted Gaussian centered at 4.05 ± 0.25 nm, and is close to higher temperature sample peaks. This data does agree partly with the observation from the AFM images of the first appearance of full NWs between 50 and 45°C, as opposed to smaller seeds which appear from 70°C (see figure 4.1 and table 4.1).



a)



b)

Figure 4.3: Frequency distributions of P3HT anisole NW heights taken from AFM scans. a) is a histogram of the heights of NWs taken from scans of samples at all deposition temperatures from 70°C down to RT and including 30 mins and 1 hour at RT. The green lines are individual Gaussian fits to the peaks and the blue line is a summation of the fits. b) shows Gaussian fits to histograms of NW heights taken from scans at separate deposition temperatures.

4.3.3 P3HT-Cyclohexanone NW Formation

Figures 4.4 and 4.5 show AFM scans of the evolution of P3HT NWs grown in cyclohexanone as a function of the temperature and time once at room temperature respectively. At 70°C (figure 4.4 a)) non-NW material was seen on the substrate with no noticable NWs. Between 60 and 70°C short 'seeds' of material were seen, these were of length 0.15~1.2 μm , with heights of 3.1 ± 1.4 nm and widths of 40.6 ± 11.3 nm. At 60 and 50°C these seeds were found individually and in clusters of up to 10 NWs per cluster. At 40 and 30°C the seeds remained unchanged but were found to be aggregated in larger clusters and with more non-NW material surrounding them.

Between 30 and 25°C a significant change was witnessed with the emergence of long NWs which were in excess of a micrometre in length; they were still highly aggregated and associated with non-NW material. Isolated wires were rarely seen. Height of the NWs were 5.31 ± 1.73 nm and widths were 24.4 ± 5.70 nm. Little change was seen from 25°C through to the last AFM scans at 5 days.

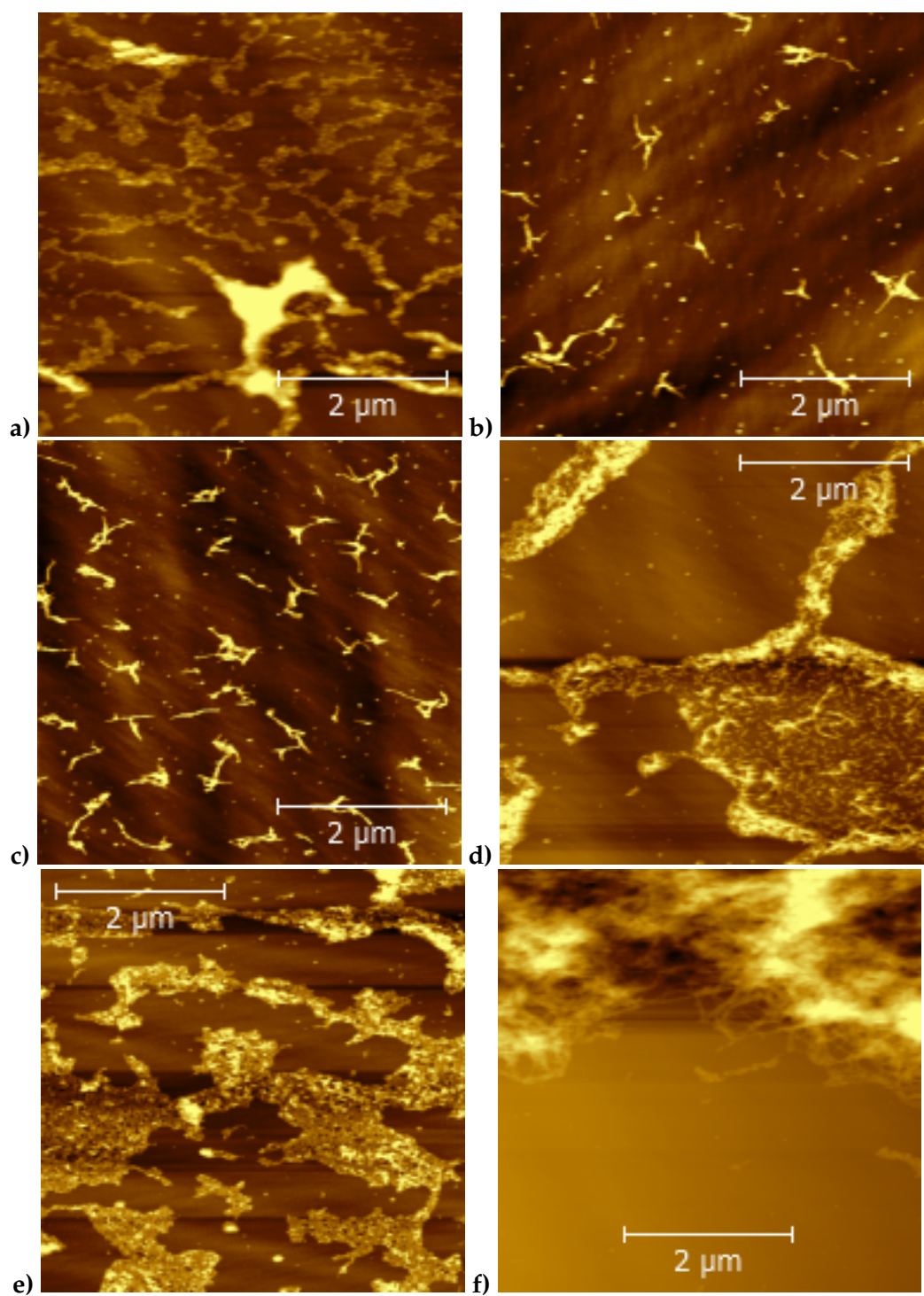


Figure 4.4: Growth of P3HT NWs in cyclohexanone. AFM scans taken of NWs deposited at a) 70°C, b) 60°C, c) 50°C, d) 40°C, e) 30°C, and f) 25°C, where the deposited solution droplets were taken from a main solution where the main solution was cooling at a constant rate of approximately 25°C/hr.

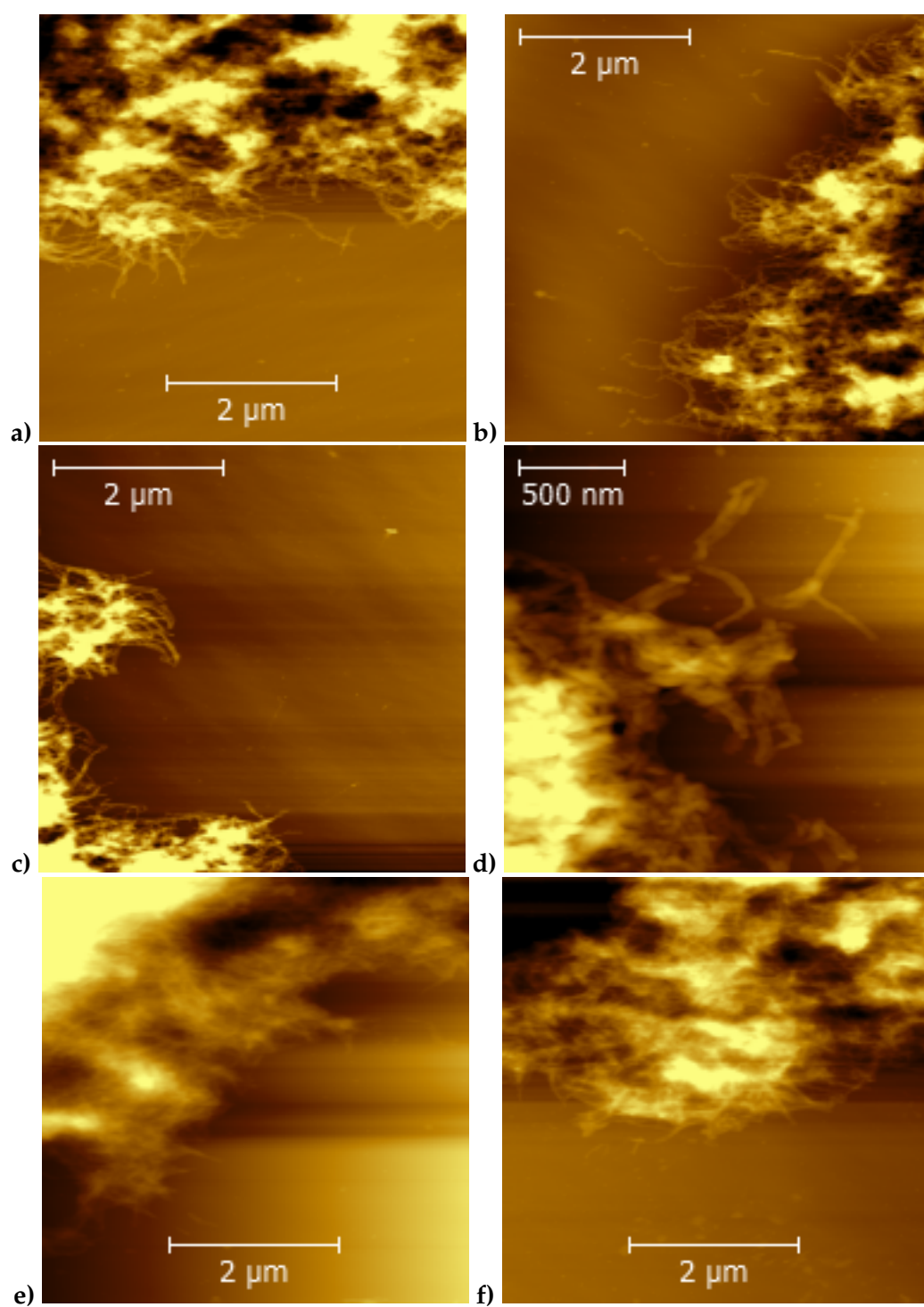


Figure 4.5: Growth of P3HT NWs in cyclohexanone. AFM scans taken of NWs deposited at a) 30 mins, b) 1 hour , c) 2 hours C, d) 3 hours C, e) 6hours, and f) 5 days at room temp.

4.3.4 PQT-12-Toluene NW Formation

Figures 4.6 and 4.7 show AFM scans of the evolution of PQT-12 NW growth in solution of toluene as a function of the temperature and time once at room temperature respectively. At 70°C non-NW material was seen on the substrate surface. The non-NW material appeared to have some degree of ordered structure although it was not believed to have arisen in solution, which remained highly transparent and bright orange in appearance. The non-NW material was 1.7 ± 0.25 nm in height. This film was seen down to 40°C.

Between depositing the NWs at 40°C and 35°C a transition, which could be temperature or time dependent, occurred where short (~ 200 nm), flat ($1.3 \sim 2.6$ nm), broad ($33 \sim 40$ nm) rough edged 'proto'-wires formed; this coincided with a darkening and increase in opacity of the solution. The 'proto'-wires lengthened over time up to $\sim 2 \mu\text{m}$ at 2 hours at room temp.

At 4 hours NWs with a different morphology appeared. A visual inspection of the AFM images revealed that they were straighter and smoother than the initial 'proto'-wires. The heights of the second stage fully-formed wires were 6.3 ± 0.4 nm, and the widths were 24.5 ± 5 nm. Both the 'proto' and fully-formed NWs were found aggregated.

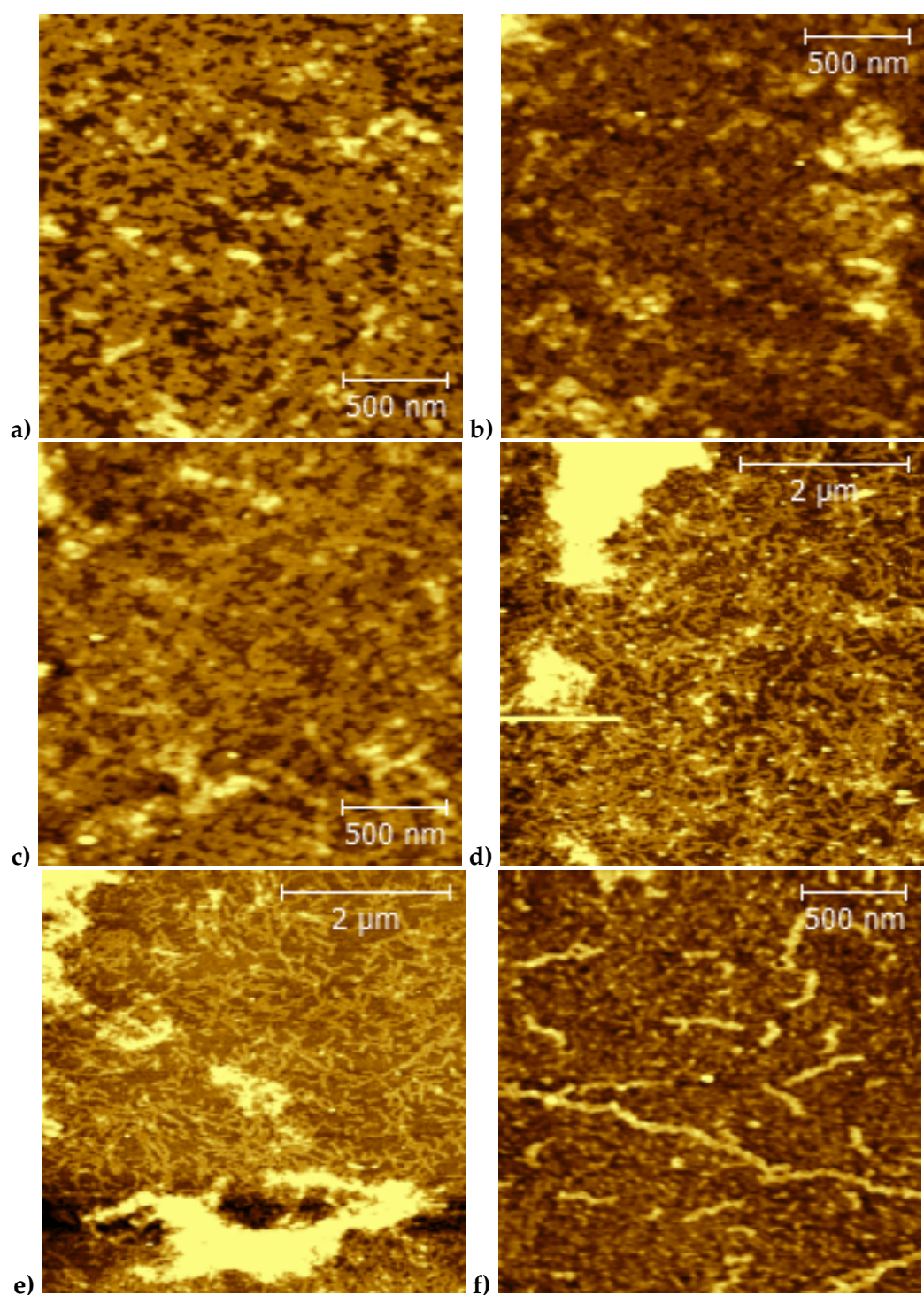


Figure 4.6: Growth of PQT-12 NWs in toluene. AFM scans taken of NW solution deposited at a) 70°C, b) 60°C, c) 50°C, d) 40°C, e) 35°C, and f) 25°C, where the deposited solution droplets were taken from a main solution where the main solution was cooling at a constant rate of approximately 25°C/hr. Non-NW material can initially be seen in the scans followed by the appearance of 'proto'-wires in scan d).

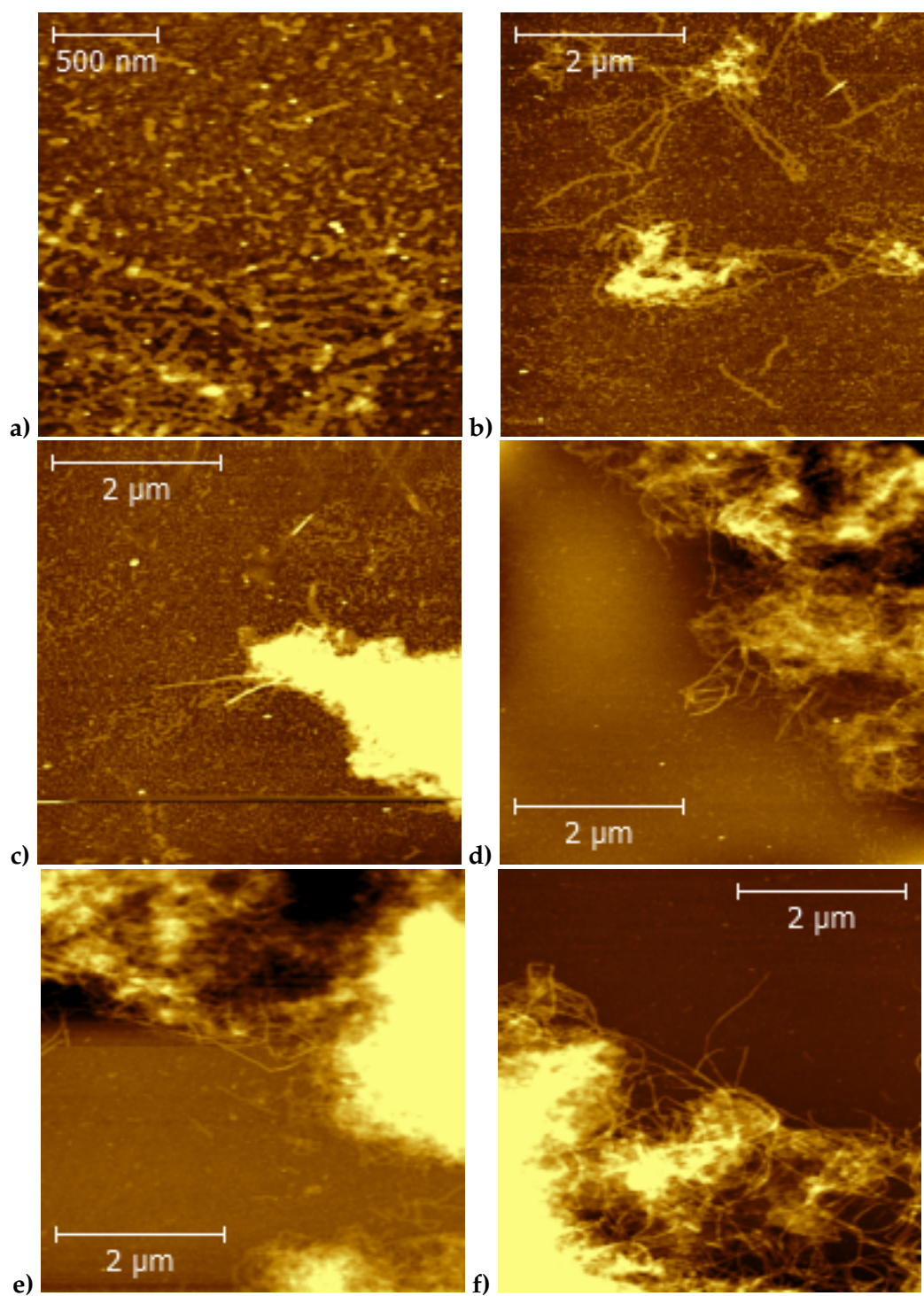


Figure 4.7: Growth of PQT-12 NWs in toluene. AFM scans taken of NW solution deposited at a) 30 mins at RT, b) 2 hours, c) 4 hours, d) 27 hours, e) 48 hours, and f) 96 hours, where the deposited solution droplets were taken from a main solution left to mature over time after reaching room temperature. Continued 'proto'-wire growth can be seen, followed by the formation of fully grown wires from scan c) onwards.

4.3.5 PQT-12-Chlorobenzene NW Formation

Figure 4.8 shows AFM scans of the evolution of PQT-12 NW growth in solution of chlorobenzene as a function of the temperature and time once at room temperature. Substrates shown in figures 4.8 a) and b) with solution deposited at 70 and 25°C respectively show non-NW PQT-12 pieces but no NW material. NWs similar in appearance to the PQT-12 toluene 'proto'-wires appeared between the solution initially reaching room temperature and 30 mins at RT, as seen in figure c). They were rough-edged, had heights of 2.40 ± 0.33 nm, widths of 91.6 ± 16.6 nm, and heights in the range of 0.3~1.2 μm .

The NWs continued to lengthen and at 3 days of maturity the NWs were 3.87 ± 0.40 in height, 76.6 ± 8.0 in width and several micrometres in length.

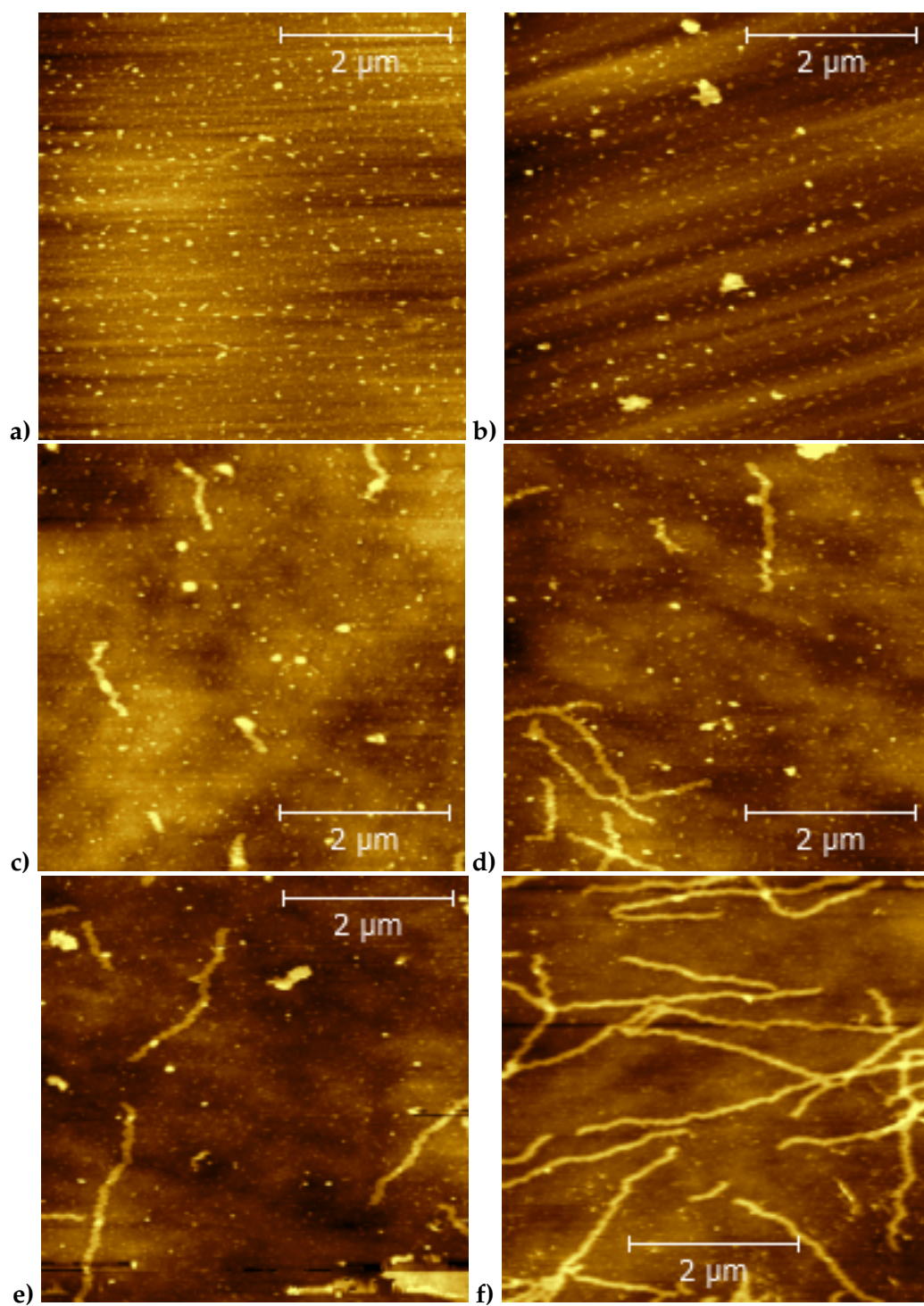


Figure 4.8: Growth of PQT-12 NWs in chlorobenzene. AFM scans taken of NW solution deposited at a) 70°C, b) 25°C, c) 30 mins at RT, d) 1 hour at RT, e) 4 hours, and f) 3 days.

4.3.6 PQT-12-Trimethylbenzene NW Formation

Figure 4.9 shows AFM scans of the evolution of PQT-12 NW growth in solution of trimethylbenzene as a function of the temperature and time once at room temperature. At 70°C very short non-NW PQT-12 pieces were seen deposited on the substrate. It is suggested that these were non-NW material and became ordered upon deposition on to the substrate as the solution was a bright transparent orange in appearance. The height of the non-NW material was 1.82 ± 0.16 nm.

Between 35 and 30°C NWs were seen when the solution was deposited on the substrate, and this was associated with an observed darkening and an increase in the opacity of the solution. The range of lengths of the NWs were 0.15~2.4 μm , with heights of 3.63 ± 0.51 nm and widths of 89.5 ± 14.3 nm.

After 4 hours at room temperature the NWs had become aggregated, appeared lengthened (visual inspection of the AFM scans), and there were far fewer short NWs. The NWs had the appearance of the toluene 'proto'-wires; they were flat and had rough edges. The 4 hour NWs had heights of 2.39 ± 0.48 nm and widths of 70.8 ± 8.5 nm.

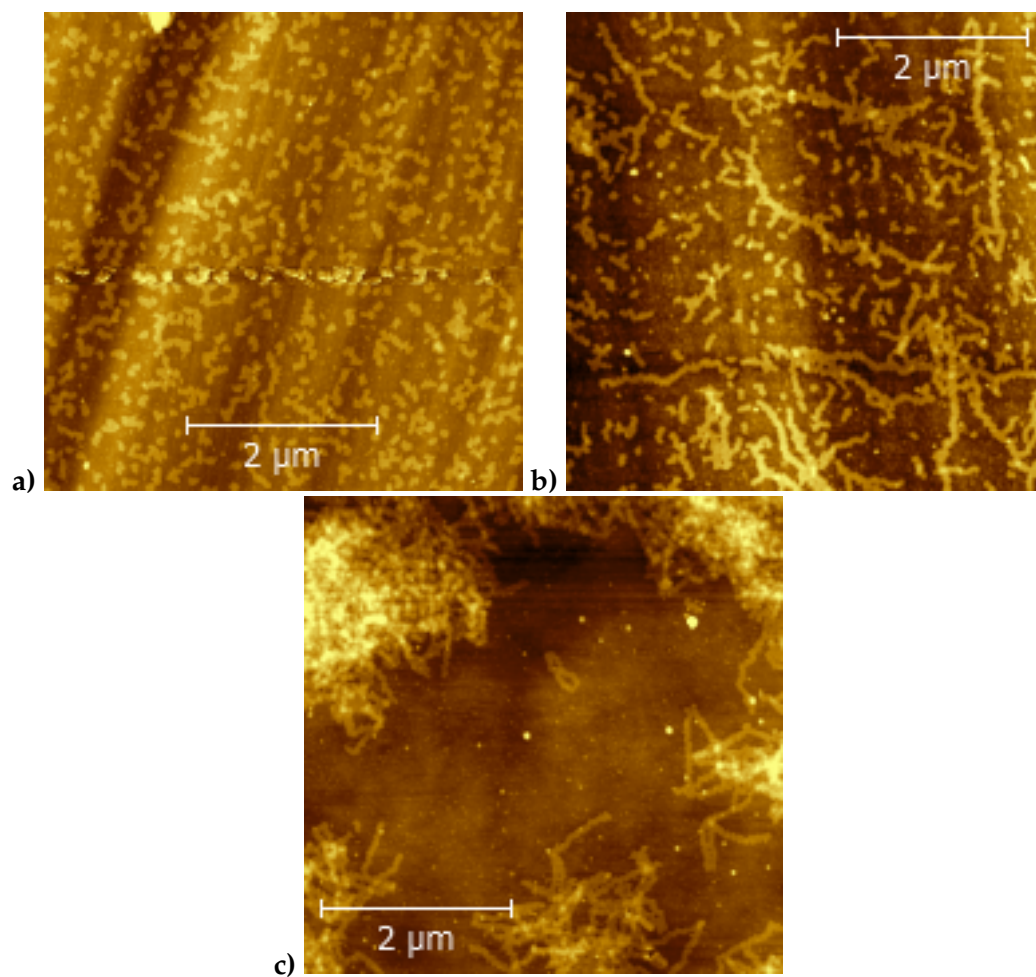


Figure 4.9: Growth of PQT-12 NWs in trimethylbenzene. AFM scans taken of NW solution deposited at a) 70°C, b) 30°C, and c) 4 hours at RT.

4.3.7 Further Polymer-Solvent Combinations

Several further polymer-solvent combinations were tentatively tested in order to achieve NW growth using the whisker method; figure 4.10 displays AFM images of some of the successful attempts.

Aside from successful growth reported previously in the chapter, growth was attempted and was successful with P3HT using Decalin, toluene and p-xylene; PQT-12 using anisole, decalin and p-xylene; P3OT using anisole. Unsuccessful attempts were made with P3HT using chlorobenzene; PQT-12 using cyclohexanone; P3OT using decalin.

P3HT While NW were observed with P3HT using toluene and p-xylene, they were produced in very low quantities, and very few examples were found during AFM scans and so morphological characterisation was difficult. The toluene NWs were found to be 2.40 ± 0.53 nm in height and 51.5 ± 8.4 nm in width. The p-xylene NWs were found to be 3.12 ± 0.75 nm in height and 31.3 ± 5.2 nm in width. Both the toluene and p-xylene NWs were of 100-2000 nm in length, and were smooth with only shallow arcs in them. The decalin NWs were interesting in comparison in that there was a medium concentration of short NWs found in the AFM topography scans (figures 4.10 a and c) which appeared to be lying on top of a film. Closer inspection of the film via the phase image (figure 4.10 b, d and e) revealed densely packed, highly order NWs.

PQT-12 PQT-12 decalin (figure 4.10 h) produced very short NWs. While the AFM image could be interpreted as ordering of film on the substrate surface, the solution underwent a colour change from a bright orange to a deep red colour (figure 4.11) suggesting that crystallisation occurred in

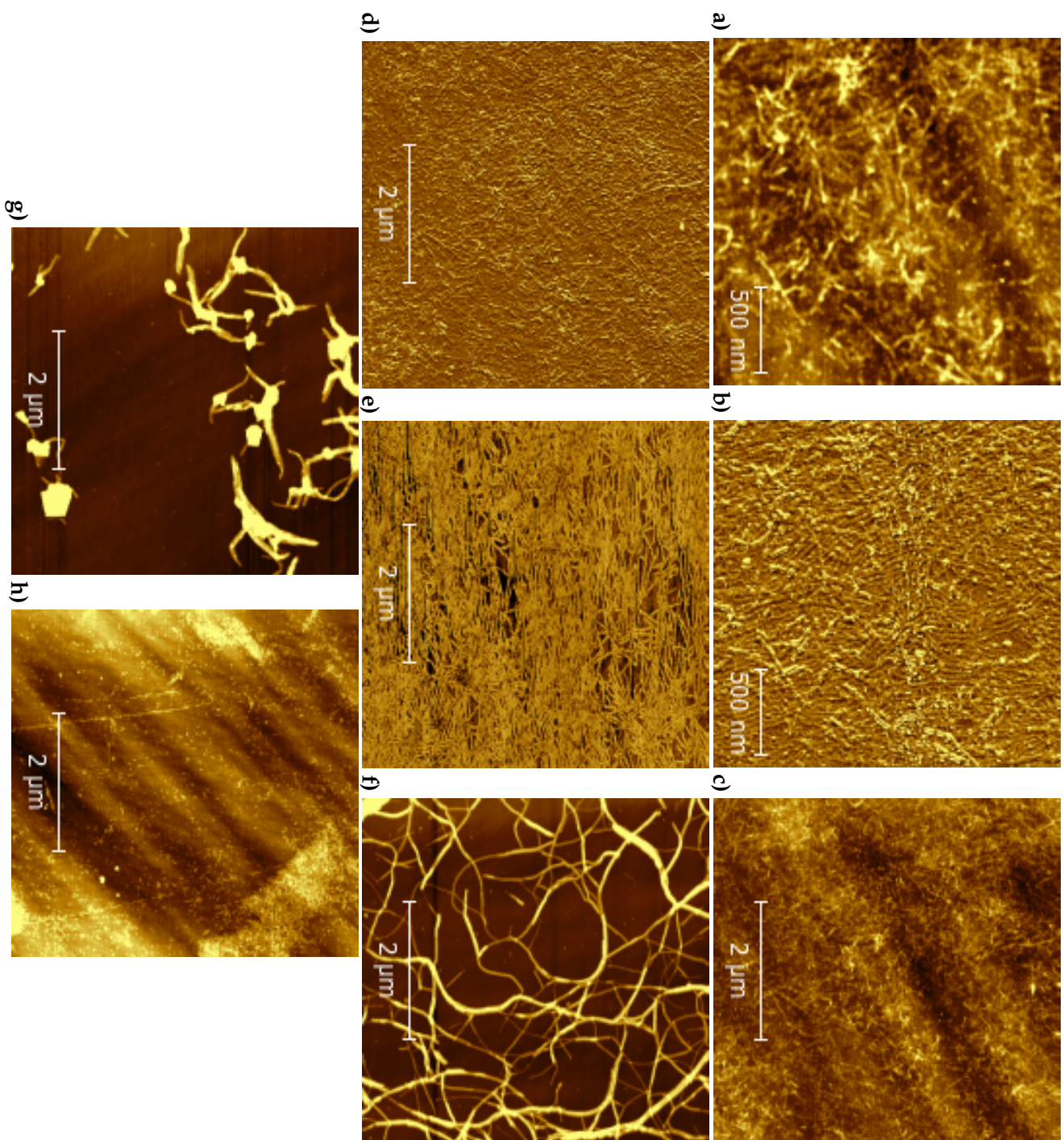


Figure 4.10: AFM scans of further polymer-solvent combinations. a+b) P3HT decalin (topography and phase), c+d) P3HT decalin (topography and phase), e) P3HT anisole (phase), f) P3OT anisole, g) PQT-12 anisole, and h) PQT-12 decalin.



Figure 4.11: Colour transistion of PQT-12 decalin solutions. Vial on the left contains PQT-12 dissolved in Decalin as a fresh heated solution and appears as translucent bright orange; the vial on the right contains a day old room temperature solution, where the opaque dark red colour suggests that NW formation has taken place.

solution[3]. PQT-12 also crystallised in solution of anisole producing NWs that are in stark contrast to those produced by other polymer-solvent combinations. The NWs were wide and aggregated into small clusters.

P3OT P3OT, the same structure as P3HT but with an eight carbon alkyl side, produced NWs in anisole. The NWs appeared similar to those produced by P3HT, where the NWs split away from each other in fingers, but with a lower density of NWs and different dimensions.

4.3.8 UV-Vis

Figure 4.12 shows the absorption spectra taken for a PQT-12 toluene NW solution as a function of time starting from the point at which the solution reached room temperature after cooling from 70°C at 25°C/hr. The peak at 595 nm, which is believe to be associated with crystalline PQT-12[17], is shown to increase with time indicating that formation of NWs is taking place. The peak continues to increase up until 24 hours where there is little change to 48 hours.

Table 4.1: Average dimensions of final wires and first appearance of nanowires for all polymer-solvent combinations

Polymer Solvent Combination	Width / nm	Height / nm	First Appearance
P3HT-anisole	32.3±4.6	4.5±1.5	seeds at 70°C, NWs at 50°C
P3HT-cyclohexanone	24.4±5.7	5.31±1.73	seeds at 70°C, NWs at 30°C
P3HT-toluene	51.5±8.4	2.40±0.83	
P3HT-p-xylene	31.3±5.2	3.12±0.75	
PQT-12-toluene 'proto'-wire	33~40	1.3~2.6	40°C
PQT-12-toluene fully-grown wire	24.5±5.0	6.3±0.4	~4 hours after reaching RT
PQT-12 chlorobenzene	76.6±8.0	3.87±0.40	RT, 0~30 mins
PQT-12 Trimethylbenzene	70.8±8.5	2.39±0.48	35~30°C

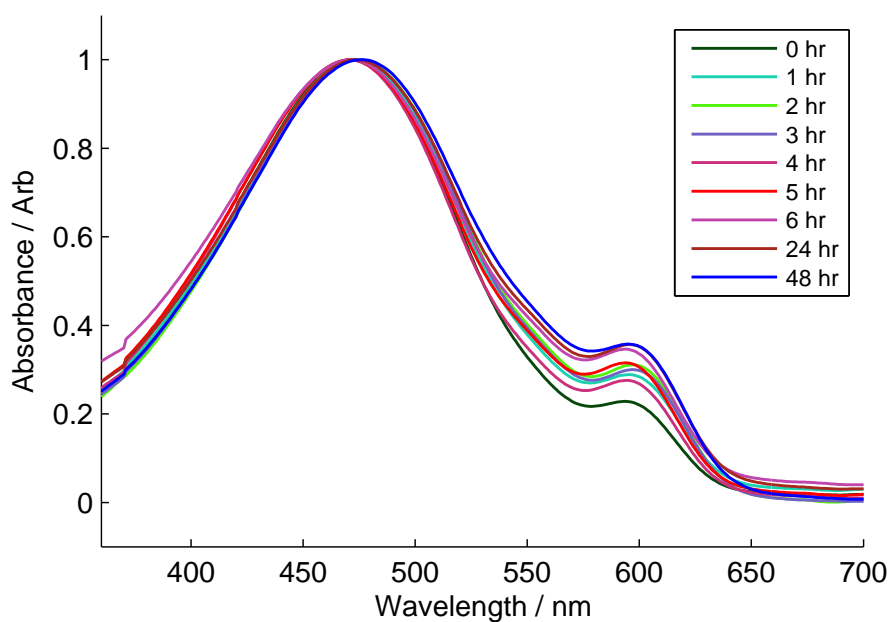


Figure 4.12: Absorption spectra describing PQT-12 toluene NW formation as a function of time from solution reaching room temp. There is a general trend for an increase in the peak at 595 nm associated with NW growth as time increases.

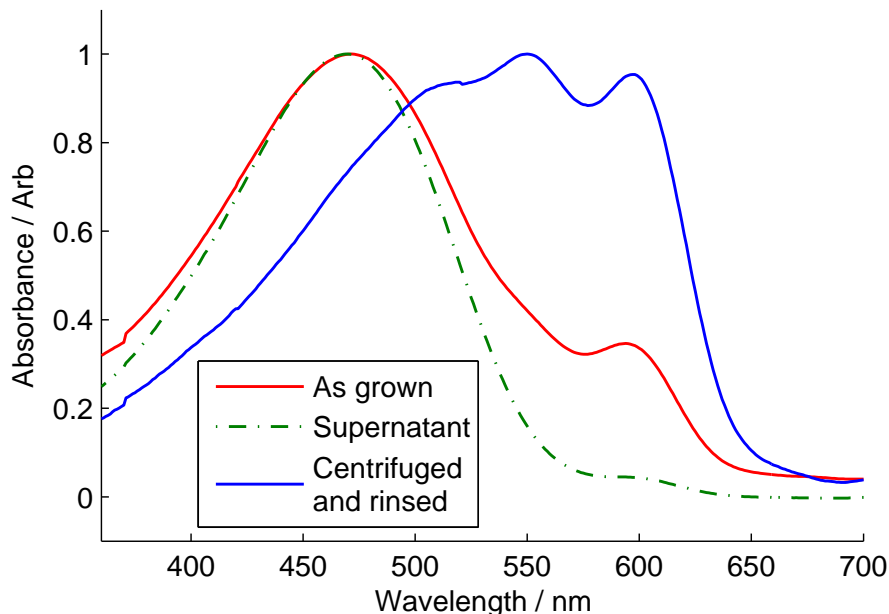


Figure 4.13: Absorption spectra for PQT-12 NW solution: as grown, rinsed, and supernatant.

Figure 4.13 shows the UV-Vis absorption spectra for a PQT-12 toluene NW solution, where the solution has been centrifuged and rinsed with toluene solvent 5 times in order to purify the NWs. The figure shows the spectrum for the solution as it was grown, the supernatant material after it had been centrifuged once, and then the final purified NWs. As reported by Berson[18], this is a highly effective method for removing non-NW material from a NW solution.

Figure 4.14 shows the absorption spectra for non-NW P3HT and isolated P3HT NWs grown in anisole, with both spectra taken in anisole. The sample preparation was the same as that for P3HT, where the solution was centrifuged and rinsed with anisole solvent 5 times in order to isolate the NWs, and the first supernatant was used to isolate the non-NW P3HT. The figure clearly shows the broad peak at 444 nm and absorption onset at ap-

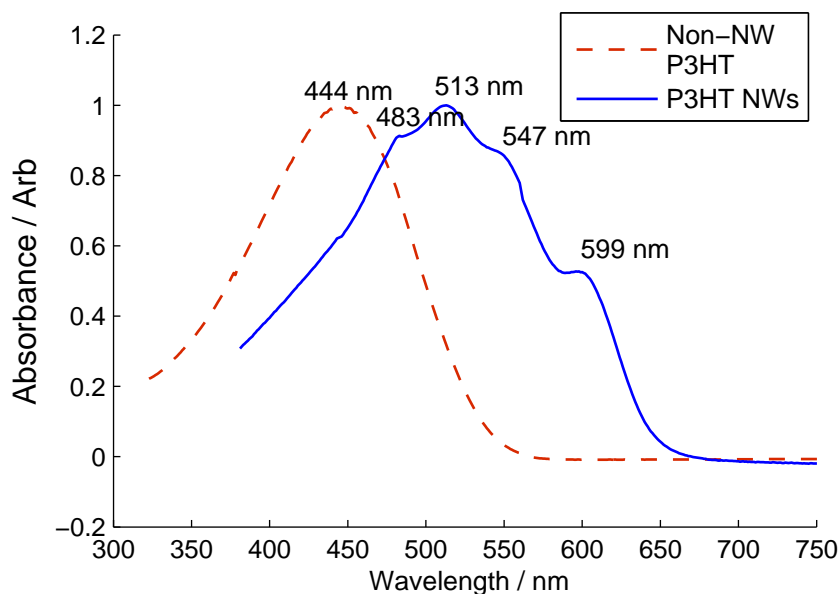


Figure 4.14: Absorption spectra for non-NW and NW P3HT in anisole.

proximately 550 nm for the non-NW P3HT. The crystalline P3HT NWs has a broad absorption curve with vibronic structure, with 4 peaks/shoulders at 483, 513, 547 and 599 nm, with absorption onset at approximately 655 nm. During growth of the NWs the relative intensity of the non-NW peak decreases and the P3HT NW peaks increases indicating a decrease in the amount of non-NW material as it crystallises into NWs.

4.3.9 XRD

P3HT

P3HT NW XRD patterns can be seen in figure 4.15. NWs made from anisole, cyclohexanone, and trimethylbenzene solvents were dropcast, following centrifugation, at high concentrations onto silicon substrates. The samples were scanned through a range of theta angles, then thermally annealed up to 140°C for 25 or 50 mins, while taking snapshots at a theta angle above the

critical angle, and then finally scanned through a range of theta angles post anneal.

There were several similarities in the diffraction patterns of the as cast samples for the three solvents. The XRD revealed that the NWs are highly ordered and well oriented. The three concentric arcs that are centred on $Q_{XY} = 0$ in the diffraction patterns, which are consistent with being the (100), (200) and (300) diffraction peaks, correspond to average d-spacings of 15.7 Å, 15.84 Å and 15.74 Å for anisole, cyclohexanone and trimethylbenzene solvent grown NWs respectively. The (100) is the a-lattice direction, or the alkyl-chain stacking, and the three peaks indicate that the NWs are oriented such that the (100) is in the out-of-plane (OOP) direction. This description of the structure of crystalline P3HT is based on the model proposed by Kayunkid[16] as is shown in figure 4.16.

The peak found at a $Q_{XY} = 1.65$ is identified in the literature as (020) [16, 19]. The (020) is seen strongly in the in-plane (IP) direction ($Q_Z = 0$), and indicates further that the NWs are strongly oriented. The (020) relates to the $\pi - \pi$ stacking of the thiophene rings and is believed to occur along the long axis of the NWs, with the polymer backbone traversing across the width of the wires[16, 19]. The $\pi - \pi$ stacking distance is known as the 'b'-lattice constant, as shown in figure 4.16 has the values of 3.77, 3.79, and 3.68 Å for anisole, cyclohexanone and trimethylbenzene respectively.

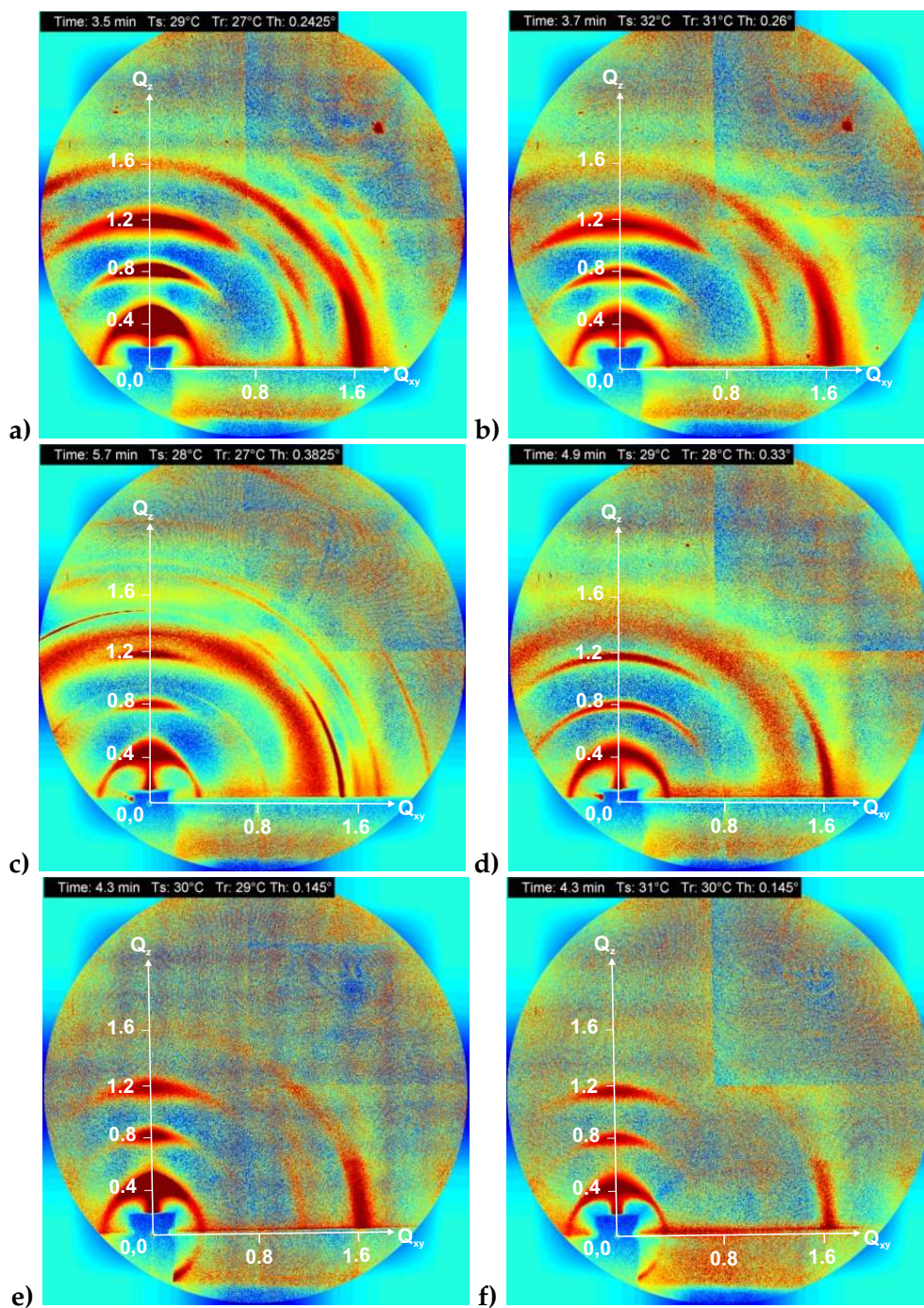


Figure 4.15: P3HT nanowire XRD patterns, a) anisole as cast, b) anisole annealed, c) cyclohexanone as cast, d) cyclohexanone annealed, e) trimethylbenzene as cast, and f) trimethylbenzene annealed

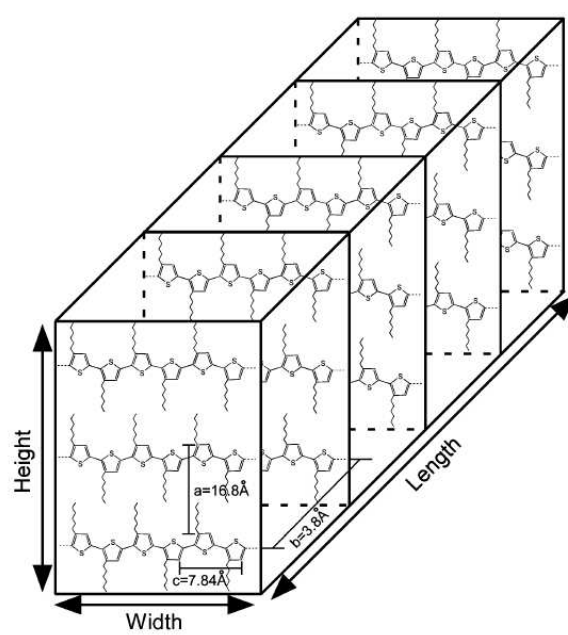


Figure 4.16: Proposed monoclinic NW crystalline structure[20]

Domain Sizes and Paracrystallinity Domain sizes (an indication of the coherence length) in the OOP a-lattice direction were measured, along with the level of paracrystallinity. The data for these measurements are presented in tables 4.2 and 4.3, and figures 4.18 and 4.19, along with the OOP line profiles in figure 4.20. The domain sizes of the NWs as cast were 136 Å, 141 Å, and 111 Å for anisole, cyclohexanone, and trimethylbenzene respectively. These domain sizes do not correlate directly with the AFM measurements of the heights of the NWs, but do relate roughly in that Trimethylbenzene possessed the smallest heights as measured with the AFM and had the shortest domain size. What may be being seen is for a highly concentrated mat of NWs, many of the NWs are stacking coherently as to increase the measured domain size.

During thermal annealing the domain sizes increased for all three types of NWs: 243 Å for anisole, 277 Å for cyclohexanone, and 160 Å for trimethylbenzene. The increase in domain size was rapid, lagging behind the increase in temperature by less than 20s, although the domain sizes of the anisole NWs and the trimethylbenzene NWs continued to increase at a very low rate of 0.0033 Å s^{-1} and 0.0063 Å s^{-1} respectively once the temperature had stabilised at 140°C.

Upon cooling back to room temperature the domain sizes decreased but remained larger than the as cast values: 215 Å (anisole), 227 Å (cyclohexanone), and 144 Å (trimethylbenzene).

The changes in domain sizes due to thermal annealing indicate that the NWs may be aligning themselves, and increasing the coherence length. The extra increase in domain size during the thermal anneal is largely due to thermal expansion of the NWs.

Paracrystallinity was measured in the NWs, which gives an indication of

Table 4.2: P3HT NW domain sizes

Solvent	Domain Size / Å		
	As Cast	During Anneal	Post Anneal
Anisole	136±5	243	215
Cyclohexanone	141±10	277	227
Trimethylbenzene	111±8	160	144

Table 4.3: P3HT NW paracrystallinity g-factor

Solvent	Paracrystallinity g-factor		
	As Cast	During Anneal	Post Anneal
Anisole	0.0446±0.0004	0.0355±0.0003	0.0400±0.0002
Cyclohexanone	0.040	0.0320±0.0008	0.0373±0.0007
Trimethylbenzene	0.0474±0.0002	0.0397±0.0071	0.0411±0.0013

the disorder and deviation from a perfect crystal. All three solvents, as cast, gave similar values, where they ranged from 0.040 for cyclohexanone up to 0.0474 for trimethylbenzene. Thermal annealing had the effect of decreasing the disorder in the NWs by between 6 and 13%. Interestingly the disorder was lowest during the anneal, approximately 16% for trimethylbenzene and 20% for the other two.

Table 4.4: P3HT NW lattice constants. OOP refers to out-of-plane diffraction at $Q_{xy} = 0$, IP refers to in-plane at $Q_z = 0$, a is the a-lattice constant or the alkyl-chain stacking of the crystalline polymer and b is the b-lattice constant or the $\pi - \pi$ stacking of the thiophene rings along the length of the NW.

Solvent	Lattice Constant	Lattice Constant / Å		Change / Å	Change / Å
		As Cast	Post Anneal		
Anisole	OOP a	15.7	16.3	+0.6	+3.8
	OOP b	3.85	3.92	+0.14	+1.8
	IP a	15.87	16.2	+0.33	+2.1
	IP b	3.77	3.73	-0.06	-1
Cyclohexanone	OOP a	15.84	16.15	+0.31	+2.0
	OOP b	4.09	4.02	-0.14	-1.7
	IP a	15.86	16.28	+0.42	+2.65
	IP b	3.79	3.75	-0.08	-1.1
Trimethylbenzene	OOP a	15.74	15.95	+0.21	1.33
	OOP b	3.76	3.90	+0.27	3.59
	IP a	15.93	16.40	+0.47	+3.33
	IP b	3.68	3.76	+0.16	2.17

Thermal Annealing Thermal annealing had the affect of increasing the a-lattice constants for all P3HT NWs. During the anneal the OOP a-lattice parameter can be seen to increase up to 17.3 Å, 17.3 Å, and 17.4 Å for anisole, cyclohexanone, and trimethylbenzene when at a temperature of 140°C. The temperature increase was rapid, rising from room temperature to 140°C in 2.5 mins with an overshoot of less than 1°, and the lattice spacing increase was equally as rapid, reaching the peak spacing at the same time. Upon cooling of the sample, which took approximately 4 mins to reach 35°, the a-lattice spacings decreased to 16.3 Å (anisole), 16.15 Å (cyclohexanone), and 15.95 Å (trimethylbenzene). This suggests that the NWs are in meta-stable structure initially, and that thermal annealing induces a more stable lower energy configuration. The NW structure largely remained unchanged throughout the annealing, just the lattice spacings differed.

The combined effects of increase in a-lattice spacing and domain sizes,

and decrease in paracrystallinity suggest that thermal annealing, when performed at 140°C, produces a more ordered mat of NWs, which are in a more stable configuration. These processes occur rapidly, almost in synchronisation with the temperature increase. While these results only demonstrate a change in the structure and morphology of a dense mat of NWs, improved ordering in organic polymers is associated with improved charge transport, and therefore, in most applications, improved device performance. It has previously been seen that thermal treatment of P3HT films is a successful route to improvement in OPVs, and in NW OPVs it has been shown to produce small gains in the performance. These results help to elucidate the processes that lead to the improved performance.

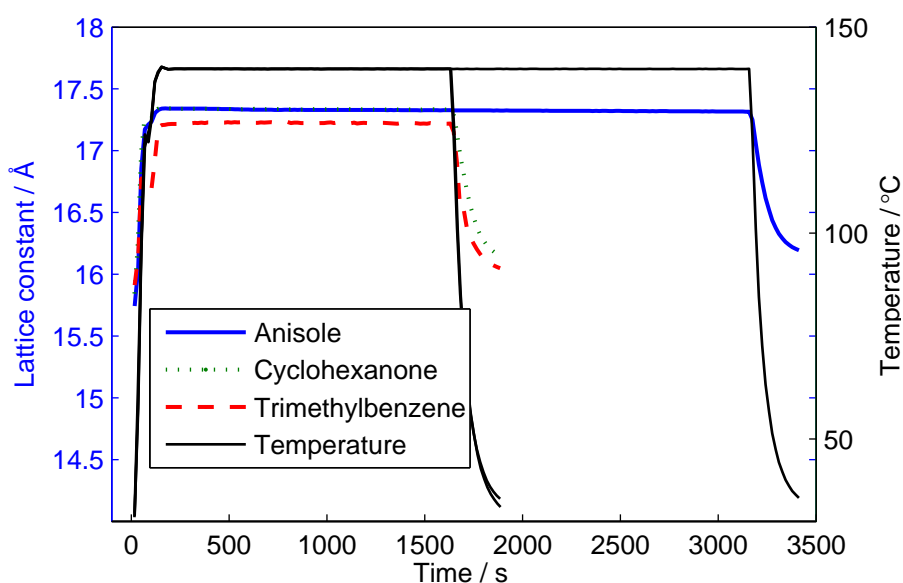


Figure 4.17: P3HT NW OOP a-lattice parameter evolution through time and temperature during thermal annealing

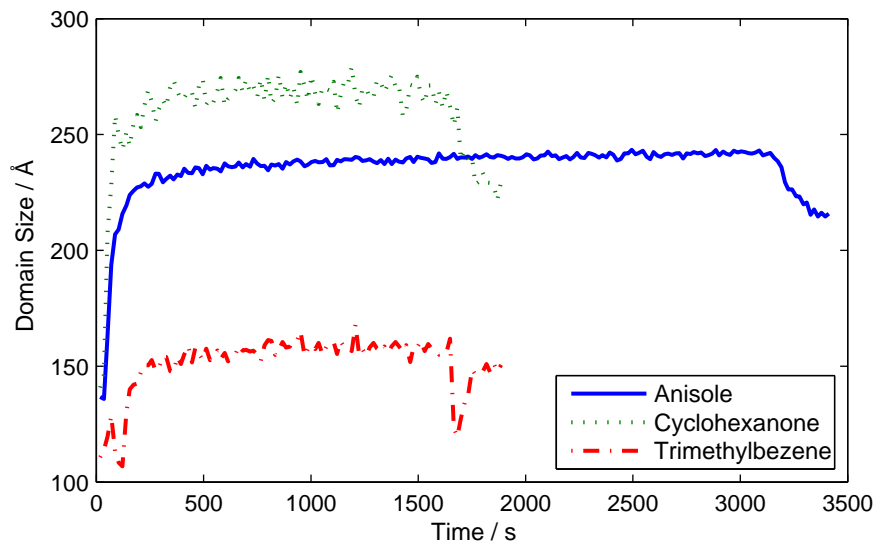


Figure 4.18: P3HT nanowire domain sizes versus time. Anisole (blue solid line), cyclohexanone (green dashed line), and Trimethylbenzene (red dash-dot line)

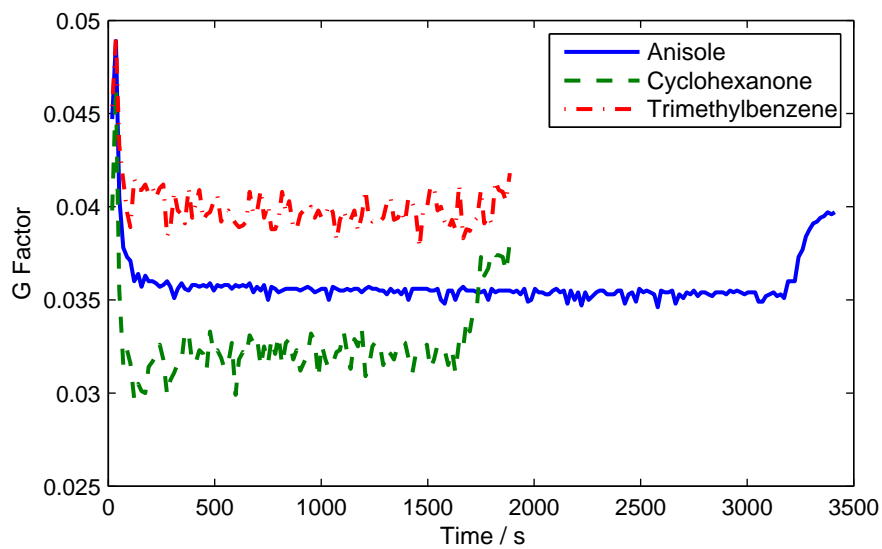


Figure 4.19: P3HT nanowire disorder versus time through annealing. Anisole (blue solid line), cyclohexanone (green dashed line), and Trimethylbenzene (red dash-dot line)

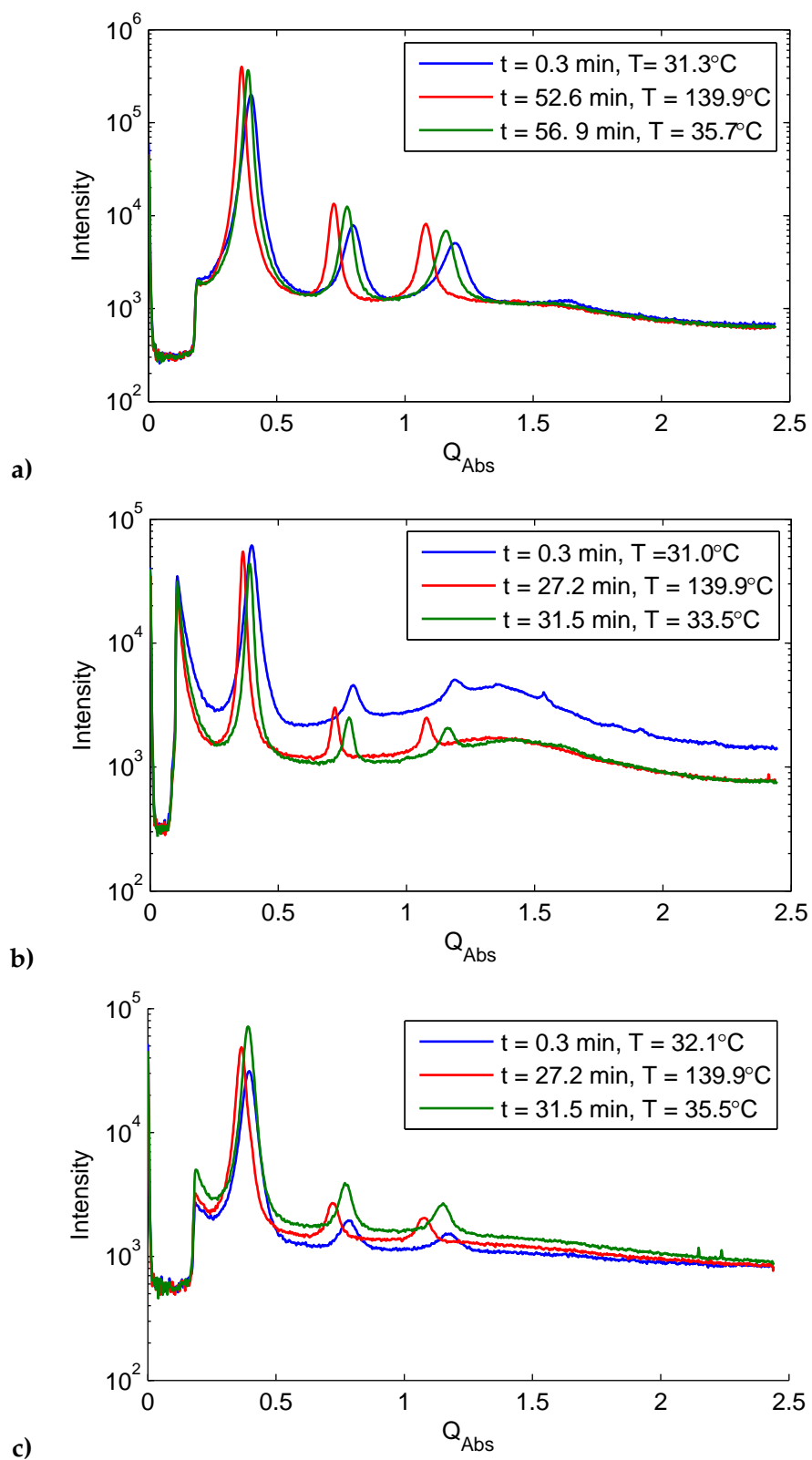


Figure 4.20: OOP line profiles for a) P3HT Anisole NWs, b) P3HT cyclohexanone NWs, and c) P3HT Trimethylbenzene NWs; taken as cast, at the end of thermally annealing, and after cooling.

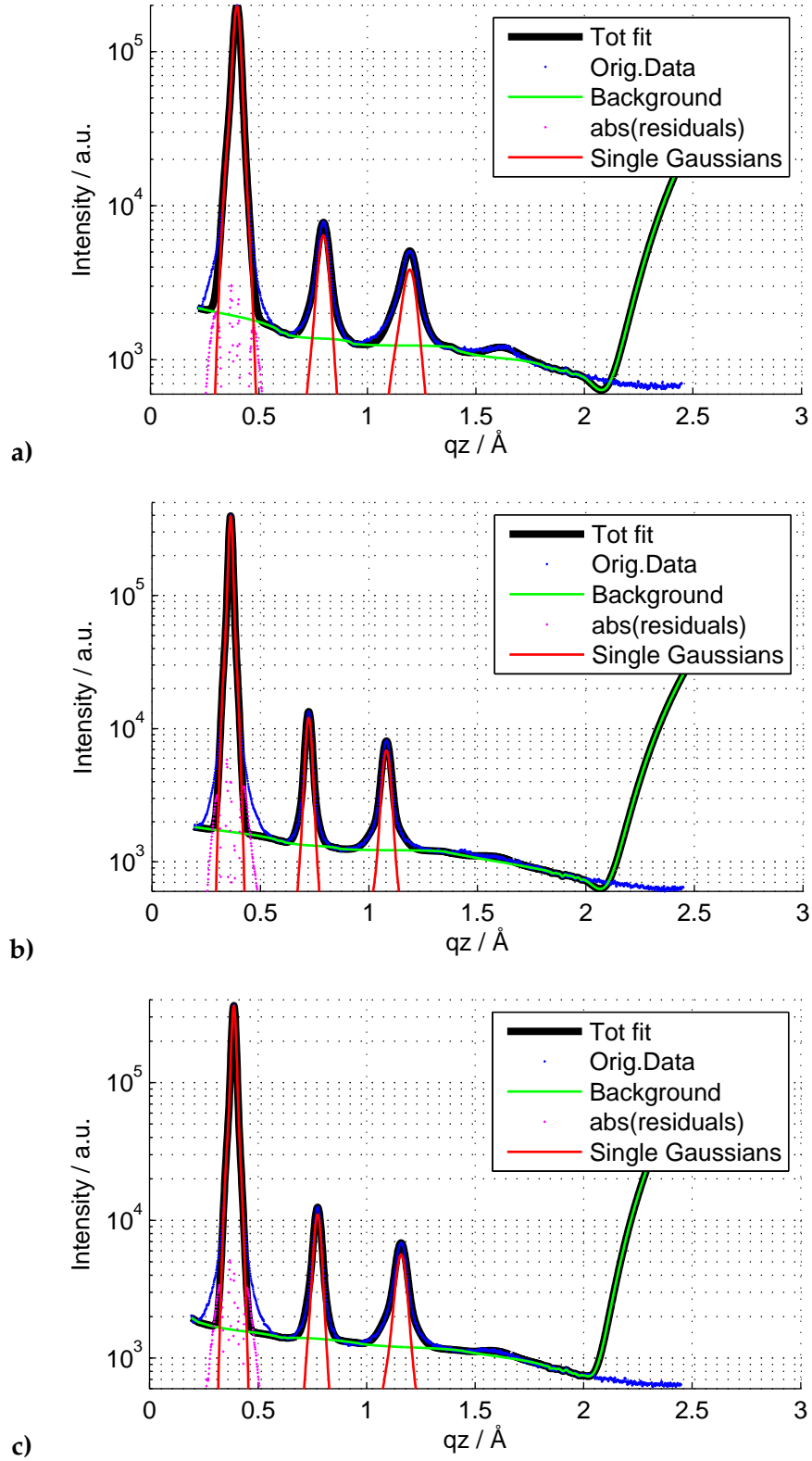


Figure 4.21: OOP line profiles for P3HT Anisole NWs with fitted Gaussians. a) As cast ($t = 0.3$ min, $T = 31.3^\circ\text{C}$), b) during thermal annealing ($t = 52.6$ min, $T = 139.9^\circ\text{C}$), c) post anneal ($t = 56.9$ min, $T = 35.7^\circ\text{C}$).

PQT-12

Grazing incidence x-ray diffraction was carried out on PQT-12 NW samples made separately in chlorobenzene, trimethylbenzene, and o-xylene; they were probed as cast and after thermal annealing at 140 °C. Typical diffraction patterns are shown in figure 4.22. Currently the structure is not known or repeated in the literature and the diffraction patterns reported here failed to yield enough quantitative information to discern the structure of the NWs, although a qualitative analysis can be made of the pre- and post-anneal patterns between different solvents.

One clear difference in the as cast patterns is seen between the o-xylene NWs and the NWs from the other two solvents. The o-xylene NWs have a very strong orientation preference, shown by the short, broad arcs that lead up out-of-plane (OOP), compared to the long, narrow arcs of the other two solvents.

Post-anneal this difference in orientation and structure disappears, indeed the structures of all three change from their as cast structure upon thermal annealing. It was seen that as the samples were heated up above 100 °C all features, apart from a broad amorphous peak, disappeared before emerging with a different pattern, indicating that the NWs were melting during the anneal before re-crystallising in an alternative structure.

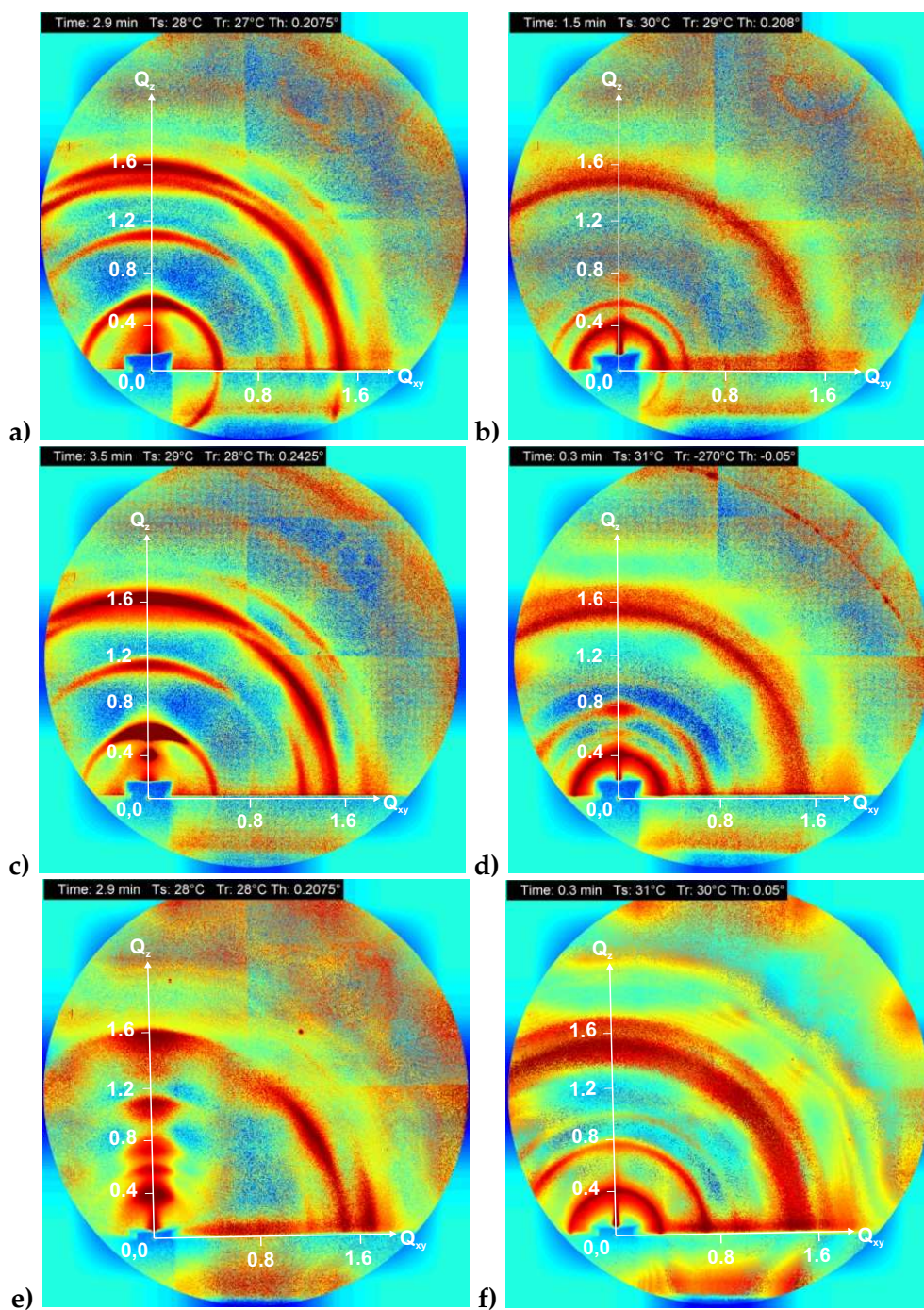


Figure 4.22: PQT-12 nanowire XRD patterns, a) chlorobenzene as cast, b) chlorobenzene annealed, c) trimethylbenzene as cast, d) trimethylbenzene as cast, e) o-xylene as cast, and f) o-xylene annealed.

Figure 4.23 shows the diffraction pattern of PQT-12 NWs grown in Trimethylbenzene taken during the thermal annealing process at 140°C. This pattern was typical of all of the PQT-12 NW samples at 140°C. The clear peaks of the as cast PQT-12 NW structure have disappeared and one broad ring is seen instead.

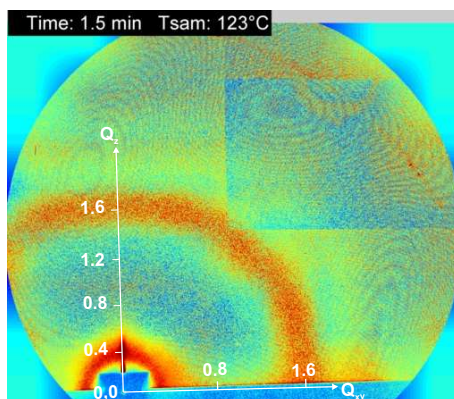


Figure 4.23: PQT-12 trimethylbenzene NW diffraction pattern at 123°C. The peaks of the as cast structure have disappeared and one broad ring is seen instead.

4.3.10 Orienting NWs

Routes to orienting NWs during deposition were explored. Achieving control of the orientation of the NWs could prove to be important in applications such as OFETs where possible conductance anisotropy of the NWs will affect the performance of the device. With all NWs aligned in one direction the charge conduction will be more predictable, and where the NWs are aligned in the direction of maximal charge carrier mobility, known to be along the polymer backbone, the device performance may be optimised.

AFM images of deposition methods that showed favourable orientation are displayed in figure 4.24. Figures a-c show the results of dipping a 1 cm square silicon substrate into a low concentration P3HT anisole solution,

and then drawing the substrate out over a period of 3s in the direction as indicated by an arrow in the figure. Figures d)-f) show the results for using the same dipping and drawing method with a low concentration P3HT cyclohexanone solution.

For both solutions there is a strong correlation between the direction of the NWs and the drawing direction. The induced orientation of the NWs is more consistent in the anisole solution where the average angle of the NWs is within the error of the drawing direction (± 5), while the cyclohexanone solution gave wires that curve away from the direction of drawing, and also suffered from large aggregations of NWs, which was also seen during the formation study of the P3HT cyclohexanone NWs.

Figures 4.24 g) and h) show AFM where a low concentration P3HT cyclohexanone NWs solution was flowed down a silicon substrate. The solution was allowed to flow down the substrate which was held at approximately 45° to horizontal. The arrows in the images depict the direction in which the solution flowed. The images show that there was some preferential orientation in the direction of the flow of the solution, although similar to the cyclohexanone solution that had been dipped and drawn some of the NWs curve away from the direction of flow and there are several groups of entangled NWs.

Finally, figure i shows an AFM image where the distribution of the NWs results from high-speed spin-coating, where the low concentration P3HT cyclohexanone NW solution was deposited on to a silicon substrate rotating at 6000rpm. Here there was much less preferential orientation, and the wires were consistently aggregated. The arrow in the figure shows the direction from the centre of the rotation where the drop of solvent made contact with the substrate out to the perimeter.

These tentative results show that there is some potential for achieving a preferred direction of orientation of NWs that could have some benefit to the performance of NW devices.

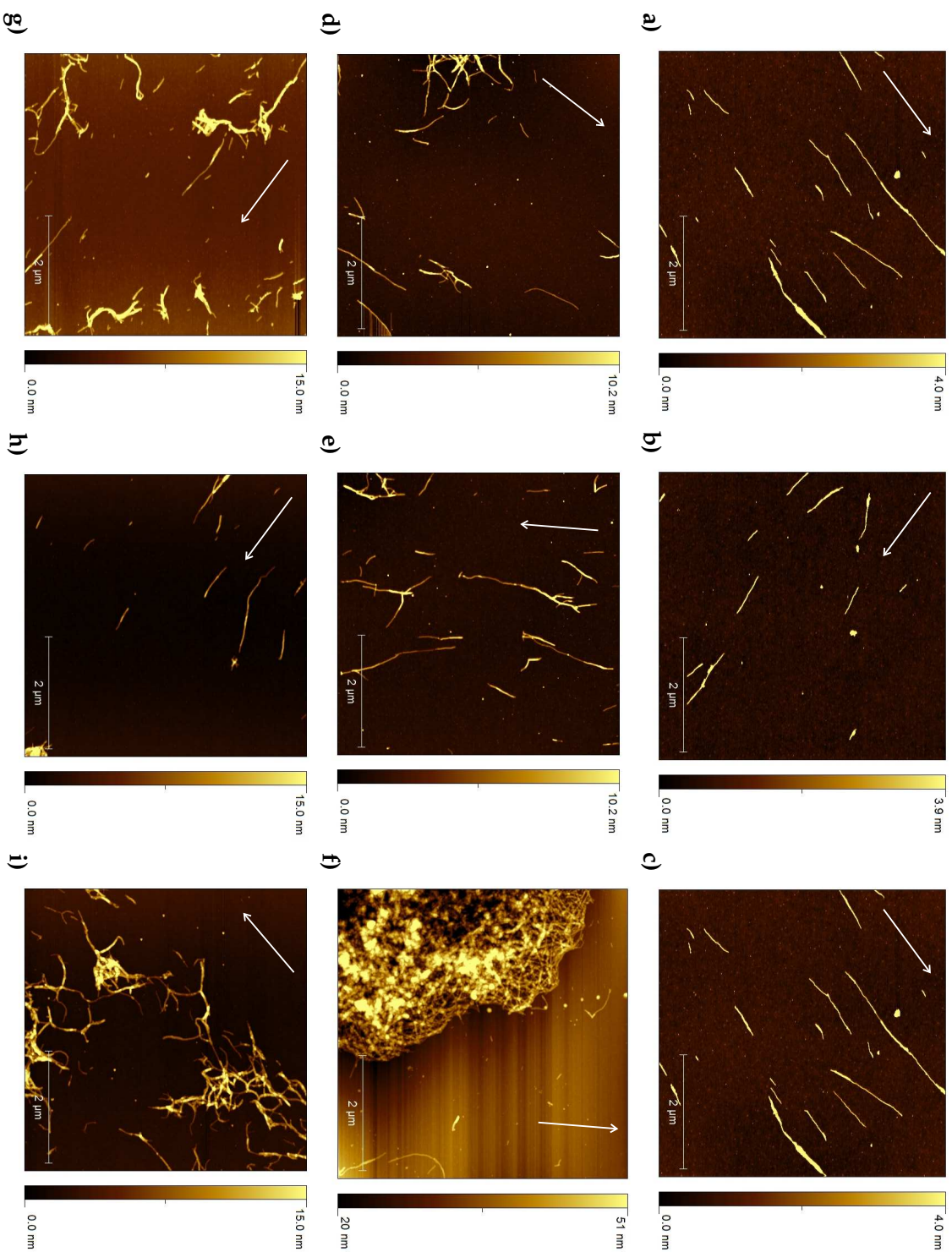


Figure 4.24: AFM scans for various deposition methods for NW orientation. a-c) P3HT anisole dipped and drawn for 3s, d-f) P3HT cyclohexanone dipped and drawn for 3s, g and h) P3HT cyclohexanone flow cast, and i) P3HT cyclohexanone high-speed spin-coating. Arrows indicate direction of drawing/flow/rotation-centre direction.

4.4 Discussion

Comparison of Nanowire Growth to Literature

In comparison to the study carried out by Samitsu et al in 2008[2] in which they attempted growth with a range of polymers using the whisker method, similar results were achieved where the same polymer-solvent combinations were used. P3HT NWs grown using cyclohexanone and p-xylene separately, were similar in appearance in both the Samitsu study and the results shown here; p-xylene NWs were isolated, short and straight, cyclohexanone wire were long curved and aggregated. Heights of the Samitsu NWs were 3~5 nm and 4~8 nm for p-xylene and cyclohexanone respectively, compared to 3.12 ± 0.75 nm and 5.3 ± 1.7 nm for the NWs grown here.

Samitsu's results with PQT-12 grown in toluene differed slightly from those reported here. The final heights of the wires were 3~5 nm compared to 6.3 ± 0.4 nm for Samitsu's and the authors work respectively. Samitsu made no mention of observing the two types of wires in the two stage growth of the PQT-12-toluene NWs and only described the fully-formed wires, although they did witness a two stage chromatic shift of the solution during cooling and maturing. The solution in Samitsu's study went from an orange colour to a red colour during the cooling phase from 70 to 20°C, and then another colour change to brown after several days. These colour changes in the solution match the formation of two separate types of NW formation witnessed in the author's work, with 'proto'-wires forming during the cooling phase and fully-formed wires appearing initially after a few hours while the solution matured.

Comparisons can also be drawn with Samitsu's work with P3ATs and anisole solvent[3], where they looked at the dimensions using two different

AFM tips. They noted that there was apparent stacking of the alkyl chains in the height direction of the NWs, where the increment size in the heights of the NWs was related to the alkyl chain length of the different P3ATs used in the study. The stacking of the alkyl chains for P3HT-anisole NWs was seen in the study presented here, where the peaks in the histogram of NW heights were seen at 2.68, 4.47, 6.43 and 11.12 nm; Samitsu identified peaks at 2~4 nm and 4~6 nm. The strongest peak in the Samitsu study was at 2~4 nm, whereas the strongest peak seen here was at 4.47 nm. Comparable NWs widths were seen; here the average width was found to be 32.3 ± 4.6 nm, and Samitsu found them to be 26~32 nm depending on which AFM tip was being used for the measurement. The morphology of the P3HT-anisole NWs were comparable in both studies.

Differences were seen in the appearance of the P3OT-anisole NWs between the Samitsu study and the results presented here. The Samitsu P3OT NWs were similar in appearance to the P3HT-anisole NWs, while those grown for this thesis were thicker, and aggregated less.

4.4.1 P3HT

P3HT NW structure The AFM studies and the X-ray diffraction appear to match the literature regarding the structure of the P3HT NWs. The proposed model[16] is that of $\pi - \pi$ stacking of the thiophene rings running along the long axis of the NWs, with alkyl chains stacking vertically and the polymer back bone running perpendicular along the width of the NWs (figure 4.16). This is supported by the appearance of the x-ray diffraction pattern with peaks matching those seen in films examined by Lilliu[21, 19] and Kayunkid[16].

The XRD pattern is highly oriented with peaks running up the centre of

the image in the out-of-plane (OOP) direction from the substrate. The lattice constant is 15.7~15.9 Å in the as cast form which relates well to the total length of the thiophene ring plus the side chain. When comparing this to the histogram of the NWs heights in the AFM study of the P3HT-anisole NWs the spacing matches up well with the histogram peak intervals. The NWs also have a morphological anisotropy, with a wider base compared to the height of the NWs which would encourage the NWs to become well oriented on the Si substrate. The 020 ring associated with the $\pi - \pi$ stacking of the thiophene rings is strongest in the in-plane (IP) direction further suggesting strong orientation of the NWs.

Lattice Constants of Films The lattice constants are shown in table 4.4. The a-lattice for NWs formed in all three solvents is 15.7-15.84 Å in the OOP direction and 15.86-15.93 Å in the IP direction. Refraction effects, which effect the OOP diffraction more greatly than the IP, may be responsible for the differences between the OOP and the IP a-lattice values. These values are not the same as the lattice constants as identified by Kayunkid[16] and Lilliu[21, 19], where Kayunkid found the a-lattice constant to be 16 Å and Lilliu found it to be 16.4 Å.

Thermal annealing Initially the as cast NWs have an OP 'a-lattice constant of 15~15.9 Å , which becomes increased through thermal annealing. The increases of the lattice constant to the final values of 15.95~16.3 Å , which are similar to the values as quoted for P3HT films by Kayunkid and Lilliu, suggest that there is a slight restructuring of the NWs. This could be a reduction of any interdigitation of the alkyl side chains that was occurring in the as cast structure. The overall diffraction pattern remains largely unchanged

after annealing suggesting no major reconfiguration of the NW structure.

During thermal annealing the OP 'a'-lattice constant increases up to 17.3~17.4 Å , which is greater than the final value after cooling. This is likely due to thermal expansion of the NW lattice and also systematic error introduced due to thermal expansion of the experimental set up, including the heater block on which the sample was mounted on, thus affecting the experimental geometry.

4.4.2 PQT-12

PQT-12 NW structure The PQT-12 diffraction patterns failed to reveal sufficient information to elucidate the structure of the NWs. Thermal annealing at a temperature of 140°C, above the melting point of PQT-12, destroyed the crystalline structure of the NWs, smearing out the XRD pattern. Upon cooling a new XRD pattern was witness suggesting the formation of a new crystalline structure, and that the initial NWs were in a meta-stable state. When o-xylene was used as the solvent for PQT-12 NWs the XRD pattern was far more oriented than that of the chlorobenzene and trimethylbenzene NWs; after annealing this difference was no longer apparent.

4.4.3 Absorption Spectra

Absorption spectra for P3HT-NWs revealed vibronic structure in the broad peak associated with the NWs^{4.14}. Four peaks/shoulders are seen which for P3HT-anisole NWs, with the spectra taken in anisole, were seen at 483, 513, 547 and 599 nm. It has been suggested that the relative intensity of the peaks at 483 and 513 nm remain the same, and the relative intensity of the peaks at 547 and 599 nm, but the relative intensity between the two

pairs of peaks varies between different processing and between P3HT films¹. The suggestion has been made that two crystalline structures exist in NWs and films, one where the thiophene rings are aligned along the long-axis of the NW and the second where the thiophene rings are offset along the length of the NWs. Both forms are present in crystalline P3HT at any one time but the relative amounts of each varies depending on the processing parameters. Each pair of peaks in the absorption spectra corresponds to each of the crystalline structures. A detailed study of the absorption spectra and XRD of isolated NWs produced from different solvents, and films may help to elucidate this matter.

4.5 Conclusions

High aspect ratio polythiophene nanowires were grown in marginal solvents using the whisker method where the polymer is dissolved in the solvent at elevated temperatures and crystallises out of solution upon cooling and/or while standing at room temperature for several hours to days. The rate of formation and the morphology of the NWs was very much dependent on the combination of polymer and solvent, although there was no discernable pattern based on the data obtained and presented here. Heights of the NWs varied from 1 to 11 nm, widths were 20 to 80 nm and lengths were from 10s of nanometres up to in excess of 10 micrometres. One key point was that PQT-12 NWs grown in toluene grew in a two stage process with flat, wide, rough-edged 'proto'-wires initially form at approximately 40°C, which then develop into smooth, tall NWs after several hours.

The absorption spectra of the NWs revealed vibronic structure with shoul-

¹S.Cook - private communication

ders and peaks at wavelengths of 483, 513, 547 and 599 nm for P3HT NWs grown in anisole solvent. UV-vis also showed that not all of the dissolved polymer becomes crystalline on the timescale of the experiment and that centrifuging and rinsing is an effective method for separating the crystalline material from the non-NW material.

X-ray diffraction experiments on mats of PQT-12 NWs revealed that the NWs exist in a meta-stable where the NW structure reconfigures after melting during a process of thermal annealing at 140°C.

X-ray diffraction experiments on P3HT NWs revealed a structure similar to that of P3HT films as reported in the literature. The NWs were highly oriented due to their shape anisotropy, with the alkyl-chain stacking oriented perpendicular to the Si substrate, and the $\pi - \pi$ stacking of the thiophene rings running along the length of the wires and the polymer backbone both in the plane of the substrate. The 'a'-lattice constant, which is related to the alkyl-chain stacking in the NWs, was found to be smaller (15.7~15.9 Å) than that of films (16~16.4 Å) and this lattice constant increased through thermal annealing at 140°C upto 15.95~16.3 Å). The 'b'-lattice constant, which is the π -stacking distance of the thiophene rings, had the values of 3.77, 3.79, and 3.68 Å for anisole, cyclohexanone and trimethylbenzene respectively, indicating that π -stacking is strongest for nanowires grown with trimethylbenzene solvent. Thermal annealing also increased the domain size of the NWs (from 136±5, 141±10, and 111±8 Å to 215, 227 and 144 Å for anisole, cyclohexanone and trimethylbenzene grown NWs respectively) and decreased the amount of disorder in the NWs (from $g = 0.0446 \pm 0.0004$, 0.040, and 0.0474 ± 0.0002 to $g = 0.0400 \pm 0.0002$, 0.0373 ± 0.0007 , and 0.0411 ± 0.0013 for anisole, cyclohexanone and trimethylbenzene grown NWs respectively).

Taking these diffraction results together, the picture that emerges of struc-

tural changes that happen during the annealing of P3HT NWs is as follows. The spacing between the backbones along the alkyl chain stacking direction is significantly lower in the NWs compared to those observed in P3HT films. There is considerable expansion along this direction during annealing, and on re-cooling the spacing becomes far closer to that observed in thin films. This indicates a highly compact arrangement, possibly involving some interdigitation of alkyl-chains, in the as-formed NWs, with that after annealing being more typical of that occurring in spin-coated films. During annealing, the domain size increases accompanied by a decrease in paracrystallinity.

Bibliography

- [1] Ihn K J, Moulton J, and Smith P. Whiskers of poly(3-alkylthiophene)s. *Journal of Polymer Science Part B: Polymer Physics*, 31(6):735–742, 1993.
- [2] Samitsu S, Shimomura T, and Ito K. Nanofiber preparation by whisker method using solvent-soluble conducting polymers. *Thin Solid Films*, 516(9):2478 – 2486, 2008. The 7th International Conference on Nano-Molecular Electronics (ICNME 2006).
- [3] Samitsu S, Shimomura T, Heike S, Hashizume T, and Ito K. Effective production of poly(3-alkylthiophene) nanofibers by means of whisker method using anisole solvent: Structural, optical, and electrical properties. *Macromolecules*, 41(21):8000–8010, 2008.
- [4] Oosterbaan W D, Vrindts V, Berson S, Guillerez S, Douheret O, Ruttens B, D’Haen J, Adriaenssens P, Manca J, Lutsen L, and Vanderzande D. Efficient formation, isolation and characterization of poly(3-alkylthiophene) nanofibres: probing order as a function of side-chain length. *Journal of Materials Chemistry*, 19:5424–5435, 2009.
- [5] Wu P-T, Xin H, Kim F S, Ren G, and Jenekhe S A. Regioregular poly(3-pentylthiophene): Synthesis, self-assembly of nanowires, high-mobility field-effect transistors, and efficient photovoltaic cells. *Macromolecules*, 42(22):8817–8826, 2009.
- [6] Xin H, Kim F S, and Jenekhe S A. Highly efficient solar cells based on poly(3-butylthiophene) nanowires. *Journal of the American Chemical Society*, 130(16):5424–5425, 2008.
- [7] Xin H, Ren G, Kim F S, and Jenekhe S A. Bulk heterojunction solar cells from poly(3-butylthiophene)/fullerene blends: In situ self-assembly of nanowires, morphology, charge transport, and photovoltaic properties. *Chemistry of Materials*, 20(19):6199–6207, 2008.
- [8] Kiriya N, Jähne E, Adler H-J, Schneider M, Kiriya A, Gorodyska G, Minko S, Jehnichen D, Simon P, Fokin A A, and Stamm M. One-dimensional aggregation of regioregular polyalkylthiophenes. *Nano Letters*, 3(6):707–712, 2003.

- [9] Kim D H, Park Y D, Jang Y, Kim S, and Cho K. Solvent vapor-induced nanowire formation in poly(3-hexylthiophene) thin films. *Macromolecular Rapid Communications*, 26(10):834–839, 2005.
- [10] Sudip Malik and Arun K. Nandi. Influence of alkyl chain length on the gelation mechanism of thermoreversible gels of regioregular poly(3-alkyl thiophenes) in xylene. *Journal of Applied Polymer Science*, 103(4):2528–2537, 2007.
- [11] Prosa T J, Winokur M J, Moulton J, Smith P, and Heeger A J. X-ray structural studies of poly(3-alkylthiophenes): an example of an inverse comb. *Macromolecules*, 25(17):4364–4372, 1992.
- [12] Prosa T J, Winokur M J, and McCullough R D. Evidence of a novel side chain structure in regioregular poly(3-alkylthiophenes). *Macromolecules*, 29(10):3654–3656, 1996.
- [13] Arosio P, Moreno M, Famulari A, Raos G, Catellani M, and Meille S V. Ordered stacking of regioregular head-to-tail polyalkylthiophenes: Insights from the crystal structure of form I' poly(3-n-butylthiophene). *Chemistry of Materials*, 21(1):78–87, 2009.
- [14] Tashiro K, Kobayashi M, Kawai T, and Yoshino K. Crystal structural change in poly(3-alkyl thiophene)s induced by iodine doping as studied by an organized combination of x-ray diffraction, infrared/raman spectroscopy and computer simulation techniques. *Polymer*, 38(12):2867 – 2879, 1997.
- [15] Aasmundtveit K E, Samuelsen E J, Guldstein M, Steinsland C, Flornes O, Fagermo C, Seeberg T M, Pettersson L A A, Inganäs O, Feidenhans'l R, and Ferrer S. Structural anisotropy of poly(alkylthiophene) films. *Macromolecules*, 33(8):3120–3127, 2000.
- [16] Kayunkid N, Uttiya S, and Brinkmann M. Structural model of regioregular poly(3-hexylthiophene) obtained by electron diffraction analysis. *Macromolecules*, 43(11):4961–4967, 2010.
- [17] Moulé A J, Allard S, Kronenberg N M, Tsami A, Scherf U, and Meerholz K. Effect of polymer nanoparticle formation on the efficiency of polythiophene based "bulk-heterojunction" solar cells. *The Journal of Physical Chemistry C*, 112(33):12583–12589, 2008.
- [18] Berson S, De Bettignies R, Bailly S, and Guillerez S. Poly(3-hexylthiophene) fibers for photovoltaic applications. *Advanced Functional Materials*, 17(8):1377–1384, 2007.
- [19] Lilliu S. *Organic Photodetectors Optimization and Nanoscale Investigation*. PhD thesis, School of Physics and Astronomy, Cardiff University, 2011.

- [20] Merlo J A and Frisbie C D. Field effect transport and trapping in regioregular polythiophene nanofibers. *The Journal of Physical Chemistry B*, 108(50):19169–19179, 2004.
- [21] Lilliu S, Agostinelli T, Pires E, Hampton M, Nelson J, and Macdonald J E. Dynamics of crystallization and disorder during annealing of P3HT/PCBM bulk heterojunctions. *Macromolecules*, 44(8):2725–2734, 2011.

Chapter 5

Doping of Nanowires and their use in Organic Photovoltaics

5.1 Introduction

This chapter describes the use of P3HT and PQT-12 nanowires as an electron donor in the active blend of organic photovoltaics. We also consider here a novel technique used in seeking improved performance which was that of intercalation of dye molecules into the nanowires, i.e. with the dye molecules slotted in a planar orientation in between the $\pi - \pi$ stacked thiophene rings. This novel doping was utilised in an effort to extend the range of wavelengths of light over which the OPV devices absorb and improve charge separation and transfer.

Following the introduction and all experimental details, the chapter is then presented in two further parts. Firstly, data from OPV testing of P3HT-NW:PCBM and PQT-12-NW:PCBM devices, and a comparison of their performance is presented.

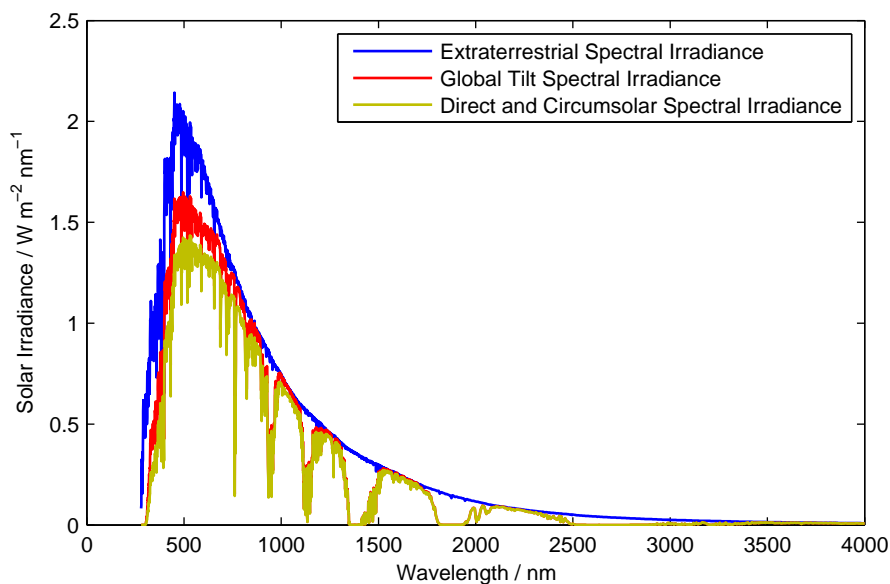
The second part describes the structure and energetics of the dyes, which

were synthesised by Dr. Andrew Hallett and Dr. Jenn Jones of Simon Pope's organic chemistry group of Cardiff University. Then the performance of OPVs produced with the dyes intercalated into P3HT-NWs and blended with PCBM, are assessed.

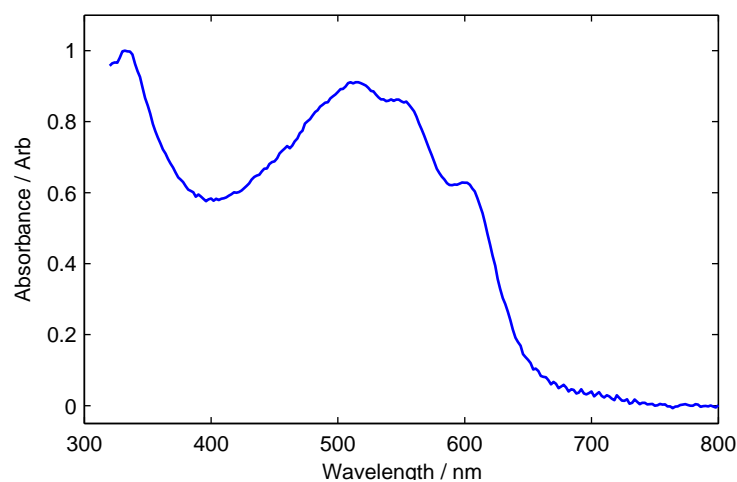
5.1.1 Why Dyes?

The power output of a photovoltaic cell is dependent on the several factors: the efficiency of the device's active material to absorb incident photons as a function of energy, the energy of the absorbed photons, the efficiency with which the bound charges resultant from photon absorption are separated, and the ability to transport the separate charges to the electrodes without recombination. Typical materials used in OPVs, for example P3HT and PCBM, have an absorption spectrum that peaks within the 1.5AM solar spectrum, but don't have a constant extinction coefficient across this range. Here we explore whether the absorption spectrum of the active blend can be improved so that increased photon absorption occurs by using an effectively designed dye molecule, with well positioned HOMO and LUMO levels.

The solar spectrum is shown in figure 5.1 a) from 100 nm to 4 μm . The solar flux this drops off significantly above 2500nm, peaking at circa 500nm. The spectrum is close to that of a blackbody with a temperature of 5800K, but due to attenuation by the Earth's atmosphere, has absorption peaks. The standard solar spectrum for testing is the AM 1.5 spectrum, which simulates the average radiation that is incident on the Earth at 48.2 ° latitude, due to the Earth's axis tilt; this represents the location of a large portion of the human populace, and hence energy requirements. At this latitude the light has passed through the equivalent of 1.5 Earth atmospheres.



a)



b)

Figure 5.1: a) Solar spectra [1], showing the extraterrestrial spectrum (top of Earth atmosphere), the "Global Tilt" (spectral radiation from the solar disc plus diffuse from sky and reflected from ground), and direct(excluding scattered sky and reflected ground radiation)+circumsolar (within $\pm 2.5^\circ$ field of view centred on the solar disc but excluding radiation from disk) b) P3HT-NW:PCBM OPV spectra, normalised to 1 at 320nm.

Figure 5.1 b) shows the combined absorption spectra for a P3HT-NW:PCBM solar cell. The absorption ranges from 310 nm to 650 nm, there is a large drop in absorption at 400 nm. As can be seen by comparing the AM1.5 spectra and the absorption of the P3HT-NW:PCBM device there is a large amount of incident radiation that is not being fully utilised by the device. It is possible that with careful design of a dye molecule the absorption coefficient can be increased near 400 nm or extended past 650 nm.

The introduction of dye molecules is a similar approach to that used in dye sensitised solar cells (DSSCs) developed by Grätzel[2]. In a DSSC (figure 5.2), a transparent electrode is coated on to a glass substrate. On the electrode a highly porous layer of TiO_2 is deposited, which in turn is coated with dye molecules. The bottom of the device is a reflective cathode, and then the device is filled with an electrolyte.

In a DSSC incident light is absorbed by the dye molecules, exciting electrons which are then rapidly transferred to the TiO_2 . The electrons are extracted at the transparent electrode, and flow through a circuit driving a load. The electrons are then injected back into the DSSC at the cathode and flow through the electrolyte back into the dye molecules where they recombine with the holes that were left behind through the initial photonic excitation.

The process of electron transfer from dye to TiO_2 is rapid enough that it occurs before recombination can occur in the dye between the excited electron and its hole.

Solid state DSSCs have been produced[3, 4, 5], where the electrolyte has been replaced with a material in the solid state, in order to alleviate some of the problems faced by using a liquid electrolyte, but the efficiencies have proven to be much lower.

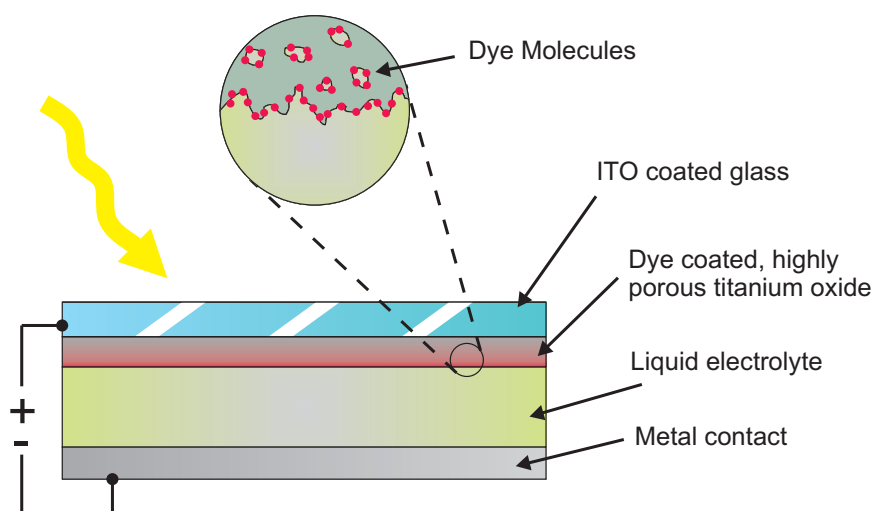


Figure 5.2: DSSC (Gratzel) OPV structure schematic

Here, we investigate whether a parallel approach to that in a DSSC can be applied in a BHJ by locating dye molecules, having a smaller bandgap than either P3HT or PCBM, selectively at the P3HT-PCBM donor-acceptor interface. This might be expected to improve efficiency at longer wavelengths and/or enhance charge separation by minimising the diffusion distance of excitons.

The novel approach of dye intercalation into the NWs as described here is similar to the ternary cells that were created recently[6, 7]. Fu incorporated cadmium selenide nanodots into P3HT:PCBM solar cells, while Machui investigated the addition of the small band gap polymer poly[2,6-(4,4-bis-(2-ethylhexyl)-4H-cyclopenta[2,1-b;3,4-b 0]dithiophene)-alt-4,7(2,1,3- benzothiadiazole)] (PCPDTBT). The results of Machui's work saw decreases in the device efficiency attributed to a reduction in the crystallinity of the fullerene phase and disruption of the electron transport, despite increased absorption in the near infra-red (NIR). Increased absorption in the NIR was also observed by Koppe using the same blend[8]. Fu found that addition of the

nanodots to P3HT:PCBM devices increased device efficiency by 1% point up to 3.05%, through greater photon harvesting combined with high intrinsic mobility of the nanodots.

5.2 Experimental Details

5.2.1 Dyes

Dyes were synthesised by the Pope group via a one-pot reductive animation procedure as reported by Jones[9].

Organic nanowires were grown via the whisker method as previously described (§ 4.2), using Anisole as the solvent for the P3HT NW formation and Toluene for the PQT-12 NW formation. PQT-12 film blends were produced using Trichlorobenzene. Intercalation of the dye took place during growth of the nanowires, where the dye molecules were added to the polythiophene solutions prior to cooling.

To investigate intercalation of the dyes into NWs, a large excess of dye was used in the solutions which, once formation had occurred, were centrifuged; the supernatant above the solid material at the bottom was removed, and fresh solvent was added. The centrifuge cycle was repeated in order to purify the material by removing the non-NW P3HT and the free dye, leaving behind the crystallised NWs with any intercalated dye. Initially anisole was used as the added solvent during each centrifuge cycle, but when results showed that the quantity of dye was decreasing the solvent was switched to diethyl ether in order to prevent the dye from being drawn out of the NWs by the anisole solvent.

UV-vis, luminescence, AFM and combustion analysis were used to determine successful intercalation of the dyes into the NWs. UV-Vis was car-

ried out using a Jasco V-570, while luminescence was carried out using a Jobin Yvon-Horiba Fluorolog spectrometer. AFM was performed using a Veeco Multimode III. Combustion analysis was carried out by University of Manchester and Imperial College London, and was used to determine the loading of the dye into the NWs.

Where there was overlap of the absorption of the dye with the NWs, such that the spectrum wasn't sufficient to determine whether intercalation was taking place, luminescence was used to determine whether the dyes were intercalated within the NWs.

Cyclic voltammetry (as described earlier, § 3.5) was used to determine the HOMO level of the dyes, and P3HT in solution, whilst the band gap was measured from the absorption onset from the UV-Vis spectroscopy. The LUMO was calculated from the HOMO and the band gap.

5.2.2 OPV Devices

All Devices

The OPV device structure is shown in figure 5.3. The OPVs consisted of ITO coated glass, followed by a 40nm spin coated PEDOT:PSS hole transporting layer. The active blend was then spun on top of the PEDOT:PSS with parameters dependent on the device blend, aiming to give a thickness of circa 100nm. Aluminium was then evaporated on top of the active blend at a thickness of 100nm, and then the device was finally encapsulated to prevent degradation via interaction with atmospheric gases. After encapsulation devices were cured under low power UV for 30 mins using a Mega LV202 exposure unit.

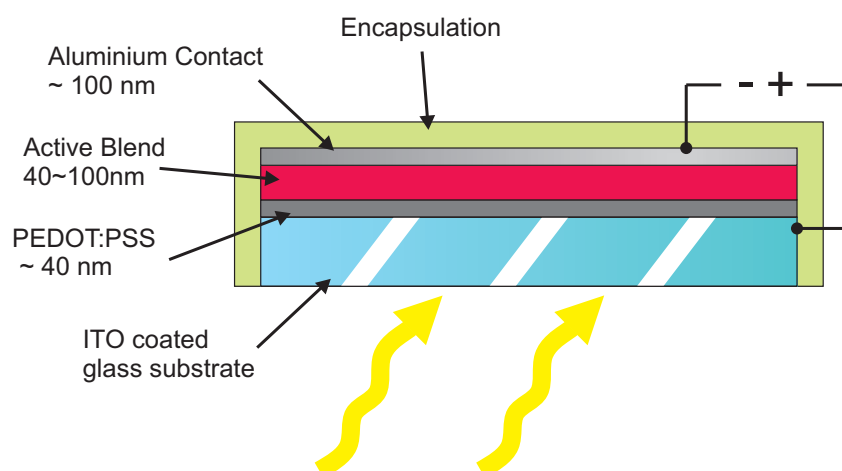


Figure 5.3: OPV device structure schematic

All devices were fabricated using the following procedure:

- Ossila standard 20x15mm pre-patterned ITO/glass substrates
- $20 \Omega/\square$ 100nm ITO/glass substrates
- HC Stark Clevios P Ai4083 PSS:PEDOT hole transport layer, spuncast at 5000rpm by dynamic dispensing, at ~40nm thickness.
- Stored on hot plate at 150°C until transferred to nitrogen filled glove-box.
- 20 μ l of active blend spuncast (at speeds determined by pretesting for thickness) by dynamic dispensing, and spun for 90 seconds.
- Al cathode deposited via evaporation to thickness of ~100nm under vacuum pressure of $< 1 \times 10^{-6}$.
- Encapsulated using a glass coverslip and Ossila EE1, cured in low power UV light for 30 mins using a Mega LV202 exposure unit).

P3HT-NW and PQT-12-NW Devices

Initial devices produced from dye free blends of P3HT-NW:PCBM and PQT-12-NW:PCBM were deposited at varying solution temperatures in order to vary the composition of the solution, by varying the ratio of crystalline to

non-NW polymer, and affecting the lengths of the NWs. Solutions were deposited at 30, 40, 50, 60 and 70°C, and a film blend deposited at room temperature was produced for comparison. This was preformed at Sheffield in collaboration with Andrew Pearson and Darren Watters.

Dye Intercalated Devices

Dye intercalated devices were prepared and tested by Ossila Ltd. as part of a commercial arrangement funded through a 12-month EPSRC follow-on grant. The active blends for the devices were prepared by the author. The blends were tested in batches, where a dye-free P3HT-NW:PCBM blend was tested in each batch in order to be able to compare the device performance effectively. Batch details are found in the OPV performance metrics table 5.3 in section 5.5.1.

Ossila fabricated dye intercalated devices were fabricated with the aim of achieving an active blend thickness of 100nm with a suitably smooth morphology that allowed successful evaporation of the Al cathode with minimal shorts.

Three devices, comprising of six 4 mm ×1.5 mm (6 mm²) pixels, were made for each blend, with each device spun at a different speed, in order to ensure enough working pixels where the viscosity of the blends made it difficult to reliably fabricate smooth films of the required thickness.

Dye intercalated blends used for OPV devices were produced as described previously although a measured amount of dye was included, where the loading quantities as taken from the combustion testing were used as discussed in §5.4.2.

In detail, 10 mg of PCBM was dissolved in 1 ml of solvent at 80°C, with the vial held in an aluminium heating block on a hot plate. 2 mg of dye (for

regular loading) was dissolved in solvent and then added to 10 mg of P3HT and heated to 80°C. Once all solutes had dissolved (after approximately 20 mins with some agitation) the PCBM was added to the P3HT/dye solution and heated for a further 10 mins, to ensure all materials were fully dissolved. The hot plate was then turned off and the solutions were then left in the aluminium heating block on the hot plate allowed to cool naturally.

No further treatment was applied to the blends until shortly prior to deposition 3-5 days later, when the blends were heated to 50°C for 30 mins, along with the pipette tips, and deposited at this temperature.

The deposition temperature was chosen based on the results of P3HT-NW:PCBM blend device testing prior to the dye intercalation experiments; in these experiments the optimum deposition temperature was found to be 60°C, but with sharp drop off in efficiency above this temperature but a shallow decrease below this temperature (see figure 5.4). The active blends were held at the deposition temperature for 30mins to ensure the solutions had stabilised, with the pipette tips also pre-heated.

OPV Testing

Devices were tested under 100 mW cm⁻² 1.5AM simulated sun light using a Newport Oriel 9225-1000 solar simulator, with a NREL certified silicon reference cell used for calibration. J-V sweeps were taken using a Keithley 237 source-meter.

5.3 P3HT-NW and PQT-12-NW OPV Device Performance

5.3.1 Results

The first tests performed were a comparison of the performance of devices fabricated using P3HT-NW:PCBM blends and PQT-12-NW:PCBM blends, and an investigation into how the deposition temperature affects the devices performance. Previous studies[10, 11] by other groups found that for P3HT-NW devices it was necessary to have some amorphous material in the blends, with the suggestion put forward that the amorphous material acts to join the nanowires into a continuous network. The ratio of amorphous to crystalline material was controlled here by altering the deposition temperature of the blends. Blends had been made in the usual manner and allowed to cool to room temperature for a few days before deposition to ensure nanowire growth. The performance metrics for P3HT-NW and PQT-12-NW devices can be seen in table 5.1 with plots shown in figures 5.4 and 5.5.

The as cast P3HT devices outperformed the as cast PQT-12 devices, with a highest average efficiencies of $0.92\pm0.17\%$ and $0.16\pm0.08\%$ respectively, achieved at a deposition temperature of 60°C for both materials. The annealed P3HT devices all showed an increase in PCE, with the highest average PCE of $1.52\pm0.28\%$ at a deposition temperature of 60°C . Little change was seen in the average efficiency of the PQT-12 devices after annealing, although the range of PCE from the devices increased.

The maximum efficiency for the P3HT devices was at a deposition temperature of 60°C , for as cast and annealed devices, above this temperature the efficiency dropped off rapidly, and below this temperature the PCE dropped off more slowly with decreasing temperature for the as cast devices, and remained within 0.17% PCE of the 60°C maximum. The PCE

temperature trend was matched by the J_{SC} for the as cast and annealed devices with maximums at 60°C. The V_{OC} for as cast and annealed devices stayed fairly constant with a small peak at 60°C, and the fill factor for the as cast was also reasonably constant, while the FF for the annealed devices dropped off above 60°C and exhibited a dip at 40°C although this is matched with a large standard deviation.

The maximum efficiency for the PQT-12-NW devices was at a deposition temperature of 60°C for as cast and annealed devices; above and below this temperature the performance dropped off rapidly. The PCE temperature trend was matched by the V_{OC} and the FF for the as cast and annealed PQT-12-NW devices, with maximums at 60°C. The J_{SC} for as cast and annealed PQT-12-NW devices was maximum for a deposition temperature of 30°C and remained steady between 0.73 and 0.85 mA cm⁻² from 40 to 70°C.

The PQT-12 film devices had PCEs of only 0.04±0.04 and 0.05±0.04 % for as cast and annealed devices respectively. PQT-12-NW devices had two to three-fold increase in PCE in comparison, the V_{OC} were 2 times greater, the J_{SC} were 1.5 times greater and the FF 1.3 times greater compared to the PQT-12 films.

Table 5.1: P3HT-NW:PCBM and PQT-12-NW:PCBM OPV device metrics

Device	Deposition Temp / °C	PCE / %		V _{OC} / V		J _{SC} / mA cm ⁻²		FF	
		Mean	Max	Mean	Max	Mean	Max	Mean	Max
P3HT-NW: PCBM As Cast	30	0.56±0.11	0.77	0.28±0.02	0.32	4.26±0.59	5.40	46.1±2.0	49.2
	40	0.64±0.18	0.86	0.28±0.06	0.34	4.79±0.62	5.77	45.6±5.8	49.6
	50	0.72±0.16	0.98	0.32±0.03	0.36	5.22±0.83	6.40	45.9±2.2	49.4
	60	0.92±0.17	1.11	0.34±0.02	0.36	5.93±1.00	7.21	45.9±2.2	50.2
	70	0.51±0.12	0.71	0.30±0.04	0.34	3.49±0.56	4.68	47.0±5.0	51.1
P3HT-NW: PCBM Annealed	30	1.40±0.16	1.68	0.52±0.02	0.54	4.82±0.38	5.48	56.3±1.8	58.8
	40	1.25±0.41	1.60	0.48±0.11	0.54	4.64±0.58	5.33	52.8±8.1	57.7
	50	1.30±0.21	1.86	0.52±0.02	0.56	4.44±0.62	6.05	56.6±1.4	58.3
	60	1.52±0.28	1.93	0.55±0.03	0.58	4.76±0.60	5.70	57.4±2.3	59.6
	70	0.77±0.30	1.13	0.51±0.10	0.58	2.81±0.49	3.40	51.1±9.4	59.0
PQT-12-NW: PCBM As Cast	30	0.00	0.00	0.00	0.00	1.56	1.86	0.0	0.0
	40	0.03±0.02	0.08	0.13±0.08	0.27	0.79±0.15	1.04	27.2±3.9	34.0
	50	0.11±0.07	0.23	0.30±0.11	0.42	0.93±0.23	1.30	34.7±6.2	42.5
	60	0.16±0.08	0.35	0.40±0.04	0.49	0.95±0.34	1.79	42.2±3.3	45.7
	70	0.12±0.05	0.27	0.37±0.04	0.47	0.82±0.23	1.45	39.5±2.7	44.5
PQT-12-NW: PCBM Annealed	30	0.00	0.00	0.00	0.00	1.30	1.51	0.0	0.0
	40	0.03±0.02	0.06	0.13±0.08	0.27	0.73±0.10	0.84	28.0±3.3	32.3
	50	0.11±0.06	0.21	0.35±0.13	0.48	0.85±0.17	1.12	34.0±5.4	40.9
	60	0.15±0.05	0.26	0.45±0.04	0.53	0.81±0.21	1.31	40.5±2.1	43.0
	70	0.12±0.05	0.26	0.41±0.08	0.53	0.75±0.20	1.31	37.5±3.1	41.5
PQT-12-film:PCBM									
As Cast		0.04±0.04	0.11	0.16±0.10	0.303	0.58±0.17	0.94	30.1±6.5	39.6
Annealed		0.05±0.04	0.13	0.20±0.12	0.37	0.57±0.17	0.91	31.2±5.5	40.5

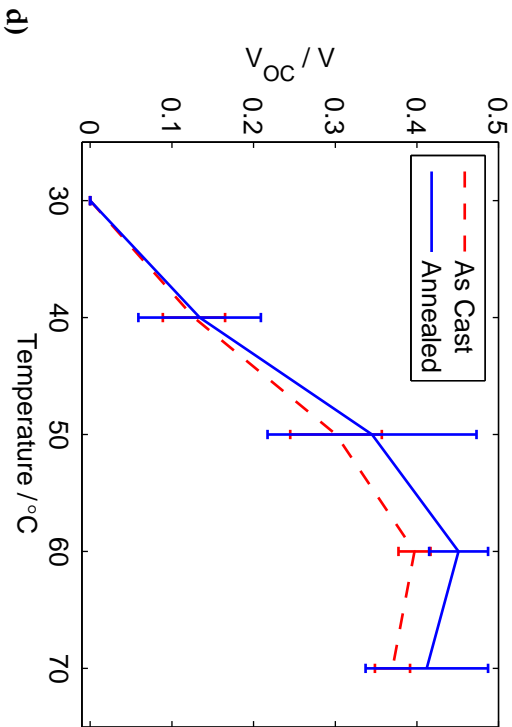
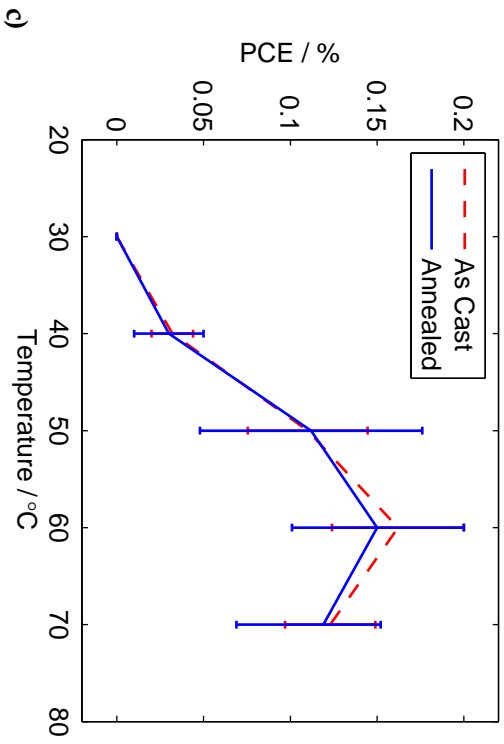
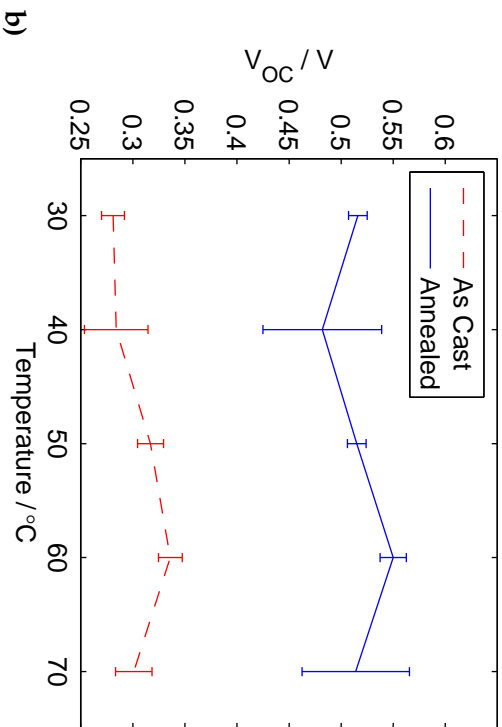
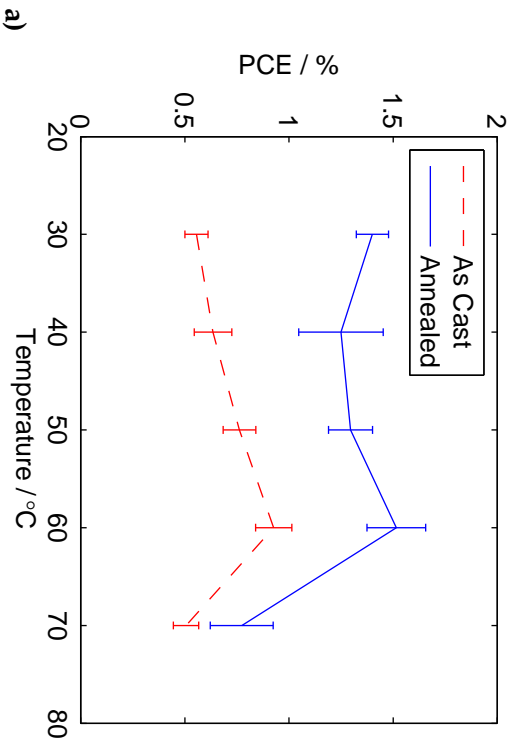


Figure 5.4: PCE (a) and c) and V_{OC} (b) and d) for varying non-NW to crystalline ratio in P3HT NW and PQT-12 NW OPV devices. a) and b) P3HT devices, as cast (red dashed line) and annealed (blue solid line). c) and d) PQT-12 devices, as cast (blue solid line). Peak PCE and V_{OC} for both device types is at 60 °C. The PQT-12 devices show fairly sharp decrease in PCE and V_{OC} either side of 60 °C whereas the P3HT devices are relatively stable below 60 °C. Annealing of the P3HT devices showed a general improvement in both the PCE and the V_{OC} at all temperatures.

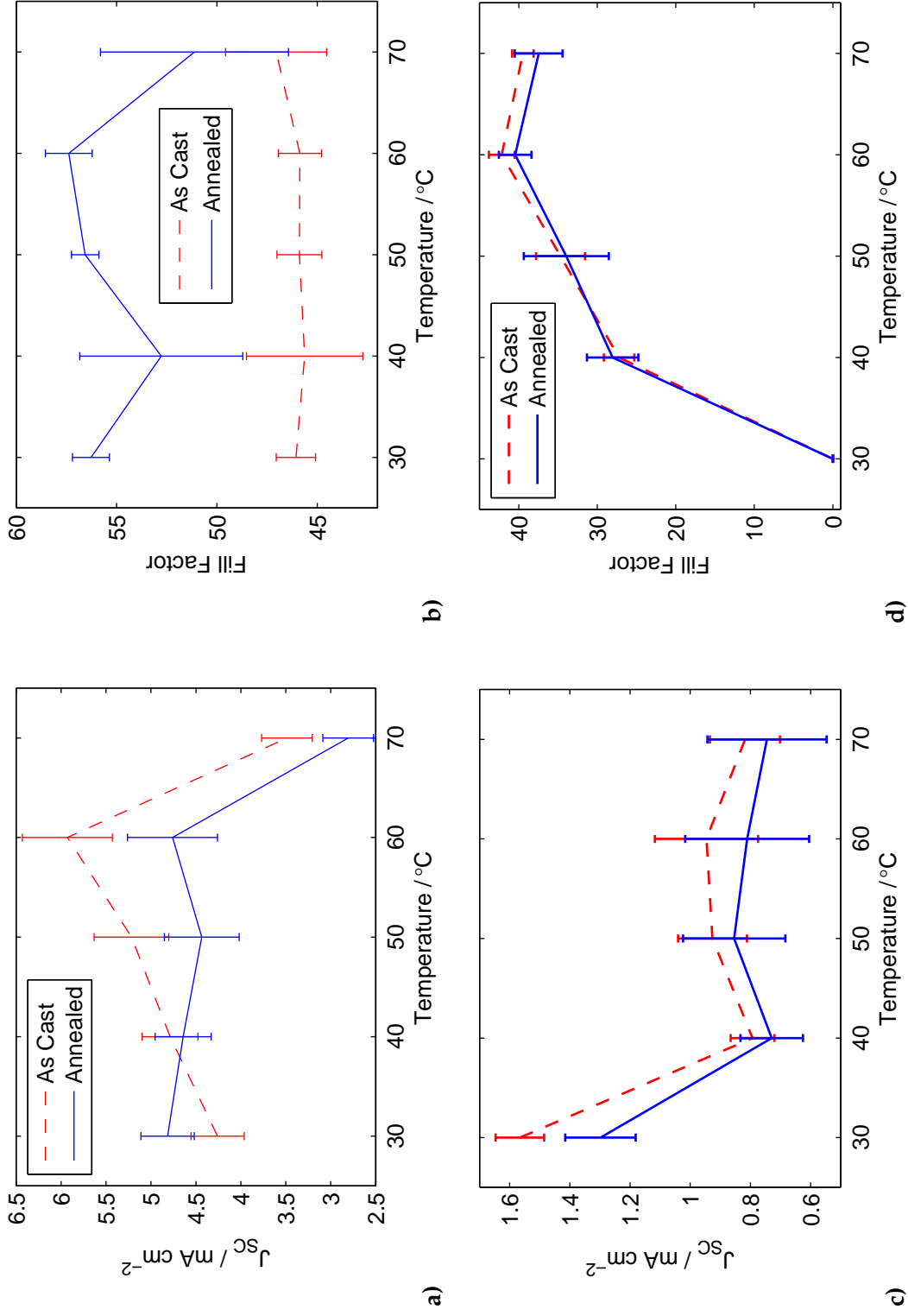


Figure 5.5: J_{sc} (a) and c) and FF (b) and d) for varying non-NW to crystalline ratio in P3HT NW and PQT-12 NW OPV devices. a) and b) P3HT devices, as cast (red dashed line) and annealed (blue solid line). c) and d) PQT-12 devices, as cast (blue solid line). In the as cast P3HT devices, J_{sc} peaks at 60 $^{\circ}\text{C}$ and decreases below this and more rapidly so above this temperature; FF remains stable at all temperatures. Annealing improves all FF but decreases the J_{sc} above 40 $^{\circ}\text{C}$, below which it is seen to increase in comparison to the as cast devices. In the PQT-12 devices the J_{sc} is fairly stable apart from at 30 $^{\circ}\text{C}$ where it is approximately double. The FF peaks at 60 $^{\circ}\text{C}$ and drops off either side.

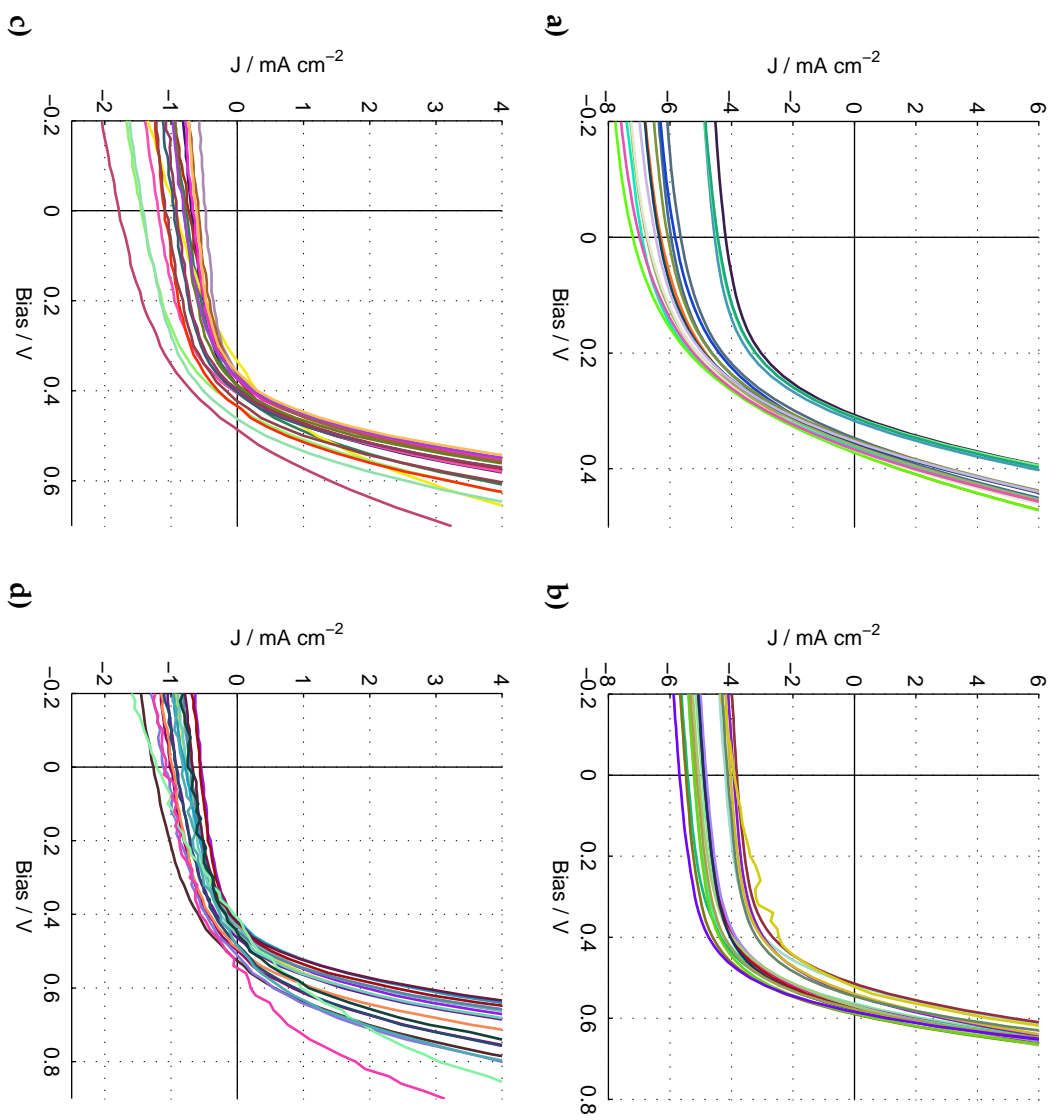
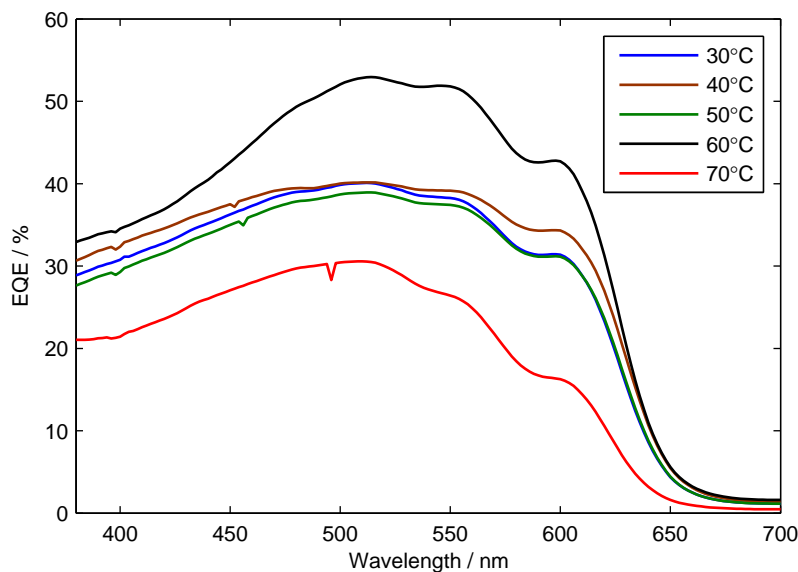


Figure 5.6: J-V curves for devices deposited at 60°C. a) P3HT asc cast - 16 out of 18 pixels (2 pixels were shorted), b) P3HT annealed - all 18 pixels, c) PQT-12 as cast (all 18 pixels), and d) PQT-12 annealed (all 18 pixels).

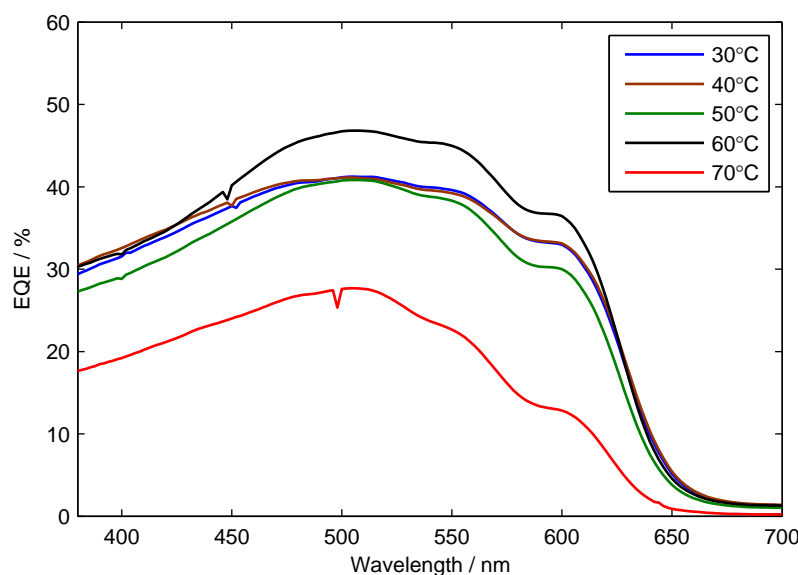
The external quantum efficiency(EQE) of the as cast P3HT devices are shown in figure 5.7 a). The device fabricated at a temperature of 60°C showed the highest EQE, rising to over 50% at 500-550 nm, and maintaining at least 40% between 450 and 600 nm. The devices fabricated at 30-50°C rose to approximately 38%, and maintained at least 30% between 380 and 600 nm. The devices fabricated at 70°C had the lowest EQE, with a peak below 30%. All of the curves displayed a similar shape, with peaks similar to those seen in the UV-Vis of P3HT NWs, suggesting that the device was absorption limited, and may be due to the narrow thickness of the active blend. The 60°C device has increased absorption between 475 and 620 nm in comparison to the slightly flatter curves of the other devices.

The EQE for the annealed devices is shown in figure 5.7 b). The device deposited at 60°C showed a slight decrease in the overall EQE, but a slight increase in the shoulder at 470 nm. The devices deposited at 30-50°C showed a slight increase in their peak EQE up to 40%, whereas the 70°C device showed a slight decrease throughout the wavelength range of approximately 4% points.

Absorption spectra were taken of the P3H-NW device films, and the individual components in solution in an attempt to provide an estimate of the ratios of non-NW and crystalline P3HT at each deposition temperature. Unfortunately, due to the variability in the pairs of peaks/shoulders in the crystalline NW phase the estimates provided no useful information.



a)



b)

Figure 5.7: P3HT-NW:PCBM OPV EQE. a) As cast: The devices deposited at 30-50°C have EQE profiles within 5% of each other. The device deposited at 60°C shows the greatest EQE, with a dramatic increase over the others between 450 and 625nm. The device deposited at 70°C had a similar EQE profile as the 30-50°C devices but approximately 10% lower. b) Annealed: The 60°C device shows the highest EQE, but has dropped compared to as cast. The devices from 30-50°C have increased slightly over the as cast devices. The EQE of the 70°C device as decreased compared to as cast.

5.3.2 Discussion

Deposition temperature It is apparent that there is a need for a proportion of non-NW material within polythiophene NW OPVs, in order to achieve maximum efficiency. The NWs are on average oriented parallel to the electrodes and so the non-NW material may act as a type of 'cement' and connect the layers of NWs, allowing for pathways to the electrodes for the separated charges.

P3HT vs. PQT-12 The P3HT-NW devices far outperformed the PQT-12-NW devices in terms of the PCE, J_{SC} and FF; only in V_{OC} did the PQT-12-NW as cast devices match or outperform the P3HT as cast devices, although this advantage was lost after thermal annealing. Examining the literature, this performance differential should be expected. PQT-12 OPV device efficiencies have generally been lower than those of P3HT, and the optimal fabrication parameters for PQT-12 OPV devices differs from what is used here. Optimal PQT-12:PCBM ratios have been found to be 1:3 in favour of the PCBM[12, 13]. The differences in performance may be explained by the higher hole mobility of PQT-12 compared to the electron mobility of PCBM, leading to unbalanced charge transport, and a build up holes in the PQT-12 domains. To compensate for the differences in the charge transport an increased quantity of PCBM should be used. This problem is not found in the P3HT devices as the charge transport properties of the two materials in the active blend are better balanced.

PQT-12 NW vs. film The PQT-12 film devices produced by Wantz[12] and by Thompson[13] required a 1:3 ratio of PQT-12:PCBM for optimal performance. At a 1:1 ratio Wantz's devices gave efficiencies of approximately

0.04%, the same as achieved in this study. Thompson's devices gave a maximum efficiency of 0.05% and Wantz's achieved approximately 0.23% at 1:3 PQT-12:PCBM. The as cast PQT-12-NW devices presented here achieved a maximum efficiency of 0.16% when deposited at 60°C, which is approximately two thirds of the efficiency of Wantz's 1:3 ratio devices but is a 4-fold increase compared to the films. It is difficult the increase in efficiency in these NW devices to an improved balancing of the charge transport as it would be expected the the improved crystallinity of the NWs would have increased mobility. The improvement may be caused by better charge separation due to improved active blend morphology. The domain sizes presented by the NWs may be better optimised for exciton diffusion than in PQT-12 films. Optimising the PQT-12-NW:PCBM blend ratios may lead to further improvements in efficiencies that could outperform blend ratio optimised film devices.

5.4 Dye-intercalation

5.4.1 Chemical Dye Structures

A total of 10 dyes were used in the production of OPVs, as shown in figure 5.8, all of which can be separated in to three groups:

1. Four dyes with anthraquinone main structure with pyridine side groups.
2. Four dyes with anthraquinone main structure with alkane side groups, analogs of group 1.
3. Two iridium complexes.

The anthraquinone structure was used with the intention that it would intercalate into the P3HT NWs, whilst the side-chains serve two purposes,

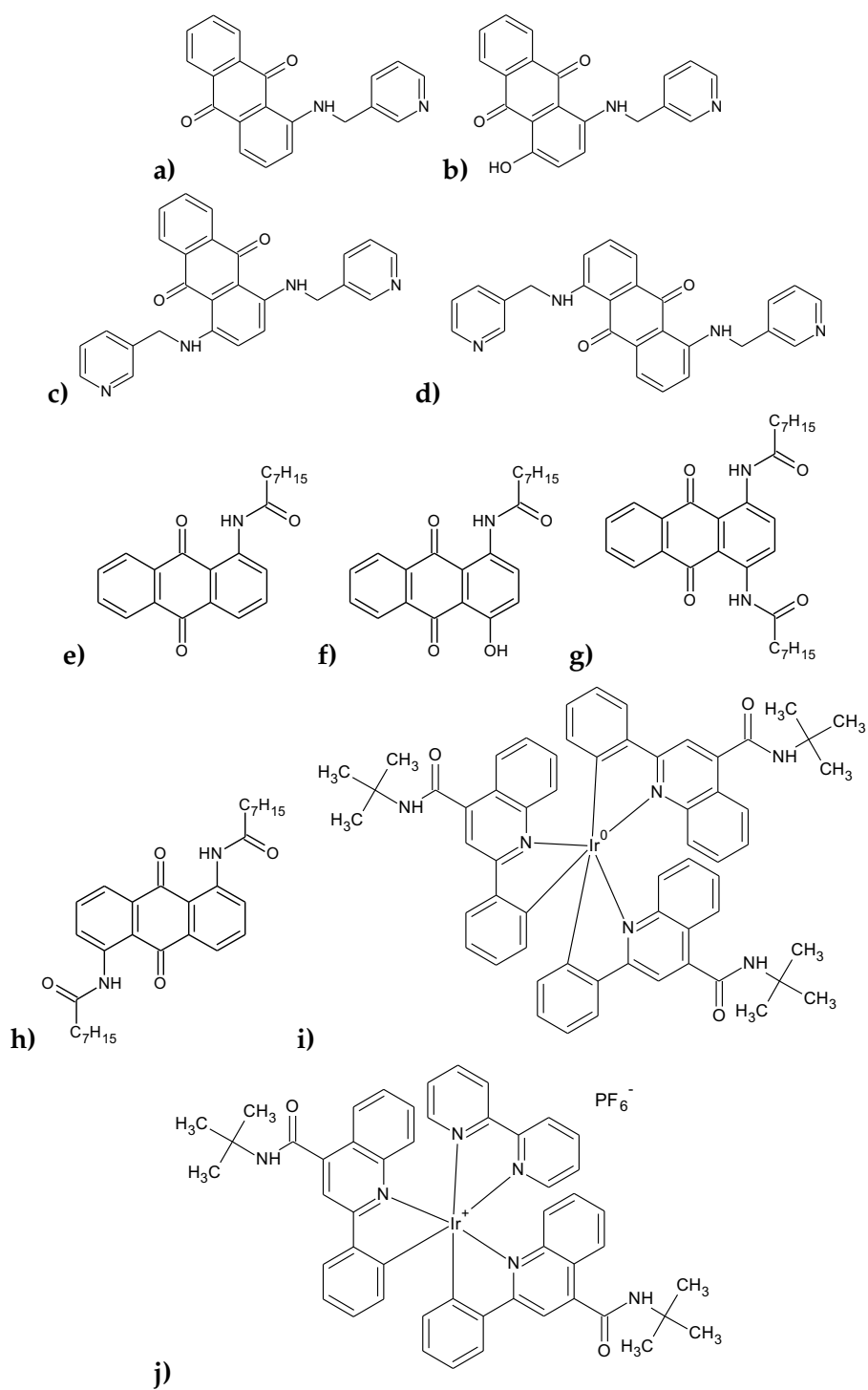


Figure 5.8: Structures of dyes a) 1a, b) 1b, c) 1c, d) 1d, e) 2a, f) 2b, g) 2c, h) 2d, i) 3, and j) 4

that of aiding solubility, and also to adjust the HOMO and LUMO levels in order that they can be tuned for optimum photon absorption, charge separation and transfer in OPV devices. The HOMO levels of the dyes were determined via cyclic voltammetry, whilst the energy gap was taken from the onset of absorption from UV-Vis spectroscopy, and the LUMO was then calculated using these two values. Comparisons of the energetics of the dyes and OPV components are shown in table 5.2 and figure 5.9.

Table 5.2: Energy levels of dyes used in intercalated OPV devices

Dye	HOMO / eV	LUMO / eV	Band Gap (E_g) / eV
1a	-5.88	-3.80	2.08
1b	-5.44	-3.58	1.86
1c	-5.18	-3.42	1.76
1d	-5.82	-3.80	2.02
2a	-5.87	-3.63	2.24
2b	-5.90	-3.73	2.17
2c	-5.94	-3.92	2.02
2d	-6.21	-3.91	2.30
3	-5.46	-3.30	2.16
4	-5.68	-3.58	2.10

5.4.2 Experimental

Dye intercalation was carried out by introducing the dye molecule to the P3HT solution prior to heating, and by following the usual procedure for NW production. NW formation was unhindered by the addition of the dye molecules, as was seen via AFM and UV-Vis techniques.

In order to remove non-NW P3HT and excess dye which has not intercalated into the NWs, the solution was processed through a series of centrifuging and rinsing, where the solution was centrifuged, the supernatant was removed, and fresh solvent was added. This had the effect of leaving the NWs with any intercalated dye behind at the bottom of the suspension, and

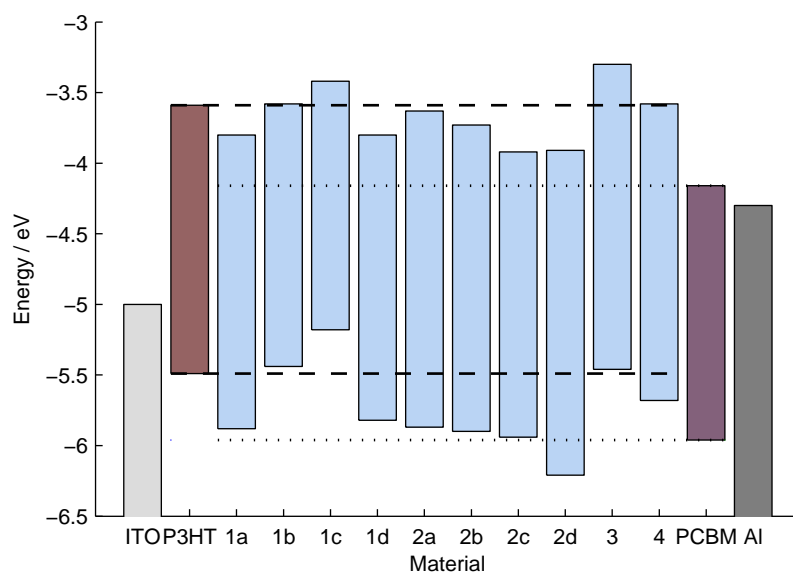


Figure 5.9: OPV material energy band diagram. The dashed line marks the HOMO and LUMO of the P3HT, while the dotted line marks the HOMO and LUMO of the PCBM.

removing the lighter non-NW P3HT and free dye within the supernatant.

5.4.3 Results

Emission Spectra

Figures 5.10 and 5.11 show normalised emission spectra for pure dyes, and dye intercalated NWs which have been centrifuged and washed once and two times, for dye 1a, 1b, 2a and 2d. Spectra for dyes 1b and 1c can be found in Appendix A.

Illumination of the samples at a wavelength of 500 nm allowed for the excitation of both the NWs and the four dyes in these figures. All NW spectra show presence of the dyes after both one and two centrifuge and wash cycle, with the peak becoming weaker after the second wash but it is still present. A bathochromic shift is seen in the dye 1a peak when it is

intercalated into the NWs, whereas a hypsochromic is seen in the peaks for 1d and 2a. No chromic shift is seen in dye 2d after intercalation of the NWs, although this was difficult to ascertain due to the noise in the data.

Combustion Analysis

Results of the combustion analysis can be found in table A.1 of Appendix A. The only source of nitrogen in the intercalated NWs was the dye as the NWs and the solvents used in their fabrication and rinsing were free from nitrogen, and so it was assumed that any nitrogen to show up during combustion analysis would be due to the presence of the dye in the NWs. The combustion analysis results showed that there was nitrogen present in the 1b, 1d, 2a and 2d dye intercalated NW samples suggesting that the dyes are present in the NWs even after two rinse cycles.

5.4.4 Discussion

The presence of the dye emission peak in the rinsed NW samples suggests that intercalation is taking place and that the dyes aren't being fully removed from the NWs, furthermore the chromic shift of the dye emission peaks when intercalated into the NWs suggests that the dyes and the NWs are interacting, adding support to the suggestion that the NWs are intercalated into the NWs rather than floating separately in the NW solutions. It is difficult to prove conclusively that the dyes are fully inserted into the π -stacked P3HT NWs rather than associated less specifically with them. This might be tested by polarised luminescence studies at a single NW level, but such experiments were impractical with our experimental setup. Finally combustion analysis shows the presence of the dyes through identification of nitrogen in the dye intercalated NW samples.

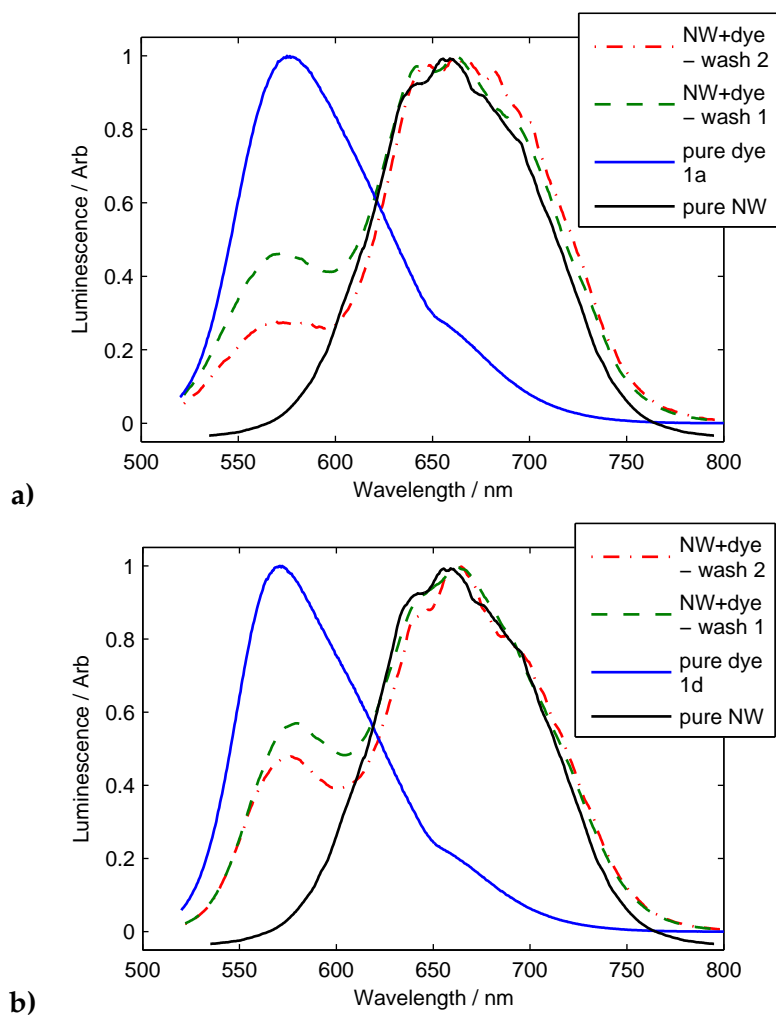
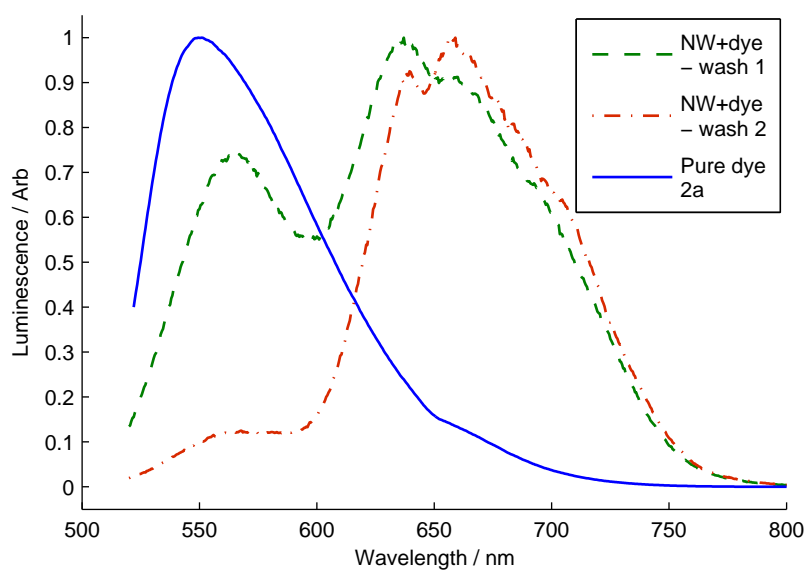
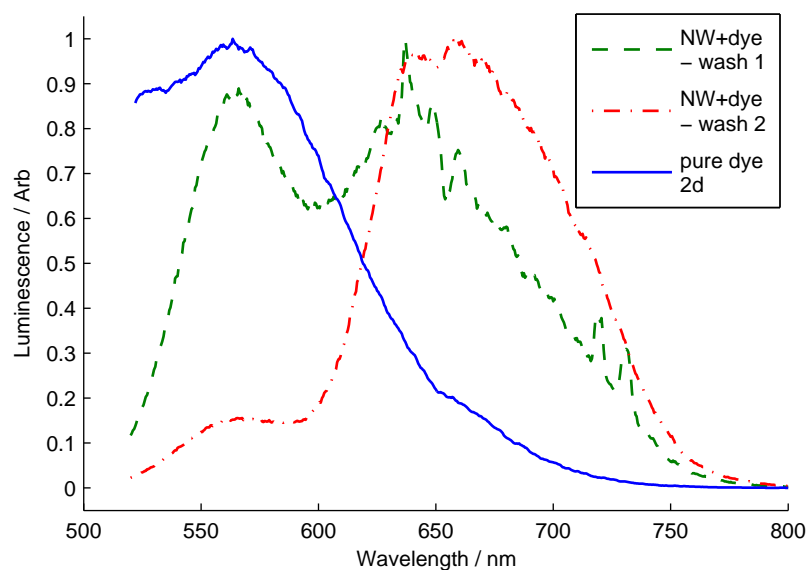


Figure 5.10: Emission of a) dye 1a and b) dye 1d, intercalated into P3HT anisole NWs, illuminated at 500 nm. The solutions containing the NWs and dyes was centrifuged and 'washed' with diethyl ether twice, with the emission shown after each cycle. The relative intensity of the dyes decreased with each wash but were still clearly visible.



a)



b)

Figure 5.11: Emission of a) dye 2a and b) dye 2d, intercalated into P3HT anisole NWs, illuminated at 500 nm. The solutions containing the NWs and dyes was centrifuged and 'washed' with diethyl ether twice, with the emission shown after each cycle. The relative intensity of the dyes decreased with each wash but were still clearly visible.

5.5 Dye Intercalated OPVs

Solutions for OPV devices were prepared as per the standard whisker method with measured quantities of dye, calculated from combustion analysis, added before heating the solutions. The solution were then used as made without centrifuging, and were deposited at 50°C. Several batches were tested which involved different dyes, or loading of the dyes. All batches contained one standard P3HT-NW blend free from dye, which was tested at the same time, which acted as a standard due to the large fluctuation of results from batch to batch.

5.5.1 Results

The performance metrics for the as cast dye intercalated devices are shown in table 5.3 and in figure 5.12. Dyes 1a-d gave low, but measurable power conversion efficiencies, and were generally outperformed by the P3HT-NW:PCBM reference devices by an order of magnitude.

Table 5.3: As cast dye OPV performance metrics

Batch	Solution	PCE / %		Voc / V		Jsc / mA/cm ²		FF	
		Mean	Max	Mean	Max	Mean	Max	Mean	Max
4	No Dye	0.282±0.245	0.847	0.18±0.13	0.36	4.60±1.23	7.14	29.8±3.5	36.2
	2d	0.533±0.413	1.016	0.26±0.17	0.44	4.05±0.94	5.13	39.3±8.5	48.9
	2d No PCBM	0.001±0.000	0.001	0.14±0.03	0.16	0.02±0.01	0.04	33.0±3.0	37.5
	1c No PCBM	0.007±0.006	0.015	0.24±0.17	0.4	0.08±0.02	0.10	42.1±6.0	49.8
	1a No PCBM	0.000±0.001	0.001	0.10±0.11	0.18	0.01±0.01	0.017	31.0±3.4	33.3
5	No Dye	0.92±0.37	1.43	0.31±0.05	0.38	6.19±2.05	8.80	46.5±3.0	52.0
	2d very low load	0.88±0.47	1.43	0.32±0.12	0.44	4.69±1.32	6.49	49.5±9.6	57.6
	2d low load	0.98±0.26	1.40	0.39±0.04	0.44	4.85±0.69	5.93	51.2±8.0	58.8
	2d normal load	0.88±0.33	1.30	0.37±0.08	0.44	4.62±0.81	5.84	48.8±8.6	59.3
	2d high load	0.96±0.39	1.43	0.38±0.09	0.44	4.51±1.17	6.29	52.1±8.3	59.7
6	2a	0.34±0.17	0.59	0.21±0.09	0.32	3.54±0.58	4.49	44.4±5.3	52.3
	4	0.11±0.05	0.16	0.14±0.05	0.18	2.26±0.58	2.84	31.8±1.0	33.7
	3	0.20±0.04	0.27	0.38±0.05	0.42	2.34±0.41	3.03	22.2±2.1	28.3
	2b	0.53±0.35	0.97	0.30±0.13	0.44	3.44±0.73	4.51	44.7±9.4	54.6
	2c	0.75±0.49	1.25	0.35±0.19	0.50	3.30±0.62	3.97	53.1±14.7	63.7
7	No Dye	0.279±0.247	0.685	0.14±0.09	0.28	5.20±1.46	6.74	29.1±8.79	36.4
	1a	0.031±0.025	0.073	0.11±0.08	0.24	0.91±0.17	1.14	30.4±6.96	48.2
	1b	0.030±0.019	0.054	0.15±0.10	0.28	0.71±0.08	0.83	27.0±3.5	33.7
	1c	0.077±0.040	0.135	0.22±0.13	0.40	1.56±0.40	2.20	23.3±5.74	33.0
	1d	0.013±0.011	0.029	0.06±0.04	0.14	0.70±0.09	0.87	28.0±9.6	34.4

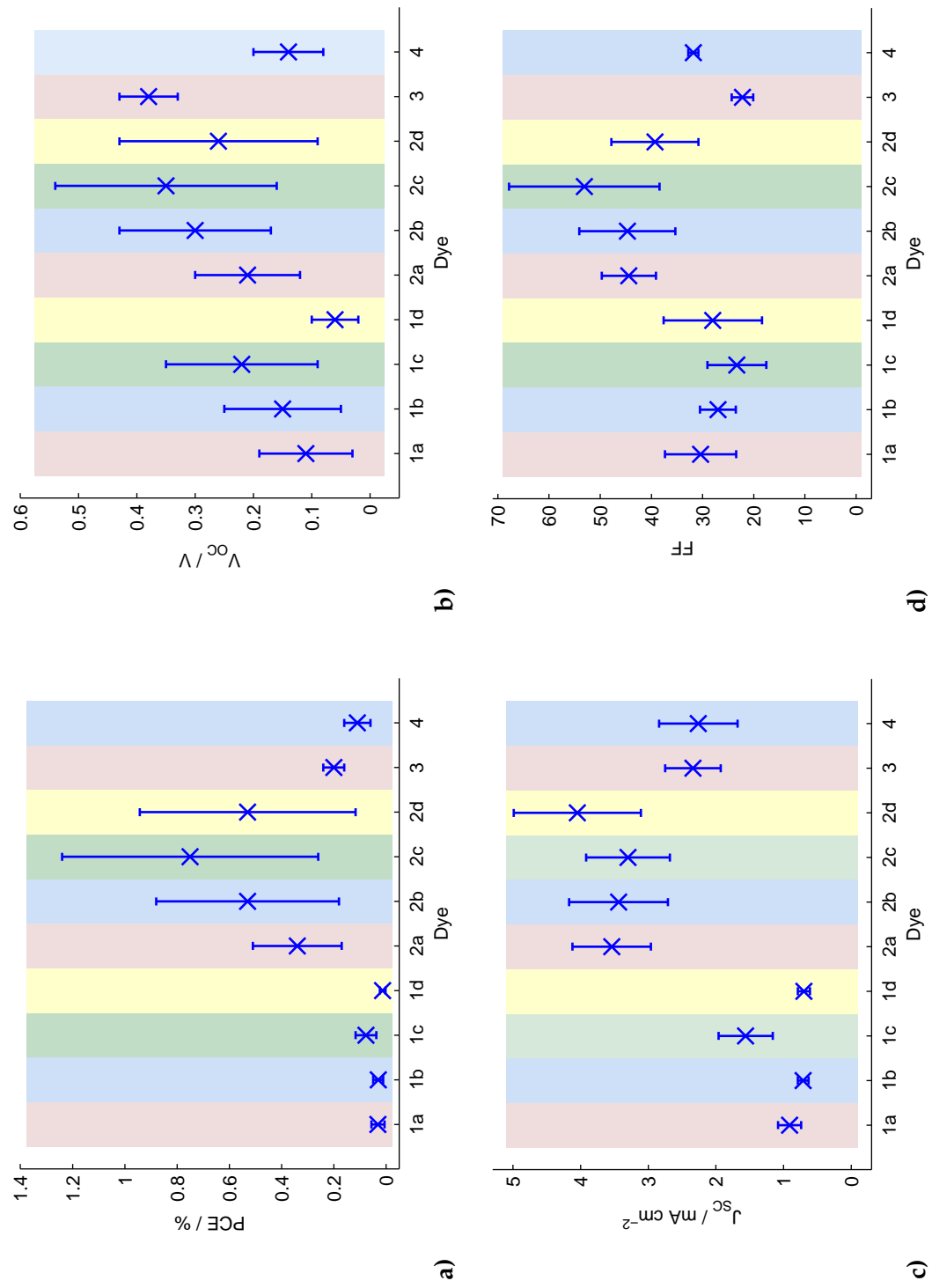


Figure 5.12: P3HT-NW:Dye:PCBM OPV performance metrics

Dyes 3 and 4 showed some power conversion efficiency, $0.20\pm0.04\%$ and $0.11\pm0.05\%$ respectively, although this was a decrease in comparison to the reference (no dye in batch 5; these two batches were produced and tested simultaneously) which gave a PCE of $0.92\pm0.37\%$. Dye three showed a slight increase in V_{OC} over the reference, 0.38 ± 0.05 V and 0.31 ± 0.05 V respectively, although there is a slight overlap of the error ranges for these values. All other performance metrics for dyes 3 and 4 showed a decrease in comparison to the reference.

Dyes 2a-d gave performance comparable to the reference. While 2c gave the highest PCE of these four dyes at $0.75\pm0.49\%$, it still had a reduced PCE in comparison to the reference (no dye from batch 5); 2d on the other hand, which was tested in a separate batch (batch 4), had an improved efficiency compared to its reference, $0.53\pm0.41\%$ and $0.28\pm0.24\%$. All of the performance metrics for dyes 2a-c were less than the reference apart from the V_{OC} and the FF of 2c, which were 0.35 ± 0.19 V and 53.1 ± 14.7 respectively, in comparison to 0.31 ± 0.05 V and 46.5 ± 3.0 for the reference.

2d gave an increase in the V_{OC} and FF, 0.26 ± 0.17 V and 39.3 ± 8.5 respectively, compared to the reference's 0.18 ± 0.13 V and 29.8 ± 3.5 . The J_{SC} decreased from 4.60 ± 1.24 mA cm⁻² of the reference down to 4.05 ± 0.94 mA cm⁻².

J-V Curves

All J-V curves for the as cast devices of batches 4-7 are shown in figures 5.13, 5.14, 5.15, and 5.16; the J-V curves for the annealed devices are shown in figures 5.17, 5.18, 5.19, and 5.20.

Batch 4 The J-V curves of devices of batch 4 containing no PCBM (figure 5.13 c-e)) show no photovoltaic behaviour; the curves all pass through the origin, indicating that no current is flowing out of the device when the device is short circuited ($V = 0V$). One explanation for the lack of PV behaviour is the excitons created upon photon absorption were rapidly recombined before they were dissociated into separate electrons and holes, or the separated charges recombined before they could be extracted at the contacts. Furthermore many of the J-V curves have steep gradients and do not display the typical 'L'-shape of a PV device. This non-diode behaviour indicates either a very low shunt resistance, or a very high series resistance. A low shunt resistance may suggest that there are connections between the external contacts of the device.

The J-V curves of the devices containing P3TH-NWs:PCBM (figure 5.13 a)) and P3HT-NWs:Dye 2d:PCBM (figure 5.13 b)) are more typical of a PV device. The familiar 'L'-shape of the J-V curve indicates diode behaviour, while the non-zero J_{SC} shows that the device is producing a current under illumination. Half of the 2d devices produced typical curves with some squareness, while the other half showed non-diode behaviour typical of the very high series resistance or very low shunt resistance. Some of the curves of the dye-free device were typical of a PV device but with fairly large series or low shunt resistance, where they weren't as square as a perfect diode. Others lacked typical diode behaviour.

Annealing (figure 5.17) these devices generally had the effect of increasing diode behaviour in the devices. Recombination remained the biggest issue with the non-PCBM devices. The illuminated current decreased in the dye free and P3HT-NWs:dye 2d:PCBM devices, and hence the J_{SC} s decreased, while the steepness of the curves decreased.

Batch 5 Many of the curves for the 2d devices of batch 5 (figures fig:JVbatch5 b-e)) showed good typical PV behaviour, with square curves, and current produced under illumination; a small number of each type of device showed non-diode behaviour. The dye-free device also showed good PV behaviour, with a greater maximum J_{SC} , but also a greater range of J_{SC} . The V_{OC} was slightly lower for the dye-free device, and the curves were less square; these results can be seen in the metrics table (5.3).

Annealing (figure 5.18) increased the squareness of the dye-free device, but generally decreased the squareness of the devices containing the dye 2d. The V_{OC} s increased while the J_{SC} s decreased. The decrease in the squareness suggests an increase in the series resistance, or a decrease in shunt resistance.

Batch 6 A large number of devices in batch 6 (figure 5.15) showed non-diode behaviour. PV behaviour (non zero J_{SC}) was seen in all devices. There was increasing squareness in the curves and increasing V_{OC} from devices containing dyes 2a (a), through 2b (d), to 2c (e). The working dye 4 devices (b) had curves which weren't very square, possibly having high series or low shunt resistances. The curves for devices containing dye 3 had an unfamiliar 'S'-shape.

Annealing (figure 5.19) removed all diode and PV behaviour from the type 4 dye devices. The previously described 'S'-shape of the as cast type 3 devices was removed through annealing, but this also decreased the PV behaviour of the devices. Squareness decreased in the type 2 devices, and a decrease in the diode type behaviour was seen, indicating an increase/decrease in series/shunt resistance.

Batch 7 The dye free devices of batch 7 (figure 5.16 a)) had steep curves and not much squareness, probably due to low/high shunt/series resistances. The curves for the type 1 dye devices typically had very low V_{OC} , but had better squareness than the dye free devices. The devices containing dye 1c (d) had 'S'-shape curves.

Annealing (figure 5.20) removed all diode behaviour from the type 1d devices, and removed all PV behaviour from all of the type 1 dye devices, so that J_{SC} became zero with no current flowing under illumination. The curves of the dye free devices became much more square, indicating a decrease in the series resistance and/or an increase in the shunt resistances.

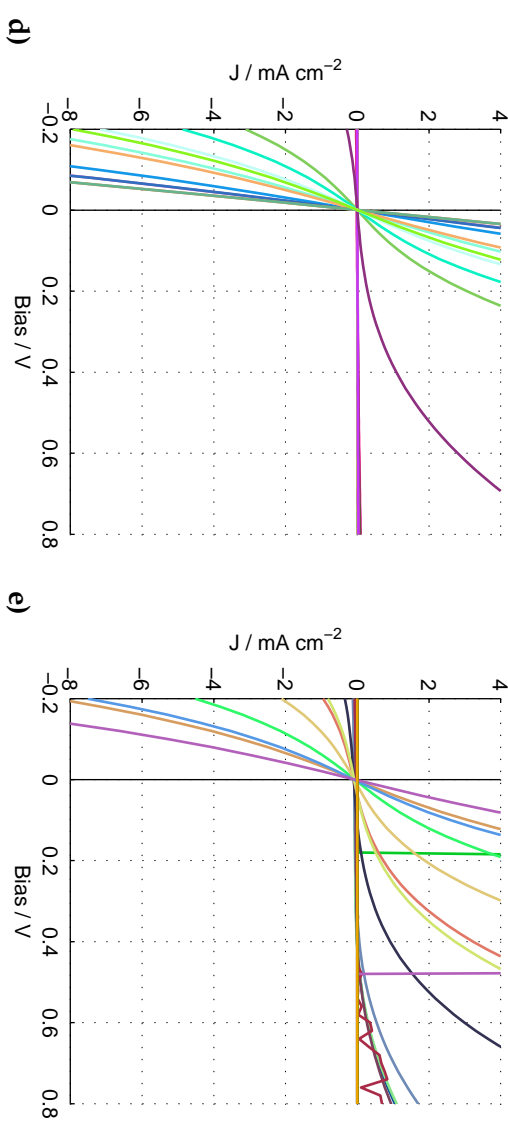
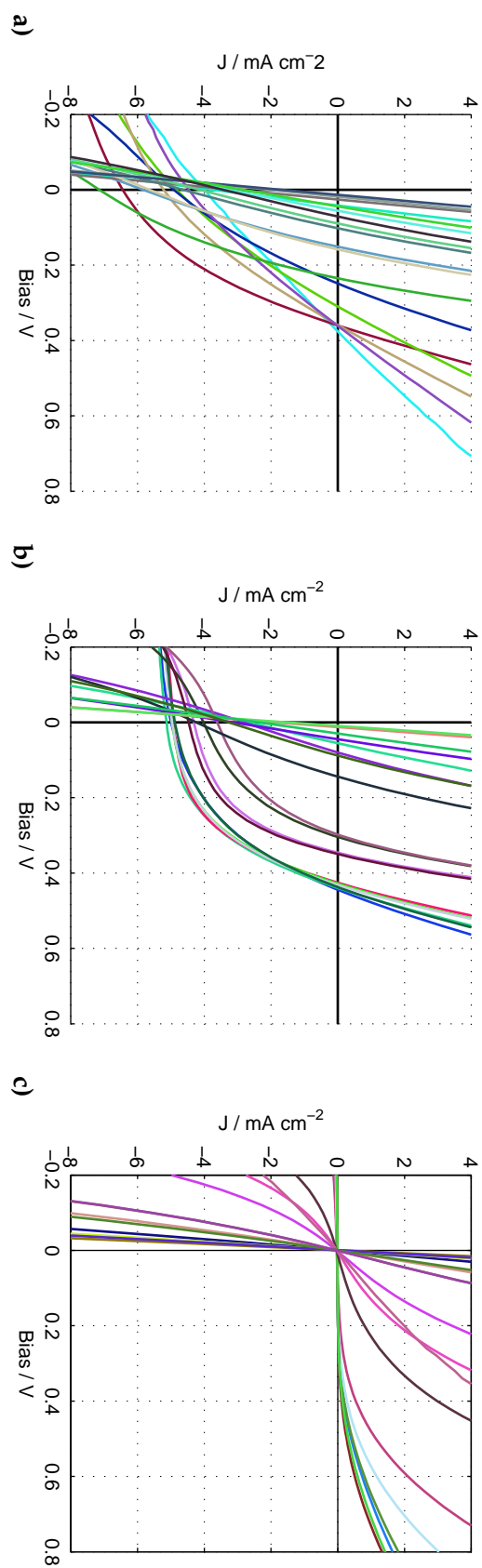


Figure 5.13: Batch 4 J-V curves

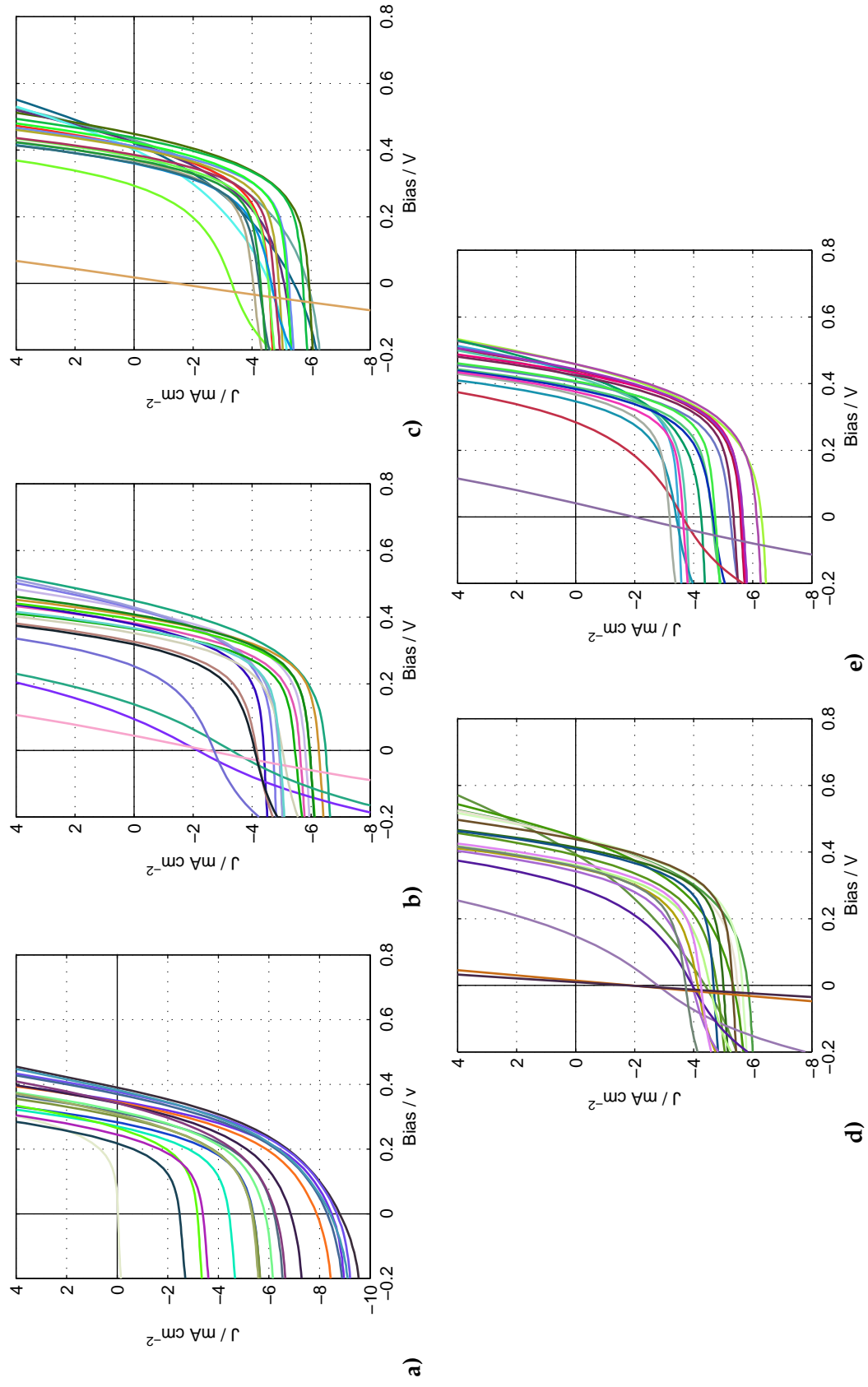


Figure 5.14: Batch 5 J-V curves

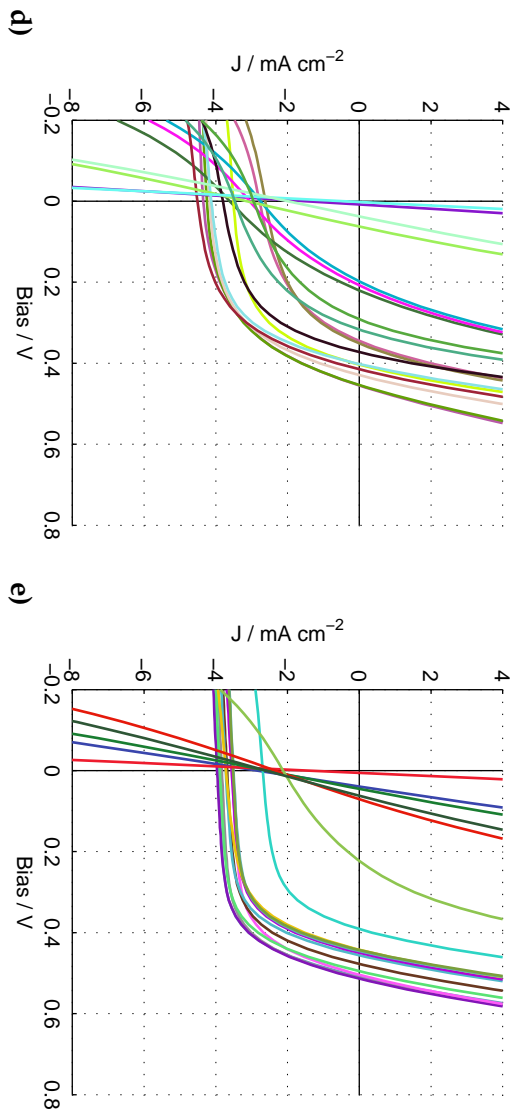
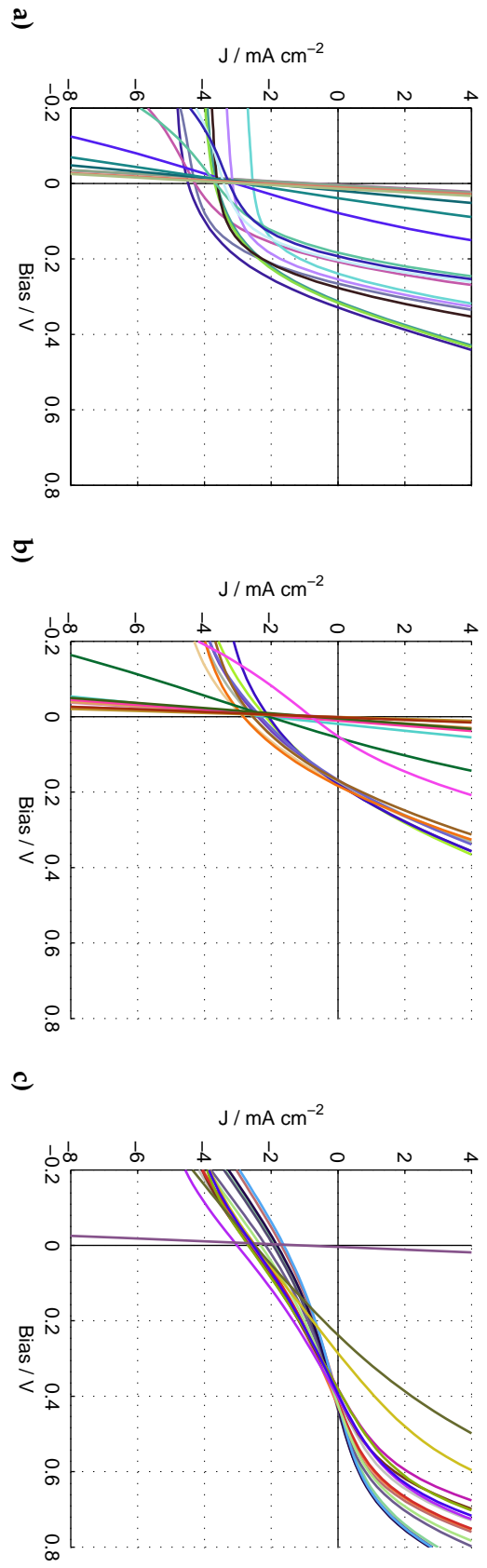


Figure 5.15: Batch 6 J-V curves

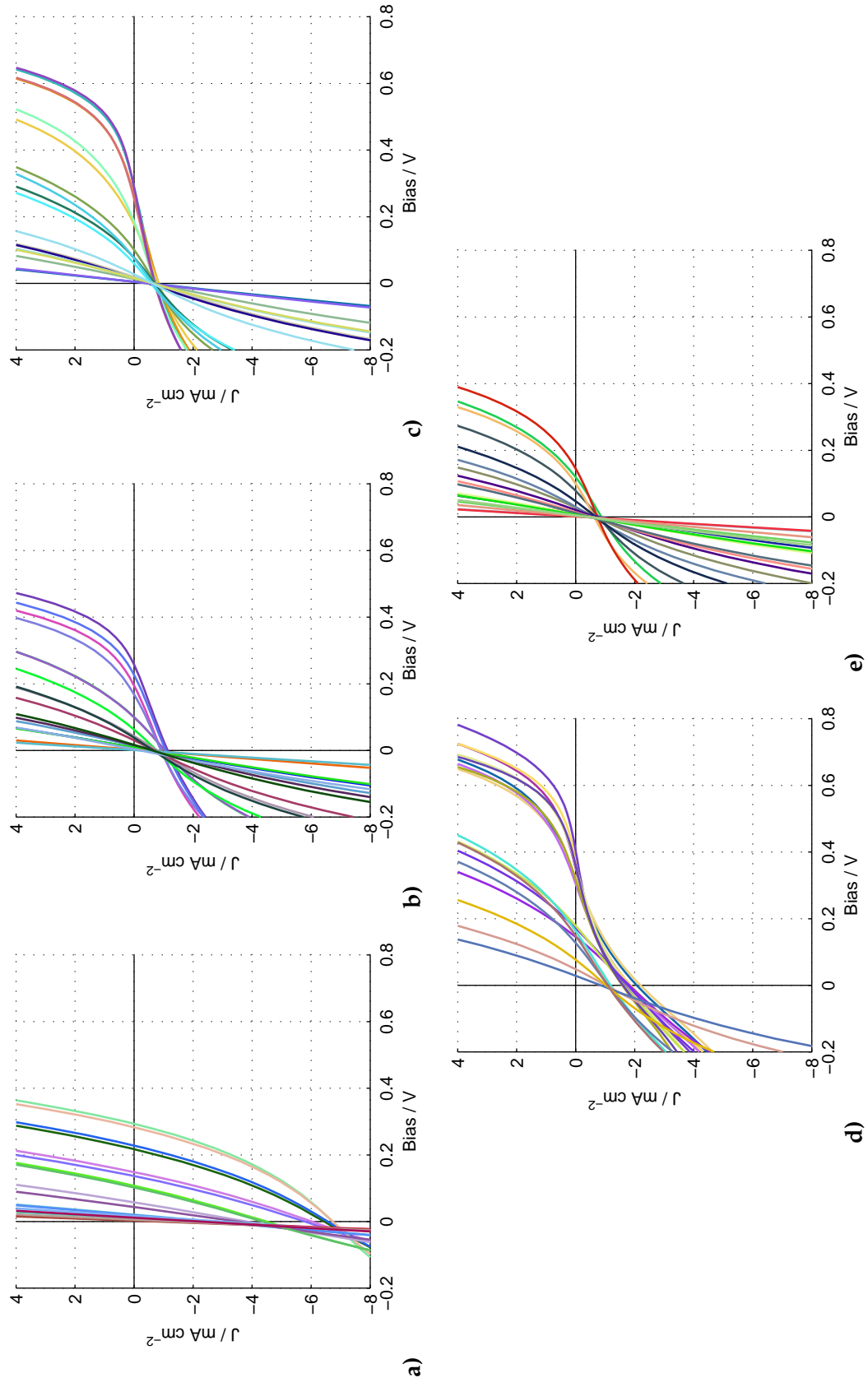


Figure 5.16: Batch 7 J-V curves

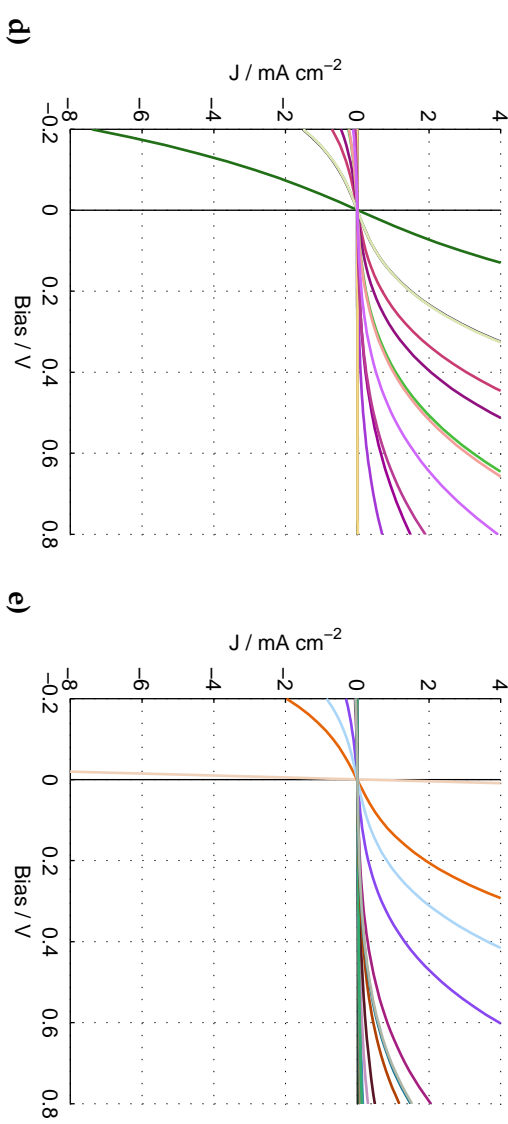
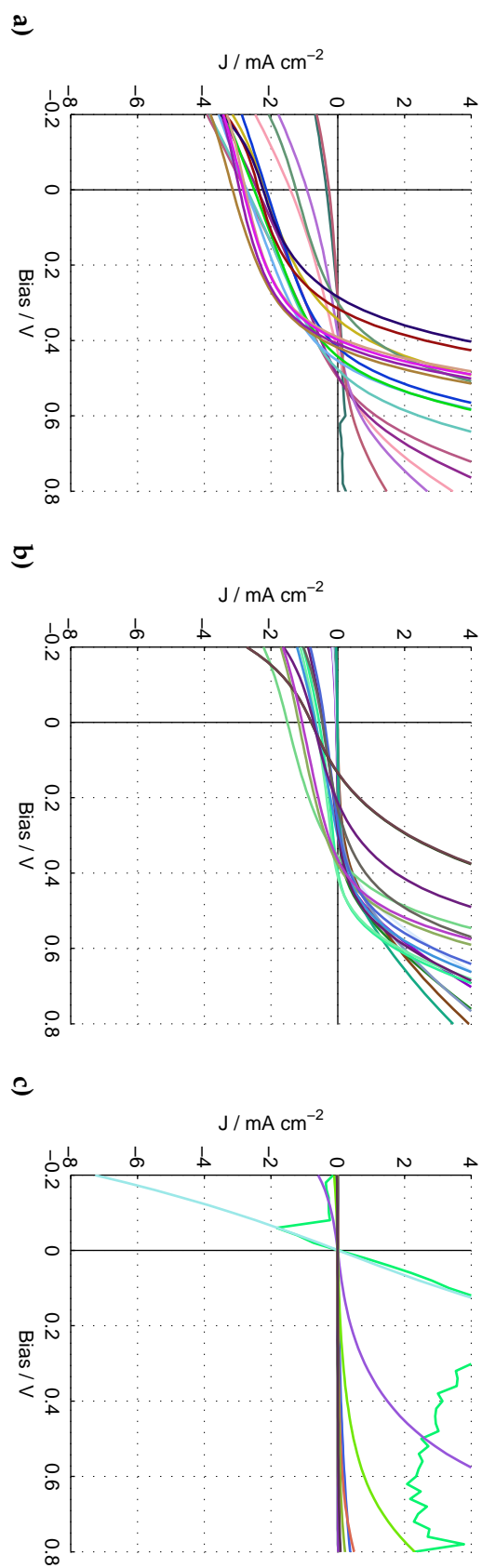


Figure 5.17: Batch 4 annealed J-V curves

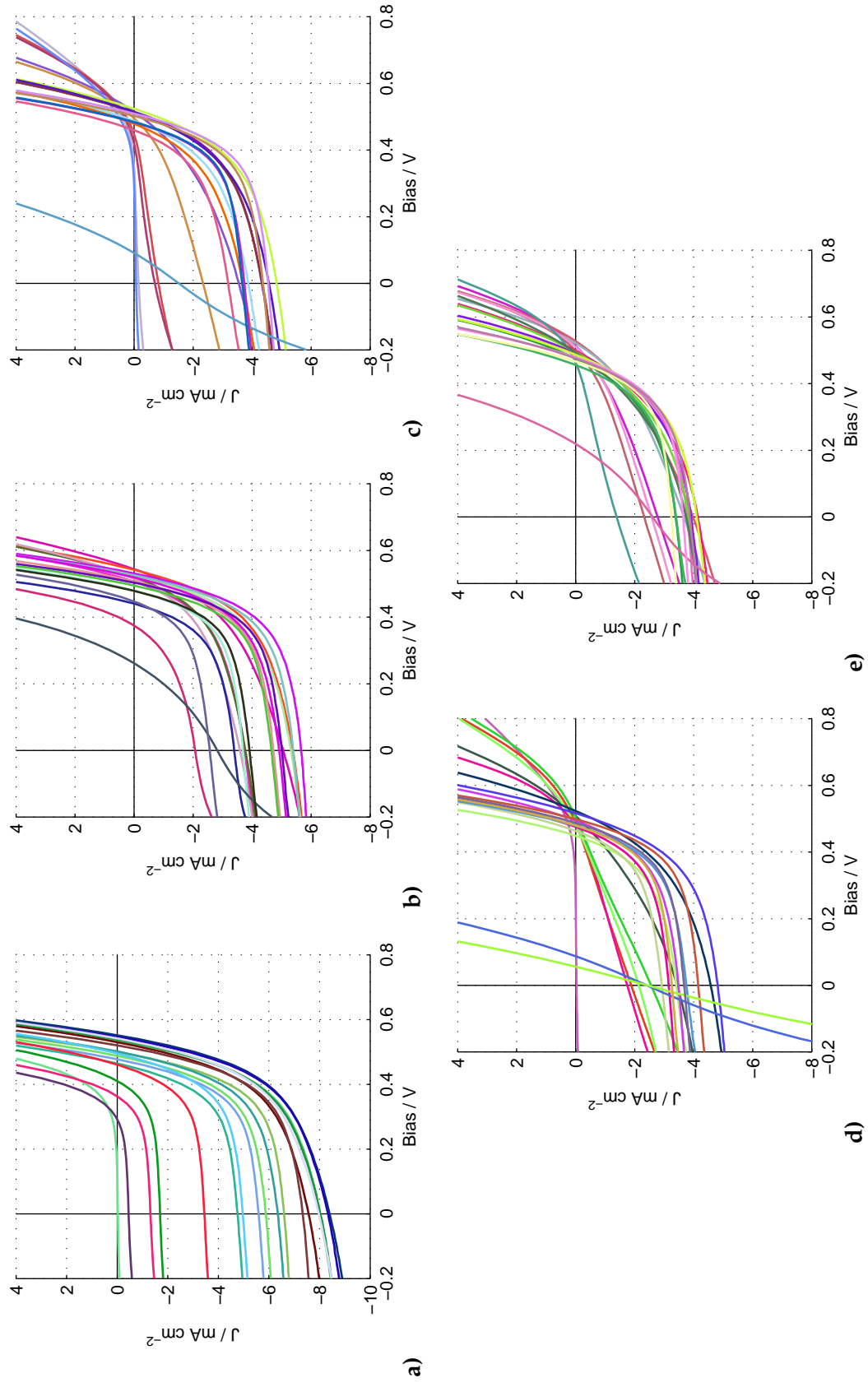


Figure 5.18: Batch 5 annealed J-V curves

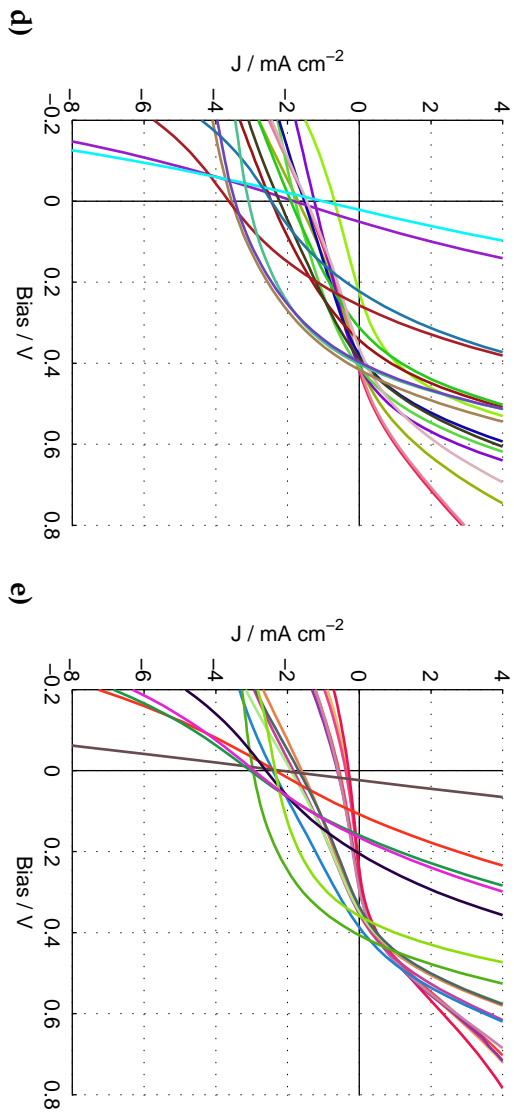
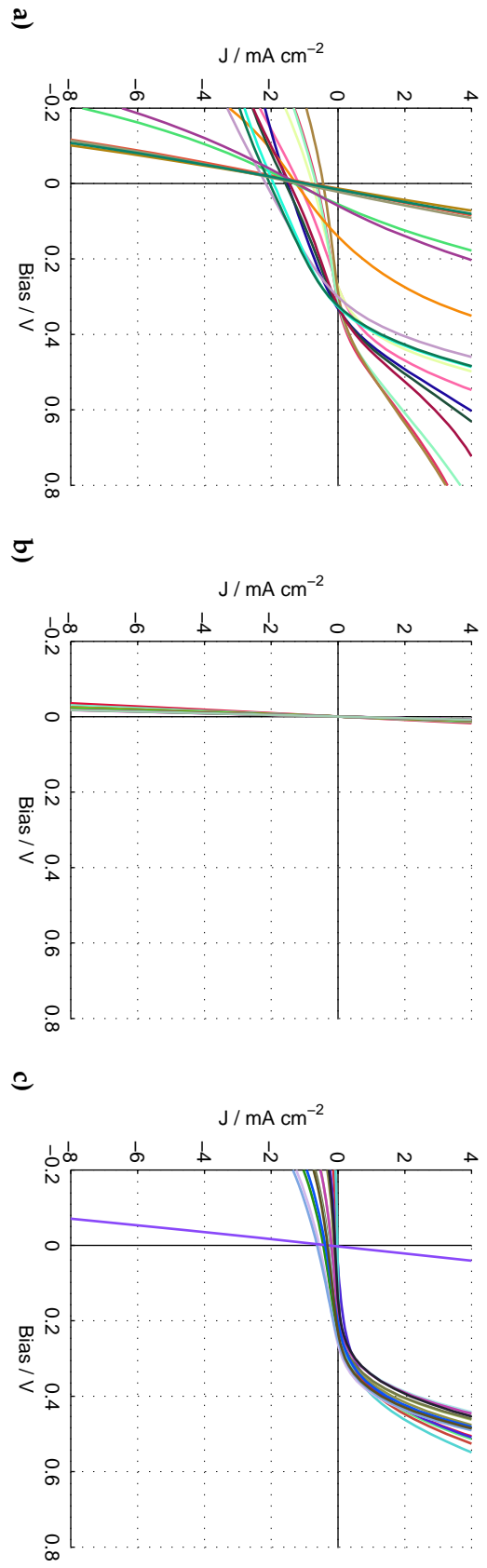


Figure 5.19: Batch 6 annealed J-V curves

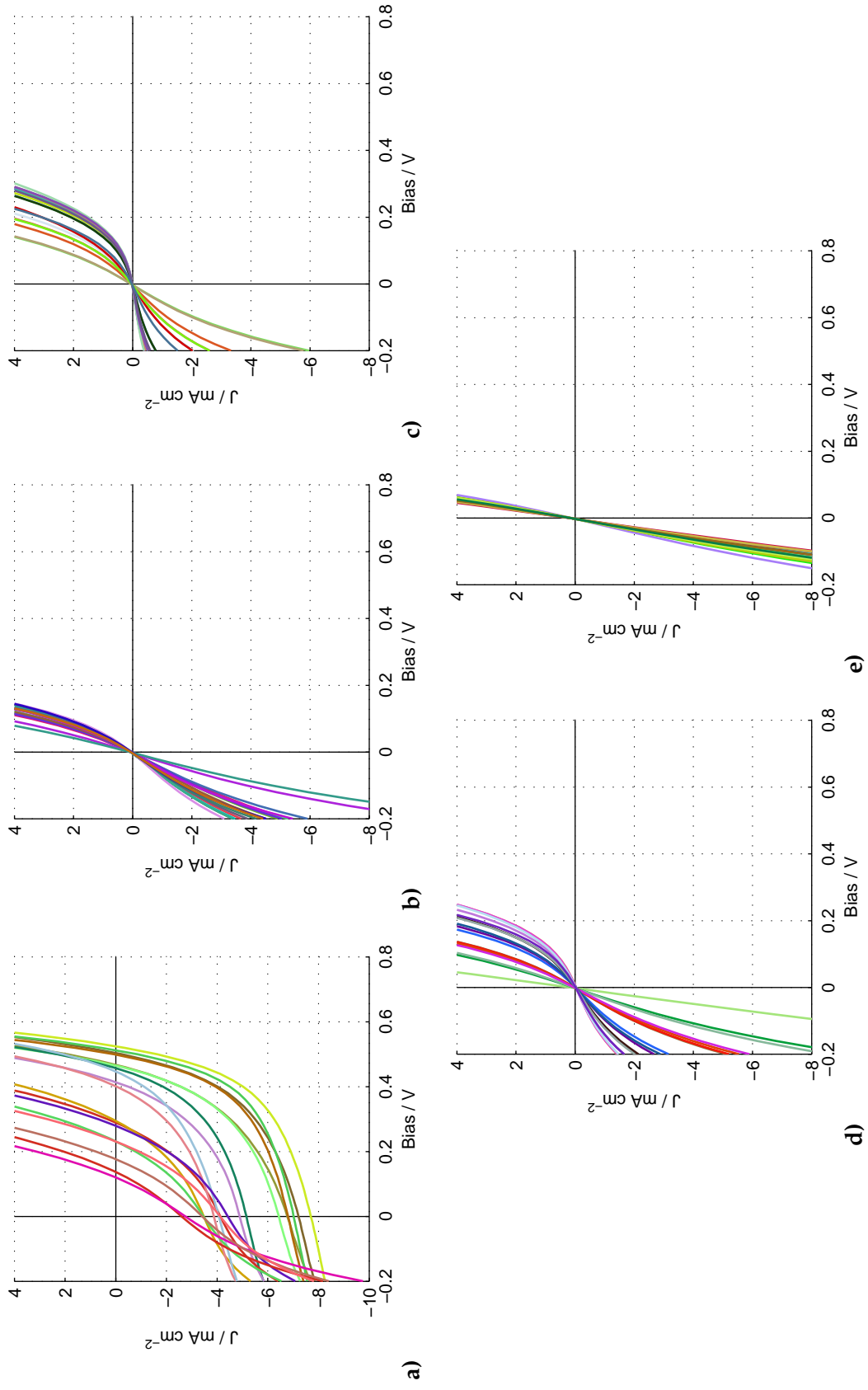


Figure 5.20: Batch 7 annealed J-V curves

Very few of the PCBM free devices produced any photovoltaic performance; it was only the devices spun at lower spin speeds that did work, and they showed very poor performance.

Annealing

Performance metrics for the thermally annealed dye intercalated OPV devices are shown in table 5.4. Devices containing no dye, and the very low loading 2d device were the only ones which showed any increase in efficiency with annealing. Increases in efficiency through thermal annealing were already seen early in P3HT-NW:PCBM devices. V_{OC} was seen to improve in the 2d devices after thermal annealing.

Annealing of the PCBM free devices of batch 4 had the effect of killing their photovoltaic performance. The performance of these devices as cast was already very poor, with efficiencies of less than 0.01 %.

Table 5.4: Annealed dye OPV performance metrics

Batch	Solution	PCE / %		V _{OC} / V		J _{SC} / mA/cm ²		FF	
		Mean	Max	Mean	Max	Mean	Max	Mean	Max
4	No Dye	0.293±0.167	0.358	0.39±0.07	0.48	2.11±0.89	3.15	33.2±8.3	44.8
	2d	0.044±0.051	0.174	0.22±0.12	0.40	0.52±0.45	1.51	28.6±5.2	43.8
	2d No PCBM	0	0	0	0	0	0	0	0
	1c No PCBM	0	0	0	0	0	0	0	0
	1a No PCBM	0	0	0	0	0	0	0	0
5	No Dye	1.47±0.82	2.37	0.46±0.11	0.54	5.37±2.84	8.40	53.3±6.43	58.7
	2d very low load	1.07±0.41	1.65	0.48±0.07	0.54	4.20±1.07	5.66	51.0±6.42	57.3
	2d low load	0.69±0.46	1.27	0.44±0.11	0.52	3.02±1.64	4.83	42.3±11.1	56.1
	2d normal load	0.61±0.40	1.24	0.42±0.14	0.52	2.99±1.14	4.82	41.7±12.8	56.6
	2d high load	0.67±0.24	0.92	0.46±0.07	0.52	3.35±0.74	4.14	41.7±8.4	55.2
6	2a	0.086±0.068	0.198	0.24±0.11	0.32	1.23±0.49	2.17	26.1±5.54	33.4
	4	0	0	0	0	0	0	0	0
	3	0.012±0.013	0.040	0.16±0.06	0.26	0.22±0.19	0.63	28.0±2.0	32.5
	2b	0.214±0.161	0.544	0.31±0.12	0.40	2.06±0.88	3.64	26.8±7.9	40.4
	2c	0.131±0.127	0.495	0.31±0.12	0.40	1.71±0.99	3.04	27.1±6.7	43.0
7	No Dye	0.856±0.649	2.037	0.35±0.14	0.52	4.91±1.66	7.70	41.2±6.8	52.5
	1a	0	0	0	0	0	0	0	0
	1b	0	0	0	0	0	0	0	0
	1c	0	0	0	0	0	0	0	0
	1d	0	0	0	0	0	0	0	0

5.5.2 Discussion

The poor performance of the type 1 dyes may have been due to shorts in the devices, where the charges produced in the blends quickly recombined. The J-V curves of these devices were typical of this process in that the J-V curves have near zero V_{OC} . The reason that this should occur in the type 1 dye devices is not understood. In the cases where the dye HOMO is above that of the P3HT it would be expected that charge trapping of the holes would occur preventing successful charge transport and producing recombination sites. This would therefore be expected in devices made from dyes 1b, 1c and 3. This therefore doesn't explain the near zero performance of dyes 1a and 1d.

The energy levels of dyes 1a and 1d are similar to 2a and 2b in that the LUMO and HOMO sit between the LUMOs and HOMOs of P3HT and PCBM; the type 2 dyes have a slightly increased band gap compared to their type 1 counterparts. Due to these similarities it is difficult to attribute the complete decline in performance of the type 1 dye devices to the positioning of the energy levels.

Meanwhile, the type 2 dye devices have an average PCE of between 0.3 and 1%, which increases relative to the dye free standard device as the HOMO deepens; Dyes 2a-c show a decline in performance compared to the dye free standard, while the dye 2d device showed a small increase in performance. Incidentally, dye 2d was the only device in which the HOMO was also deeper than that of the PCBM.

The type 2 dyes showed increasing performance with successively deepening LUMOs. However, it is unclear whether this is the cause of the performance increase. For instance, there is an improvement in performance between dyes 2c and 2d, where the difference in LUMO level is minimal.

One important aspect that hasn't been explored here that is known to possess a large influence over the performance of P3HT:PCBM OPV devices is the morphology of the blends. While no evidence of disruption of the NW formation due to introduction of the dye molecules was witnessed, the morphology of the spuncast blends may have been unfavourable for efficient charge separation and charge transport. Production of the devices had been such that the blends were made with a small excess of dye, and were not rinsed in order that a proportion of non-NW material would remain as this has been seen to be necessary for optimum performance in NW OPVs. The excess dye, although small, may disrupt the formation of a favourable morphology. In the case of dyes 3 and 4, this may be one of the key reasons for a decrease in device performance when these dyes were expected to be too bulky for intercalation to occur.

The very small amount of dye in the very low loading device may have allowed the device to operate much like a dye free device, with very little effect caused by the presence of a small amount of dye, particularly during thermal annealing.

5.6 Conclusions

P3HT-NW:PCBM OPV devices achieved a maximum performance when the deposition temperature of the active blend was 60°C. Thermal annealing of these devices improved all aspects of their performance apart from the J_{SC} which showed a small decrease. The maximum efficiency of a P3HT-NW:PCBM OPV was $1.52 \pm 0.28\%$ at an active blend deposition temperature of 60°C, and after thermal annealing.

These results confirm that which is seen in the literature and suggests

that a quantity of non-NW material is required in the active blend, possibly to act as a filler between the NWs and producing contiguous pathways to the electrodes, and hence efficient charge extraction.

PQT-12-NW:PCBM OPV devices achieved a maximum performance when the deposition temperature of the active blend was 60°C. Thermal annealing of these devices increased V_{OC} , decreased J_{SC} slightly and left PCE and FF largely unchanged. The maximum efficiency of a PQT-12-NW:PCBM OPV was 0.16 ± 0.08 % for an as cast device at an active blend deposition temperature of 60°C. The PCE was lower than that of P3HT by a factor of 10. Review of the literature suggests that the blend composition should be adjusted by increasing the ratio of PQT-12 to PCBM to compensate for the imbalanced charge transport in the two materials, therefore decreasing space charges and recombination.

PQT-12-NW devices outperformed their film counterparts by a 4-fold increase in PCE, and gave improved V_{OC} , J_{SC} and FF.

The doping of the NWs led to a small increase in efficiency of an OPV device fabricated using a dye intercalated-P3HT-NW:PCBM blend, where the 2d intercalated NW device gave an as cast PCE of 0.533 ± 0.413 % compared to the dye free P3HT-NW:PCBM standard device which had a PCE of 0.282 ± 0.245 %. It was difficult to ascertain from these results what led to an increase in the efficiency of the devices produced with this particular dye, although the dye had a significantly lower HOMO than all of the other dyes and it was also lower than that of the PCBM. Typically it would be expected that having a lower HOMO than that of the PCBM would cause holes to be trapped on the dye and lead to recombination and a drop in performance, so further investigation would be needed to elucidate the processes that are causing the increased PCE here.

While initial performance results from dye intercalated devices were not overly positive, fine tuning of the dye molecules could yield improved results. Further refinement in the experimental procedure, such as isolation of the separate blend components into dye-intercalated NWs, non-crystalline P3HT, and PCBM, followed by controlled mixing may allow for greater control over the composition and morphology of the blend improving the likelihood that the dye stays intercalated into the NWs.

The key point of this chapter was that a novel and facile form of P3HT doping was achieved via intercalation of dye molecules into P3HT NWs during the first step of processing. Indirect evidence for intercalation was provided for emission spectroscopy and combustion analysis of centrifuged and rinsed dye intercalated-NWs. As noted previously, single NW polarised luminescence studies were not available to test unambiguous intercalation. However, anthraquinone are known to intercalate intensively in DNA[14]. Furthermore, dye intercalated P3HT NWs could hold potential in other applications such as sensors where the dye is designed to add analyte specificity.

Bibliography

- [1] NREL. Reference solar spectral irradiance: Air mass 1.5. url-
<http://rredc.nrel.gov/solar/spectra/am1.5/>, 2012. [Online; accessed
14-May-2012].
- [2] O'Regan B and Grätzel M. A low-cost, high-efficiency solar cell based
on dye-sensitized colloidal TiO_2 films. *Nature*, 353(6346):737–740, 1991.
- [3] Tennakone K, Kumara G R R A, Kumarasinghe A R, Wijayantha K G
U, and Sirimanne P M. A dye-sensitized nano-porous solid-state pho-
tovoltaic cell. *Semiconductor Science and Technology*, 10(12):1689, 1995.
- [4] O'Regan B and Schwartz D T. Large enhancement in photocurrent effi-
ciency caused by UV illumination of the dye-sensitized heterojunction
 $\text{TiO}_2/\text{RuLL'NCS}/\text{CuSCN}$: initiation and potential mechanisms. *Chem-
istry of Materials*, 10(6):1501–1509, 1998.
- [5] Bach U, Lupo D, Comte P, Moser J E, Weissörtel F, Salbeck J, Spreitzer H,
and Grätzel M. Solid-state dye-sensitized mesoporous TiO_2 solar cells
with high photon-to-electron conversion efficiencies. *Nature*, 395:583–
585, 1998.
- [6] Machui F, Rathgeber S, Li N, Ameri T, and Brabec C J. Influence of a
ternary donor material on the morphology of a P3HT:PCBM blend for
organic photovoltaic devices. *Journal of Materials Chemistry*, 22:15570–
15577, 2012.
- [7] Fu H, Choi M, Luan W, Kim Y-S, and Tu S-T. Hybrid solar cells with an
inverted structure: Nanodots incorporated ternary system. *Solid-State
Electronics*, 69(0):50 – 54, 2012.
- [8] Markus Koppe, Hans-Joachim Egelhaaf, Gilles Dennler, Markus C.
Scharber, Christoph J. Brabec, Pavel Schilinsky, and Claudia N. Hoth.
Near ir sensitization of organic bulk heterojunction solar cells: Towards
optimization of the spectral response of organic solar cells. *Advanced
Functional Materials*, 20(2):338–346, 2010.

- [9] Jones J E, Kariuki B M, Ward B D, and Pope S J A. Amino-anthraquinone chromophores functionalised with 3-picolyl units: structures, luminescence, DFT and their coordination chemistry with cationic Re(i) di-imine complexes. *Dalton Transactions*, 40:3498–3509, 2011.
- [10] Berson S, De Bettignies R, Bailly S, and Guillerez S. Poly(3-hexylthiophene) fibers for photovoltaic applications. *Advanced Functional Materials*, 17(8):1377–1384, 2007.
- [11] Bertho S, Oosterbaan W D, Vrindts V, D’Haen J, Cleij T J, Lutsen L, Manca J, and Vanderzande D. Controlling the morphology of nanofiber-P3HT:PCBM blends for organic bulk heterojunction solar cells. *Organic Electronics*, 10(7):1248 – 1251, 2009.
- [12] Wantz G, Lefevre F, Dang M T, Laliberte D, Brunner P L, and Dautel O J. Photovoltaic solar cells using poly(3,3-didodecylquaterthiophene). *Solar energy materials and solar cells*, 92(5):558–563, May 2008.
- [13] Thompson B C, Kim B J, Kavulak D F, Sivula K, Mauldin C, and Fréchet J M J. Influence of alkyl substitution pattern in thiophene copolymers on composite fullerene solar cell performance. *Macromolecules*, 40(21):7425–7428, 2007.
- [14] Guin P S, Das S, and Mandal P C. Interaction of 1,4-dihydroxy-9,10-anthraquinone with calf thymus dna: A comparison with anthracycline anticancer drugs. *Journal of Solution Chemistry*, 40:492–501, 2011.

Chapter 6

Organic Field-Effect Transistors and Sensing

6.1 Introduction

In this chapter organic-field effect transistors (OFETs) produced using P3HT and PQT-12 nanowires, and novel nanowire water-gated OFETs are characterised; this is then followed by exploratory work on the NWs response to octylamine vapour and humidity where it was seen that the conductance of P3HT NWs decreases in the presence of octylamine, and increases in the presence of humidity with a greater response than that of a P3HT film. The work in this chapter was carried out with assistance from Antonis Dragoneas, and Abdullah Al Naim of Martin Grell's research group at Sheffield University.

6.1.1 Publications

One manuscript has been published and one further manuscript has been submitted for review as a result of work completed as part of this chapter:

- A. Al Naim, R.T. Grant, A. Dragoneas, A. Hobson, **M. Hampton**, C. Dunscombe, T. Richardson, J.E. Macdonald, and M. Grell. Water-gated organic nanowire transistors. *Organic Electronics*
- A. Dragoneas, M. Grell, **M. Hampton**, J.E. Macdonald. Morphology-driven sensitivity enhancement in organic nanowire chemiresistors. *Sensor Letters* Under review.

6.1.2 Background to Sheffield Group Research

The research team at Sheffield University, headed by Martin Grell, has a focus on building odour sensing OFETs[1]. Their interest has been in producing organic sensors with two main areas of focus: building a hand held sensor with real-time feedback, utilising organic materials as the active component in the sensor[2]; and sensing water-borne analytes using water-gated OFETs.

The requirement of a real-time feedback system that could operate from a small hand-held device led to the design of the test circuit shown in figure 6.1. A small-scale version of this circuit means that it is of a size that can fit in a hand-held device while also requiring only a small power source, such as a 9V battery. This does away with the traditional OFET testing equipment of a large voltage source and current sensor for the source-drain and a voltage source for the gate.

The circuit (figure 6.1 maintains the gate and drain at ground, while applying an oscillating signal to the source, which in effect keeps the device working in the saturation regime. The output signal is amplified and fed to an oscilloscope; there is a feedback resistor to maintain a setpoint output voltage. The maintenance of a setpoint voltage using a variable resistor is in contrast to the usual method of measuring $I(V)$ with known gain settings,

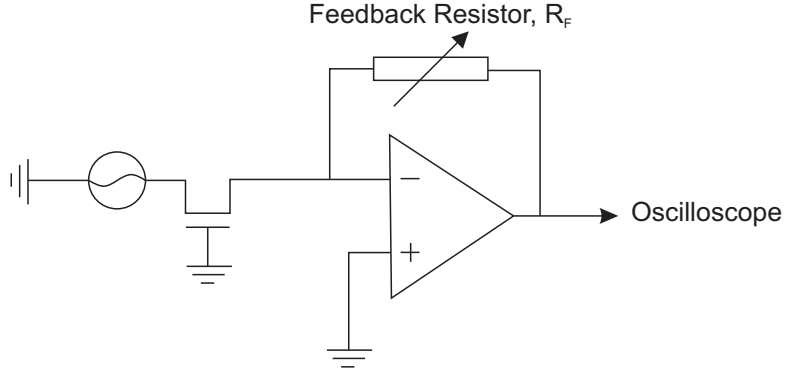


Figure 6.1: Schematic of OFET test circuit, in which the gate and the drain biases are held at ground and a signal is applied to the source contact of the OFET. The output signal from the drain is fed to an oscilloscope via an op-amp and feedback resistor.

and is purely aesthetically motivated. Sample plots from this circuit set up are shown in figure 6.2, where a sinusoidal input signal was applied to the source in a) and a square wave in b).

From the output signal it is possible to extract the threshold voltage V_T , which is the input voltage at the point at which the output voltage begins to increase from zero (figure 6.3 a)). Physically V_T marks the bias at which sufficient charge carriers have accumulated and the traps along the channel are filled such that charge carriers can move between the source and drain under a source-drain bias. The resistance of the sample can be extracted from the output data and from knowing the feedback resistance of the circuit; if the device geometry is known, the conductance of the active material can be calculated.

The mobility can be calculated from the output using the following equation,

$$\mu C_i = \frac{2L}{WR} \frac{|V_p|}{(V_{max} - |V_T|)^2} \quad (6.1)$$

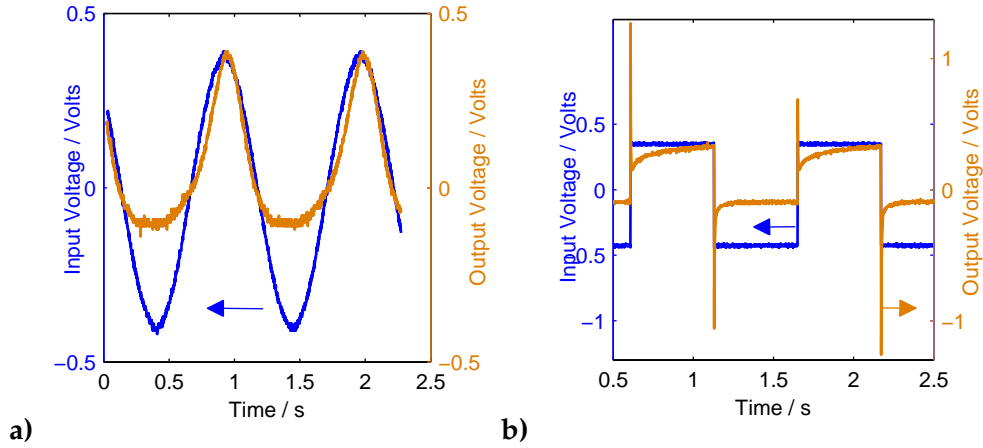
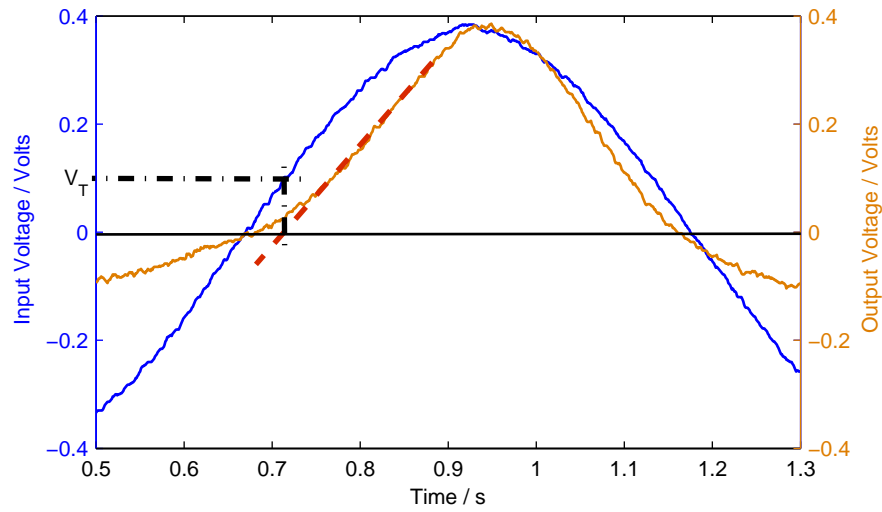


Figure 6.2: Example OFET test circuit outputs. a) sinusoidal input, b) square-wave input.

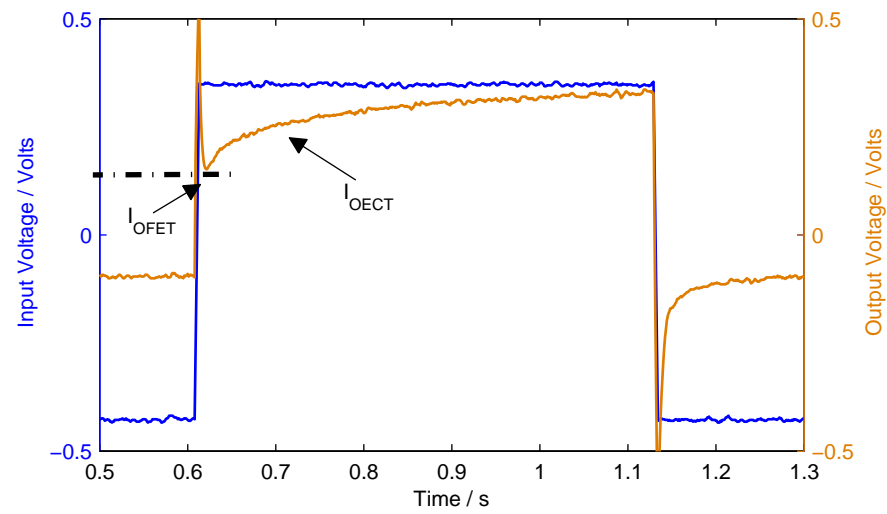
where V_p is the maximum output voltage, V_{max} is the maximum input voltage, V_T is the threshold voltage, L and W are the channel length and width respectively, R is the feedback resistance and C_i is the capacitance per unit area of the gate dielectric. In reality, it is difficult to calculate the mobility for a NW device due to the unknown fill-factor of the channel due to the 'mesh' morphology of the NW film.

Upon applying a square wave to the water-gated OFETs the output signal consists of two portions; one is the contribution from the field-effect (I_{OFET}), and is the initial rise in output voltage, and the second portion is the electrochemical effect due to the redox of the semiconductor (I_{OECT} , which is the second curved portion of the output voltage (figure 6.3 b)).

One of the other important features of the Grell OFETs is the gate and gate dielectric material and processing, which allows for operation of the device with low source-drain, and gate voltages, which in turn reduces power consumption of the device[3, 4]. The gate/dielectric is composed of Al:Al₂O₃, and is grown electrochemically via an anodising process, at a bias



a)



b)

Figure 6.3: Example data extraction from OFET output graphs.

of approximately 5V, with a dielectric thickness of circa 5nm. The device can be successfully operated with single figure biases on the source-drain and the gate. Breakdown of the dielectric will occur if the field about the dielectric exceeds the bias used to grow it, in this case approximately 5V. One further advantage of this process is that the anodised films are pinhole-free, homogeneous oxide layers of a precisely controlled thickness; the lack of pinholes prevents shorts through to the gate, and the homogeneity ensure a highly uniform gate electric field.

6.1.3 Exposure Effects of Air on Polythiophenes

Polythiophenes have been known to be affected by ambient air[5, 6]; water and molecular oxygen are the two main components that the effects have been attributed to. Both P3HT and PQT-12 have also shown a conductivity change in response to variety of inorganic and organic volatile chemicals[7, 8, 9]. While these effects need to be avoided in high performance organic electronic devices, such as OFETs, and can be avoided to some extent via encapsulation of the device[10], response to humidity, oxygen, and organic and inorganic volatile chemicals[11] can be used to build a useful sensor. These previous investigations have been performed on thin films. Here we investigate the use of nanowires of these polymers as the active component in vapour and liquid sensors, motivated by the possibility of faster response or higher sensitivity arising from their larger surface to volume ratio.

Humidity

P3HT FETs show a large increase in off-state conduction, and deterioration in the saturation behaviour when exposed to humidity[7], this is in contrast to the near unchanged behaviour of operation under an N₂ atmosphere, and

the small increase in conductivity and slight drop in field-effect mobility upon exposure to O₂.

Hoshino [7] believed that moisture affects the conductance of the P3HT via adsorption on to the surface of the semiconducting layer, where the large dipole moment of the water molecules then generate holes, and increase the number of free charge carriers. This process is used to explain the resultant increase in the off-current and lack of saturation of the FET devices exposed to moisture, as the drain current is now dominated by charge carriers moving along the upper surface of the semiconducting region rather than through the gate-controlled channel. This would also correlate with the results of top gate P3HT devices of Rost et al[12] which showed little degradation under ambient conditions and normal saturation behaviour, suggesting that the gate and dielectric were preventing the water molecules from adsorbing to the surface of the semiconductor between the electrodes.

In contrast to the Hoshino study reported above, when Knorr[13] looked at P3HT sandwiched between Cu bottom electrodes and Au top electrodes and subsequently operated under increased humidity, they found that the after removal of the P3HT the Cu electrode had become pitted, suggesting that water had been absorbed into the polymer and electrochemical reactions had taken place. Knorr found a 1.2% relative weight increase of the P3HT film under 91% relative humidity, due to the water.

Humidity has been shown to decrease the field-effect mobility and increase the rate of trapping of charge carriers in PQT-12 TFTs[14], where this effect has been attributed to the interaction of the absorbed water with the charge carriers in the film.

Leary[15] performed quantum calculations of the specific interactions between water and oligothiophenes that explained how water vapour effec-

tively gates thiophenes; a phenomenon that is not commonly observed when humidity interacts with other organic semiconductors. A solvation-shell was formed around the thiophenes, which shifted the electron transport resonances, greatly increasing the conductance.

Oxygen

The effect of oxygen on polythiophenes is not a simple one; three mechanisms reduce fluorescence of P3HT upon exposure to oxygen: collisional quenching, polymer-oxygen CTC formation, and polymer photo-oxidation[16, 17]. These processes may also be responsible for changes in conductance when exposed to oxygen. It has also been seen that ozone in the ambient atmosphere, rather than O_2 , acts a dopant to PQT-12, P3HT and well as other polythiophenes[18], by forming a complex with the polythiophene which acts as a shallow acceptor. Chabinye[18] showed exposure to ambient air, and ozone increased the off-state current and threshold voltage (more positive), while purified air, free from ozone, gave no changes.

Effects of Further Analytes

A number of studies have looked at polythiophenes as sensors for inorganic and organic compounds[19, 20, 21, 22, 23].

6.1.4 Water-Gated OFETs

Water-gated OFETs[24, 25, 26] (schematic shown in figure 6.4)have developed from electrolyte-gated OFETs (EGOFET), via the ion-sensitive OFET (ISOFET), which was an adaptation of the organic electrochemical transistors (OECT) first developed by Wrighton et al[27].

Kergoat introduced water-gated OFETs in 2010[24]. Water-gating an OFET has the advantage over using an electrolyte, is that it is suitable for use with biomolecules. These devices operate through a potential range such that no electrochemical doping or electrolysis of water occur, while the threshold potential of the device can be tuned by changing the work function of the gate electrode.

So far it has been shown that water-gated devices can be used to detect DNA[25]. A carboxylic derivative acid derivative of P3HT was used as the semiconductor, which allowed for direct attachment of biomolecules. DNA strands were immobilised onto the semiconductor, and led to a significant drop in the drain current of nearly two orders of magnitude and a drop in the threshold voltage. These effects were attributed to prevention of ion-penetration into the semiconductor bulk.

Using an electrolyte as the gating medium leads to screening of the biomolecules by the cations due to electrostatic interaction; this effect was seen in the experiments of Kergoat et al when the water-gate was replaced by an electrolytic medium.

Currently nanowires have not been used in water-gated OFETs, it is believed here that the nanowires will have a greater, more rapid response to an analyte compared to a film due to the larger surface area of the NWs.

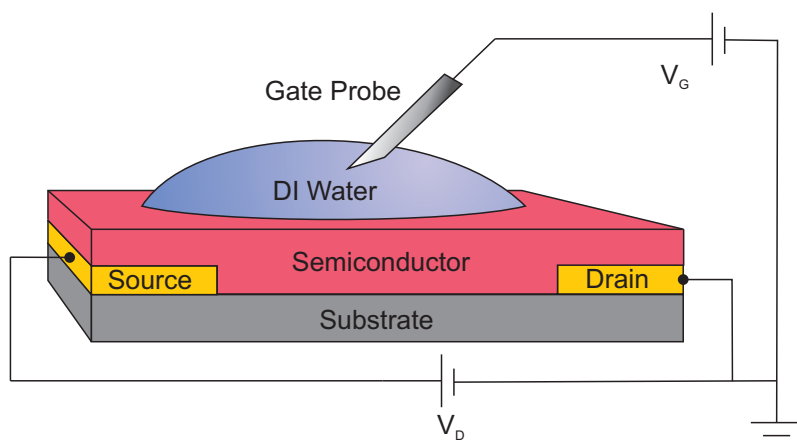


Figure 6.4: Schematic of water-gated OFET

6.2 Experimental

6.2.1 Device Preparation

Au top-contact, Al:Al₂O₃ bottom-gate transistor devices were fabricated on silicon substrates. The Al:Al₂O₃ gate was anodised using a constant current density of 5 mA/cm² up to an anodisation voltage of 5 V in a 1nM citric acid solution[3, 4]. The polythiophene was then spincoated or dropcast on to the substrate, and then Au top contacts separated by a 10μm channel were evaporated.

Organic nanowires were produced using the whisker method[28]. 5.2mg of P3HT was fully dissolved in 1.0ml of anisole solvent and heated to 70°C, before being allowed to cool to room temperature.

6.2.2 Environment Control System

The environment control system for humidity and octylamine sensing measurements is shown in figure 6.5. The measurements were carried out in a sealed chamber with an inlet line with mixer and an outlet. Dry nitro-

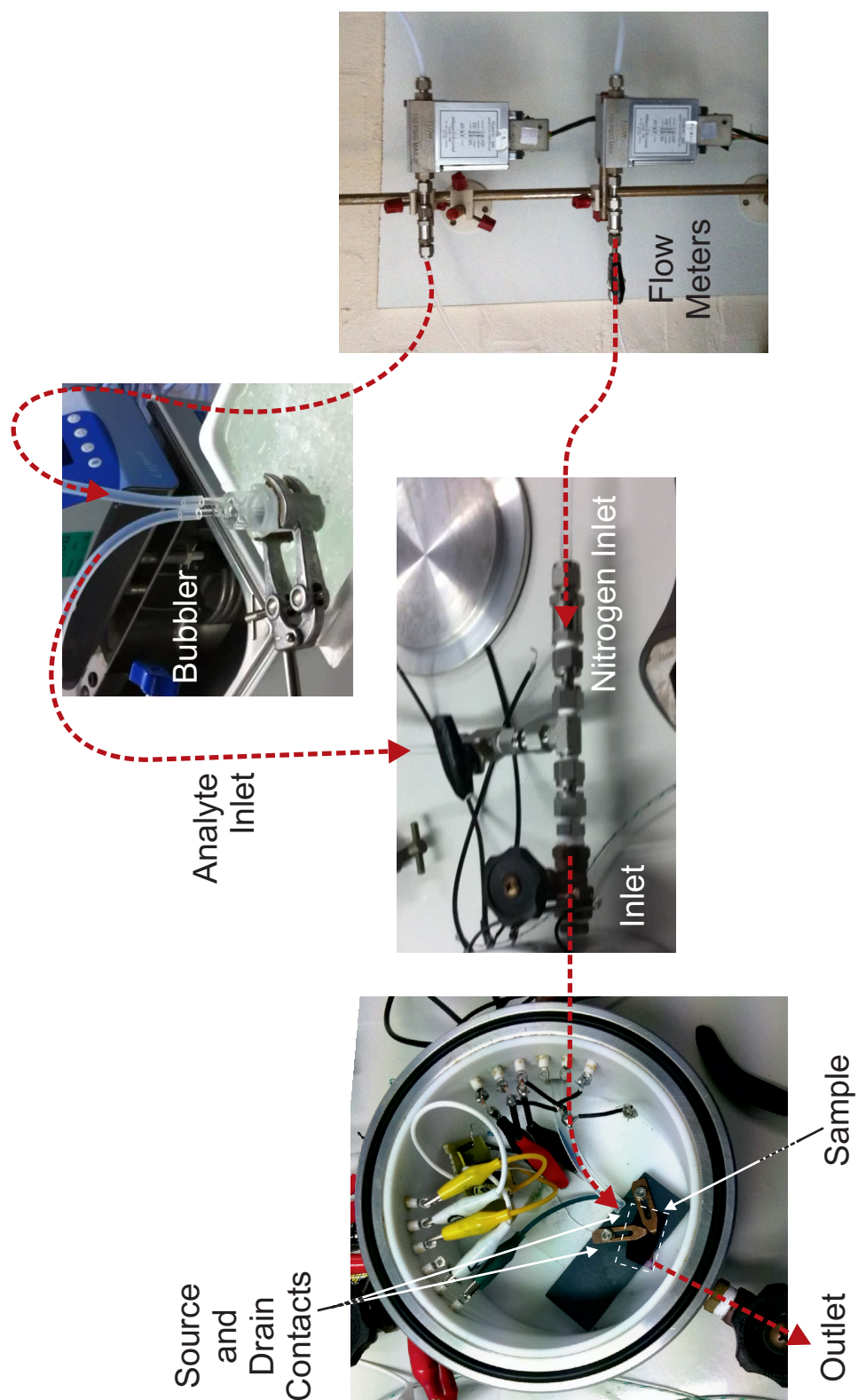


Figure 6.5: Diagram of the gaseous analyte environment control system set-up. Two flow rate meters allowed for controlled ratios of N_2 to analyte infused N_2 . The analyte line fed N_2 through a temperature controlled bubbler containing the analyte. The two flow lines were then mixed before passing through the inlet valve into the sealed chamber via a tube placed millimetres from the sample. An outlet valve allowed for continual flow of the inlet gas.

gen was flowed through one line, and was mixed with dry nitrogen that had been passed through a bubbler containing temperature regulated de-ionised water. Adjustments of the flow rates allowed for controlled analyte levels flowing into the sealed chamber. For the octylamine experiments the bubbler was kept at 0°C, at which temperature the vapour concentration is known to be 360ppm, this was then diluted further by controlled mixing with the pure N₂ line. For the humidity experiments the bubbler was held at 25°C. A Honeywell HIH-4010 commercial humidity sensor was placed inside the chamber as a reference to accurately measure the humidity.

6.2.3 Device Characterisation

Characterisation of the devices was carried out using the circuit shown in figure 6.1) and as used by Hague[29]. The circuit consisted of: a signal generator applying a sinusoidal input voltage to the source contact of the device; an op-amp connected to the drain contact of the device via its inverting input; the op-amp output connected to an oscilloscope via a current to voltage converter; a feedback resistor between the inverting input and output of the op-amp; and the device gate and the non-inverting op-amp input connected to ground. To connect with the gold contact pads of the device, tungsten needles were dropped on to the source and drain contact pads using Karl Süss probeheads, and a third needle was dropped on to the gate electrode.

Heating

During general characterisation of the devices and during the heating experiments, a sinusoidal input voltage was applied to the source contact while the drain and gate remained effectively grounded. This technique had the effect of operating the device constantly in the saturation regime.

During heating experiments the device was placed onto a hotplate. The temperature of the hot plate was increased up to 100°C at a rate of 10°C/min, in increments of 10°C, and held at each temperature point for 1 minute before recording a resistance measurement. The device was then cooled using the same process. The threshold voltage was taken from the onset of output voltage from the device, as depicted in figure 6.3. Second order polynomials were fitted to the resistance data in the increasing temperature regime, the decreasing temperature regime, and the combined increasing and decreasing temperature regime.

Octylamine and Humidity Sensing

The characterisation of the devices was carried out in the same manner as for the heating experiments apart from the disconnection of the gate electrode. This meant that the device was now operating as a resistor-sensor rather than as a gated OFET.

The reason for this was due to the design of the environment chamber not having sufficient connections to allow connection to the gate contact. Devices were chosen for the environment chamber experiments such that their initial resistance was low enough so that a measurable signal could be detected.

Transconductance was calculated from the peak output voltage divided by the product of the feedback resistor and the peak input voltage, ie. the ratio of the output current to the input voltage.

WGOFET

As with the dry OFET test, the WGOFETs source and drain pads were contacted by dropping two tungsten needles on to them using Karl Süss probe-

heads. A droplet of de-ionised water was applied over the channel region using a microlite syringe, and was then contacted via a third tungsten needle and probe. Either a sinusoidal or a square wave input voltage was applied to the source contact, and the drain and gate contacts were effectively grounded.

6.3 Results

6.3.1 Dry-gated OFETs, and Chemiresistor Sensors

P3HT-NW Resistor Heating

Figure 6.6 shows the resistance of a P3HT NW resistor device that was heated and cooled at a rate of approximately $10^{\circ}\text{C}/\text{min}$. The device resistance change is quadratic with temperature with a minimum of $5.2 \pm 0.1 \text{ M}\Omega$ at 65°C , rising from an initial resistance at room temperature of $17.0 \pm 0.1 \text{ M}\Omega$, and reaching $14.0 \pm 0.1 \text{ M}\Omega$ at 100°C , the maximum the device was tested at. There is some hysteresis in the resistance of the device under cooling, with lows in the resistance of $11.6 \text{ M}\Omega$ at 80°C , and $11.8 \text{ M}\Omega$ at 65°C .

During the heating and cooling measurements of the threshold voltage were taken, although there was no correlation between the V_T and the temperature of the device.

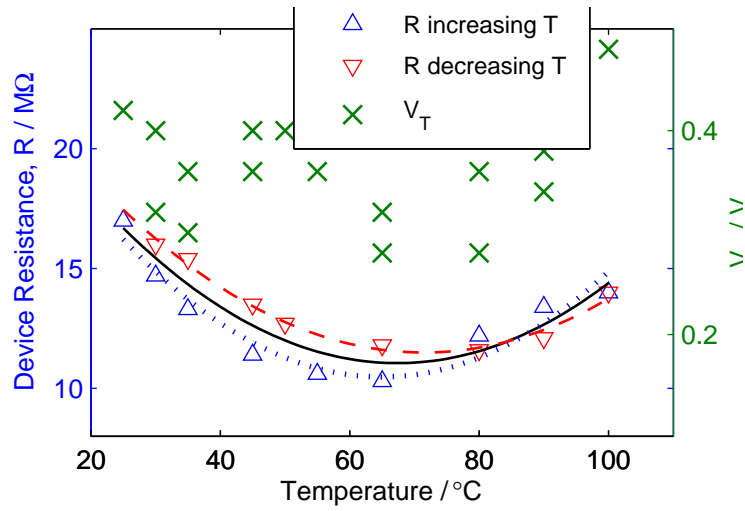


Figure 6.6: Device resistance and V_T response during heating of a P3HT NW OFET device. The dashed curve is the fit to the decreasing temperature points, the dotted curve is the fit to the increasing temperature points and the solid line curve is the fit to all temperature points. There appears to be no correlation between V_T and the temperature of the device. There is a quadratic response to R_F , and the decreasing T points show hysteresis in the curve.

P3HT-NW Chemiresistor Octylamine Sensing I

Preliminary experiments involving an octylamine soaked cotton bud suggested that P3HT NW OFET devices showed an increase in resistance R , during exposure to the odour. Further exploratory work was carried out where the concentration of octylamine was controlled. The experiments were not systematic but served to prove that octylamine had an effect on the resistivity of the NWs, where these experiments led to controlled humidity testing of the NWs. Figure 6.7 shows the response of a P3HT NW OFET device during a controlled vapour experiment, where the device was placed inside a sealed chamber, and exposed to nitrogen and octylamine vapours, followed by exposure to ambient air. After initial exposure to N_2 , while the chamber is purged for 30 mins, the device had a resistance of $17.9 \pm 0.05 \text{ M}\Omega$. Upon

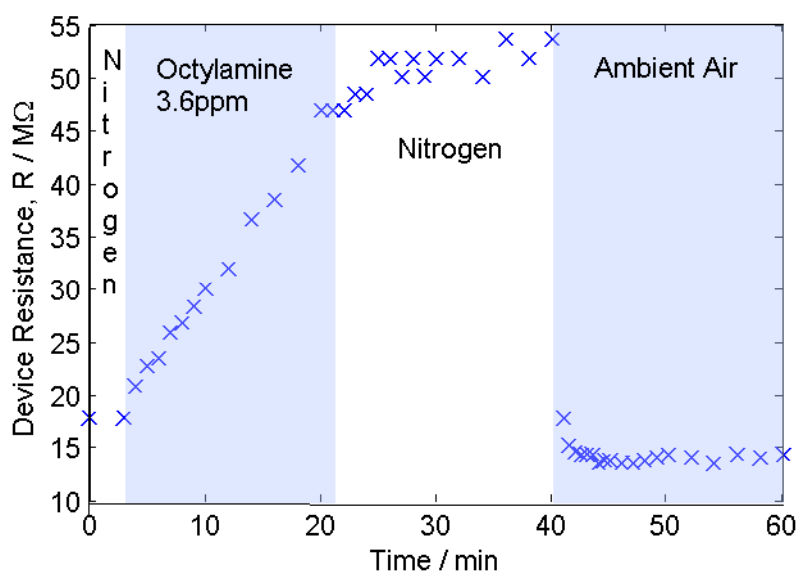


Figure 6.7: Resistance response of P3HT NW OFET device during exposure to 3.6ppm octylamine, nitrogen and ambient air. The graph shows a constant increase in R from the baseline of 18 MΩ up to 48 MΩ during exposure to octylamine, continued increase and settling at 52 MΩ after octylamine exposure has been suspended, and then a sudden drop to 14 MΩ upon exposure to ambient air.

exposure to 3.6ppm of octylamine the device immediately exhibits an increase in resistance. R reaches 46.9 ± 0.05 MΩ after 16 mins of exposure upon which the octylamine was turned off and the chamber was purged with N_2 . There is a steady increase in the resistance while exposed to 3.6ppm of octylamine, and does not reach a maximum within the 20mins before the flow is reverted back to nitrogen. R continues to creep up even after the octylamine is replaced with nitrogen flow, but can be explained by the fact that it takes time for the chamber to be purged of the octylamine.

At the point at which the chamber is opened up to the ambient air at 40mins, R instantly drops to below 20 MΩ and reaches a steady 14.1 ± 0.3 MΩ.

P3HT-NW chemiresistor octylamine sensing II

A further, non-systematic but more extensive investigation was carried out on a P3HT-NW chemiresistor to investigate the effects of octylamine vapour; the results are shown in figure 6.8.

Initial N₂ flow increased the device resistance from the air exposed-baseline of R=16.3 MΩ up to 46.4 MΩ, with an initial jump upto 29.3 MΩ within the first 15s. Stopping all flow of gas in the chamber kept the device resistance at 46.4 MΩ. Exposure to air again dropped the resistance to 20.1 MΩ.

The sample was exposed to 3.6 ppm octylamine in N₂ after being exposed to pure N₂. The resistance gradually rose from a steady 48.0 MΩ under the N₂ flow upto 118.0 MΩ after 20 mins, upon which the gas flow was switched back to N₂ and the resistance continued to rise and began to fluctuate. Air was then flowed through the chamber and the resistance dropped rapidly to 31.6 MΩ within 30s.

The sample was exposed to 36 ppm octylamine after being exposed to N₂. The resistance rose sharply from a steady 71.6 MΩ upto 322 MΩ within 8 mins and remained steady for 3 mins under octylamine flow and for 9 mins under the subsequent N₂ flow. The sample was then exposed to air again and experienced a rapid drop in resistance down to 42.3 MΩ in under 30s, and decrease to 24.0 MΩ over 12 mins.

Subsequent exposures to N₂ and air saw increases and rapid decreases in resistance respectively.

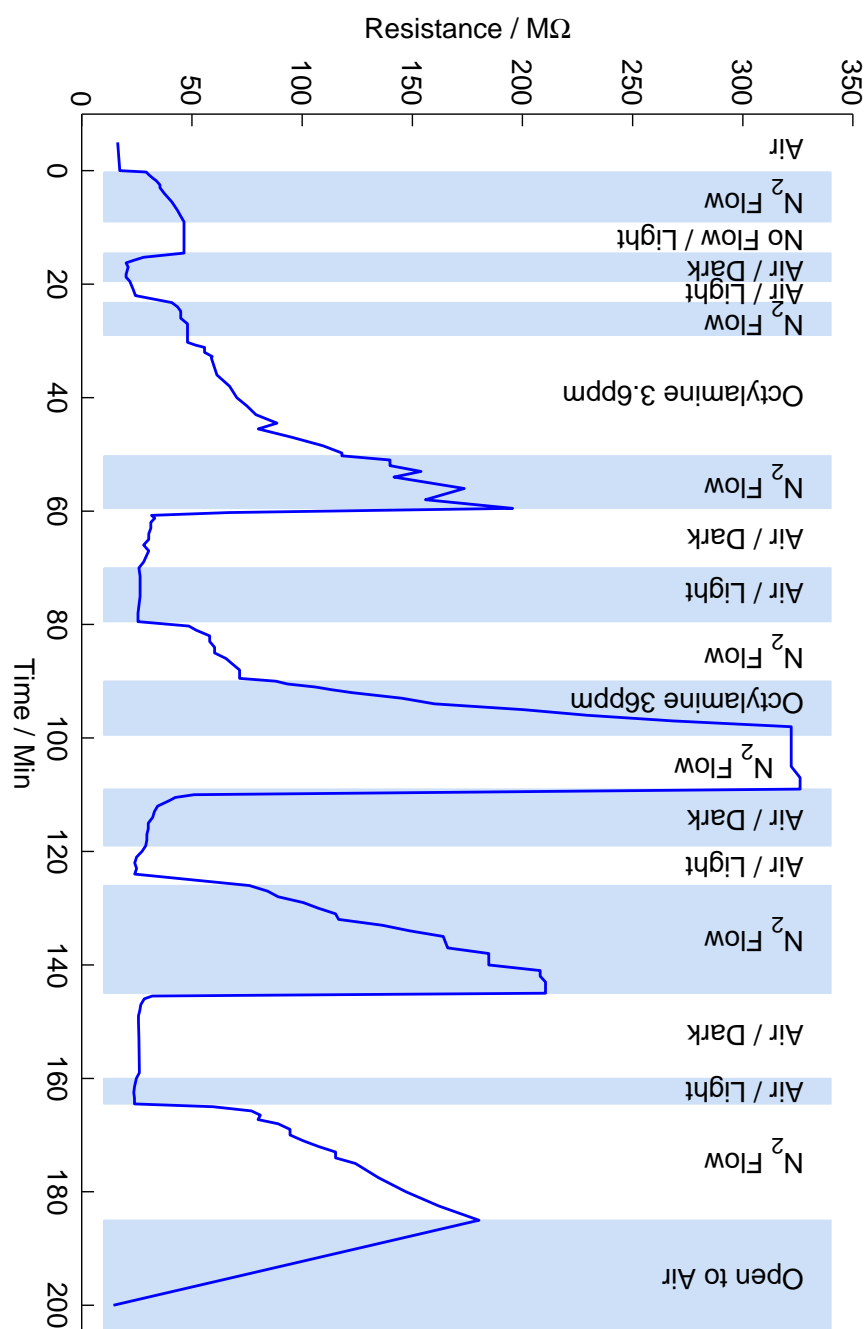


Figure 6.8: Device resistance response of P3HT nanowire OFET device to multiple exposures to octylamine. The device was repeatedly exposed to air, N₂, and octylamine infused N₂, and exposed to dark and light conditions in order to explore the response of the NWs. The N₂ flow had the effect of increasing the resistance, while the octylamine, particularly at the higher concentration of 3.6ppm increased the resistance more dramatically. The exposure to air very rapidly decreased the resistance of the device.

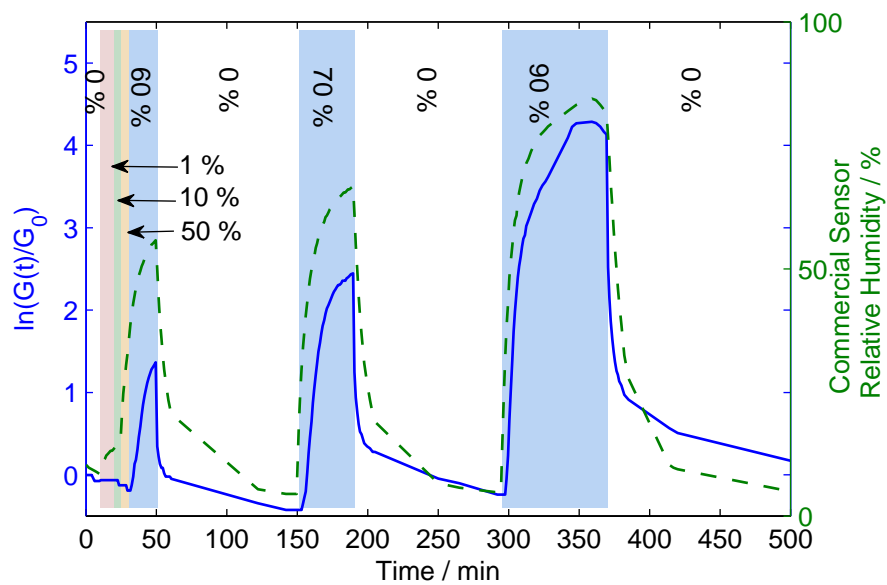
P3HT Humidity Sensing

It was seen that the P3HT NW devices were sensitive to water vapour. Figure 6.9 a) shows the change in conductance for a device exposed to varying relative humidity, against the relative humidity levels as measured with a commercially available sensor. The conductance increases from a base level of $0.02\mu\text{S}$ to $0.088\mu\text{S}$ at 55%, $0.26\mu\text{S}$ at 66% and $1.62\mu\text{S}$ at 84%.

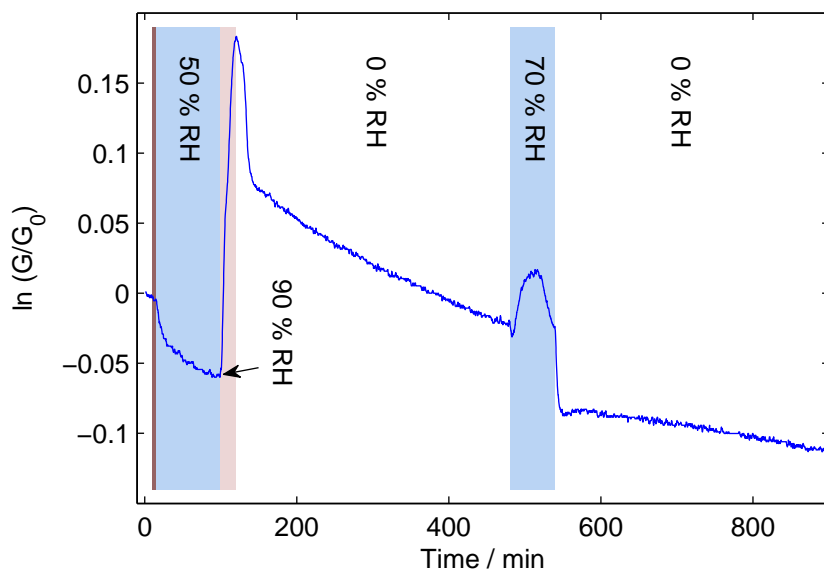
Figure 6.10 shows AFM images across and within the channels of the P3HT NW and P3HT film devices used in the humidity experiments; the NW image is typical of all of the P3HT NW OFET devices tested in this chapter. The morphology of the device semiconducting materials were distinctly different; the film device has a rather smooth, uniform appearance, whereas in the NW device a mesh of inter-penetrating wires can clearly be seen. AFM images taken in §4.3.2 show that the meshes of wires are made up of many wires that 'finger out' in several directions and many overlapping and crossing wires.

This NW device showed a response only slightly lagging behind the commercial sensor when the humidity was increased and showed a slightly faster response to decreases in humidity.

Figure 6.9 b) shows the conductance of a P3HT film OFET in response to varying relative humidity. In contrast to the NW device, the response was significantly less. The devices began with an initial base level conductance of $0.057\mu\text{S}$, which showed a general decrease throughout the experiment down to $0.050\mu\text{S}$ after 21 hours the cycling of humidity and dry air. At 70% RH the conductance was $0.058\mu\text{S}$ where the base level was $0.056\mu\text{S}$ under dry air immediately before introduction of humidity, and at 90% the conductance rose to $0.069\mu\text{S}$.



a)



b)

Figure 6.9: Transconductance of a) P3HT NW OFET and b) P3HT film OFET in response to varying levels of relative humidity compared to commercial sensor. a) The NW device shows an exponential increase (log scale) in σ with increasing RH, and has a very rapid decrease in σ when RH is decreased. b) The film device shows a continual degradation in conductance and no correlation to RH.

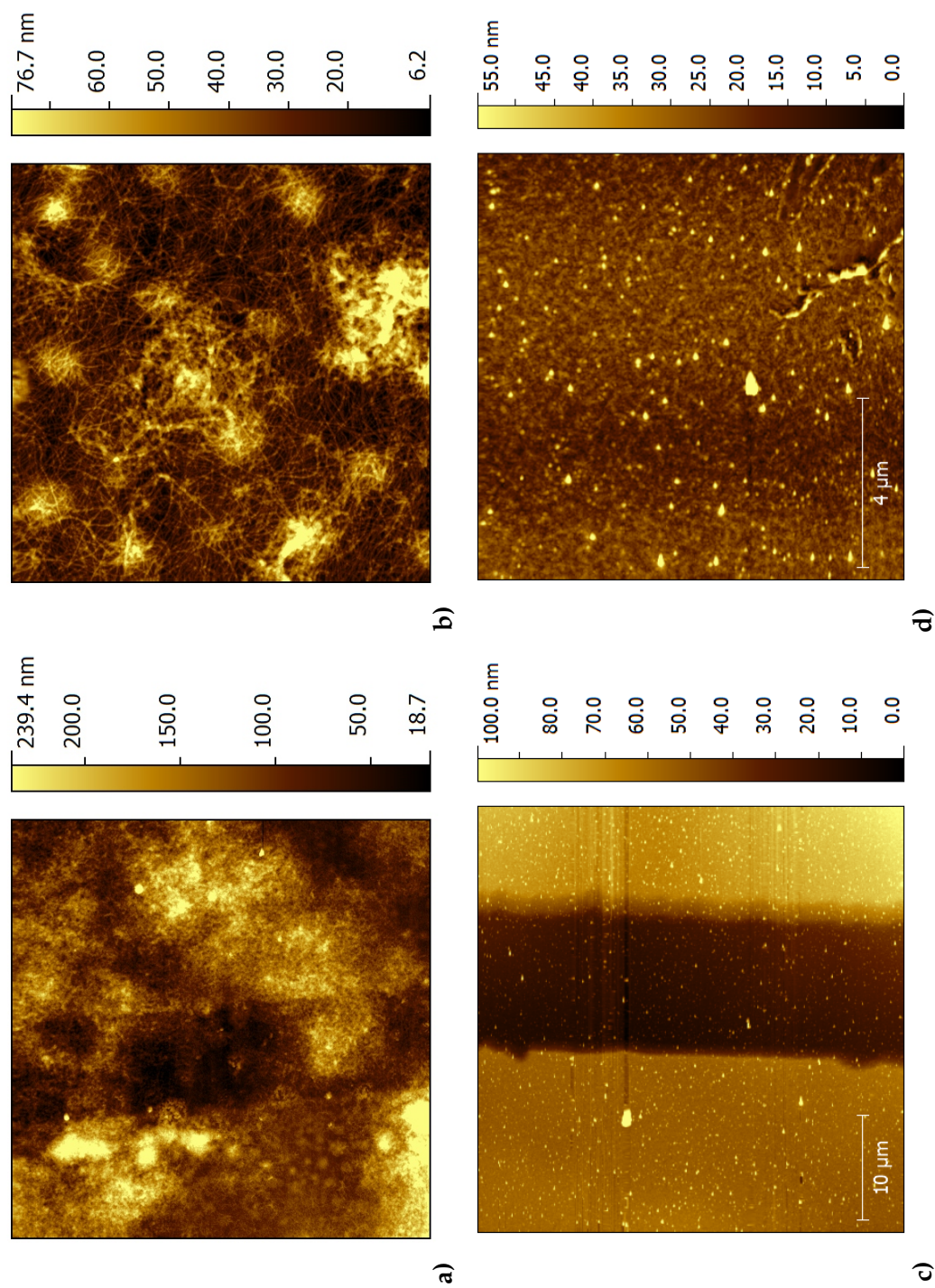


Figure 6.10: AFM images of humidity tested devices; a+b) P3HT NWs; c+d) P3HT film. Image sizes: a) and c) 40x40μm, b) and d) 10x10μm. The device channel is clearly seen in scan a). Close inspection suggests that the channel has a coverage of approximately 90%, while the thickness ranges from single nanowires to 200nm.

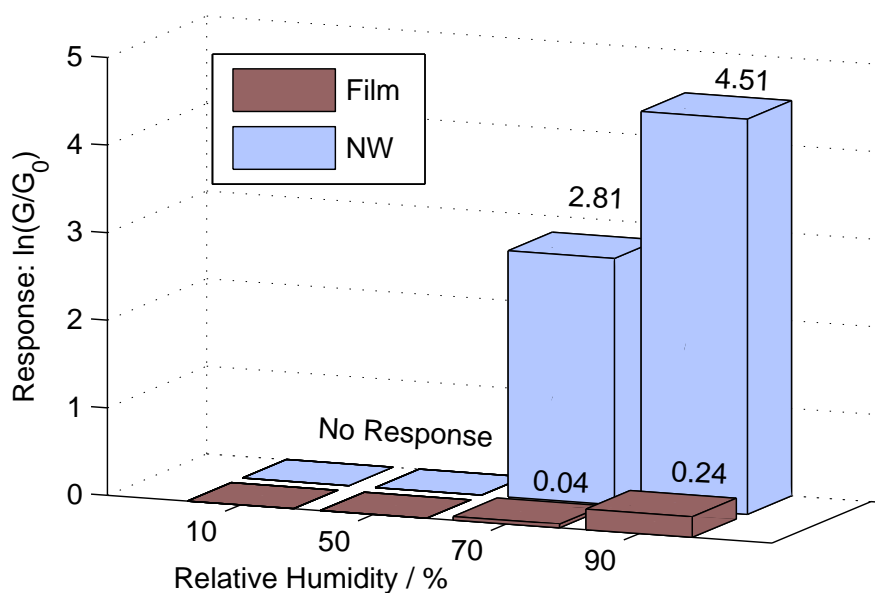


Figure 6.11: NW-Film conductance response vs. RH comparison. Both the film and the NWs have a threshold of approximately 50% RH. The NWs have a 75-fold increase in conductance at 90% compared to the base line while the film has a 20% increase at 90%.

Figure 6.11 clearly shows the difference in the conductivity response between the NWs and the film. A threshold of approximately 50% RH is reached before there is any change in conductivity is seen in both the film and NW devices. The NW device saw a 75-fold increase in conductance at 90% RH, and 11.5-fold increase at 70%. The film device had a response of 20% at 90% RH, and 1% at 70% RH.

6.3.2 Water-Gating

Surface Treatment Effects

Presented in table 6.1 are the measured contact angles for a de-ionised water droplet on the channel area of the WGOFETs. It is apparent that the surface treatment has a dramatic affect on the contact angle, with device E with a substrate of glass with no surface treatment giving a contact angle more than 20° less than the other PQT-12 NW device with a substrate of HMDS treated SiO₂ and 29° or more than all of the other devices. The P3HT devices gave a greater contact angle than the PQT-12 devices with the P3HT film giving the greatest contact angle at 109.22°. The PQT-12 film device gave a greater contact angle than the PQT-12 NW devices, but less than the P3HT NWs.

The contact angle gives a measures the hydrophobicity of the surface, and it is known that a smaller contact angle indicates that the device will have a higher mobility [30]. Also, the smaller the contact angle the better packed the film therefore less interaction is expected between the film and the ions of the water, and so the device will display greater FET dependence and less electrochemical dependence. The P3HT film device would therefore be expected to exhibit a weaker FET dependence and stronger electrochemical dependence than the P3HT NW device. The PQT-12 NW devices would be expected to show the strongest-FET/least-electrochemical dependence, with the PQT-12 NW on untreated glass to have the weakest electrochemical dependence.

Water-Gating Response

P3HT Figure 6.12 shows the time evolution of the output signal of device G, a P3HT NW WGOFET on an OTS treated glass substrate. The device

Table 6.1: Water-gated FET contact angles

Sample	Semiconductor	Substrate	Contact Angle, θ / °
A	PQT-12 NW	SiO ₂ HMDS	92.25
B	P3HT NW	SiO ₂ HMDS	104.43
C	PQT-12 film	Glass OTS	100.66
D	P3HT NW	SiO ₂ HMDS	107.63
E	PQT-12 NW	Glass No Surface Treatment	71.87
F	P3HT film	Glass OTS	109.22
G	P3HT NW	Glass OTS	106.40

was tested under ambient conditions. Initially the device was conducting and showed no rectifying behaviour and had a resistance of 100 ± 1 k Ω when tested dry with no gate bias applied. Upon application of a gate bias applied through a de-ionised water droplet the device began showing semi-rectifying behaviour with the current being dominated by hole transport, and it had a resistance of 43 ± 0.5 k Ω at 10s after application of the water droplet. Over the course of 180 seconds the resistance had risen to 51 ± 0.5 k Ω and the rectifying behaviour had decreased.

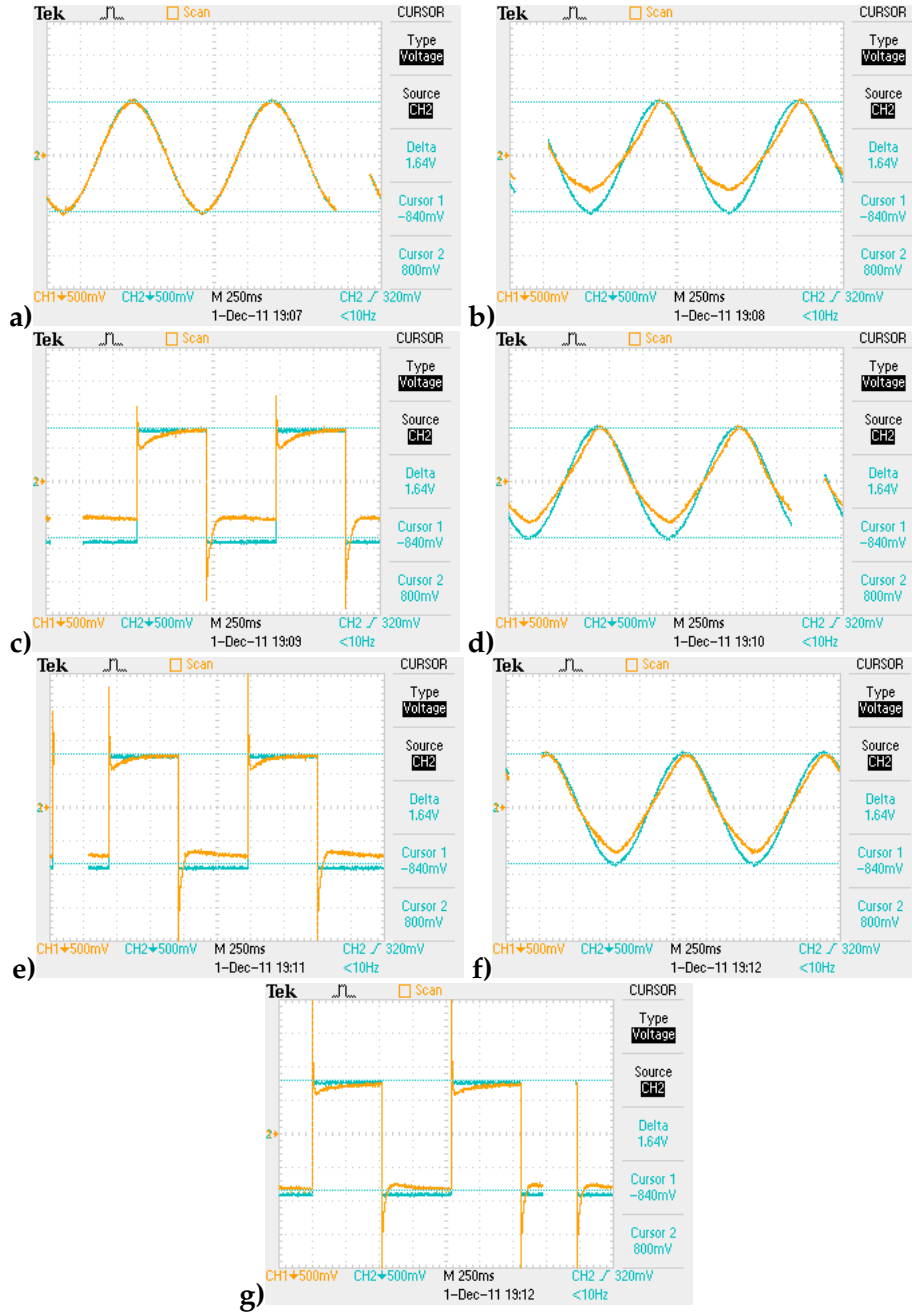


Figure 6.12: Time evolution output curves from water-gated P3HT NW OFETs. a) Ungated dry device, $R_F = 100 \text{ k}\Omega$. Water-gated at b) 10s, $R_F = 43 \text{ k}\Omega$; c) 35s, $R_F = 37 \text{ k}\Omega$; d) 100s, $R_F = 49 \text{ k}\Omega$; e) 140s, $R_F = 42 \text{ k}\Omega$; f) 180s, $R_F = 51 \text{ k}\Omega$; g) 230s, $R_F = 47 \text{ k}\Omega$.

The device showed a $I_{\text{OECT}}/I_{\text{OFET}}$ ratio of 0.67 ± 0.2 at 40s, with this decreasing to 0.28 ± 0.2 at 230s, showing that the field-effect became more dominant with during continued stress of the device. V_T was found to be 0.07 ± 0.05 V.

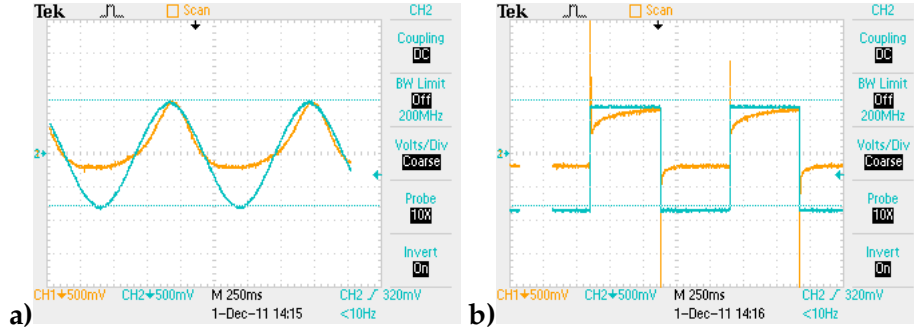


Figure 6.13: Time evolution output curves from water-gated P3HT film OFETs. a) 15s, $R_F = 60$ kΩ; b) 60s, $R_F = 23$ kΩ

Figure 6.13 shows the output curves for device F, a P3HT film WGOFET on an OTS treated glass substrate (further output curves are shown in appendix B). This device also showed non-rectifying conducting behaviour when dry and un-gated, similar to the P3HT NW device and had a resistance of 480 ± 1 kΩ, nearly a five-fold increase over the NW device. The device when water-gated showed much greater rectifying behaviour than the NW device, and had a resistance of 23 ± 0.5 kΩ, approximately half that of the NW device after a similar time. The resistance increased to 49 ± 0.5 kΩ after 210 seconds and had not changed at 300 seconds.

The $I_{\text{OECT}}/I_{\text{OFET}}$ ratio went from 1.23 ± 0.02 at 60 seconds to 0.85 at 250 seconds and 0.95 at 345 seconds. Again the field-effect has become more dominant with stressing of the device, this time the change in the ratio was 23% compared to 66% as exhibited by the NW device. V_T for the film device was found to be 0.15 ± 0.03 V.

PQT-12 PQT-12 NW and film devices showed no gating behaviour, they had very high resistances ($>100\text{M}\Omega$) and were very noisy. No useful data could be gained from any of these devices.

6.4 Discussion

6.4.1 Dry-gated OFETs, and Chemiresistor Sensors

P3HT-NW Resistor Heating

The initial decrease in the resistance of the P3HT NW device through heating could be due to a thermally activated transport mechanism, where charge carriers energy barriers via energy transfer from thermal phonons. A thermally activated hopping process in P3HT NWs was proposed by Merlo[31] in the form of multiple trap and release (MTR) and variable range hopping (VRH) models. At increased temperatures, above 65°C , the increased vibrational energy of the polythiophene chains may disrupt charge transport at increased temperatures, although XRD data (§4.3.9) suggests that thermal treatment improves crystallinity and decreases disorder in P3HT NWs and so a continued drop in resistance should be expected. It may be more likely that the elevated temperatures are causing water molecules to be driven out of the NWs, leading to a de-doping of the NWs and hence an increase in resistance. It is known that NWs are sensitive to doping by water vapour[7], and further data from this chapter (figure 6.9) agrees with this. An increase in resistance due to de-doping through heat induced removal of water molecules seems a highly likely explanation.

Octylamine Sensing

Two mechanisms are proposed for the increase in resistance observed in P3HT-NW chemiresistor devices exposed to octylamine vapour. One mechanism involves the decrease in free charge carriers due to an effective dedoping of the NWs; the second mechanism is a decrease in the mobility of free charge carriers due to the presence of the octylamine molecules within the NWs.

Octylamine molecules diffusing into the NWs may disrupt the coherence length of the NWs such that the overlap of the π -orbitals is disturbed and the path of the charge carriers is blocked.

Alternatively, the lone pair of the nitrogen in the amine may be interacting with the dopants in the NWs. P3HT is known to be doped by molecular oxygen[16, 17] and by water[7]. Our data is consistent with the octylamine adsorption neutralising or releasing these oxygen/water-induced dopants leading to increased resistance. Our data also provides evidence that N₂ flow may have a similar neutralising effect on these dopants at a slower rate than octylamine.

P3HT Humidity Sensing

The greater response in the conductivity to the RH in the NW device is attributed to the increased surface area of the semiconducting material. The AFM image of the NW device showed a large mesh of NWs where there were many faces of the NWs exposed to the atmosphere; in comparison the film device is relatively smooth, with far less surface exposed to the atmosphere. The greater surface area of the NWs would have allowed the water molecules to interact with and gate the thiophene rings as suggested

by Leary[15].

The reason for the threshold of both devices of approximately 50% RH, below which no change in conductivity was witnessed, is unknown. The author suggests that either some unremovable humidity may be permanently attached to the P3HT, and therefore provide permanent doping. An alternative theory is that there is doping by oxygen where O_2 is known to form a CT complex with P3HT.

The use of dry N_2 as opposed to dry air may help to elucidate the reason for the threshold RH, by eliminating the O_2 , although this may be somewhat more complicated.

Further investigation into the response of the P3HT nanowires to humidity is required to ascertain the exact relationship between the relative humidity and the conductance change of the device. It would appear that there is an exponential increase in the conductance as the RH increases, and that there is a threshold RH of 50% before there is an increase in the conductivity, although there is insufficient data to confirm this.

6.4.2 WGOFETs

The P3HT film devices were found to have a lower resistance compared to the NW devices when water-gated; this could be explained by the effective channel width being wider for the film as the NWs may not completely fill the channel due to gaps in the wire 'mesh'. This was discussed by Briseno[32] in his review of NW transistors and was also seen in further work that followed on from this chapter. A greater off-current was seen in the NWs, this is attributed to gate leakage due to penetration of the NW mesh, by the water, through to the source and drain contacts. This problem could be addressed by using a thicker mat of NWs, and by a redesign of

the electrodes to minimise exposure to the gate water droplet (see §6.5). The threshold voltage V_T , of the NW devices was found to be lower than that of the film devices. An explanation for this is that due to the greater surface area of the NWs and hence more interaction with the water molecules, they are more sensitive to the gating effect of the water. Also, it was predicted that the improved crystal packing of the NWs would lead to a lower ratio of electrochemical current to field-effect current, $I_{\text{OECT}}/I_{\text{OFET}}$. This was observed during the experiments, with the NWs having an initial ratio of 0.67 ± 0.2 to the P3HT films 1.23 ± 0.02 .

The failure of the PQT-12 NWs and film to operate as WGOFETs currently remains unexplained.

6.5 Design of New Electrodes

In light of problems experienced in the WOGFETs with shorts from the gate electrode through to exposed parts of the source and drain electrodes via the water droplet leading to high off-currents in particularly in NW devices, improved device geometry was proposed. The designs for these are seen in figures 6.14 and 6.15. A high aspect ratio was still required, so that a measurable current would be passed through the semiconducting channel, yet a small area was required to connect the electrodes to the contact pads so that the exposed electrode and possible pathways from the gate to the source and drain electrodes was minimised. A photolithography mask was proposed so that electrodes could be patterned using a photolithography process followed by Cr and Au evaporation and lift, or thin-foil or silver nitride shadow masks could be produced from the photo mask and Cr and Au electrodes could be patterned via evaporation through the shadow masks.

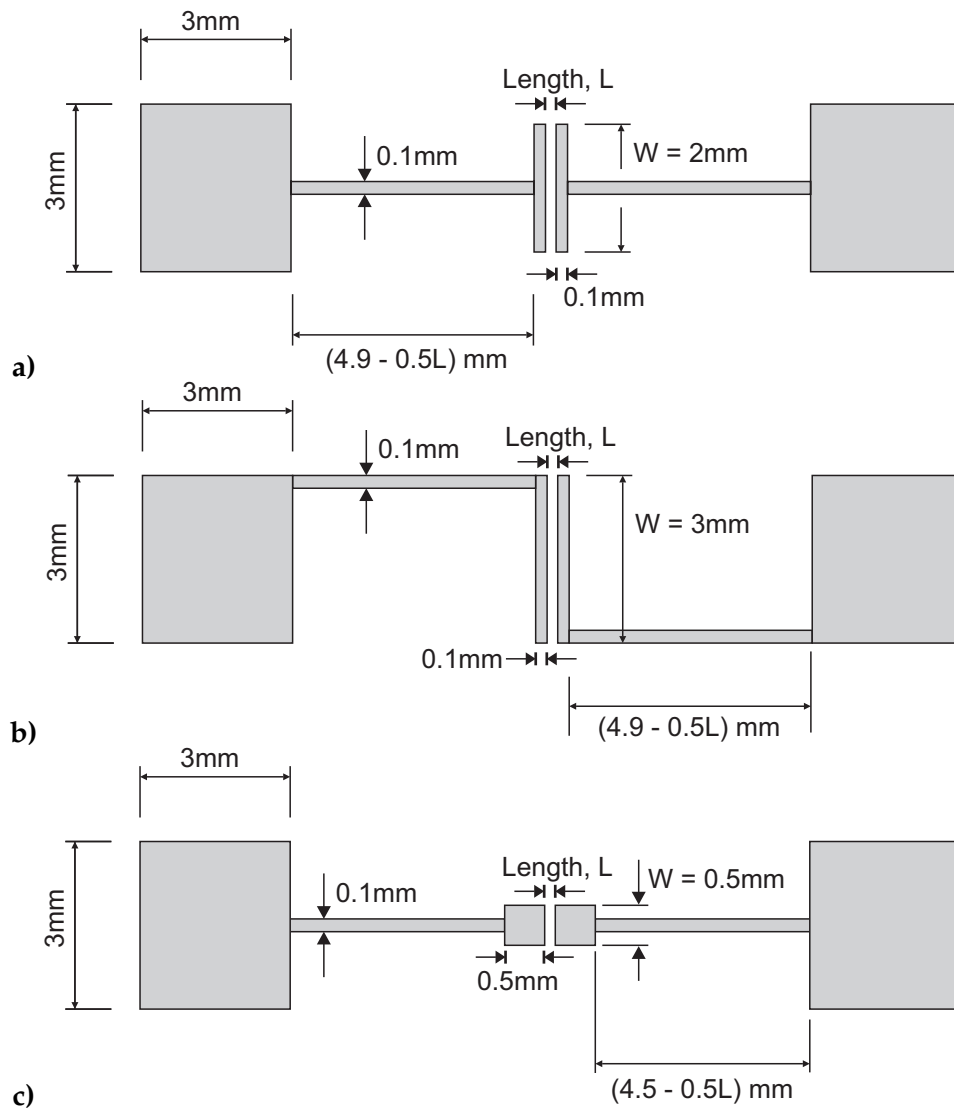


Figure 6.14: Photolithography and metal foil shadow mask electrode designs. The Dark portions was glass in the actual mask, while the surrounding area was chromium coated glass.

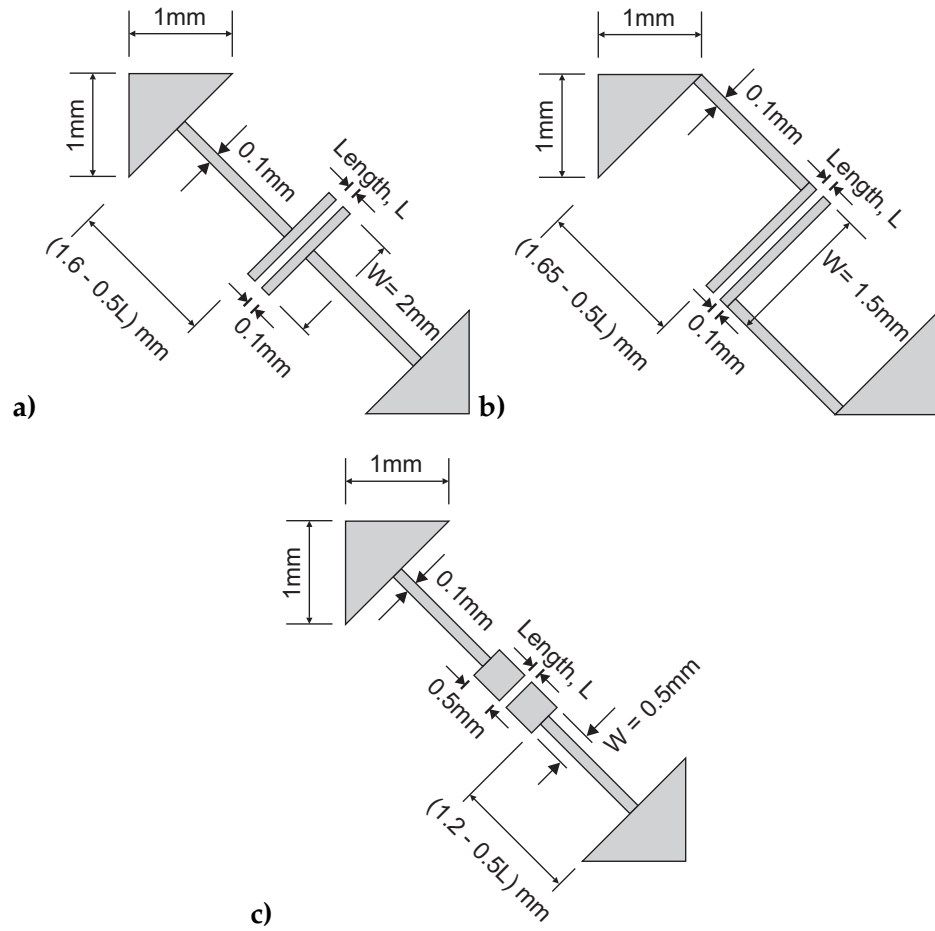


Figure 6.15: Electrode design for silicon nitride shadow masks; the individual designs were such that they would sit within a $4 \times 4\text{ mm}$ silicon nitride frame. The Dark portions was glass in the actual mask, while the surrounding area was chromium coated glass.

A GDS file (figure B.2 in appendix B) was produced using KLayout, which was used by Compugraphics Jena GmbH to produce the mask.

6.6 Conclusions

P3HT and PQT-12, films and NWs were tested in standard-gated and water-gated OFETs, and were explored as potential sensors for humidity and octyl-amine; P3HT showed that it is capable of being water-gated in NW and film morphologies.

Heating of a P3HT NW OFET affected the resistance, where the resistance decreased to a minimum at 65°C before increasing again as the temperature continued to rise to 100°C. Subsequent cooling showed that this process was semi-reversible with the resistance returning to close to the original value of resistance with some hysteresis. The initial decrease in resistance is consistent with the conduction models proposed for P3HT in the literature, which are multiple trap and release, and variable range hopping, and are both thermally activated processes. Above 65°C the elevated temperatures may be driving moisture out of the NWs and de-doping them leading to an increase in resistance.

P3HT NWs were shown to increase in resistance upon exposure to octyl-amine vapour, where exposure to 3.6ppm of octyl-amine increased the resistance of the P3HT NWs chemiresistor, and a ~13-fold increase in resistance upon exposure to 36ppm of octylamine was seen. The rate of resistance increase was far more rapid when the NWs were exposed to octylamine compared to when exposed to dry N₂, and it was found to be reversible when exposed to air. It is proposed that the NWs are doped by molecular oxygen and/or water and then the octylamine neutralises or releases the dopants.

A similar effect occurs due to the presence of N_2 but with a far slower rate.

As humidity sensors, both the P3HT NWs and film had a threshold of 50% relative humidity before showing any significant change in conductance. The P3HT NWs were more responsive than the films, showing a 75-fold increase in conductivity at 90% RH compared with a 25% increase for the film. It is believed by the author that the reason for increased responsiveness of the NWs to the water vapour compared to the film, is due to the increased surface area of the NWs.

P3HT-NW WGOFETs had higher resistance than P3HT film WGOFETs, with $R=43\pm0.5\text{ k}\Omega$ and $23\pm0.5\text{ k}\Omega$ respectively, which was attributed to the effective channel width of the NW devices being smaller than that of the films due to gaps in the NW mats. A greater off-current was seen in the P3HT-NWs compared to the film, which was believed to be due to penetration of the NW mesh through to the source and drain contacts by the water droplet. P3HT-NWs were found to be more sensitive to water-gating with $V_T = 0.07\pm0.05\text{ V}$ compared to the P3HT film's $0.15\pm0.03\text{ V}$. Greater sensitivity to water-gating, as indicated by the lower threshold voltage, was that the greater surface area of the NWs increased the interaction by the water molecules. The ratio of electrochemical current to field-effect current, $I_{\text{OECT}}/I_{\text{OFET}}$ was lower for the NWs compared to the film.

Bibliography

- [1] Das A, Dost R, Richardson T, Grell M, Morrison J J, and Turner M L. A nitrogen dioxide sensor based on an organic transistor constructed from amorphous semiconducting polymers. *Advanced Materials*, 19(22):4018–4023, 2007.
- [2] Das A, Dost R, Richardson T H, Grell M, Wedge D C, Kell D B, Morrison J J, and Turner M L. Low cost, portable, fast multiparameter data acquisition system for organic transistor odour sensors. *Sensors and Actuators B: Chemical*, 137(2):586 – 591, 2009.
- [3] Majewski L A, Grell M, Ogier S D, and Veres J. A novel gate insulator for flexible electronics. *Organic Electronics*, 4(1):27 – 32, 2003.
- [4] Majewski L A, Schroeder R, and Grell M. Flexible high capacitance gate insulators for organic field effect transistors. *Journal of Physics D: Applied Physics*, 37(1):21, 2004.
- [5] Taylor D M, Gomes H L, Underhill A E, Edge S, and Clemenson P I. Effect of oxygen on the electrical characteristics of field effect transistors formed from electrochemically deposited films of poly(3-methylthiophene). *Journal of Physics D: Applied Physics*, 24(11):2032, 1991.
- [6] Liao H-H, Yang C-M, Liu C-C, Horng S-F, Meng H-F, and Shy J-T. Dynamics and reversibility of oxygen doping and de-doping for conjugated polymer. *Journal of Applied Physics*, 103(10):104506, 2008.
- [7] Hoshino S, Yoshida M, Uemura S, Kodzasa T, Takada N, Kamata T, and Yase K. Influence of moisture on device characteristics of polythiophene-based field-effect transistors. *Journal of Applied Physics*, 95(9):5088–5093, 2004.
- [8] Street R A, Chabinyc M L, and Endicott F. Chemical impurity effects on transport in polymer transistors. *Physical Review B*, 76:045208, Jul 2007.

- [9] Street R A, Chabinyc M L, Endicott F, and Ong B. Extended time bias stress effects in polymer transistors. *Journal of Applied Physics*, 100(11):114518, 2006.
- [10] Cros S, de Bettignies R, Berson S, Bailly S, Maisse P, Lemaitre N, and Guillerez S. Definition of encapsulation barrier requirements: A method applied to organic solar cells. *Solar Energy Materials and Solar Cells*, 95, Supplement 1(0):S65 – S69, 2011. Special Issue : Thin Film Photovoltaic Applications (TFPA).
- [11] Fukuda H, Yamagishi Y, Ise M, and Takano N. Gas sensing properties of poly-3-hexylthiophene thin film transistors. *Sensors and Actuators B: Chemical*, 108(1-2):414 – 417, 2005. Proceedings of the Tenth International Meeting on Chemical Sensors - IMCS - 10 2004.
- [12] Rost H, Ficker J, Alonso J S, Leenders L, and McCulloch I. Air-stable all-polymer field-effect transistors with organic electrodes. *Synthetic Metals*, 145(1):83 – 85, 2004.
- [13] Knorr N, Wirtz R, Rosselli S, and Nelles G. Field-absorbed water induced electrochemical processes in organic thin film junctions. *The Journal of Physical Chemistry C*, 114(37):15791–15796, 2010.
- [14] Chabinyc M L, Endicott F, Vogt B D, DeLongchamp D M, Lin E K, Wu Y, Liu P, and Ong B S. Effects of humidity on unencapsulated poly(thiophene) thin-film transistors. *Applied Physics Letters*, 88(11):113514, 2006.
- [15] Leary E, Höbenreich H, Higgins S J, van Zalinge H, Haiss W, Nichols R J, Finch C M, Grace I, Lambert C J, McGrath R, and Smerdon J. Single-molecule solvation-shell sensing. *Physical Review Letters*, 102:086801, Feb 2009.
- [16] Lüer L, Egelhaaf H-J, Oelkrug D, Cerullo G, Lanzani G, Huisman B-H, and de Leeuw D. Oxygen-induced quenching of photoexcited states in polythiophene films. *Organic Electronics*, 5(1 - 3):83 – 89, 2004. Current Trends in Crystalline Organic Semiconductors: Growth Modelling and Fundamental Properties.
- [17] Hintz H, Egelhaaf H-J, Lüer L, Hauch J, Peisert H, and Chasseé T. Photodegradation of P3HT – a systematic study of environmental factors. *Chemistry of Materials*, 23(2):145–154, 2011.
- [18] Chabinyc M L, Street R A, and Northrup J E. Effects of molecular oxygen and ozone on polythiophene-based thin-film transistors. *Applied Physics Letters*, 90(12):123508, 2007.

- [19] Ellis D L, Zakin M R, Bernstein L S, and Rubner M F. Conductive polymer films as ultrasensitive chemical sensors for hydrazine and monomethylhydrazine vapor. *Analytical Chemistry*, 68(5):817–822, 1996.
- [20] Gonçalves V C, Nunes B M, Balogh D T, and Olivati C A. Detection of volatile organic compounds using a polythiophene derivative. *Physica Status Solidi (a)*, 207(7):1756–1759, 2010.
- [21] Weerakoon K A, Shu J H, and Chin B A. A chemiresistor sensor with a poly3-hexylthiophene active layer for the detection of insect infestation at early stages. *Sensors Journal, IEEE*, 11(7):1617 –1622, july 2011.
- [22] Crone B, Dodabalapur A, Gelperin A, Torsi L, Katz H E, Lovinger A J, and Bao Z. Electronic sensing of vapors with organic transistors. *Applied Physics Letters*, 78(15):2229 –2231, apr 2001.
- [23] Torsi L, Tafuri A, Cioffi N, Gallazzi M C, Sassella A, Sabbatini L, and Zambonin P G. Regioregular polythiophene field-effect transistors employed as chemical sensors. *Sensors and Actuators B: Chemical*, 93(1&A33):257 – 262, 2003. Proceedings of the Ninth International Meeting on Chemical Sensors.
- [24] Kergoat L, Herlogsson L, Braga D, Piro B, Pham M-C, Crispin X, Berggren M, and Horowitz G. A water-gate organic field-effect transistor. *Advanced Materials*, 22(23):2565–2569, 2010.
- [25] Kergoat L, Piro B, Berggren M, Pham M-C, Yassar A, and Horowitz G. Dna detection with a water-gated organic field-effect transistor. *Organic Electronics*, 13(1):1 – 6, 2012.
- [26] Kergoat L, Battaglini N, Miozzo L, Piro B, Pham M-C, Yassar A, and Horowitz G. Use of poly(3-hexylthiophene)/poly(methyl methacrylate) (P3HT/PMMA) blends to improve the performance of water-gated organic field-effect transistors. *Organic Electronics*, 12(7):1253 – 1257, 2011.
- [27] White H S, Kittlesen G P, and Wrighton M S. Chemical derivatization of an array of three gold microelectrodes with polypyrrole: fabrication of a molecule-based transistor. *Journal of the American Chemical Society*, 106(18):5375–5377, 1984.
- [28] Ihn K J, Moulton J, and Smith P. Whiskers of poly(3-alkylthiophene)s. *Journal of Polymer Science Part B: Polymer Physics*, 31(6):735–742, 1993.
- [29] Hague L, Puzzovio D, Dragoneas A, and Grell M. Simplified real-time organic transistor characterisation schemes for sensing applications. *Science of Advanced Materials*, 3(6):907–911, 2011.

- [30] Park J W, Lee D H, Chung D S, Kang D-M, Kim Y-H, Park C E, and Kwon S-K. Conformationally twisted semiconducting polythiophene derivatives with alkylthiophene side chain: High solubility and air stability. *Macromolecules*, 43(5):2118–2123, 2010.
- [31] Merlo J A and Frisbie C D. Field effect transport and trapping in regioregular polythiophene nanofibers. *The Journal of Physical Chemistry B*, 108(50):19169–19179, 2004.
- [32] Briseno A L, Mannsfeld S C B, Jenekhe S A, Bao Z, and Xia Y. Introducing organic nanowire transistors. *Materials Today*, 11(4):38 – 47, 2008.

Chapter 7

Conclusions

The growth and formation of P3HT and PQT-12 NWs in various organic solvents were examined using AFM, and UV-Vis, while the structure was investigated using XRD. Further to this, a novel method for doping NWs was developed. Doping involved intercalation of dye molecules into the NWs by addition of the molecules during the first step of the NW growth process. Emission spectroscopy suggested that intercalation was successful. P3HT-NW OPVs, with the NWs deposited at varying temperatures, were compared to PQT-12 NW OPV devices, with the PQT-12 NW OPVs further compared to PQT-12 film devices. Dye intercalated P3HT-NWs were then investigated as OPVs. Finally, P3HT-NWs were explored in OFETs and chemiresistors, and P3HT and PQT-12 in NW and film morphologies were investigated in WGOFETs. The P3HT OFETs were subject to heat, while chemiresistors were demonstrated for their potential as sensors by exposure to octylamine and humidity in an atmosphere controlled chamber.

7.1 Nanowire Growth and Structure

Polythiophene nanowires of high aspect ratio were grown using the whisker method. The polymer was dissolved in a marginal solvent at elevated temperatures, and crystallised out of solution during cooling and/or when left to stand at room temperature. In order to investigate the growth and formation of the NWs, a small droplet of solution was deposited onto silicon substrates at regular temperature and time intervals and then imaged using AFM. NW dimensions and rates of growth varied depending on the polymer-solvent combinations. Widths of the NWs were found to be 20~80 nm, heights were 1~10 nm and the lengths were from 10s of nanometres upto in excess of 10 micrometres. The P3HT-toluene combination formed NW in two stages; firstly, flat, wide, rough-edged 'proto'-wires formed at approximately 40°C, and this was followed by development into smooth, tall NWs after several hours.

UV-Vis spectra of P3HT-anisole NWs revealed vibronic structure with peaks and shoulders at 483, 513, 547 and 599 nm. The absorption spectra also showed that some non-NW P3HT remained in the solution, but this could be removed through a process of centrifuging and rinsing.

Grazing-incidence x-ray diffraction was performed on mats of P3HT and PQT-12 NWs grown in various organic solvents. P3HT NWs were found to be highly oriented, with alkyl side-chain stacking in the out-of-plane direction of the substrate, $\pi - \pi$ -stacking along the long-axis of the wires and the polymer back bone both in the in-plane direction of the substrate. The P3HT NW structure was revealed to have a similar structure to P3HT films found in the literature but with a smaller 'a'-lattice constant, that of the alkyl chain stacking. The 'a'-lattice was found to be 15.7~15.9 Å in

the NWs compared to 16~16.4 Å as seen for films in the literature. Thermal annealing at 140°C increased the 'a'-lattice constant upto 15.9~16.3 Å. Domain sizes increased as a result of thermal annealing from 136±5, 141±10, and 111±8 Å to 215, 227 and 144 Å for anisole, cyclohexanone and trimethylbenzene grown NWs respectively. Disorder decreased in the NWs as a result of thermal annealing with 'g' values from $g = 0.0446 \pm 0.0004$, 0.040, and 0.0474 ± 0.0002 decreasing to $g = 0.0400 \pm 0.0002$, 0.0373 ± 0.0007 , and 0.0411 ± 0.0013 for anisole, cyclohexanone and trimethylbenzene grown NWs respectively.

The following is a description of the structural changes that occur in P3HT NWs through the process of thermal annealing, as discerned from the diffraction results. The spacing between the backbones along the alkyl chain stacking direction is significantly smaller the NWs compared to that observed in P3HT films. During thermal annealing there is considerable expansion along this direction, and upon re-cooling the spacing is then much more similar to that observed in thin films. This indicates a highly compact arrangement, which may involve some interdigitation of the alkyl-chains, in the as-formed NWs, with that after annealing being more typical of that occurring in spin-coated films. During annealing the domain size increases accompanied by a decrease in paracrystallinity.

PQT-12 NWs were found to be in a meta-stable structure as cast which became amorphous during thermal annealing at 140°C and recrystallised in a new form upon cooling.

7.2 Nanowire Doping and OPVs

P3HT-NW:PCBM and PQT-12-NW:PCBM blends were deposited at varying temperatures as the active blend in OPV devices in order to control the NW to non-NW ratio. The optimal temperature for deposition was 60°C for both blends and gave efficiencies of 0.92 ± 0.17 % for P3HT-NW devices and 0.16 ± 0.08 % for PQT-12-NW devices. Thermal annealing of the P3HT devices improved all performance metrics apart from J_{SC} which saw a small decrease. After thermal annealing the best efficiency was the device where the blend was deposited at 60°C, which gave an efficiency of 1.52 ± 0.28 %. Thermal annealing of the PQT-12-NW devices increased V_{OC} , decreased J_{SC} slightly and left PCE and FF largely unchanged.

PQT-12-NW devices outperformed their film counterparts by a 4-fold increase in PCE, and gave improved V_{OC} , J_{SC} and FF.

A novel and facile method for doping NWs was created. Dye molecules were intercalated into the NWs by addition of the molecules at the first step of NW processing. Emission spectroscopy and combustion analysis of centrifuged and rinsed dye intercalated NWs provided indirect evidence that intercalation was taking place. The emission spectra showed the peaks of the dyes even after rinsing, while the combustion analysis showed presence of nitrogen which is in the dyes structure but not in the NW structure. Anthraquinone molecules are known to intercalate into DNA which leads the author to believe that there is a high probability that intercalation of the dye molecules into the NWs is taking place here. Future work comprising of single NW polarised luminescence studies could provide unambiguous evidence for successful intercalation.

OPV devices fabricated with P3HT NWs that were doped with dye '2d'

saw small increases in the efficiency; 0.533 ± 0.413 % compared to the dye free P3HT-NW:PCBM standard device which had a PCE of 0.282 ± 0.245 %. From the data presented here it is not definitely clear as to the cause of the increase in PCE of the this particular dye in comparison to the dye-free device and the devices containing the other dyes. Dye '2d' had a significantly deeper HOMO in comparison to the other dyes and is the only dye with a HOMO that is deeper than that of the PCBM. It would be expected that this would lead to trapping of the holes in the blend, leading to recombination of charges and a drop in performance. Further investigation would be required to ascertain the processes that are causing the increase in PCE. While initial performance results from dye intercalated devices were not overly positive, fine tuning of the dye molecules could yield improved results. Furthermore, dye intercalated P3HT NWs could hold potential in other applications such as sensors where the dye is designed to add analyte specificity.

7.3 Organic Field-effect Transistors and Sensors

P3HT and PQT-12, films and NWs were tested in standard-gated and water-gated OFETs, and were explored as potential sensors for humidity and octylamine; P3HT showed that it is capable of being water-gated in NW and film morphologies.

Heating of a P3HT NW OFET affected the resistance, where the resistance decreased to a minimum at 65°C before increasing again as the temperature continued to rise to 100°C . Subsequent cooling showed that this process was semi-reversible with the resistance returning to close to the original value of resistance with some hysteresis. Thermally activated hopping models for the charge transport in P3HT such as variable range hopping

and multiple trap and release as proposed in the literature are consistent with the initial decrease in resistance of device. The increase in resistance at temperatures above 65°C may be as a result of disruption of the charge transport due to excessive vibrational energy of the polymer chains.

P3HT NWs were shown to increase in resistance upon exposure to octyl-amine vapour, where exposure to 3.6ppm of octyl-amine increased the resistance of the P3HT NWs chemiresistor, and a ~13-fold increase in resistance upon exposure to 36ppm of octyl-amine was seen. When the devices were exposed to octylamine the resistance increase was far more rapid than that occurring due to exposure to N₂. The resistance increase was found to be reversible when the devices were re-exposed to air. It is proposed that the NWs are doped by exposure to molecular oxygen and/or water in air, and then the dopants are neutralised or released by the octylamine. N₂ may be causing a similar effect but at a much slower rate.

As humidity sensors both the P3HT NWs and film had a threshold of 50% relative humidity before showing any significant change in conductance; the P3HT NWs were more responsive than the films, showing a 75-fold increase in conductivity at 90% RH compared with a 25% increase for the film. The greater surface area of the NWs in comparison to the films were deemed to be responsible for the greater sensitivity to the water vapour.

P3HT-NW WGOFETs had greater resistance than P3HT film WGOFETs, with $R = 43 \pm 0.5 \text{ k}\Omega$ and $23 \pm 0.5 \text{ k}\Omega$ respectively. The increased resistance was believed to be due to the smaller effective channel width of the P3HT-NW devices caused by gaps in the NW mesh. A greater off-current was seen in the P3HT-NWs compared to the film which was again attributed to gaps in the NW mesh which allowed penetration by the water droplet through to the source and drain contacts. P3HT-NWs were found to be more

sensitive to water-gating with $V_T = 0.07 \pm 0.05$ V compared to the P3HT film's 0.15 ± 0.03 V, and was believed to be due to greater interaction between the water molecules and the P3HT-NWs because of their greater surface area. The ratio of electrochemical current to field-effect current, $I_{\text{OECT}}/I_{\text{OFET}}$ was lower for the NWs compared to the film.

7.4 Future Potential

Where organic electronics are concerned nanowires have potential to make some impact and enhance the performance of devices. Facile pre-device processing makes nanowires an attractive material for many organic electronic applications. Where flexible devices are desired, such as roll-away displays, and solar cells for clothes and bags, substrates that exhibit these properties may not cope with post-fabrication heat treatment, such as the thermal annealing that consistently increases the performance of typical P3HT:PCBM OPVs. The ready made crystals that are NWs can circumvent this procedure and still produce reasonable performances.

The ability to intercalate dye molecules into the NWs, as demonstrated in this thesis, could prove to be a valuable tool in producing OPVs with higher efficiencies through improved light absorption, and rapid charge transfer and separation. This approach was investigated, but the resulting efficiency values were disappointing compared with conventional optimised P3HT:PCBM bulk heterojunction devices, the best of which yield PCE values of 4-5%. The intercalation of dyes in nanowires was observed to influence J-V curves and devices efficiencies compared with corresponding P3HT-NW:PCBM devices. No clear interpretation of the effects of the dye could be identified, though charge trapping and recombination is a likely

cause of the relatively poor performance.

Furthermore, intercalation of these dye molecules into the NWs could prove to be an effective and facile means to producing selectivity in NW chemisensors. If the functional groups attached to the anthraquinone moiety were designed to interact with specific analytes, such as heavy metals or other toxic species then a low cost, highly sensitive, and selective sensor could be easily realised and commercialised.

Where organic electronics may only occupy a niche market and not compete directly with traditional inorganics, NW devices will surely be apart of the field for their unique potential that they hold.

Appendix A

Chemistry Data

Presented here are the data used to determine the dye molecules' energy levels and successful intercalation, which includes cyclic voltammetry plots, UV-Vis absorption spectra, emission spectra and combustion analysis data.

Table A.1: Combustion analysis results

Dye	Elemental Content / %wt/wt		
	Carbon	Hydrogen	Nitrogen
1a	71.20	8.40	0.00
1b	71.52	8.44	0.09
1c	71.47	8.35	0.00
1d	70.97	8.01	0.72
2a	71.63±0.04	8.56±0.02	1.05±0.03
2c	71.76±0.02	8.49±0.03	1.08±0.05

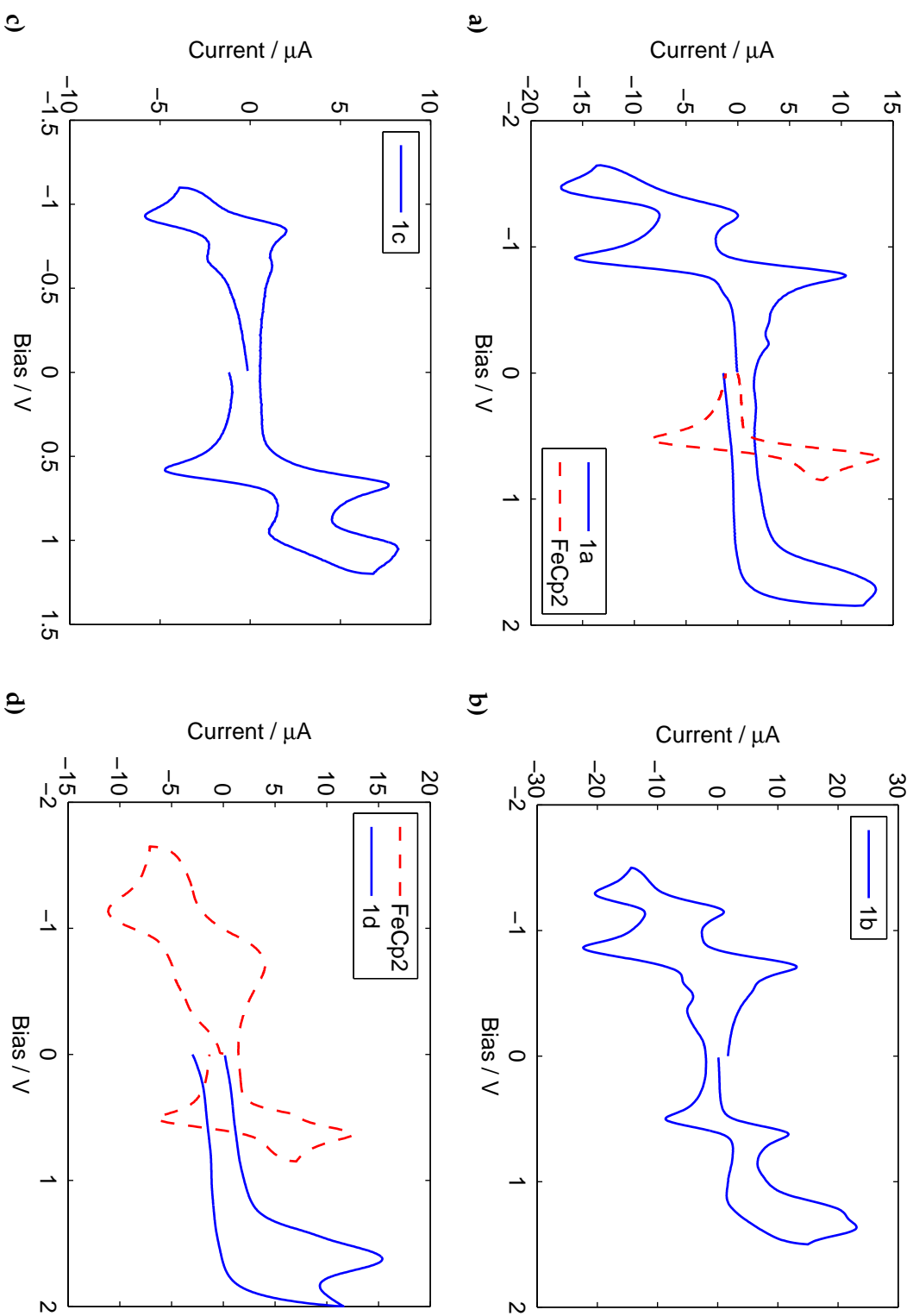


Figure A.1: Cyclic voltammograms of a) 1a (solid blue line) and FeCp₂ calibrant (red dashed line), b) 1b including FeCp₂ calibrant with characteristic oxidation peaks circa 0.46V, c) 1c including FeCp₂ calibrant with characteristic oxidation peak circa 0.46V, and d) 1d (solid blue line) and FeCp₂ calibrant (dashed red line)

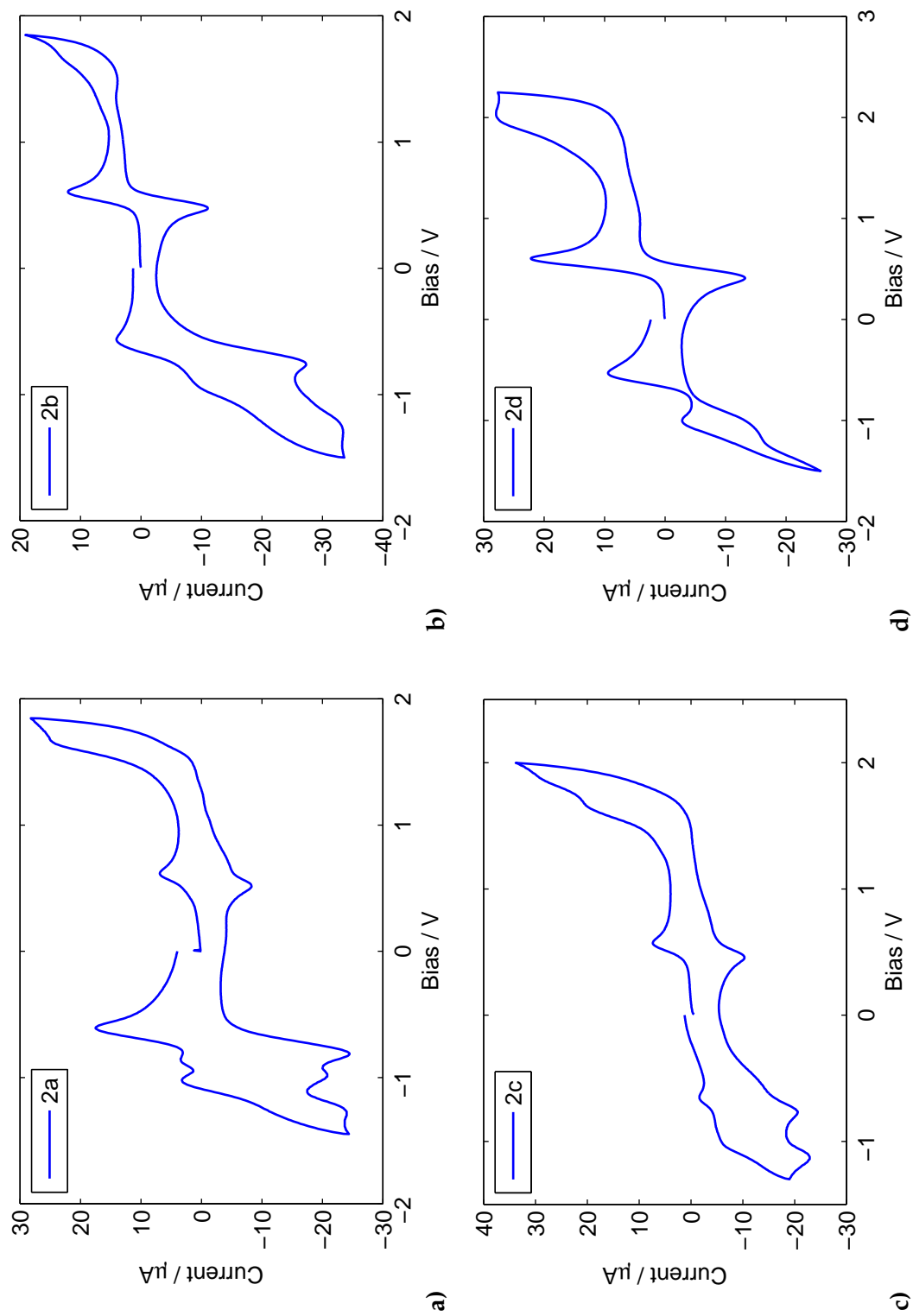


Figure A.2: Cyclic voltammograms of a) 2a, b) 2b, c) 2c, and d) 2d. All samples include FeCp₂ calibrant with characteristic oxidation peaks circa 0.46V

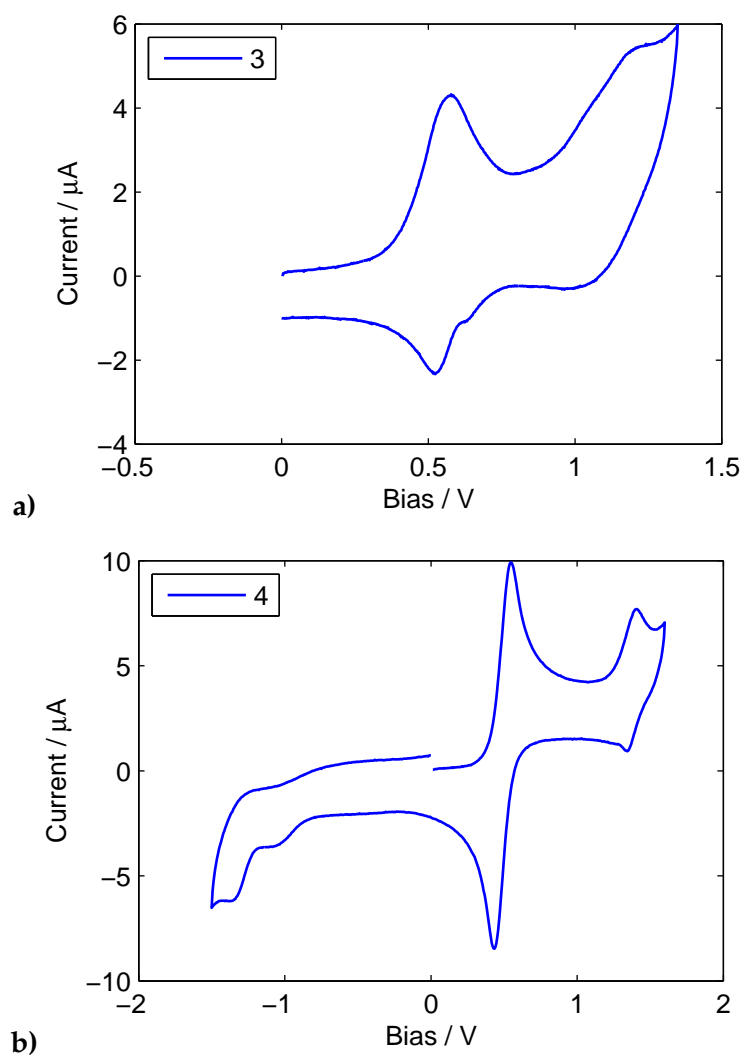


Figure A.3: Cyclic voltammograms of a) 3, b) 4. All samples include FeCp_2 calibrant with characteristic oxidation peaks circa 0.46V

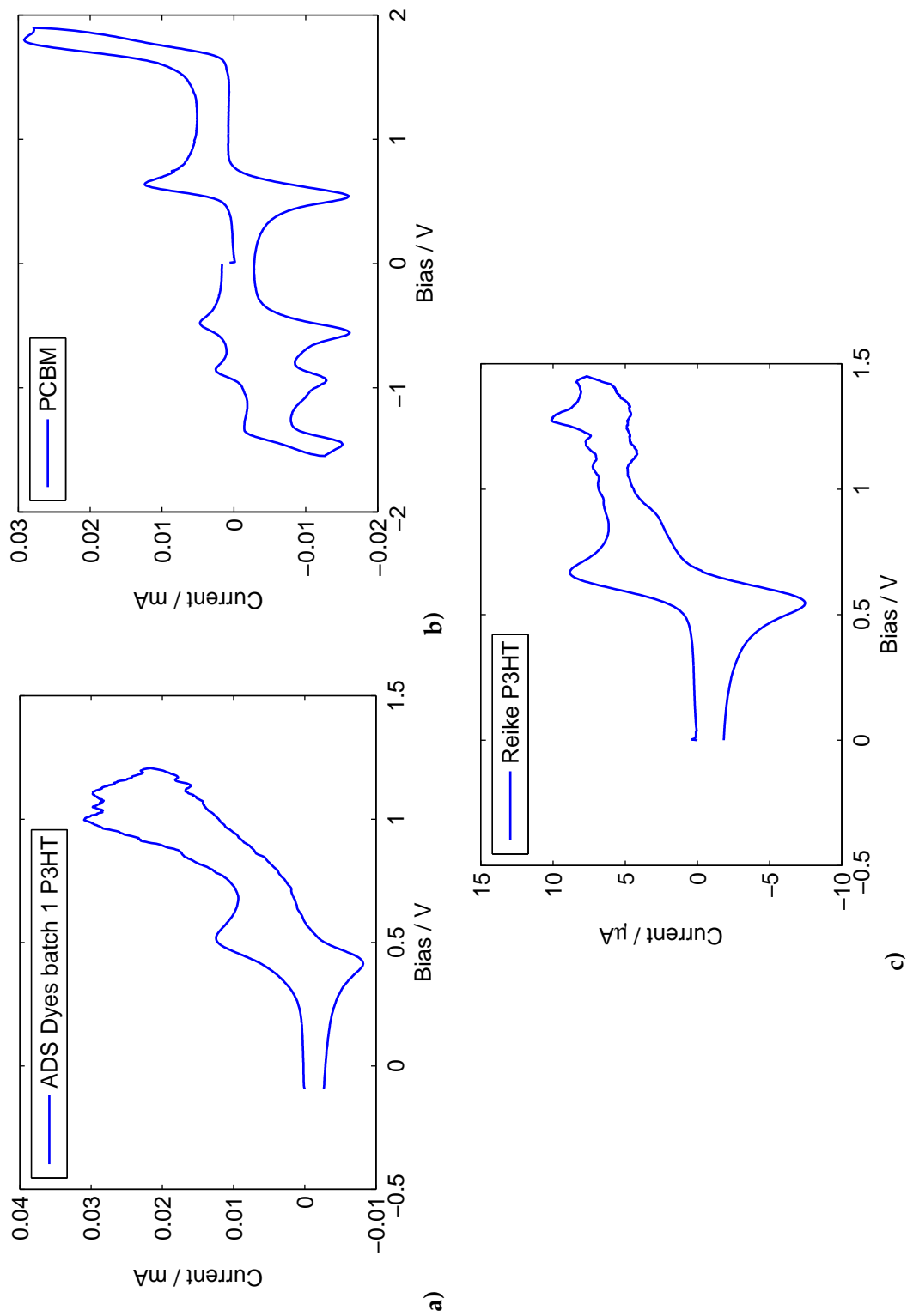
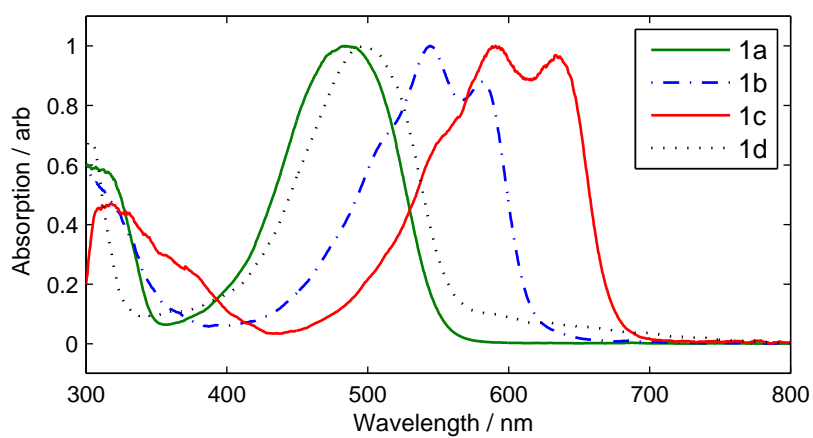
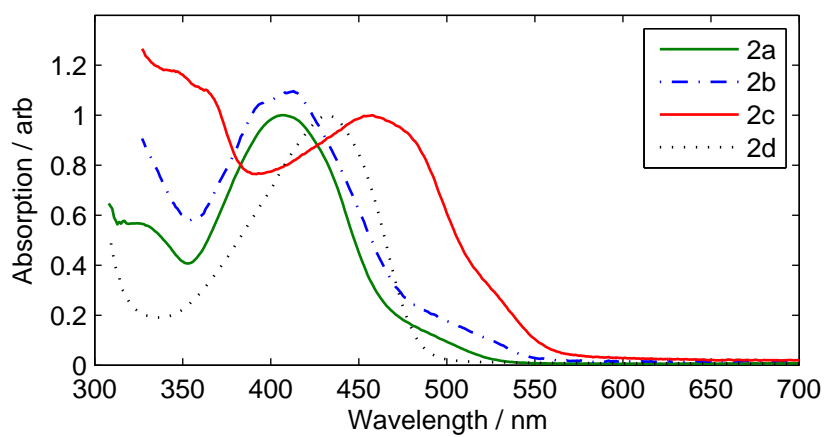


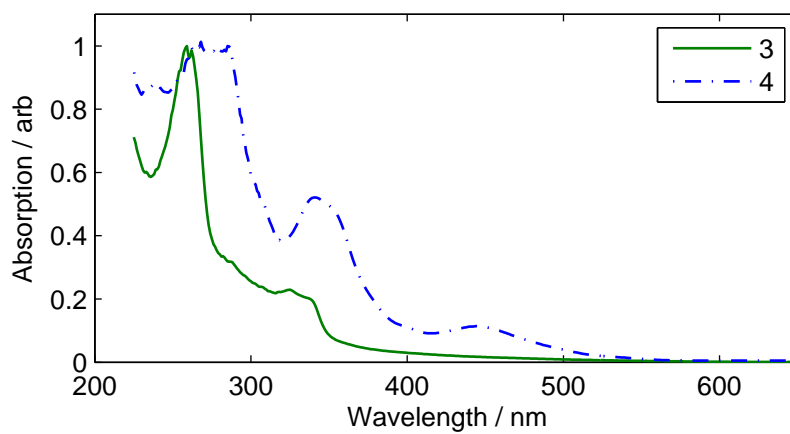
Figure A.4: Cyclic voltammograms of a) ADS Dyes first batch P3HT, b) PCBM, and c) Reike P3HT. All samples include FeCp₂ calibrant with characteristic oxidation peaks circa 0.46V.



a)

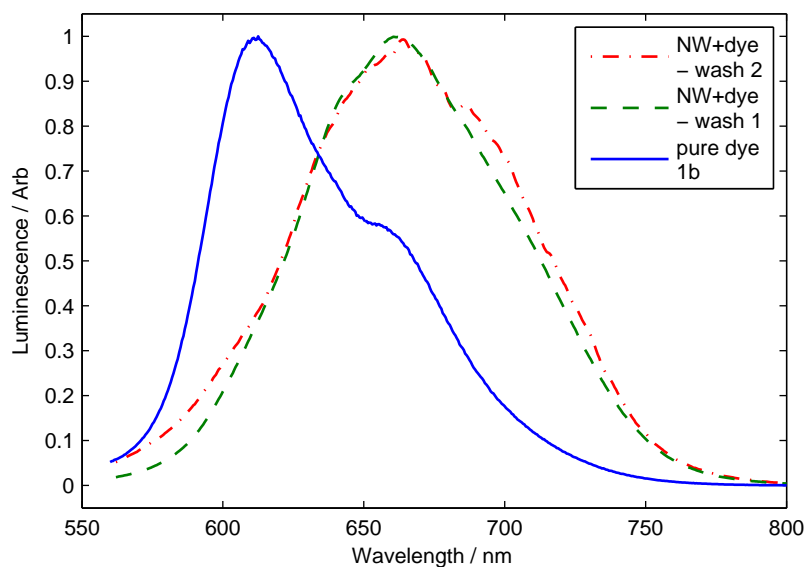


b)

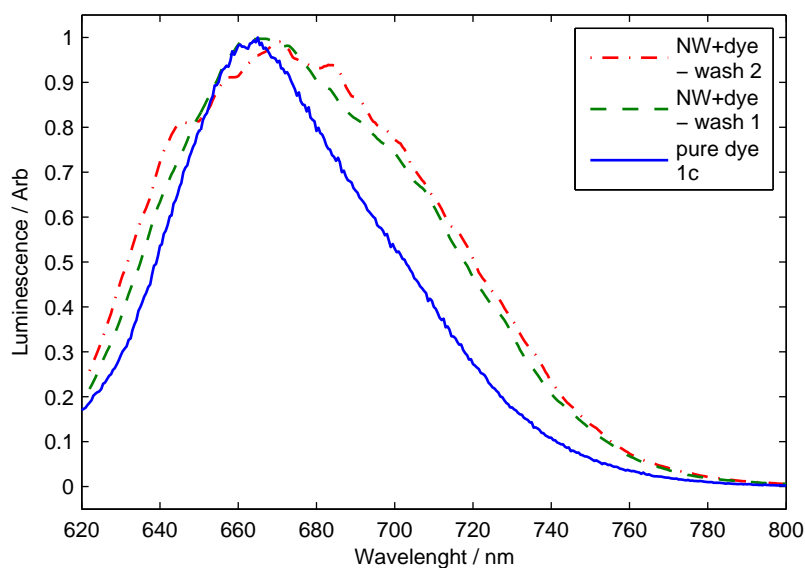


c)

Figure A.5: UV-Vis spectra for dyes 1a,1b,1c, and 1d.



a)



b)

Figure A.6: Emission of a) dye 1b and b) dye 1c, intercalated into P3HT anisole NWs, illuminated at 540 nm and 600 nm respectively. The solutions containing the NWs and dyes was centrifuged and 'washed' with diethyl ether twice, with the emission shown after each cycle. Due to the overlap of the dye emission with that of the NWs, and the relatively low emission from the dye it was difficult to ascertain whether the intercalation was successful in these cases.

Appendix B

OFET and Sensor Data

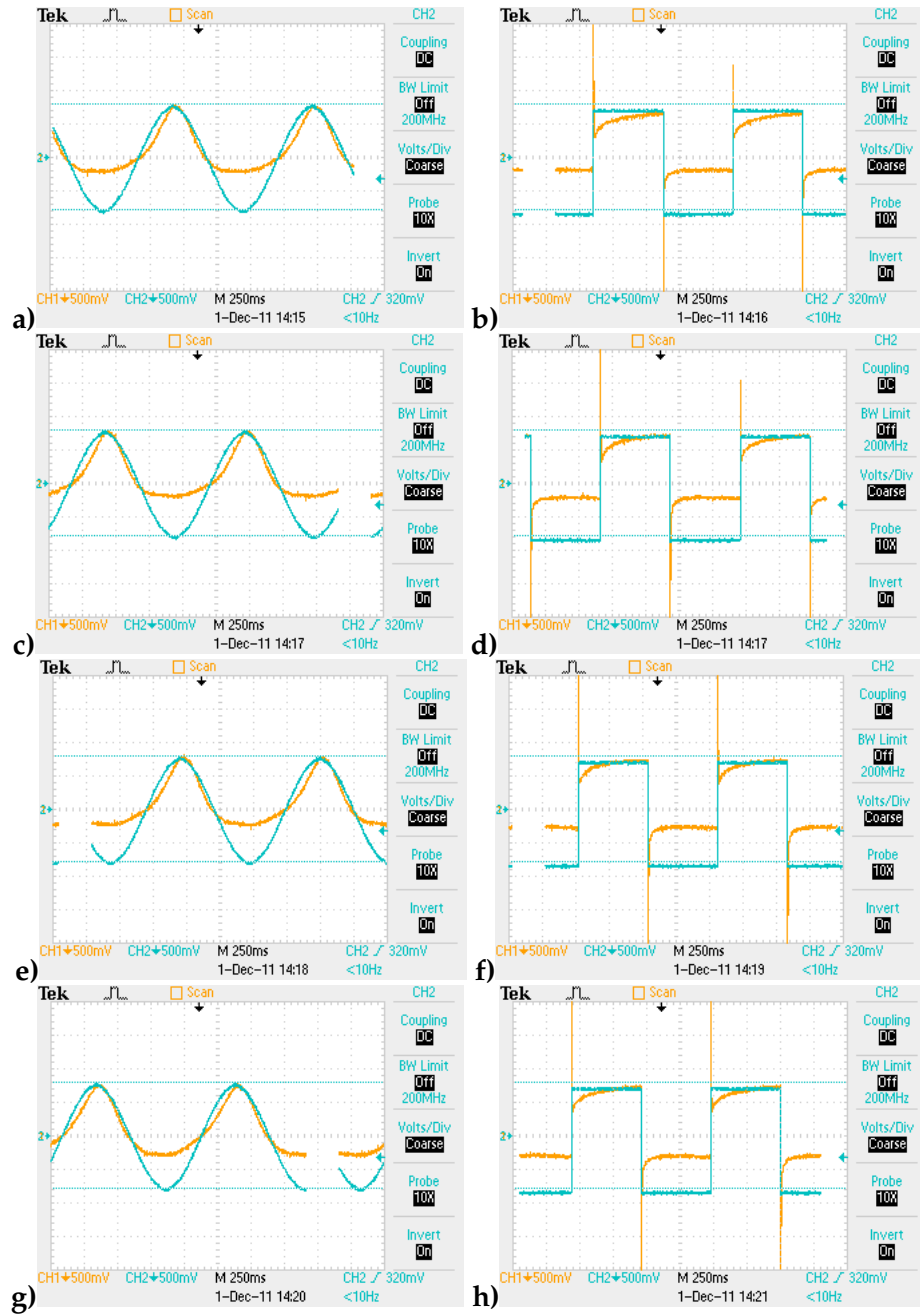


Figure B.1: Time evolution output curves from water-gated P3HT NW OFETs. a) Ungated dry device, $R_F = 100 \text{ k}\Omega$. Water-gated at b) 10s, $R_F = 43 \text{ k}\Omega$; c) 35s, $R_F = 37 \text{ k}\Omega$; d) 100s, $R_F = 49 \text{ k}\Omega$; e) 140s, $R_F = 42 \text{ k}\Omega$; f) 180s, $R_F = 51 \text{ k}\Omega$; g) 230s, $R_F = 47 \text{ k}\Omega$; h) .

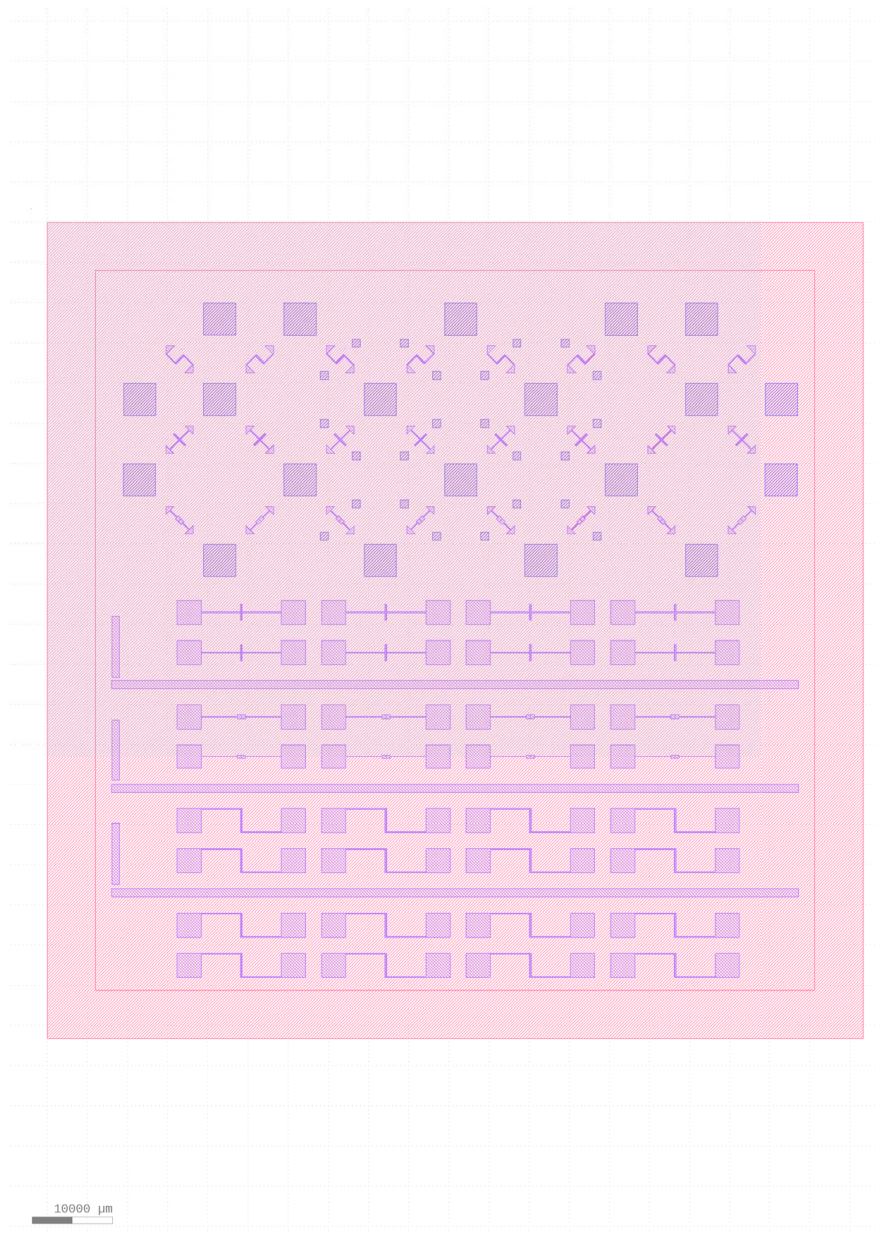


Figure B.2: Electrode design from KLayout GDS file. The dark portions are clear glass, while the lighter portions are chromium coated glass. The lower portion of the mask was composed of designs for normal photolithography and subsequent Cr and Au evaporation of electrodes on to OFET substrates. The top portion of the mask was for patterning silicon nitride masks for use as shadow masks. Also seen are viewing windows for mask alignment during photolithography.